UNIVERSITY OF LIVERPOOL

Heat Transfer, Fluid Transport and Mechanical Properties of Porous Copper Manufactured by Lost Carbonate Sintering

Thesis submitted in accordance with the requirements of the University of Liverpool for the Degree of Doctor in Philosophy

by

Zhu Xiao

November, 2013

Abstract

Over the last few decades, porous metals have received a growing interest in industry due to their unique physical and structural properties and many potential applications ranging from light weight structure, filtration, energy and sound absorption to thermal management and electromagnetic shielding. In thermal applications, high energy consumption units demand higher and higher heat transfer performance. Porous copper is an ideal option for these applications due to its high specific strength, excellent thermal conductivity and high surface area. The Lost Carbonate Sintering (LCS) method is an efficient and simple manufacturing process to produce porous copper with a large range of porosity, various pore sizes and pore shapes.

The main objective of this study is to investigate the heat transfer, fluid transport and mechanical properties of porous copper fabricated by the LCS method. The permeability, thermal conductivity, heat transfer coefficient and mechanical properties were studied on a number of porous metal specimens with different porosities/relative densities, copper particle sizes, pore sizes, pore shapes and combinatorial structures.

A purpose-built apparatus was used to study the effects of pore structure on permeability. The results showed that pressure drop of LCS porous copper fits well with the Forchheimer-extended Darcy equation. The permeability increased with porosity and copper particle size, but decreased with pore size. The permeability can be predicted well using the modified Carman-Konezy relationship by introducing the tortuosity of LCS porous metal for both single and double layer structures.

The thermal conductivity of LCS porous copper increased with relative density and pore size, but decreased with copper particle size. The thermal conductivity decreased with the size ratio between copper particle and pore at any given porosity. An empirical equation was established to describe for this relationship.

Heat transfer coefficients were measured for a large number of samples. Compared with an empty channel, introducing a porous copper sample enhanced the heat transfer coefficient by a factor of 2–10. The samples with low porosities and large pore sizes showed high heat transfer coefficients. There was an optimal porosity range for good heat transfer performance at a given pore size. The heat transfer coefficient of LCS porous copper with double-layers was sensitive to the placement-order of the layer. A segment model was developed to predict the heat transfer coefficient of multilayer structures and the predictions agreed well with the experimental results.

The mechanical properties of LCS porous copper fabricated with fine copper particles were studied by compression, bending and tensile tests. The mechanical strength and apparent modulus, decreased with porosity. The porous copper samples with large pore sizes had better mechanical performance. The extended Mori-Tanaka model was used to predict the modulus and the predictions agreed well with the experimental data.

Declaration

This thesis is submitted for the degree of Doctor in Philosophy in the faculty of Engineering at the University of Liverpool. The research project reported herein was carried out, unless otherwise stated, by the author, in the School of Engineering at the University of Liverpool between March 2010 and July 2013.

I confirm that the thesis is my own work that I have not presented anyone else's work as my own and that full and appropriate acknowledgement has been given where reference has been made to the work of others.

Zhu Xiao

November 2013

Acknowledgments

Primarily I would first like to sincerely thank Dr. Y.Y. Zhao and Dr. L. P. Zhang for their supervision and guidance throughout the PhD programme. Their help, knowledge, and insight are invaluable.

I would also like to express my gratitude to Prof. Z. Li, Prof. B. Zhang and Dr. S. Gong for their kind help in the experimental and theoretical modeling work during the time of the PhD programme.

I wish to acknowledge the studentship from the University of Liverpool and Chinese Scholarship Council.

Many thanks go to those who help in the experimental aspects of this research. They are: Mr. D. Atkinson for preparation of samples, Mr. D. Neary and Mr. J. Mathew for setting up the heat transfer facility and Mr. S. Pennington for mechanical testing.

I would also like to show my gratitude to all my friends for their support and encouragement throughout the PhD.

Finally, I would like to thank my family, especially my dearest wife, Dr. M. Fang, who took on many extra responsibilities so that I could concentrate on my PhD study. They remain a constant source of support and strength.

List of Publications

Xiao, Z., Zhao, Y. Y. 2013. Heat transfer coefficient of porous copper with homogeneous and hybrid structures in active cooling. Journal of Materials Research, 28:2545-2553 (DOI: 10.1557/jmr.2013.190)

List of Figures

List of Tables

List of Symbols

A	Cross section area	m^2
a b	Fitted constant	
C	Drag form coefficient Volume fraction of the pores in Eq.(5.42)	m^{-1}
c_F	Inertial coefficient	m
c_p	Specific heat	J/Kg K
d D	Diameter	m
D_c	Characteristic length	m
D_h	Hydraulic diameter	m
D_p	Mean particle diameter	M
E	Elastic modulus	Pa
f	Thickness fraction	
g	Gravitational constant	m^3 /kg s^2
h	Heat transfer coefficient	W /m^2K
H	Height or depth	m
J	Total heat transfer rate	W
j	Scale factor in Eq.(5.35)	
K	Permeability	m^2
k	Kozeny constant	
k_0	Shape factor	
L	Length	m
L_e	Average path length of flow for tortuosity calculation	m
L^e	Equivalent stiff matrix for porous metal	
L^m	Stiff matrix of the solid	

m	Constant in Eq.(5.29)	
M	Mass	Kg
n	Exponent or fitting constant or group number	
N	Variable constant in Eq. (5.42)	
Nu	Nusselt number	
P	Pressure , or Counting point number	Pa
Pr	Prandtl number	
p	Partition factor in Eq.(5.36)	
Q	heat flow	W
q	heat flux	W /m^2
r	Initial particle radius in Eq.(2.13)	
R	Gas constant	J/K mol
R^2	Coefficient of determination	
Re	Reynolds number	
s	Size ratio between copper particle and pore	
S	Eshelby's tensor	
S_0	Specific surface area based on solid's volume	mm^2/mm^3
S_v	Specific surface area based on the whole volume	mm^2/mm^3
T	Temperature	°C, K
t	Thickness	mm
	Time	s
u	Volume flow rate	m^3 /s
V	Volume	m^3
v_d	Darcian velocity	m/s
v_p	Pore velocity	m/s
W	Width	m

Greek symbols

α	Fitted constant	
β		
δ	Deflection	
δ_{ij}	Kronecker delta	
ε	Porosity	%
ε_n	Nominal porosity	%
θ	Deflection angle	
λ	Thermal conductivity	W/mK
λ_m	Lamé constants	
μ	Dynamic viscosity	Kg/ms
μ_m	Shear modulus	Pa
ρ	Density	Kg/m^3
τ	Tortuosity	

Subscripts

ave	Average
b	Bending
bl	Heating Block
c	Compression
cond	Conduction
conv	Convection
crit	Critical
Cu	Copper
eff	Effective
f	Fluid
h	High porosity or high permeability layer
in	Inlet

inter	Intersection
K_2CO_3	Potassium carbonate
l	Low porosity or low permeability layer
out	Outlet
part	Particle
pl	Heating plate
pore	Pore
pr	Pressure
r	Radiation
re	Relative
s	Solid
t	Tensile
test	test line
tot	Total

Table of Contents

Chapter 1

Introduction

Porous metals are cellular structural materials with a large volume fraction of pores. Compared to bulk metals, porous metals offer some interesting physical properties such as low density, high specific strength, good impact energy and sound absorption and excellent thermal management abilities. There are a large number of porous metals that can be produced with various metals and alloys. This new class of materials offers a combination of properties and has attracted the attention of many scientists and engineers.

1.1 Background and Motivation of Research

Over the last decade, porous metals have been widely used in medical equipment, home appliances, electric components, transformers, motors, aircraft and navigation systems, etc., and have become an important and indispensable class of materials in industry and everyday life. Porous metals, however, have only several decades of history and are still in the relatively early stages of development.

The first patent for producing porous metal was developed by Sosnick (1948) who proposed an idea to produce aluminium foam through gasification of mercury in molten

aluminium. Elliott & Madison (1956) further developed Sosnick's idea and successfully produced aluminium foam for industrial applications. A tremendous amount of work on production methods, properties and applications of porous metals has been done by researchers in the next several decades. In recent years, the interest in the multi-functionality of porous metal has increased. New advanced methods of manufacture decreased the cost of production and improved the properties of porous metals. Novel research methods and materials design methodology have been developed for porous metals and the knowledge in this field is expanded rapidly.

Porous metals can show different and special characteristics in physical, mechanical, thermal, acoustical and electrical properties by having different pore parameters and different internal structures. There are several common features for porous metals: low density, relatively high specific strength, high specific surface area, good permeability and energy absorption ability. The greatest strength of porous metals is their ability to combine two or more functions to give multi-functions from a single method.

High energy consumption units, such as the large-scale integrated circuit systems, have a very high heat transfer demand. The heat removal devices need to bear both high mechanical load and high heat flux. Open-cell porous metals with large specific surface area and good permeability for coolant are the best candidates for application in multifunctional heat exchangers and heat sinks. Vibration sensing units, such as gauge

boards in aircraft, require certain strength and high damping capacity to maintain high accuracy and stability during service. Porous metals with high specific strength and energy absorption capability could be a good choice for these applications.

The Lost Carbonate Sintering (LCS) process is a space-holder based fabrication method developed by Zhao et al. (2005). This technique has attracted much attention in recent years as an efficient and simple manufacturing process to produce open-cell porous metal with a large range of porosity, various pore sizes and pore shapes. The thermal properties and heat transfer performance of porous copper manufactured by the LCS method are of particular interest. The prominent thermal properties of copper in its solid form, combined with the unusual pore morphology and topography resulting from the LCS process, give rise to some fascinating and unconventional thermal characteristics. It is timely to study the heat transfer performance and mechanical behaviour of open-cell porous copper, which could provide a guidance for the design of compact heat exchangers and heat sinks with good heat transfer performance and mechanical properties.

1.2 Objectives of Research

The main objective of this study is to investigate the heat transfer, fluid transport and mechanical behavior of porous copper fabricated by the LCS method.

Several basic physical parameters, including permeability, thermal conductivity and heat transfer coefficient, are necessary to evaluate the heat transfer characteristics of porous metals. It is essential to investigate these properties for porous copper used in advanced, compact and lightweight thermal management systems. The porous copper studied in this thesis is not intended for structural applications, however, their mechanical properties are important for the target applications, like electrodes, catalyst supports, sound absorbers, electromagnetic shields and filters. The mechanical properties are also important for handling, shipping and assembling, in addition to the in-service requirements.

The permeability, thermal conductivity and heat transfer coefficient will be studied on a number of porous metal specimens with different porosities, pore sizes, pore shapes and combinatorial structures. The mechanical behaviour of LCS porous copper will be investigated by means of bending, tensile and compression tests.

1.3 Structure of Thesis

There are six chapters in this thesis. Chapter 2 reviews the literature on the relevant work in the field. The methods and techniques to produce closed-cell and open-cell porous metals and their advantages and disadvantages will be introduced. The techniques used to characterise the microstructure and physical properties, including pore parameters, fluid permeability, thermal conductivity, heat transfer coefficient and

mechanical properties, will be reviewed. Different types of porous metals and their properties will be reviewed. Some engineering applications of porous metals, especially the thermal applications of porous metals as heat exchangers and heat sinks, will also be discussed.

Chapter 3 gives a detailed description of the manufacturing method and experimental procedures used in this work. The fabrication procedures and conditions of the LCS method to produce porous copper test samples are explained. The structural characterization and analysis techniques are presented. The experimental equipment, measurement method and test procedure for fluid permeability, thermal conductivity, heat transfer coefficient and mechanical properties are described.

Chapter 4 presents the results obtained from the experiments in graphical and tabulated forms. The microstructure and pore structure parameters of porous copper are described. The effects of pore parameters on fluid permeability, thermal conductivity, heat transfer coefficient and mechanical properties are described in detail. The heat transfer coefficient of the porous copper with a double-layer structure is presented in detail.

Chapter 5 discusses and gives a detailed analysis of the experimental results presented in Chapter 4. Particular attention is paid to theoretical correlation of permeability, thermal conductivity, heat transfer coefficient and elastic modulus with pore parameters.

Chapter 6 summarizes the conclusions obtained from this study and makes some suggestions of possible areas for future research.

Chapter 2

Literature Review

Porous metals are a new class of materials with low densities and novel physical, thermal, acoustic and mechanical properties. So far, they are still imperfectly characterized and research on this new materials accelerates rapidly. It is anticipated that the new knowledge on porous metals will expand quickly over the next decades.

2.1 Introduction to Porous Metals

Porous metal can be defined as a cellular structure of a solid metal containing a dispersion of gas-filled pores or voids. Its density is lower than that of the bulk metal because of the existence of pores. The pores can be either sealed or interconnected, depending on the production method chosen for potential applications. Compared with bulk materials, porous metals possess a number of unique and fascinating properties due to its relatively low density combined with some physical properties. Porous metal can be used as either a structural material or a functional material, or a combination of both structural and functional material. In recent years, a large number of porous metals based on different metallic materials, such as aluminium, copper, steel, magnesium, zinc and their alloys, have been exploited. So far, several commercially available

porous metals, such as porous aluminium, porous nickel and porous copper, have been used in engineering applications.

Porous metals attracted scientists' attention in last century and are still receiving a growing interest in recent years due to their unique physical and structural properties (Ashby et al. 2000). Considerable attention in both academia and industry is focused on their low density, relatively high specific strength, air and water permeability, and thermal and acoustic properties. Although a lot of research on the potential applications of porous metals has been carried out, the applications are still confined in a limited number of engineering fields due to technological and economic issues. Theoretical and practical studies on the fabrication and properties of porous metals are still in progress.

Porous metals can be fabricated by either the traditional casting-foaming process or a solid forming process. Early production methods for porous metals or "metal foams" are mainly based on casting and foaming techniques (metals with pores deliberately integrated into their structure through a foaming processing). The most successful example of foaming being the commercial aluminium foam, which can be obtained by injecting air into and mechanically agitating a mixture of molten aluminium and SiC particles. The solid forming process usually refers to the powder metallurgy technique, where the metal powder can be sintered independently or mixed with a foaming agent (e.g. TiH_2) or a space holder (e.g. NaCl). A large number of new production methods

have recently been developed, such as high temperature self-propagation synthesis, electrodeposition and laser foaming.

Closed-cell porous metals are often used as structural materials, such as impact energy absorbers, electromagnetic shields and decoration materials for the construction industry. Open-cell porous metals are used as noise absorption materials, filters and biomaterials, etc. Open-cell porous metals are particularly suited to heat exchange applications because they have a high specific surface area, a good thermally conducting solid matrix and a tortuous internal network of pores promoting turbulence and mixing of the coolant (Boomsma 2003). Good thermally conducting metals, such as aluminium and copper, can be used for the matrix of porous metal.

2.2 Production Methods and Techniques

There are a number of methods and techniques available to produce porous metals. Some of the production methods have been applied in industrial manufacture and new novel techniques are developed to achieve better properties and lower production cost.

2.2.1 Closed-cell porous metals

Closed-cell metallic foams can be manufactured in many different ways. In most cases, they are formed by injecting gas or decomposing a chemical blowing agent in the metallic melt. Recent research is mainly centred on the investigation of foaming and

stabilisation mechanisms, the development of new blowing agents, the optimisation of the fabrication processes and the reduction of the fabrication costs (Degischer & Kriszt 2002). Different production methods are described as follows.

2.2.1.1 Foaming

The first reported method to produce closed-cell metal foams was developed in the USA (Sosnick 1948). The process involved melting bulk metals and mercury in a closed chamber preventing escape of the mercury vapour. The boiling point of mercury is about 357^{o} C, and its vapor pressure may be increased to the point where the mercury in the mixture is stabilized. The molten mass was then released from the high pressure chamber to a low pressure space. The volatilization of mercury in the mass caused it to become foamy or sponge-like. Upon cooling a sponge metal resulted.

The process was used to produce solidified metals containing the enclosed voids. Examples of mixtures suitable for forming sponge metals are: magnesium/mercury, aluminium/mercury, chromium/cadmium and gold/mercury. The porosity is greatly dependent upon the capacity of the enclosure to produce a desired vapour pressure. Therefore, it is not easy to control the pore parameters using this method. Furthermore, mercury is an extremely toxic substance and harmful to the environment.

2.2.1.2 Gas injection in melt

Metal foam can be produced by directly injecting gas into a metallic melt. Pores can be formed from the gas bubbles in the melt during the solidification of the melt. This process, however, is not easy to control. The gas bubbles can separate and exhaust from the liquid very fast, so that there is insufficient time to keep bubbles in the metallic melt before the solidification, however, it is possible to foam metallic melt using this method by adding an amount of indissolvable ceramic particles, like Al_2O_3 or SiC, which are used to increase the viscosity of the metallic melt (Niebyski et al. 1974, Jin et al. 1992). The gas is blown into the melt using a tube assisted by specially designed, rotating impellers. When the gas is injected, the bubbles form and rise to the surface of the melt slowly because of the high liquid melt viscosity. The melt begins to solidify after a relatively uniform distribution of bubbles is formed in the melt. The foaming gas can be air, nitrogen, carbon dioxide or inert gases (Niebyski et al. 1974).

It is relatively simple to implement this method to produce porous aluminium, because aluminium has a low density and oxidation of molten aluminium is not serious when exposed in air or other gases because of the dense Al_2O_3 protective film forming on the surface of molten aluminium. Several techniques based on this method to commercially manufacture aluminium foam have been developed and several companies, such as CYMAT Technologies Ltd. (Canada) and NORSK HYDRO ASA (Norway), produce commercial output from the process. Although the cost of this production method is

quite low, it is only suitable to manufacture aluminium foam with relative density between 0.03-0.1 (Ashby et al. 2000).

2.2.1.3 Decomposition of gas-releasing particles in melt

This method is similar to gas injection as it uses gas to form the pores, however, in this case a foaming agent, which releases gas after heating to produce pores in the metallic melt is used. The most common foaming agent is titanium hydride (TiH_2).

Elliott (1956) successfully produced foamed aluminium using this method. Currently, several typical metal foams, for example, Alporas aluminium foam (Alporas, USA), have been made by this method, shown in figure 2.1 (Ashby et al. 2000). The aluminium is firstly melted and the temperature of the melt is maintained between 670-690^{o}C. 1-2% calcium is added to the melt, which quickly oxidizes to form uniformly distributed CaO and $CaAl_2O_4$, increasing the viscosity of the liquid melt. TiH_2 particles (1-2%) in the size range 5-20 μm are added whilst the molten metal is stirred. Once these particles are dispersed throughout the melt, stirring is stopped and a froth begins to appear in the melt. The whole process is controlled by adjusting the pressure, system temperature and operation time. It usually takes about 10 minutes for the decomposition of TiH_2. After frothing, the melt is cooled to a solid and the hydrogen escapes from the material. Finally, a solid cellular structure is obtained, which is removed from the furnace for further processing.

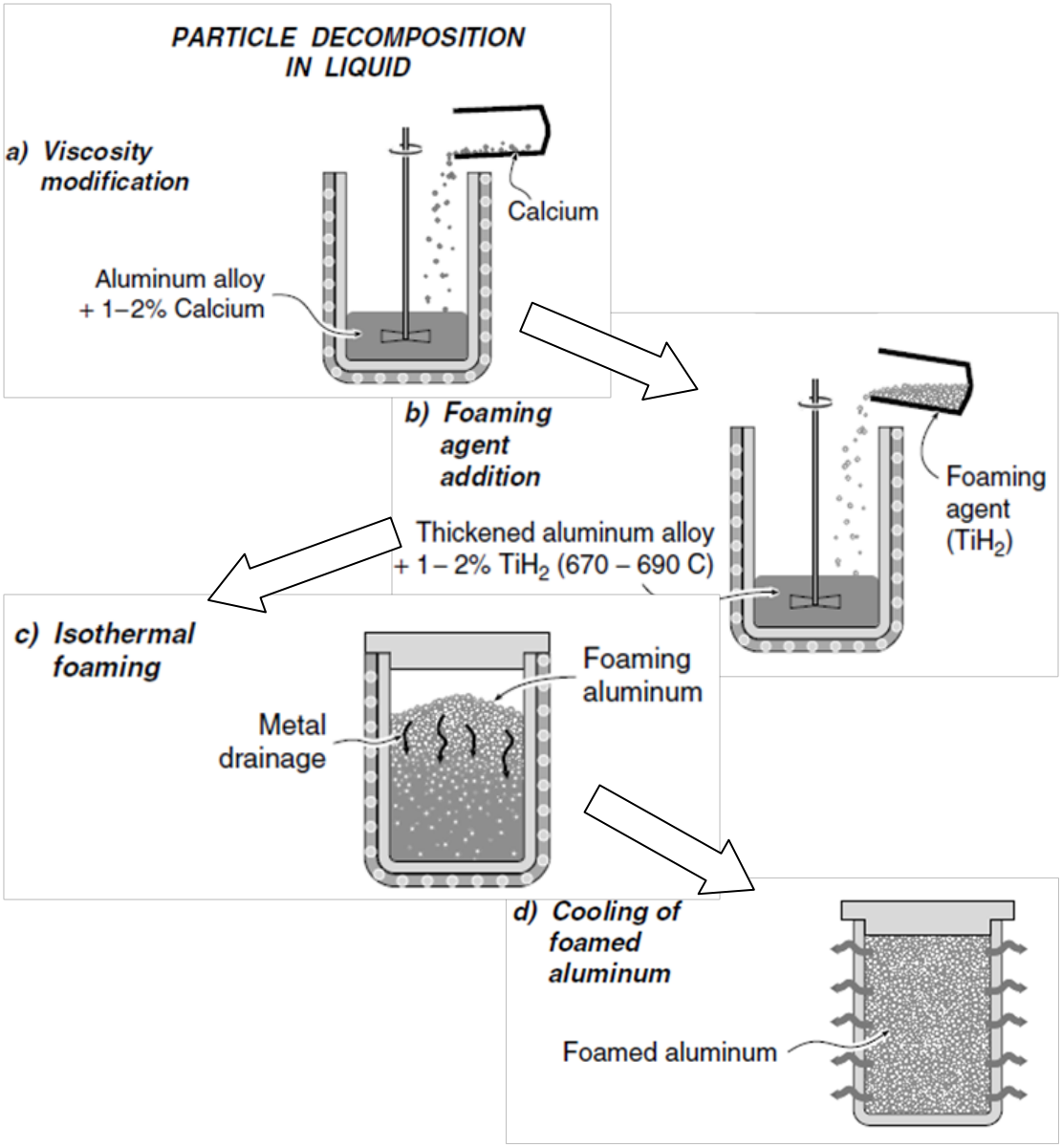

Figure 2.1 *Production process of Alporas aluminium foam (Ashby et al. 2000).*

Figure 2.2 shows the pore structure of a typical foam fabricated using this method. The relative density of the foam is determined by the amount of additives, including calcium and TiH_2. The pore size is determined not only by the amount of additives, but also by the cooling conditions of the system during production. Alporas foam has closed-cells,

with relative density between 0.07-0.2 and pore size between 0.5-5mm. This manufacturing method, however, has some disadvantages: the pore size and pore size distribution cannot be accurately controlled, and this lack of control results in a larger pore density at the centre of the sample. Furthermore, TiH_2 cannot be used to produce foams from some metals or alloys, typically like zirconium, high carbon steel and ferro-alloys, because of hydrogen embattlement sensitivity.

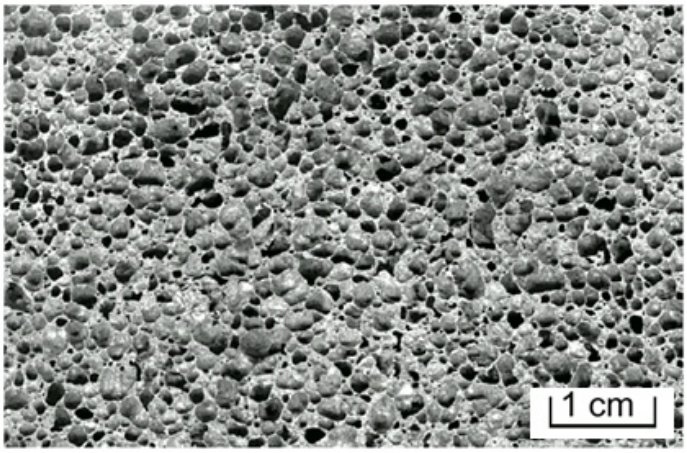

Figure 2.2 *Pore structure of close-cell Alporas aluminium foam (Banhart 2000).*

Improvements have been made to overcome these problems. It is recommended to use high speed mixing to disperse the blowing agent throughout the molten metal in a very short space of time to avoid a non-uniform pore size and pore size distribution. Increasing the viscosity of the molten metal by using specific agents or using specific alloys as the bulk material is also a method to aid in preventing the escape of gas

bubbles. Some other foam agents, like nitrate or carbonate, can be used to replace the TiH_2, making it possible to produce porous steel, nickel and their alloys.

2.1.2.4 Gas-metal eutectic solidification

This method uses the metal-hydrogen eutectic reaction characteristics and the directional solidification technique to produce porous metal. Numerous alloys, including Al-, Be-, Cr-, Cu-, Fe-, Mg-, Mn- and Ni-based alloys, have eutectic reactions with hydrogen (Schwartz & Shih, 1998). The alloy is melted, saturated with hydrogen under pressure, and then directionally solidified, progressively reducing the pressure. During solidification, solid metal and hydrogen simultaneously form by a gas eutectic reaction, resulting in a porous material containing hydrogen-filled pores. Generally, largely elongated pores oriented in the direction of solidification are formed (see Figure 2.3). These materials are referred to as GASARs with “lotus” structure (Shapovalov 1993).

In order to use the process to make copper foam, a furnace placed within a pressure vessel is used to melt the copper under an appropriate pressure of hydrogen (typically 5-10 atmospheres). The melt is then poured into a mould where directional eutectic solidification is allowed to occur. This results in an object containing a reasonably large (up to 30%) volume fraction of pores. The process variables include melt over-pressure, melt superheat (which affects the hydrogen solubility of the liquid metal), the

temperature field in the liquid during solidification, and the rate of solidification. With so many process variables, control and optimisation of the pore structure are difficult. The method poses certain safety issues and, in its present form, is a batch process; as a result, although the materials were among the first highly porous materials to attract significant interest, they remain confined to academic research and are not yet commercially available.

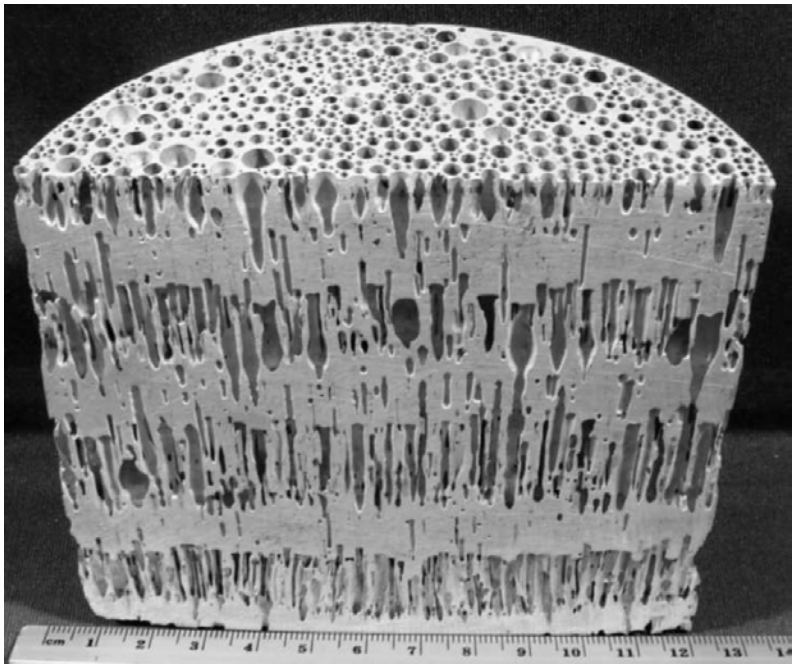

Figure 2.3 *Pore structure of Gasar (Shapovalov & Withers 2011)*

2.2.1.5 Metal expansion by trapped gases

This method is based on porous materials, where the pores are filled with high pressure inert gases. When the material is heated, the pressure in the pore increases, which makes the metal material expand through creep.

In this process, the porous particles are sealed in a metal container with the same material as the particles. The container is vacuumed and filled with 0.3-0.5MPa inert gas. It is then compacted by HIP to a densification of 0.9-0.98. The pressure in the pore is now increased by up to 8 times, but it is still too low to expand the metal. Hot-rolling is then introduced to improve the pore structure. The pores are deformed and elongated along the rolling direction. The wall of pores may contact and bond together, which leads to smaller gas voids. Tandem rolling can improve the uniformity of the pore distribution. The last procedure is to swell the metal at high temperature for 20-30 hours. Normally, the pressure in the pore increases to 10-16MPa, and the metal sample expands by creep. Schwartz & Shih (1998) produced Ti-6Al-4V porous metal by this method.

Sandwich structure parts with titanium foam interlayer can be made by this method. The porosity of the core plate can be up to 50%, while the pore size is 10-300 μm. This technique, however, is complex and costly, which makes it unsuitable for industrial manufacture.

2.2.2 Open-cell porous metals

Open-cell metal foams with high porosity and permeability are well known and have been widely used for decades. They show a wide range of physical and mechanical

properties and may be adapted to multiple requirements. Several methods have been used to produce open-cell porous metals as described here.

2.2.2.1 Mould casting

Mould casting is a unique method of producing metallic foams. This process is used to produce metallic foams with the same shape as a foam template. It involves filling the pores of a plastic foam with a refractory material, which is then hardened and heated until the plastic foam is vaporized, leaving the refractory material as a porous mould. A molten metal is then poured into the porous frame and allowed to cool. Once solidified, the refractory material is removed by hammering the casting body and a metal foam of the same configuration of the plastic foam remains.

Open-cell polymer foams with low relative densities and a wide range of cell sizes of great uniformity are available from numerous sources. They can be used as templates to create investment-casting moulds into which a variety of metals and alloys can be made in this way including copper (Davies & Zhen 1983). Mould casting slurry is often used as the refractory material, which can be baked to harden into a mould. The method can be used to produce open-cell foams with pore sizes of 1-5 mm and relative densities as low as 0.05 (Banhart & Baumeister 1998).

Only metals with a low melting point can be used as the base material for these materials. These metals include copper, aluminium, lead, zinc, tin and a number of different alloys (Davies & Zhen 1983). A commercially available metallic foam under the trade name DUOCEL made by mould casting method is shown in Figure 2.4.

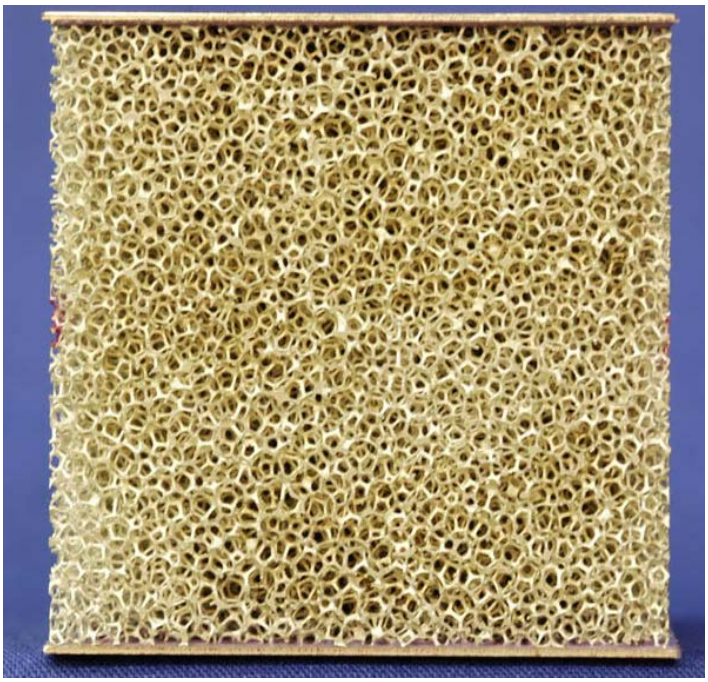

Figure 2.4 *Photograph of DUOCEL aluminium foam manufactured using mould casting (Jang & Kyriakides 2009).*

2.2.2.2 Fibre or wire metallurgy

As well as metal powders, metal fibres and wires can also be sintered resulting in porous metals with some unique properties (Lee et al. 2006, Zou et al. 2008). Various methods can be used to produce porous metal with the metal fibres and metal wires, and sintering is also a conventional technique. After sintering, the metal fibres and wires retain their strength, resulting in a porous metal which offers good mechanical

properties. Additionally, the porosity is highly controllable and the pore structure is such that high permeability can be achieved.

An example using metal wire to fabricate metal foam is a multi-layered Kagome truss periodic structure named “Wire-Woven Bulk Kagome (WBK)” truss (Lee et al. 2006). The fabrication is based on the assembly of helical wires in six directions. The structures are periodic and very uniform, have good specific properties and are highly permeable (Figure 2.5). This high permeability makes porous metals manufactured using this technique ideal candidates for use as filters. Metals used in this process include copper, stainless steel, nickel and Ni-Cr alloy.

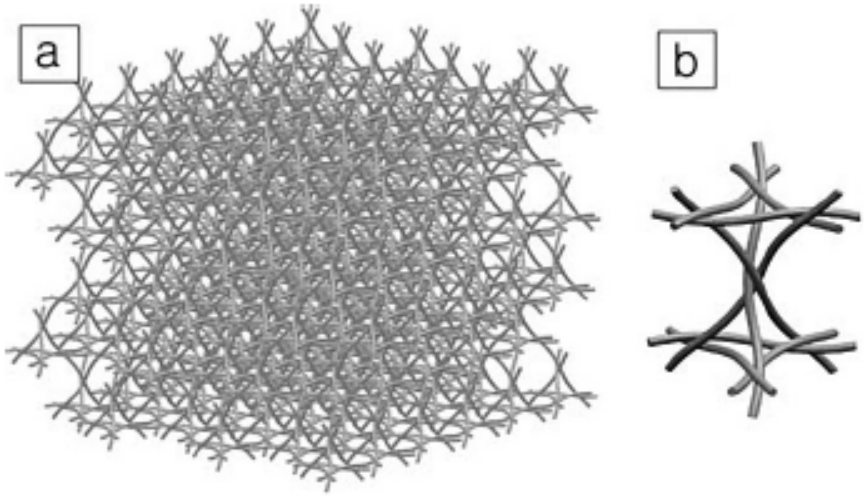

Figure 2.5 *Wire-woven Bulk Kagome (WBK) structure (a) and unit cell (b) (Lee et al. 2006).*

2.2.2.3 High temperature self-propagation synthesis (SHS)

SHS is a combustion synthesis process used to produce special porous metals (Chu et al. 1997, Li et al. 2000). There are two modes of SHS: one is thermal explosion, and the other is self-propagation combustion. The former works by heating the metal powders to a high temperature in a short time, and is mostly used to fabricate dense metal. The latter works by igniting the metal powders at one side and allowing the metal powders to self-propagate to the other side of the material. Using this technique porous metal with a porosity of 30-70% can be produced (Li et al. 2000). This technique is simple, low cost and energy efficient, however, the pore size is not easy to control and the final products are often brittle.

2.2.2.4 Electrodeposition

Metallic foams with high porosities and uniform pore distribution can also be manufactured using electrodeposition. A subtle way of making an open-cell foam is to start with an open-cell plastic foam as the mould, deposit an electrical conduction layer of carbon on it by vapor deposition, and subsequently electroplate metal onto the surface. Finally the construct is heated to remove polymer, resulting in an open-cell foam with hollow struts. Metals that can be deposited by electroless plating include copper, zinc, nickel and silver (Davies & Zhen 1983). The most common method of "plating" the carbon onto the plastic foam is by CVD/PVD, and the high production cost restricts its industrial application.

2.2.2.5 Powder sintering

Traditional powder sintering involves mixing, forming and sintering processes. The metal powder can be either cold or hot pressed prior to sintering to promote metallurgical bonding of the metal particles. Sometimes, liquid-state sintering is necessary to increase the densification of the materials.

Sintering is a process that the particles of a powdered aggregate coalesce by atomic diffusion at an elevated temperature. Metal powder particles are in contact with each other and could mechanically bond after pressing. Theoretically, atomic diffusion could occur in any materials at a temperature above absolute zero, but it is extremely slow at low temperature. Therefore, the sintering process often operates at high temperature to accelerate diffusion. Sintering necks often form along the contact surfaces of adjacent particles at high temperature, and the particle boundary becomes metallurgical bond with increasing the sintering time. After sintering, the voids between the particles develop into pores.

It is easy to produce porous metals with any shape as long as there is a mould to contain the powders. This makes the process an ideal candidate for the production of complex porous metal structures. The porosities of porous metals produced using this method are relatively low (usually between 20% and 50%). To achieve higher porosities using this method, a spacing agent can be added to the powder before sintering. This agent can

be an inorganic salt (Li et al. 2009, Wang et al. 2010) or a metal (Aydoğmuş & Bor 2009), which can be removed by dissolution after sintering or decomposed or evaporated during sintering. Sodium chloride is the common agent as space holder to produce open-cell porous metals (Zhao et al. 2009, Wang et al. 2010). There are some other agents available, such as magnesium, ammonium acid carbonate and urea. Recently, Zhao et al. (2005) has developed a “Lost Carbonate Sintering’” method using potassium carbonate as the pore-creating agent. This technique can be used to produce porous materials with various metals, for example, aluminium, steel, titanium, copper and their alloys. All the porous samples in the present study were produced using this method.

The Lost Carbonate Sintering (LCS) process has been proved to be an efficient powder metallurgical manufacturing method to produce porous metals with controlled pore parameters, such as porosity, pore size, pore shape and pore distribution, which are important in determining the properties of porous metals (Zhao et al 2005, Mahmoud 2012, Paravanian & Panjepour 2013). It involves mixing copper particles and potassium carbonate powders, compacting the powder mixture, sintering, and decomposition or dissolution process. In LCS, pores are created by removing the carbonate. Carbonate removal can be achieved by two different routes. One is to dissolve the potassium carbonate with water after sintering, and the other is to decompose the potassium carbonate by sintering the compact at a temperature higher than the melting point of

potassium carbonate (891˚C) (Zhao et al. 2005). The former route takes longer and placing the sample in hot water for a long time can result in the oxidation of copper. The porous metals produced by the latter route generally have better properties than those produce by the former. LCS method is an efficient process to produced porous metals with porosity in the range 50-85% and cell sizes in the range 53-1500 μm. In principle LCS can be used for manufacturing foams of any metals that can be sintered, including copper, iron, nickel and their alloys. The LCS porous metals shows a strong bonding between the metal particles, leading to their good thermal and mechanical properties (Zhao et al 2005, Thewsey & Zhao 2008, Parvanian & Panjepour 2013).

Of all the manufacturing methods available for producing porous metals, sintering methods are considered to be the most promising, capable of economically producing millions of components annually (Haack et al. 2001).

2.3 Fluid Transport of Porous Metals

The important of transport phenomena in porous media has been emphasized by scientists and engineers, as they relate to the many materials in everyday life which are familiar to us (Dullien 1979). The permeability of open-cell porous metals is of particular importance as it often determines the application of porous metals.

2.3.1 Darcy's law and permeability

Permeability is one of the most important characteristics of open-cell porous media that allow fluid flow through them. It describes the conductivity of a porous medium with respect to fluid flow and how easily a fluid is able to move through the porous material. Permeability is related to the connectivity of the void spaces and the pore size. It is essential to characterise this property for permeable porous metals when they are used for thermal management, filtration, electrochemistry, acoustic absorption and medical implants.

Fluid transport in porous media can generally be analyzed by Darcy's law (Darcy 1856), which gives a simple expression to describe the relationship between fluid pressure gradient and Darcy velocity. Specifically, Darcy velocity, v_d, is directly proportional to the fluid pressure gradient, ∇P, and the permeability K.

$$v_d = -\frac{K}{\mu}\nabla P \tag{2.1}$$

where μ is the viscosity of the fluid.

Rearranged Eq.(2.1), the pressure gradient can be expressed as:

$$\nabla P = -\frac{\mu}{K} v_d \tag{2.2}$$

Darcy law was the basic equation governing permeability, which states that the rate of flow is directly proportional to the pressure gradient causing flow. The permeability, K,

is usually experimentally determined with units of square of length. The values of permeability vary widely, normally ranging from 10^{-20} to 10^{-7} m^2 (Bear, 1979).

Darcy velocity, v_d, is not a physical velocity but a superficial velocity defined as the volume flow rate divided by the entire cross section of the porous medium, not just the fluid flow cross-section. The pore velocity, v_p, which is based on the real fluid flow cross-section, is related to Darcy velocity and the porosity of the porous medium, ε, by:

$$v_p = \frac{v_d}{\varepsilon} \tag{2.3}$$

A number of researchers have verified that Darcy's law applies for slow, viscous flows, where the pressure drop is linearly proportional to the flow rate. Mokadam (1961) derived a general equation for flow through porous media using irreversible thermodynamics and showed that Darcy's equation is a special case, when the system of fluid flow was assumed to be isothermal conditions and the inertial and viscous effects were neglected. Ridgway et al. (2003) used Darcy's equation to compare the liquid permeability coefficient with the air permeability coefficient and found a close agreement between the two values. The gas permeability is close to the liquid permeability of a perfectly wetting liquid (Ridgway et al. 2003).

Darcy's law does not describe the fluid flow through the porous media accurately when the Darcy velocity is high. It was found that the effects of inertia friction and turbulence

become greater at higher flow velocities, resulting in larger pressure gradient through the porous media (Antohe & Lage 1997). The mechanism responsible for this turbulence is the drag force imposed on a fluid by the pore walls which impede the flow (Carman, 1956). In steady viscous or streamline flow, the resistance arises solely from viscosity. As the velocity increases, the regular pattern of streamline flow becomes unstable, and gives way to a regime where large number of small, randomly distributed local eddies form spontaneously. This results in the dissipation of the kinetic energy of fluid motion as heat and hence increases the resistance to flow. This resistance can be described as inertial resistance and depends on the kinetic energy per unit volume of the fluid, i.e. on $\rho_f v^2$. Therefore, in general engineering applications, the law governing this fluid flow is a modified version of Darcy's equation, with inertial resistance superimposed on the viscous resistance (Dupuit 1863; Forchheimer 1901):

$$\nabla P = -\frac{\mu}{K} v_d - \rho_f C v_d^2 \tag{2.4}$$

where K is the Darcian permeability of the medium, v_d is the Darcian velocity of the fluid, ρ_f is the density of the fluid and C is the drag form coefficient of the medium. The term $\rho_f C v_d^2$ accounts for the inertia effects or non-linear flow resistance in the flow.

Recently, Joseph et al. (1982) modified the Forchheimer equation based on the work of Ward (1964) by introducing an inertial coefficient, c_F, to Eq. (2.4):

$$c_F = C\sqrt{K} \tag{2.5}$$

The inertial coefficient, c_F, has been discussed extensively in the previous literature. The experimental work by Ward (1964) indicated that c_F is a universal constant for all permeable materials and equals to 0.55. Later work indicates that different values of c_F were obtained for materials with different characteristics, such as fibrous metal foams and polyethylene particles of random shape (Beavers & Sparrow 1969, Schwartz & Probstein 1969). Recently, Antohe & Lage (1997) reported that c_F varies from 0.3 to 0.9 for aluminium foams. Nield and Bejan (1999) summarised several sets of experimental data and found that c_F is a function of the porous medium and can be as low as 0.1 for fibrous metal foams.

2.3.2 Pore parameters of permeable material

Permeability of open-cell porous media is of particular significance when they are used as a functional material. A number of factors, such as porosity, pore size, and pore morphology can affect the permeability.

2.3.2.1 Porosity

The most important characteristic parameter is relative density, ρ / ρ_s (where ρ and ρ_s are the density of the porous material and the density of the bulk material, respectively), or porosity of the porous media, ε ($\varepsilon = 1 - \rho / \rho_s$). The larger the porosity, the more voids or pores in the porous media. This means that the fluid can

flow much more freely in the porous media because of more space and less barrier for the fluid. Therefore, permeability will always increase with porosity.

2.3.2.2 Pore size and characteristic length

Pore size is another parameter of porous media. Unlike porosity, it is impossible to give an accurate value of pore size in most porous media, as it is difficult to make porous media with constant pore size. Normally, average pore size is used when the pores in porous media are relatively regular and distributed uniformly. Bhattacharya et al. (2002) found experimentally that the permeability increases with average pore diameter, while the inertial coefficient changes very slightly with pore diameter, with the values of 0.085 for sample with pore diameter of 400 μm and 0.084 for sample with pore diameter of 180 μm at a given porosity of 91%.

Pore size is just one apparent parameter describing the porous media. Pore size in porous media firstly refers to the diameter of cylindrical tubes in porous media. Theoretically, only if the pores were cylindrical tubes of uniform diameter or perfect spheres, the pore size would be unique (Dullien 1991). Porous media, however, often have different pore morphologies. For many properties of porous media, such as permeability and heat transfer parameters, the characteristic length should be used to define the characteristics of the pores. Some examples of characteristic length are: the diameter of a cylindrical channel (Ming et al. 2010, Odabaee et al. 2011), the diameter

of a sphere (Childs & Collis-George 1950, Masuoka & Takasu 1996) or pore (Kim & Jang 2002), the diameter of a fibre (Vallabh et al. 2010) or wire (Dyga & Placzek 2010), or hydraulic diameter (Chiba et al. 2010, Qu et al. 2000, Richardson et al 2000, Shen et al. 2006). For complex shapes, the characteristic length may be defined as the volume of the fluid body divided by the surface area of matrix.

2.3.2.3 Specific surface area

The specific surface area of a porous media can be defined as the interstitial surface area of the voids and pores either per unit mass or per unit bulk volume of the porous media. There are three methods to determine specific surface areas, according to Collins (1961) and Scheidegger (1974):

1) Adsorption. This method uses the principle of lack of thermodynamic equilibrium between the gas or vapor and the solid surface in contact with it, as all gases below their critical temperatures tend to adsorb as a result of van der Waal's forces between the gas molecules and the solid surface. Equilibrium is achieved by accumulation of the molecules of the gas or vapor. The surface area is usually obtained based on unit mass of the sample.
2) Quantitative stereology. This method uses photomicrographs of one section of the sample with sufficient contrast to clearly distinguish the pores from the solid matrix. The detailed information will be described in Section 3.2.2.2. Quantitative

stereology is an easy and effective method to estimate the value of specific surface area of porous media.

3) Fluid flow. Permeability has been related to the specific surface area of the samples and can be used to calculate the specific surface area. The simplest example is modeling the fluid flow through a packed bed with spherical particles.

Recent research has been conducted to characterise the specific surface area of porous media with uniform pore using a cylinder to represent the pore, both of which have the same diameter, d_{pore}, and the same internal surface area, the specific surface area per unit volume of solid, S_0, is given by (Kaviany 1995, Richardson et al. 2000, Liu et al. 2006) :

$$S_0 = \frac{4\varepsilon}{d_{pore}(1-\varepsilon)} \tag{2.6}$$

2.3.2.4 Tortuosity

As the pores are the flow channel, the pore structure is vital to the flow of fluid in porous media. The path of the fluid that flows through the porous medium is determined by the pore distribution and can be characterised by tortuosity (Epstein 1989). A smaller tortuosity represents a more straight flow channel for fluid, which corresponds to a larger permeability. Numerical study also reveals that tortuosity of granular soils decreases almost linearly with increasing porosity, resulting in high

permeability (Koponen et al. 1996, Ghassemi & Pak 2011). Tortuosity in porous media, τ, is defined as the ratio of the average pore length, L_e, to the length of the porous medium, L_0, along the major flow or diffusion axis; i.e., $\tau=L_e/L_0$ (Epstein 1989). Generally, $L_e > L_0$ and $\tau>1$.

Tortuosity is an important parameter of a porous medium which affects the flow through it. Carman (1956) proposed that tortuosity could be expressed as $\sec\theta$, where θ was the average deflection angle between the real flow direction and the horizontal direction of the porous medium. For a packed bed, they suggested $(L_e/L_0)^2=2$ with $\theta = 45^\circ$, which was experimentally confirmed by some work in literatures (Carman 1956). Recent research showed that tortuosity varies according to the factors related to motion of fluid coupled with the structural characteristics of the porous media (Delgado 2006).

There have been several empirical correlations between tortuosity and porosity:

$$\tau = 1 + a(1-\varepsilon) \tag{2.7}$$

$$\tau = 1 - aIn(\varepsilon) \tag{2.8}$$

$$\tau = \varepsilon^{-n} \tag{2.9}$$

where a and n are constants. (The reference for expressions 2.6, 2.7 and 2.8 are Weissberg 1963, Comiti & Renaud 1989, and Iversen & Jørgensen 1993; Weissberg

1963, and Koponen et al 1996; and Archie 1942, Bear 1972, Dullien 1979, Mota et al. 2001, and Dias et al. 2006, respectively.)

Several other important parameters influence the permeability of porous media, these including pore surface morphology, roughness of pore wall and pore shape.

2.3.3 Geometric permeability models

The permeability of porous media is often determined experimentally, because it is difficult to model the permeability of porous metals using intrinsic structural parameters. A number of investigations have been carried out and many models have been set up. Some investigations qualitatively described the permeability as a function of porosity and pore size (Khayargoli et al. 2004, Medraj et al. 2007). Some obtained empirical correlations in the power-law form $K=\alpha\varepsilon^{\beta}$, or in the exponential form $K=ae^{b\varepsilon}$, where α, β, a and b are fitted constants that depend on the type of the foam (Dukhan 2006, Innocentini et al. 1999a).

Geometric permeability models based on the structure of porous media were reported in the literature. Some models were based on statistics (Andersson et al 2011, Katz & Thompson 1986), and the others based on well-defined geometry. These models require the knowledge of pore structure (Antohe & Lage 1997, Despois & Mortensen 2005). The simplest geometrical model consists of a bundle of straight cylindrical capillaries of

uniform cross section. Other, more sophisticated, geometrical models have been suggested by several authors.

Most of the geometrical models are based on Carman-Kozeny model, which is widely accepted and is based on Hagen-Poiseuille equation (Carman 1956, Kozeny 1927). The permeability of porous media is expressed in Carman-Kozeny model as:

$$K = \frac{\varepsilon D_h^2}{16k} = \frac{\varepsilon^3}{k_0 \tau^2 (1-\varepsilon)^2 S_0^2} \tag{2.10}$$

where k_0 is a "shape factor" (k_0=2.0-2.5 for most rectangular, elliptical and annular shape pores), S_0 is the specific surface area based on the solid's volume, and $\tau = L_e/L$ is tortuosity (L is the length of the porous medium along the direction of fluid flow and L_e is the average path length of flow), $D_h=4\varepsilon/[S_0(1-\varepsilon)]$ is the hydraulic diameter, and $k=k_0\tau^2$ is the "Kozeny constant",.

The Carman-Kozeny model forms the basis of most geometric models (Wong et al. 1984, Bhattacharya et al. 2002, Vidal et al. 2009), which differ only in the method of calculating the mean hydraulic diameter and in the value used for Kozeny constant, $k_0\tau^2$. According to Carman (1956), the best value of Kozeny constant to fit most experimental data on packed beds is 5. Defining the mean particle diameter D_p as the diameter of the hypothetical sphere with the same S_0 as the pore, i.e. $D_p=6/S_0$, Carman-Kozeny equation changes to:

$$K = \frac{D_p^2 \varepsilon^3}{180(1-\varepsilon)^2} \tag{2.11}$$

Similar expressions were also derived by Ergun (1952), Bear (1979) and Kovács (1981).

There are some limitations of the Carman-Kozeny equation. It assumes that the range of pore shapes is such that k_0 is unlikely to change, and the tortuosity is also not very susceptible to variations in pore geometry. In practice, the tortuosity is often found to be much larger than the assumed values. Another important limitation is the assumption that pore size can be represented by the hydraulic radius, which is not always accurate, e.g. for capillary pore space. This model is suitable for granular media, but not necessarily suitable for porous metals with different structures.

Du Plessis & Roos (1994) devised a pore-scale granular model. They adopted a volumetric averaging approach to calculate the flow resistance of a fluid through a periodic unit cell shaped of a cube containing three perpendicular solid rods of rectangular cross-sections located along three of its edges. The hydrodynamic permeability, K, can be expressed as a function of the porosity, ε, and the grain diameter, D_p:

$$K = \frac{D_p^2}{63} \frac{\varepsilon[1-(1-\varepsilon)^{1/3}][1-(1-\varepsilon)^{2/3}]}{(1-\varepsilon)^{1/3}\mu} \tag{2.12}$$

The model agreed well with experimental data obtained on ERG aluminium foams with high porosity between 92% and 96%, however, a modification to the model was required to fix the ratio between the edge length of the cell and the average pore diameter. This issue was resolved when Fourie & Du Plessis (2002) calculated the ratio between the cubic pore size and a more realistic tetrakaidecahedral pore shape. This model showed very good agreement with experimental data obtained.

Recently, Despois and Mortensen (2005) studied the permeability of aluminium open-pore foams produced by the replication process and developed a model by considering the effect of the obvious 'bottlenecks' on pressure drop. The model was finally compared with Darcy's law and gave the expression of permeability as follows:

$$K = \frac{\Delta r^2}{\pi}\left[\frac{\Delta - \Delta_0}{3(1-\Delta_0)}\right]^{3/2} \tag{2.13}$$

where r is the initial particle radius (close to the average pore radius in a foam), Δ is the pore density in a particle compact (the pore volume fraction in a foam), and Δ_0 is the initial packing density of the spherical particles ($\Delta_0 = 0.64$ for random dense packing of monosized spheres).

The 'bottleneck' model seems to agree well with the experimental data for the permeability in their study, and shows the same results with the predictions of Du Plessis et al. (1994) for low-density foams.

2.4 Thermal Properties of Porous Metals

Thermal transport in porous metals, including conduction and convection, are often of particular significance when they are used in the thermal management devices. It is important to evaluate the thermal properties of porous metals as they play important roles in applications.

2.4.1 Thermal conduction in porous materials

When the temperature distribution is non-uniform, i.e., the temperature of the substance on one side is higher than that on the other side, heat will be conducted from a region of higher temperature to a region of lower temperature within a substance. This phenomenon is called thermal conduction. The ability of a particular substance to conduct heat is characterised by its thermal conductivity.

2.4.1.1 Mechanisms of thermal conduction

In fluids, thermal conduction depends on the collisions of molecules during their random motion (Long 2009). Molecules with high temperature move very quickly and are in a state of high energy, while molecules with low temperature move slowly and are in a state of low energy. Thermal energy is transported from high energy molecules to low energy molecules via the collision of molecules.

In solids, the atoms vibrate about their equilibrium locations and cannot transport

thermal energy in the form of collision between atoms. Thermal energy in solids is conducted by two mechanisms: lattice vibration and migration of free electrons. The sum of these two contributions represents the total thermal conductivity of the solid medium (Kreith et al. 2001). Normally, thermal energy transport due to lattice vibration occurs when adjacent atoms vibrate against one another, with the transport direction being the motion of the lattice waves, or phonons. Free electrons can also transport thermal energy, and the transport due to free electrons is more effective than that due to vibrational energy in the lattice structure because of the light weight of electrons. In metals, there are a lot of free electrons which can conduct heat efficiently. The contribution of lattice waves to heat conduction in metals can be ignored, and the conduction of heat mainly results from the migration of free electrons. Thus, metals have a higher thermal conductivity than fluids and non-metallic solids.

2.4.1.2 Thermal conductivity

Thermal conductivity can be considered using a bar with one end of the bar at a higher temperature T_1 and the other end at a lower constant temperature T_2. Heat is conducted from the hot end to the cold end at a steady rate as both sides are completely insulated. In steady-state conditions, providing the heat energy passing through any positions is the same within the bar, the heat flow is proportional to the temperature gradient and the area of the cross section:

$$Q = \lambda A \frac{dT}{dx} \tag{2.14}$$

where Q is the heat flow, λ is the thermal conductivity, A is the cross-sectional area perpendicular to the direction of heat flow, and dT/dx is the temperature gradient through the medium conducting heat.

Thermal conductivity depends strongly on the chemical composition and crystal structure of the material, both of which influence the lattice vibration and electron migration in the material. Table 2.1 lists the thermal conductivity of some common materials at room temperature (Long 2009, White 2011). Temperature is also an important factor which influences the thermal conductivity of a material. Normally, the thermal conductivity of pure metals decreases with temperature, while the thermal conductivity of alloys increases with temperature (Long 2009). There often is a linear relationship between thermal conductivity and temperature (Aksoz et al. 2010).

Table 2.1 *Thermal conductivity of some common materials at room temperature* (Long 2009, White 2011).

Materials	Thermal Conductivity (W/mK)
Natural Diamond	2200
Pure Copper	390
Pure Aluminium	235
Brass Cu63%	125
Pure Nickel	91
Pure Iron	55.4
Carbon Steel	54
Water	0.6
Air	0.025

Generally, the experimentally measured values of thermal conductivity are used for engineering calculations. A kinetic theory has been developed to predict the experimental values accurately for gases at moderate temperatures (McLaughlin 1969). This theory, however, is not adequate to predict thermal conductivity of fluids or solids to a satisfactory level of accuracy (Klemens 1969, McLaughlin 1969). For the thermal conductivity of two phase materials, i.e., binary mixtures, three basic models have been established to predict the effective conductivity of mixtures: one for parallel arrangements, one for series arrangements and one for random continuous arrangements (Laudauer 1952). The equations of the models are as follows:

Parallel model: $\lambda = V_1\lambda_1 + V_2\lambda_2$ (2.15)

Series model: $\lambda = \dfrac{1}{V_1/\lambda_1 + V_2/\lambda_2}$ (2.16)

Continuous model (EMT model): $V_1\dfrac{\lambda_1 - \lambda}{\lambda_1 + 2\lambda} + V_2\dfrac{\lambda_2 - \lambda}{\lambda_2 + 2\lambda} = 0$ (2.17)

where λ is the effective conductivity of the mixture, λ_1 and λ_2 are conductivities of the two phases, and V_1 and V_2 are volume fractions of the two phases, respectively.

2.4.1.3 Heat conduction in porous metals

Heat conduction through a matrix fully saturated with fluid (e.g., porous metals) depends on the structure of the matrix and the thermal conductivity of each phase. According to Gibson & Ashby (1988), the effective thermal conductivity of a porous metal can have four contributions: conduction through the solid phase, conduction via

the gas phase within the pores, convection conduction within the pores and radiation conduction through the pore walls and across the pore voids. This can be summed up by:

$$\lambda = \lambda_s + \lambda_f + \lambda_{conv} + \lambda_{radi} \tag{2.18}$$

where λ is the total thermal conduction, and λ_s, λ_f, λ_{conv} and λ_{radi} represent the thermal conductivity contributions through solid conduction, gaseous conduction, convection and radiation, respectively.

1) Conduction through the solid phase:

The effective thermal conductivity of a porous metal will be less than that of the bulk material. The contribution, λ_s, is produced by the conductivity of the fully dense solid and its volume fraction multiplied by an efficiency factor which allows for the tortuous shape of the cell walls (Schuetz & Glicksman 1984). Thus the heat transported by conduction in the solid may be reduced by decreasing the volume fraction of the solid present. Impurities and metal oxides contained within porous metals may also contribute to a reduction of the total thermal conductivity (Degischer & Kriszt 2002).

2) Conduction via the gas phase:

In most cases, the gas contained within the pores is air. According to Table 2.1, the thermal conductivity of air at room temperature and atmospheric pressure is as low as 0.025 W/mK. This means that heat transfer in stagnant gas will be very slow. Compared with the thermal conductivity of solid phase (λ_s), λ_f is negligible.

3) Convection conduction:

Convection occurs because of hot fluid rising to displace cold fluid caused by local density difference of the fluid. Two types of convection currents can occur: free and forced convection. In free convection, fluid motion is due to buoyancy forces within the fluid. Forced convection is possible where an external agent induces the motion of the gas; this occurs in metallic foams used as heat exchangers. Convection conduction within the pores is only important when the Grashoff number (which describes the ratio of the buoyant force driving convection to the viscous force opposing it) is greater than approximately 1000 (Gibson & Ashby 1988). Using data appropriate to air at 1 atmosphere, this value is achieved when the pore size exceeds 10mm in diameter. For pore sizes smaller than this, thermal conduction through convection, λ_{conv}, can be ignored.

4) Radiation conduction:

Radiation often contributes to heat transfer through foams with transparent structure. In the case of optical nontransparent metals, however, radiation through the pore walls is less significant. Lu & Chen (1999) reported that the transport of heat is dominated by solid conduction when the thermal conduction in the solid phase of the porous metal is greater than 20W/mK. Therefore, the contribution of radiation, λ_{radi}, can be ignored.

According to what mentioned above, the overall effective thermal conductivity of porous metal (λ_{eff}) is mainly related to the porosity of the metal matrix (ε) and the individual thermal conductivities of the solid (λ_s) and fluid (λ_f) phases.

Based on the parallel thermal conductivity model of two phase materials in Eq. (2.15), Kaviany (1995) gives the following expression to describe the effective thermal conductivity of porous metal:

$$\lambda_{eff} = \varepsilon\lambda_f + (1-\varepsilon)\lambda_s \tag{2.19}$$

The pores or voids within the porous metal, however, are often distributed randomly and do not obey parallel model. A resistor model to estimate the effective thermal conductivity of a random two-phase medium was proposed by Singh & Kasana (2004), based on numerical simulations. Their study introduced a correlative term, *F*, to take account of high conducting phase, non-linear flow of heat flux lines and random distribution of the phases. They found that in addition to the physical parameters such as porosity and the ratio of the thermal conductivity of the constituent phases, *F* was also dependent on the pore shape factor and formation resistivity factor.

Calmidi & Mahajan (1999) investigated the effective thermal conductivity of high porosity aluminium foams experimentally and derived an empirical correlation between effective thermal conductivity and porosity:

$$\lambda_{eff} = \varepsilon\lambda_f + a(1-\varepsilon)^n\lambda_s \tag{2.20}$$

where a and n are fitting constants. The best fit was obtained when n=0.793 with the value of a being 0.181 for air and 0.195 for water.

A model was also produced based on assumption of a two-dimensional foam consisting of an array of hexagons and was validated with the experimental data. An improvement to this model, based on an idealized three-dimensional basic cell of a foam with open-cell structure in the form of tetrakaidecahedron cells, was made by Boomsma & Poulikakos (2001). Most recently, Bhattacharya et al. (2002) extended the analysis of Calmidi & Mahajan (1999) to develop a model with a circular intersection and showed that the effective thermal conductivity of the foam depended strongly on the porosity and the ratio of the cross-sections of the intersection.

Wang et al. (2008b) proposed a symmetric and interconnected skeleton structure (SISS, structure shown in Figure 2.6) model to predict the thermal conductivity of porous metals with hollow and solid struts. The SISS divides a unit cube into six unique composite rectangular prisms parallel to each other. The effective thermal conductivity for each prism and the overall thermal conductivity of porous metal are calculated by the parallel model or series model. They found that the effective thermal conductivity of solid-strut foam was larger than that of hollow-strut foam, and the effective conductivity of porous metal with solid-strut can be expressed as:

$$\lambda_{eff} = \lambda_s \left\{ 0.5 - \cos\left[\frac{\pi + \arccos(2\varepsilon - 1)}{3} \right] \right\}^2 \tag{2.21}$$

The prediction values of this model were consistent with the experimental data for both open-cell and closed-cell metal foams.

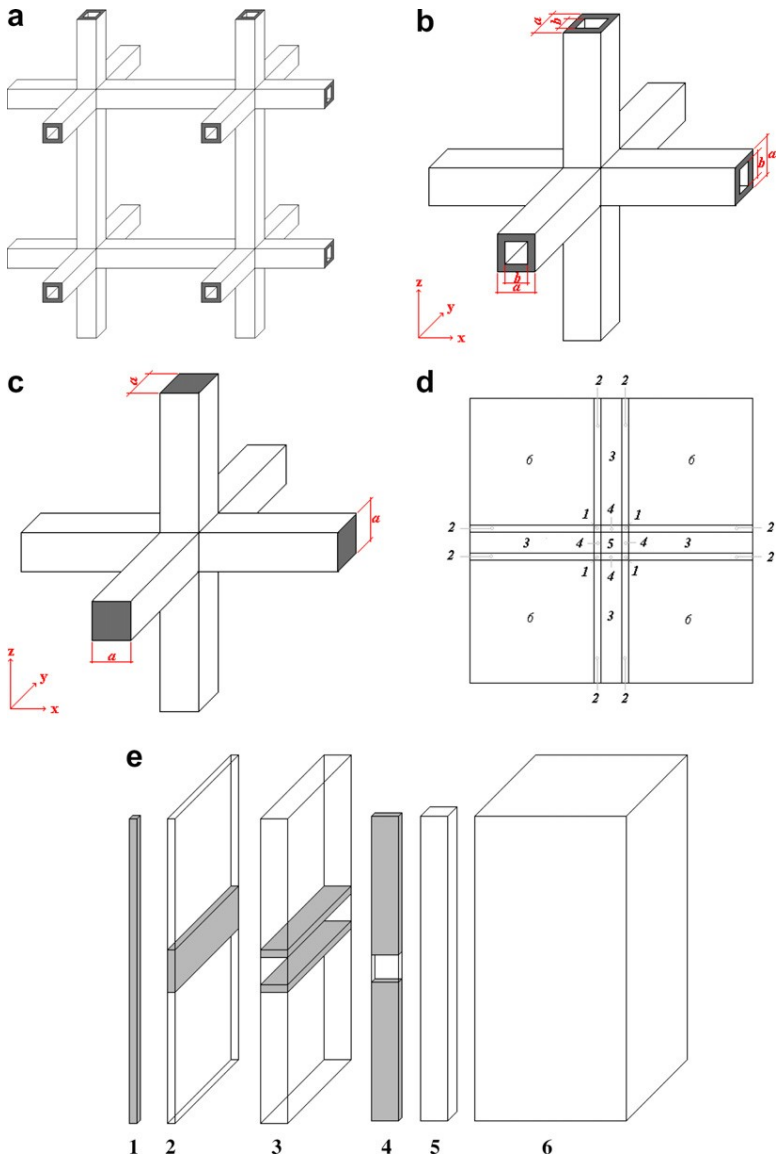

Figure 2.6 *Symmetric and interconnected skeleton structure (SISS) model with hollow struts: (a) hollow-strut SISS; (b) unit cell of the hollow-strut SISS; (c) unit cell of the solid-strut SISS; (d) plan view of cross-section of the hollow-strut SISS unit cell at the mid-point in the z direction showing the location of the six composite parallel prisms; (e) structures of the six composite parallel prisms in (d). (Wang et al. 2008b)*

Ogushi et al. (2004) fabricated lotus-type porous copper with many straight pores and carried out an experimental and analytical investigation on the effective thermal conductivity of porous copper parallel and perpendicular to the pores. They found that the effective thermal conductivity parallel to the pores ($\lambda_{eff//}$) was higher than that perpendicular to the pores ($\lambda_{eff\perp}$), and $\lambda_{eff//}$ is proportional to $(1-\varepsilon)$. More recently, the thermal conductivity of porous copper with different porosities and pore sizes fabricated by lost carbonate sintering method was studied by Thewsey and Zhao (2008). They found that the effect thermal conductivity of porous copper had a power law relationship with porosity. The pore size, however, had no significant effect on the thermal conductivity.

2.4.2 Heat convection

Heat convection (convection heat transfer) is the transfer of heat from the surface of a solid to a fluid. The process of transfer of heat from a solid to a fluid requires not only transfer of heat by motion of the fluid, but also conduction of heat through the boundary layer between the solid and fluid, i.e., contacting area. There are two forms of heat convection. One is the natural convection, which can be caused by movement of a fluid by means of buoyancy caused by the density difference of fluid. The other one is forced convection, which means that the fluid is forced to flow by an external source such as fans.

Heat convection between a solid and a fluid can be described by Newton's law of cooling, with the introduced physical parameter of heat transfer coefficient (Lienhard IV & Lienhard V, 2005):

$$\frac{dQ}{dt} = -hA\left[T(t) - T_{\infty}\right] \tag{2.22}$$

where Q is the thermal energy, A is the contacting area between solid and fluid, $T(t)$ is the time-dependent temperature of the solid's surface, T_{∞} is the temperature of the oncoming fluid, and h is the heat transfer coefficient, which is independent or relatively independent of the temperature difference.

In many engineering applications, heat convection occurs within the porous media that are combinations of a stationary solid and a fluid. Normally, the porous medium is saturated with fluid when working. A large number of experimental and analytical investigations on heat convection in porous media have been carried out. The basic principles and comprehensive reviews of heat transfer in porous media in general have been summarized by Kaviany (1995). Lee & Cunnington (2000) investigated conduction and radiation heat transfer in high porosity fiber insulation. An experimental investigation of natural convection heat transfer of polymer pin fin heat sinks was reported by Bahadur & Bar-Cohen (2005), while Calmidi & Mahajan (2000) and Zhao et al. (2005) gave a combined experimental and numerical study on natural convection and forced convection in open-celled metal foams.

2.4.3 Heat transfer performance of porous metals

Porous metals have been considered for the design of heat exchangers to enhance convective thermal transport and to maximize heat transfer, as the thermal conductivity of metals is relatively high (copper or aluminium is usually used due to their high conductivity values) (Ashby et al. 2000). Generally, heat transfer performance of the heat exchangers can be substantially enhanced by porous metals. Jiang et al. (2004) reported that particle-sintered bronze samples with porosities from 40% to 46% enhanced the heat transfer performance up to 15 times for water and up to 30 times for air in comparison with an empty channel. Porous copper samples with high porosities from 88% to 94% enhanced the heat transfer performance by about 17 times in comparison with an empty channel (Zhang et al. 2005b, Zhao et al. 2004). Boomsma et al. (2003) conducted an experimental study on aluminum foams and found that the thermal resistance of the foams was up to three times lower than that of commercially available heat exchangers under the same pumping power. Zhang et al. (2009) investigated the heat transfer performance of LCS porous copper with different porosities and pore sizes and found that porous copper could increase the heat transfer coefficient by 2 to 3 times compared to the empty channel and up to 100% compared with particle-sintered copper. The size of the sample is 10 mm in diameter and 4 mm in thickness, and it can remove a heat flux of 1.3 MW/m^2 at the coolant flow rates from 0.3-2.0 l/min. The measurement setup used in their work, however, had an axial-radial,

or impingement flow configuration, which makes it difficult to compare their results with theoretical models and the results obtained by other researchers.

The heat transfer performance of porous metals is affected by several factors. Kim et al. (2000) investigated the heat transfer performance of high porosity aluminium foams with three different pore densities (10 PPI 20 PPI and 40PPI (pores per inch),) under the condition of forced air convection. They found that use of aluminium foam dramatically enhanced overall heat transfer rates from the thermal systems compared with the channel without foam materials, and the heat transfer performance of aluminium foam was improved by increasing the pore density. Tamayol & Hooman (2011) assessed theoretically the heat transfer through metal foam heat exchangers under forced convection condition. They modeled the microstructure of metal foams as interconnected solid ligaments with simple cubic array structures and proposed a thermal resistance model of heat transfer process by considering the conduction inside the solid ligaments, the interfacial convection heat transfer, and convection heat transfer to the solid bounding walls. Heat transfer rate of foams was shown to increase with the pore density but decreases with the porosity.

Recently, an investigation of the heat transfer in forced convection of air across aluminium foams was carried out by Mancin et al. (2010). The authors tested the heat transfer performance of aluminium foams with different sample thicknesses (20mm and

40mm samples) under different air mass flow and heat fluxes (25.5 kW/m^2, 32.5 kW/m^2, and 40 kW/m^2). They found that heat transfer coefficients increased with the air mass flow rate but were not influenced by the imposed heat flux. The sample with 40 mm thickness, however, had larger heat transfer coefficient than that with 20 mm height. Tamayol & Hooman (2011) conducted a theoretical study on the forced convection flow through a metal foam and found that the heat transfer rate increased with the thickness of metal. The augmentation, however, did not have a linear relationship. Shih et al. (2006) investigated the thickness effect on heat transfer characteristics of cylindrical alumimum foam with diameter of *D* and thicknesst of *t*. They introduced a dimensionless height, *t/D* to characterise the effect of height on heat transfer performance and found that the alumimum foam with dimensionless height between 0.23 and 0.31 had the best heat transfer performance.

The studies mentioned above all used air as coolant. In cooling electronics which generate an excessive amount of heat, water is preferred to air due to its greater thermal conductivity and specific heat capacity. The convection heat transfer coefficient using water as a coolant could be 10-1000 times higher than that using air as a coolant (Lienhard IV & Lienhard V 2005). Boomsma et al. (2003) conducted an experimental study of the performance of open-cell 6101-T6 aluminium foam as compact, high performance heat exchangers with water as coolant. The foams had porosities between 60.8% and 88.2% and were tested in a forced convection condition. The experimental

results showed that the Nusselt number (the ratio of convective to conductive heat transfer across normal to the boundary) was zero for a zero coolant flow velocity and increased monotonically with the coolant velocity. The aluminum foam with porosity of 67% had the best heat transfer performance under the lower coolant flow velocity range, up to 0.729 m/s. The heat transfer of liquid cooled, open–cell porous copper heat sinks was investigated experimentally by Zhang et al. (2005a). The tested samples made by electrodeposition method had four porosities ranging from 60% to 90% and two different pore densities, 60 PPI and 100 PPI. They found that the samples with the lowest porosity of 60% gave the lowest thermal resistances. Higher pore densities led to lower thermal resistances for porous copper sinks in their experiment.

A number of investigations have been carried out on the use of porous metals as a highly compact replacement for convectional heat exchangers. A comparison between metal foam heat exchangers and several commercially available heat exchangers was made by Mahjoob & Vafai (2008). Metal foam provide substantially more heat transfer surface area and more boundary layer disruption, both of which led to considerably higher heat transfer rates. The introduction of porous metal, however, increases the pressure drop. A compromise between the heat transfer rate and pressure drop has to be made, for metal foams to be considered for a specific application. More recently, Dai et al. (2013) compared an open-cell metal-foam heat exchanger to a conventional, flat-tube louver-fin heat exchanger. They found that under the same input power and

heat transfer rate, the metal-foam heat exchanger can be significantly smaller in volume and lighter in weight over a wide range of design space, for the same cost under the baseline conditions in their study.

2.4.4 Thermal applications of porous metals

The thermal properties of porous materials are of considerable practical interest in a number of fields. There are two types of applications: thermal insulator and heat exchanger. Metallic foams with closed cells are suitable for thermal insulator due to their relatively low thermal conductivity compared with the bulk metals (Lu & Chen 1999). Open-celled metallic foams are more suited to compact heat exchangers due to a high specific solid-fluid interface area, a good thermally conducting solid matrix and a tortuous internal network of pores which promotes turbulence and mixing of the coolant (Boomsma et al. 2003).

Porous metals have relatively low thermal conductivity and are fireproof, which make them ideal materials for flame arresters to prevent flame propagation along pipe-work and enclosures. A low thermal conductivity is beneficial to fire resistance as it prolongs the time required for the temperature of the unexposed surface to reach its critical temperature, while the high melting point is an advantage for them to be used in high temperature (Lu & Chen 1999). Work carried out by the Electrical Research Association has proved that the RECEMAT metal foam (RECEMAT International, Netherlands)

was capable of arresting hydrogen-oxygen flames where the initial gas pressure was 2.75 bar-g, and a 6mm sample had ability to stop hydrocarbon flames travelling at 210 m/s (Davies and Zhen 1983).

The advantage to use porous metals for thermal insulators is not obvious compared with some heat insulation materials when the temperature during work is not very high, as the thermal conductivity of metal is much higher than traditional heat insulation materials.

There has been increased demand for heat transfer for high performance and multifunctional devices in recent years. In some high performance electronic chips such as computer processors, the nominal heat flux is up to 500-1000KW/m^2 and there is no doubt that much higher demand will be made in the future (Bastawros & Evans 1997). Metals with good thermal conduction ability, such as aluminium or copper, can be used to produce the porous matrix as heat exchangers. The mere presence of these metals in a static fluid can increase the overall effective thermal conductivity of the fluid system significantly (Calmidi & Mahajan, 1999). Open-cell porous copper and porous aluminium are the common porous metals used as heat exchangers, because of their permeability to fluids and the good thermal conductivity of the base metal. A large number of pores give rise to a high surface area, plus a good thermal conduction in the matrix, allowing heat to be transferred efficiently in the system (Boomsma et al. 2003,

Mancin et al. 2010, Zhang et al. 2005a).

One example of using porous metal as heat exchanger is for integrated gate bipolar transistors (IGBTs) for motor drives. The heat flux with high power density in the motor drives when operating can be dispersed to the coolant by a heat sink comprising a fin-pin array subject to flowing air generated by a fan (Ashby et al. 2000). This single-phase, liquid-cooled micro-channel heat sink, featuring channel hydraulic diameters smaller than 1 mm and a large surface to volume ratio, is considered the most promising technology for high heat flux applications. Porous metals could be used as the heat sinks, mostly, made by etching in silicon or precision machining in metals such as copper or aluminium.

Another example of the application is the use of ERG DUOCEL open-celled aluminium foam (mentioned in session 2.2.2.1) in the space-shuttle atmospheric control system (Ashby et al. 2000). Figure 2.7 shows the structure of this fluid-fluid heat exchanger. The DUOCEL range of metal foams, which include both aluminium and copper, have open porosity, low relative density and high matrix thermal conductivity. This would clearly be advantageous for space flight, where weight consideration is of major importance.

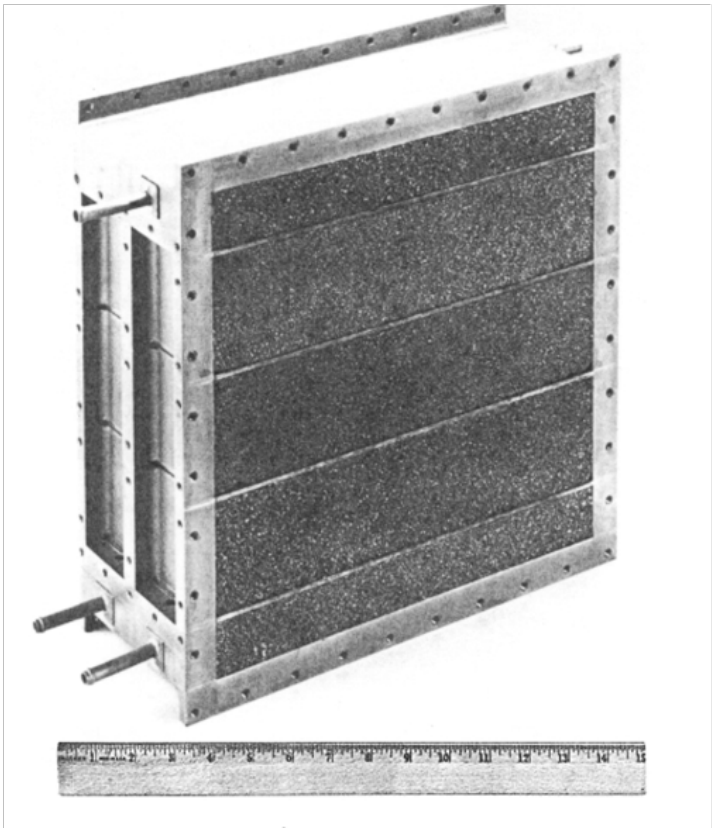

Figure 2.7 *DUOCEL foamed aluminum used as the heat-exchange medium for the space shuttle atmospheric control system. (Ashby et al. 2000).*

2.5 Mechanical Response of Porous Metals

As mentioned above, porous media have been candidates for many applications. In some cases, the parts need to possess a moderate strength. Compared with other porous media, porous metals have relatively high specific strength and can bear higher load before they fail. This offers porous metals an opportunity to be used in some parts that require high strengths.

The mechanical behaviour of metals has been studied for a long time and is well documented. Unlike bulk metals, porous metals with a cellular structure are

complicated because of the different pore parameters in porous metals. There have been a large amount of experimental work on mechanical properties of porous metals and the consensus is that they depend significantly on the porosity and this dependence can be characterised by empirical power-law functions. Beside porosity, fabrication technology also plays an important role in affecting mechanical properties of porous metals. Koo & Jung (2006) produced porous copper from hollow spheres by sintering and found that the hardness and compression strength of the hollow spheres increased with sintering temperature as the size and amount of pores decreased with temperature. The appropriate temperature for copper sphere sintering was found to be over 850ºC in order to obtain good strength.

The percolation theory is suitable to model the mechanical properties of porous media produced by powder consolidation, as this model in general describes connectivity problems well. Kovácik (1998) investigated the tensile behaviour of porous copper and porous nickel fabricated by the solid-gas eutectic solidification. It was found that a non-linear dependence of the tensile properties of porous metals can be described by the percolation power-law. Kovácik (1999) also found that the Young's modulus-porosity relationship of porous materials can be described fairly well by the percolation model. In both cases, however, the model failed for the samples with high porosity. The suggestion was that it is necessary to investigate the material fabricated by the same method from the same raw materials in a porosity range as wide as

possible, in order to incorporate the properties of the solid material into the fitting process to estimate the percolation threshold.

Qiao et al. (2008) investigated the compressive property and energy absorption of porous sintered fiber metals produced by vacuum sintering. The typical compressive stress-strain curves of porous fiber metals exhibited three distinct deformation regions: elastic region, stress plateau region and densification region. The energy absorption capacity of the samples increased more than three times when relative density was increased from 0.177 to 0.355. This relationship accorded with Gibson-Ashby theory.

Another method to predict the mechanical properties of porous metals is the Mori-Tanaka model, which considers the stress field in the bulk material with dispersed inclusions. Sevostianov et al. (2006) produced aluminium foam with relative density in the range of 0.45 to 0.85 by a powder metallurgy method, having a Young's modulus between 3-12 GPa. The Mori-Tanaka model was found to give the best predictions for the Young's modulus. This result was also consistent with that reported by EI-Hadek & Kaytbay (2008), who found porous copper with relative density between 0.5-0.85% having a Young's modulus of 10-30 GPa, and the Young's modulus could be predicted by Mori-Tanaka model.

Porous metals possess excellent damping properties and can absorb a large amount of impact energy in a short time. In structural sandwich panels, they offer lower weight but higher stiffness than conventional honeycomb and therefore have much better energy absorbing property (Gibson 2000). Sandwich panels with aluminium foam as the core have been widely used in high precision machines.

Sandwich structures also found applications in passive safety, which is one of the most important targets in vehicle design. Fuganti et al. (2000) designed a crashbox using aluminium foam as the filler of a generic crashbox structure to improve the energy absorbing efficiency. They found that using aluminium foams would improve vehicle crashworthiness, due to their properties derived from cellular structure to absorb energy. In particular, the lightness of porous aluminium was also an advantage for application. This application guaranteed weight saving of approximately 10%, crashbox length reduction of about 30% and volume reduction of about 60%.

Chapter 3

Experimental

The Lost Carbonate Sintering (LCS) process developed by Zhao et al. (2005), described in Section 2.2.2.5, was used in this study for the fabrication of all the porous metal test samples. In order to simplify the fabrication procedure and improve the mechanical properties of the as-fabricated porous metals, the decomposition route was used. The fluid permeability, thermal conductivity, heat transfer and mechanical properties of these samples were investigated. The experimental procedures are described in detail in the following sections.

3.1 Preparation of Test Samples by LCS

The LCS process involves four basic stages: mixing, compaction, sintering and dissolution or decomposition (Zhao et al. 2005). The decomposition route was used because increasing sintering temperature to above the decomposition temperature of potassium carbonate not only improves the mechanical properties but also speeds up the removal of potassium carbonate. Figure 3.1 is a graphical presentation of the LCS process. The detailed procedure of each fabrication stage is described separately below.

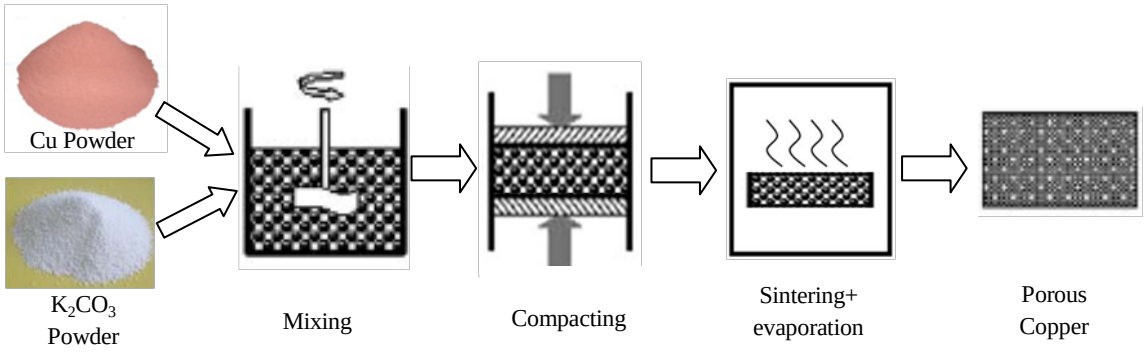

Figure 3.1 *Graphical presentation showing each stage involved in the LCS process.*

3.1.1 Raw materials

Copper powder with a high purity of 99.5% supplied by Ecka Granules UK Ltd was used. Three types of copper powder with different particle sizes (50-100 μm, 100-300μm and 600-1000 μm) were chosen. The typical copper powder particles are shown in Figure 3.2. The shape of the particles is spherical. The copper particle size should normally be smaller than the size of the required pores, i.e. the size of the potassium carbonate granules. The mean diameter of the copper powder particles used for most of the test samples was approximately 75 μm, with the particle size ranging between 50 and 100 μm. However, the other two types of copper powder with large particle sizes, 100-300 μm and 600-1000 μm, were also used for comparison experiments.

The potassium carbonate granules were supplied by E.E. Muri & Sons Pty. Ltd., Melbourne, Australia, and had a purity of 99% as quoted by the manufacturer. Figure 3.3 shows the SEM micrograph of the potassium carbonate granules, which have a spherical shape. The required pore size and pore shape of porous copper samples can be obtained by selecting the particle size and shape of the carbonate granules. The carbonate powder was sieved and categorized into four different size ranges: 250-425 μm, 425-710 μm, 710-1000 μm and 1000-1500 μm.

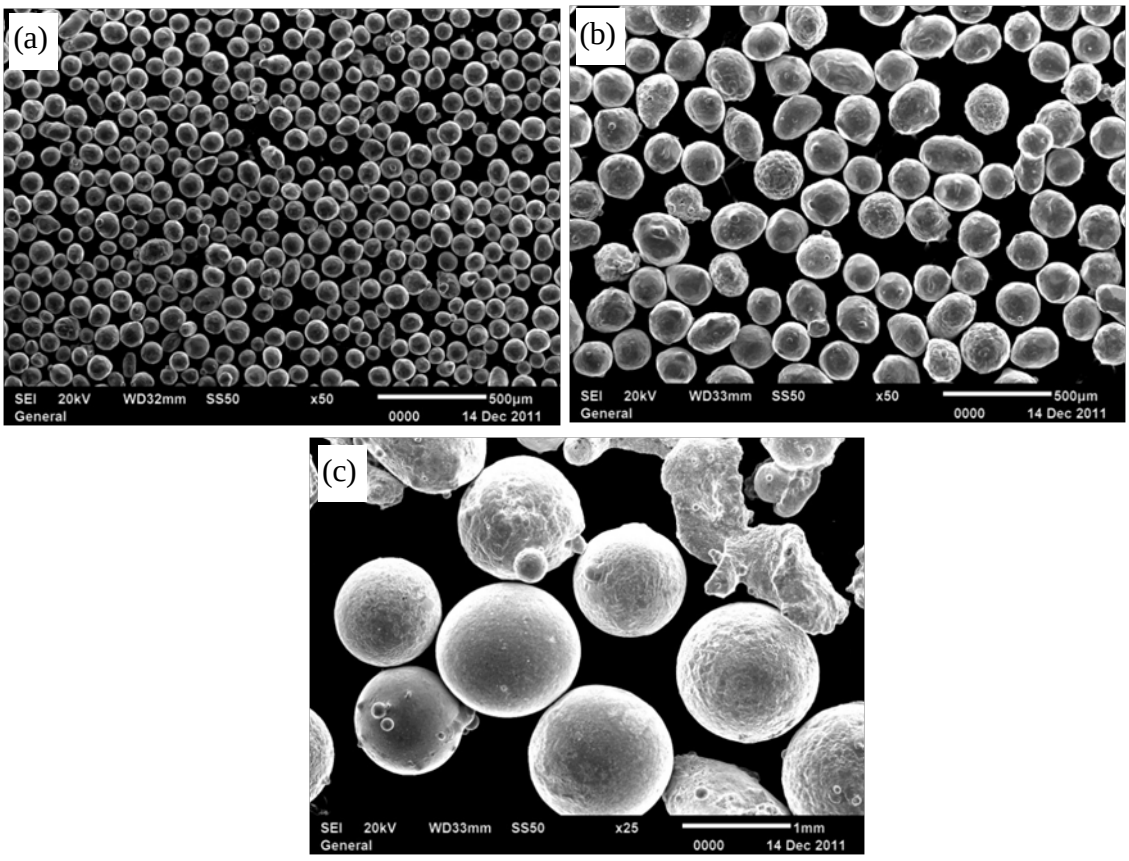

Figure 3.2 *SEM micrographs of copper powder particles with different sizes: (a) 50-100 μm; (b) 100-300 μm; (c) 600-1000 μm*

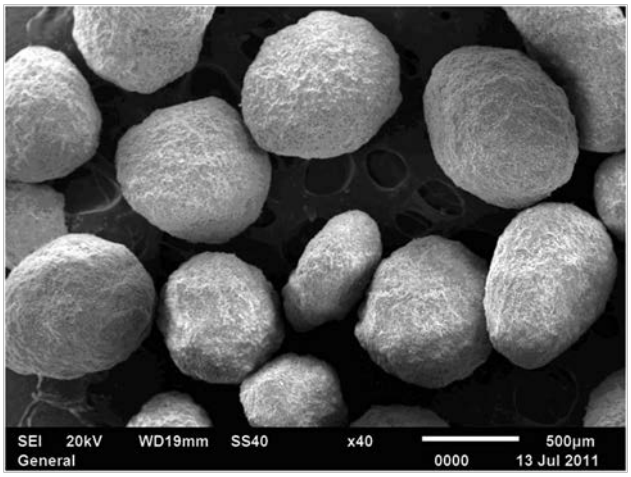

Figure 3.3 *SEM micrograph of the potassium carbonate granules with the particle size of 425-710µm.*

The final porosity of porous copper was largely determined by the pre-specified ratio of the amounts of copper powder and carbonate granules used for the powder mixture. If the spaces between the particles in the copper powder/potassium carbonate powder mixtures are negligible, the volume of the resultant sample should be equal to the total volume of the copper and carbonate powders, and the volume ratio between the carbonate powder and the resultant sample should be equal to the porosity of the resultant sample. The masses of the copper powder, M_{Cu}, and the carbonate powder, $M_{K_2CO_3}$, required for fabricating a porous copper sample with volume V and porosity ε_n (expressed as a nominal porosity) were therefore determined by:

$$M_{Cu} = (1-\varepsilon_n)V\rho_{Cu} \tag{3.1a}$$

$$M_{K_2CO_3} = \varepsilon_n V\rho_{K_2CO_3} \tag{3.1b}$$

where ρ_{Cu} =8.9 g/cm^3 is the density of copper and $\rho_{K_2CO_3}$ =2.3 g/cm^3 is the density of potassium carbonate, both of which are supplied by the manufacturers. It should be mentioned that the actual porosity of the resultant sample (ε) is a slightly (approximately 2%) higher than the nominal porosity (ε_n) because of the gaps between the copper and potassium carbonate particles.

3.1.2 Mixing and compaction

The copper powder and potassium carbonate powder were weighed in the pre-specified ratio according to the final porosity required and mixed in a plastic beaker. A small amount of ethanol (approximately 1-2 vol.% of the mixture) was added to the mixture to act as a binding agent between the copper and carbonate particles. The beaker was sealed and manually shaken for 30-60 seconds until no clear separation between the copper and carbonate particles was observed, i.e., nearly every potassium carbonate particle was covered by a layer of copper particles.

Two mild steel dies with different cavity sizes were used to compact the mixed powders. The one used for fabricating permeability and heat transfer test samples has a cavity size of 40 mm in length × 30 mm in width × 12 mm in height and the one for thermal conduction and mechanical test samples has a cavity size of 55 mm in length × 30 mm in width × 40 mm in height. Figure 3.4 is a schematic diagram of the mild steel die used in the experiment. The copper/carbonate mixture was added to the die and then

compacted using two punches in a hydraulic press at a pressure of 200 MPa for approximately ten seconds. This compaction pressure was selected according to the principle laid down in the previous research (Zhao et al. 2005). Two punches, upper and lower, were used to ensure a relatively uniform pressure in the sample during the compacting process. The green compact was then pressed out and placed in a silica-gel desiccator to prevent the carbonate from hydration before sintering.

The fabrication procedure for the double-layer samples was slightly modified. In the compaction stage, the powder mixture for the first layer was first compacted in the mould at a pressure of 50 MPa for approximately five seconds. Subsequently, the powder mixture for the second layer was added in the mould and compacted at a pressure of 200 MPa for approximately ten seconds.

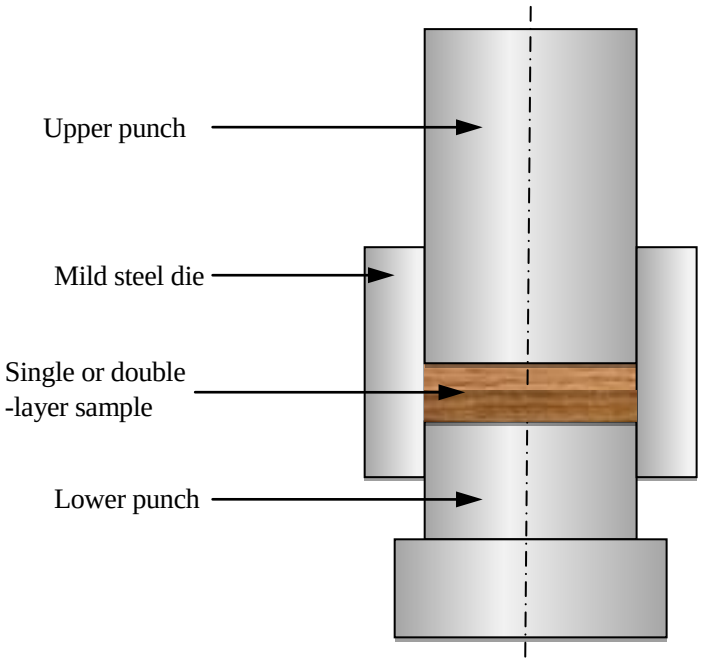

Figure 3.4 *Schematic diagram of a mild steel die used for compaction.*

3.1.3 Sintering

A VTS vacuum furnace was used for the sintering process. The green compacts were put on a steel plate and then placed at the centre of the cold furnace to allow for even heat distribution. A piece of aluminium silicate fiber mat was placed between the samples and the steel plate to avoid bonding between them during the sintering process. A schematic diagram of the sintering process is shown in Figure 3.5. After a vacuum of 10^{-1} Pa was achieved, the furnace was heated first up to 200ºC and kept at this temperature for 20 minutes to remove water and ethanol. It was then heated up to 500ºC and kept at this temperature for 20 minutes to remove vacuum grease. Sintering process was conducted at first sintering temperature of 850ºC and held at this temperature for 2 hours. This sintering temperature was selected such that the particles of potassium carbonate, which has a melting point of 891ºC, remained in the solid state. In order to remove the carbonate, the temperature was then increased to 950ºC and maintained for 2 hours for carbonate decomposition and further sintering. The heating rate during all heating stages is 10 ºC/min. The samples were subsequently furnace cooled. Typical porous copper samples after sintering are shown in Figure 3.6.

3.1.4 Shaping

The porous copper samples were cut to the required sizes and shapes using a small handsaw, and were ground using carborundum papers ranging between 320 and 1000 grits to achieve accurate dimensions and smooth surfaces.

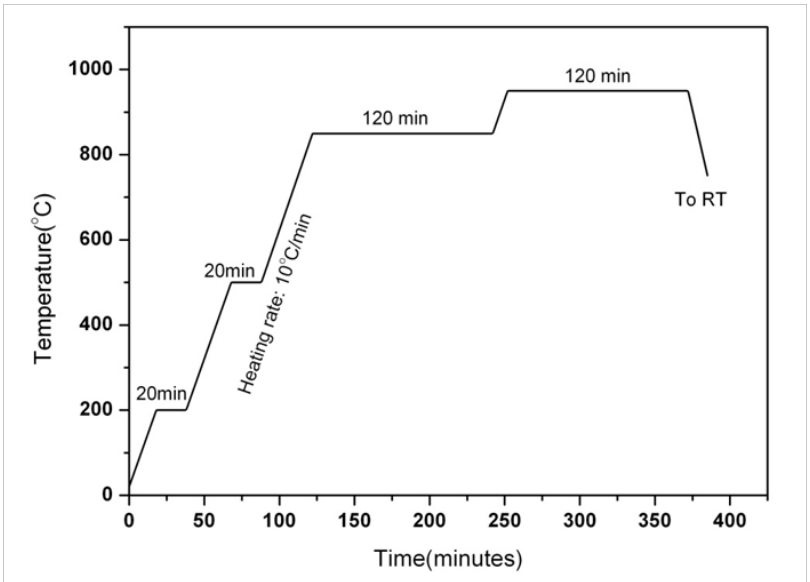

Figure 3.5 *Schematic diagram of sintering procedure.*

Figure 3.6 *Typical porous copper samples assembly after sintering.*

3.2 Structure

In this section, the experimental results of the microstructure, porosity, specific surface area and tortuosity of porous copper samples will be given.

3.2.1 Optical microscopy and SEM analysis

The microstructure and macrostructure of the porous copper samples were observed by Optical Microscopy (OM) and Scanning Electron Microscopy (SEM) (S-2460N, Hitachi, Japan). To analyze the internal structure of a porous copper sample by OM and SEM, the cross section of the sample was first ground carefully using 1000 grit papers carefully, and then cleaned in an ultrasonic bath for 20 minutes to remove any loose particles from the surface. The sample was subsequently immersed in 90% ethanol for 5 minutes and then dried by hot air.

The cross-sectional surface was observed using a Nikon optical microscope at low magnifications to check the homogeneity of pore distribution between batches of samples and to take micrographs of various samples for quantitative metallography. SEM was used to observe the morphology of porous copper samples.

3.2.2 Measurements of porosity and specific surface area

Quantitative stereology metallography was used to as one of the method to determine the porosity and specific surface area (Underwood 1970). A counting grid was superimposed onto a micrograph of the measurement area of the sample. Figure 3.7 shows an example of the counting grid superimposed on the micrograph of a test sample. The micrographs were processed by the software ‘Image-Pro Plus 6.0’ (Media Cybernetics Inc., USA) to identify the intercepts between grid lines and pore perimeters.

The number of points located in the pores, P_{pore}, the total number of testing points within the selected area, P_{tot}, and the number of intercepts between the testing lines and the pore boundary, P_{inter}, were counted. For P_{pore} and P_{tot} counting, those points fell on the boundary were counted as 1/2 (Shen et al. 2006). The porosity, ε, is defined as the volume fraction of the pores and can be calculated by:

$$\varepsilon = \frac{P_{pore}}{P_{tot}} \tag{3.2}$$

The specific surface area, S_V, is defined as the ratio of the total internal surface area to the total volume of the sample and can be obtained by:

$$S_V = 2P_L = \frac{2P_{inter}}{L_{test}} \tag{3.3}$$

where P_L is the number of intercepts generated per unit length, and L_{test} is the whole length of the testing lines.

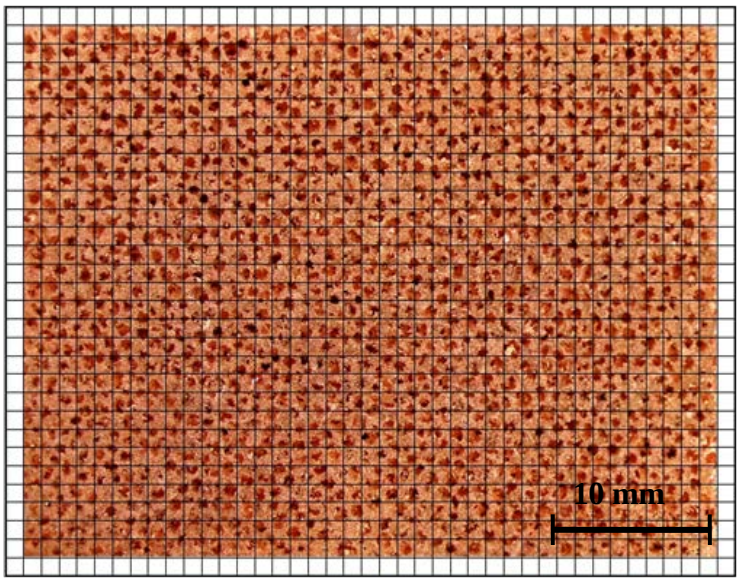

Figure 3.7 *Micrograph of a test sample superimposed with a counting grid*

Two further methods were used to obtain porosity by measuring the density of the porous copper. Both methods measured the mass of the sample using an electronic balance. The first method determined the volume of the sample by measuring the dimensions of the sample using a vernier caliper. The length, width and height of each sample were measured five times at the different positions on the sample, and the average values were taken. The second method used the Archimedes principle and determined the volume of the sample by measuring the buoyancy force the sample experienced in water. To prevent infiltration of water into the sample during the measurement, the surface of the sample was sealed with Vaseline. The sample was then sunk into the water in a container on an electronic balance and held by a thin thread to minimise the error caused by the volume of the thread in the water. The weight increase of the water container is equal to the buoyancy force, which is the product of the volume of the sample and the density of water. Given the density of water, the volume of the sample can be easily obtained. The second method is far more accurate than the first method, especially when the physical measurements of the dimensions of a sample are difficult, e.g. when the sample is damaged or has an irregular shape. In this study, the Archimedes method was employed as the main method to measure the volume of the porous copper samples, from which the relative density and porosity were calculated.

3.2.3 Tortuosity measurements by acoustic test

The tortuosity of the porous copper samples was calculated by the analytical solution and extrapolation approach from the acoustic absorption curve of the porous copper sample, as described by Zhu et al. (2012). The porous copper samples for the acoustic test have a diameter of 30 mm and a height of 10 mm. The acoustic tests were conducted by Prof. B. Zhang from Ningxia University, China. The samples were either located directly against the back-plate of the test sample holder within the impedance tube (B&K 4206, Denmark), or with a gap of 20 mm or 50 mm between the sample and back-plate. Measurements were taken in the range of 500-6500 Hz. During the test, vaseline was applied around the perimeter of the test sample to ensure that any pores or cavities were filled between the tube and the sample and that there was a total incident surface. Before the tests began, the sound absorption coefficient of the back plate of the impedance tube was measured. It had an average of just 0.05 over all frequencies tested, so its effect on the measurements was deemed to be negligible. The typical acoustic curves were shown in Figure 3.8. Johnson-Champoux-Allard model (Allard et al. 2009) was used to theoretically calculate the acoustic absorption coefficient at different frequency by a set of postulated pore parameters. Analytical solution and extrapolation approach by comparing the theoretically calculated and measured acoustic absorption curves, was used to determine the tortuosity of the porous copper. Detailed information of this approach is given in Appendix A.

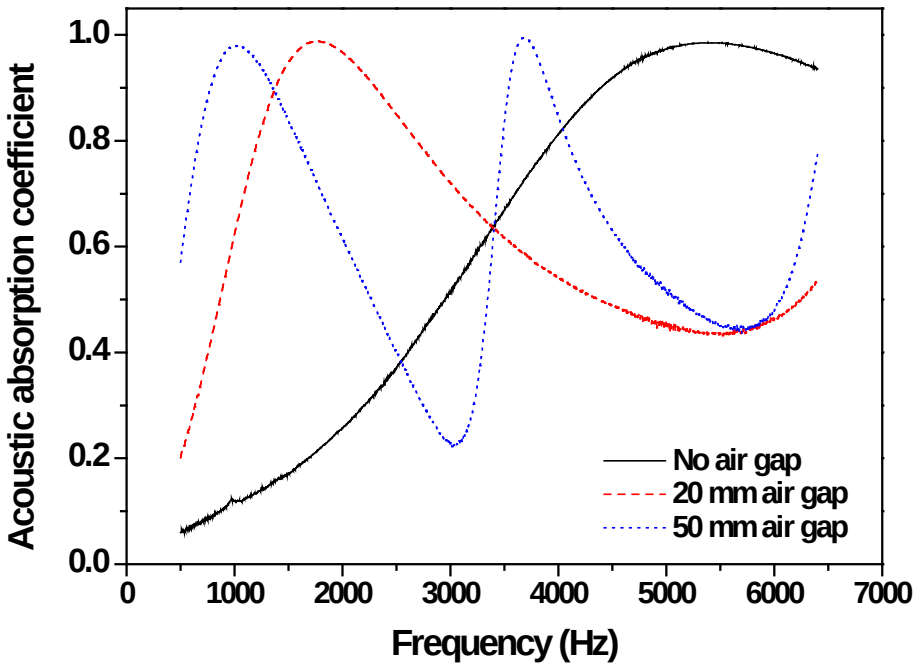

Figure 3.8 *Typical acoustic curves.*

3.3 Permeability

Permeability is a property of porous medium with respect to how well the fluid can flow through the porous medium. It is often used to evaluate the ability of porous medium to transmit fluid, and an increase in permeability usually indicates a more open structure in the porous medium.

3.3.1 Principle for permeability measurements

As described in Section 2.3.1, pressure drop across a homogeneous porous medium for steady fluid flow can be described by the Darcy model (Darcy 1856), which was the

first mathematical model to describe the linear relationship between the permeability and pressure gradient of a porous medium based on experimental observations. Later research found that Darcy's model is only good for approximate calculations at the low fluid velocities and is not appropriate to describe the pressure drop in porous solid at medium or high fluid velocities. A more accurate description is the Forchheimer-extended Darcy equation including a quadratic term (Forchheimer 1901, Venkataraman & Rao 2000, Dukhan 2006):

$$\frac{\Delta P}{L} = \frac{P_{in} - P_{out}}{L} = \frac{\mu}{K} v_d + \rho_f C v_d^2 \tag{3.4}$$

where ΔP is the pressure drop, L is the length of the sample, μ is the viscosity of fluid, P_{in} and P_{out} are inlet and outlet pressure, ρ_f is the density of fluid, v_d is the Darcian velocity of the fluid, which is the flow rate of the fluid divided by the cross-Sectional area. K is the permeability of porous medium, and C is the form drag coefficient related to the structure of the permeable medium. In Eq. (3.4), P_{in}, P_{out} and v_d can be measured in the experiment.

Eq. (3.4) is the general equation for incompressible fluid, such as water, and was used to calculate the water permeability through the porous metal. In the case of gas flow, owing to the compressibility of the gas, both the volume flow rate and the velocity vary with pressure from one end of the sample to the other. This poses a dilemma because the original integral form of Darcy's law assumes that these quantities are constant. The

way out of this apparent dilemma is to integrate the differential form of Darcy's law, using the condition that is appropriate to gas flow, i.e., that at constant temperature and in the steady state the product of pressure and velocity is constant throughout the sample. The Forchheimer-extended Darcy equation can be revised for air as (Innocentini et al. 1999b):

$$\frac{P_{in}^2 - P_{out}^2}{2P_{out}L} = \frac{\mu}{K} v_{out} + \rho_f C v_{out}^2 \tag{3.5}$$

where v_{out} is outlet velocity of air and has a relationship with Darcian velocity of $v_{out} = (P_{in} + P_{out})v_d / 2P_{out}$.

3.3.2 Experimental apparatus

Two types of fluid, air and water, were used in the tests. A schematic diagram and a photograph of the experimental apparatus used for air permeability tests are shown in Figure 3.9. In the air permeability test system, air flowed through a ball valve, a filter and regulator, a T-type thermocouple and a flowmeter, the input pressure transducer, the porous copper sample contained in the sample holder, the output pressure transducer and a flowmeter. Both the input and output transducers were rugged pressure transmitters (PXM219-001G, OMEGA, USA, pressure range of 0-1 bar with a ±0.25% full scale accuracy), located 1cm before and after the sample. Flow rate was measured by a panel mount flowmeter (FL50252A, OMEGA, USA, flow velocity range of 0.5-4.5 SCFM with ±5% full scale accuracy).

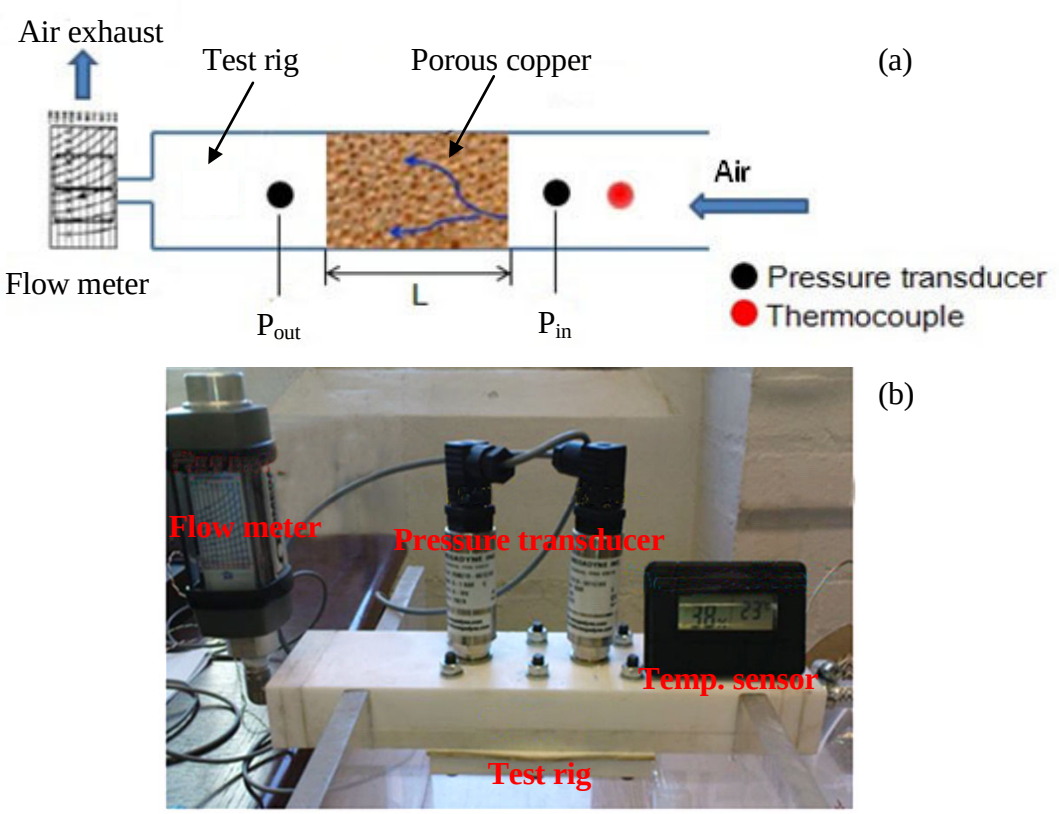

Figure 3.9 *Schematic diagram (a) and photograph (b) of the experimental apparatus used for the air permeability tests.*

A schematic diagram of the water permeability test apparatus is shown in Figure 3.10. The same apparatus was also used for heat transfer tests, which will be described in Section 3.5.1. The apparatus was connected to the mains water supply through a 19mm copper pipe. The water flowed through a filter, a ball valve, the input pressure transducer, the porous copper sample contained in the sample holder, the output pressure transducer and a flowmeter. The input pressure was measured by a rugged pressure transmitter (PXL 219-004GI, OMEGA, USA, pressure range of 0-4 bar with a ±0.25% full scale accuracy), and the output pressure was measured using the other rugged pressure transmitter (PXM219-001, OMEGA, USA, pressure range of 0-1 bar with a ±0.25% full scale accuracy). The flow rate was measure by panel mount

flowmeter (FL50001A, OMEGA,USA, flow velocity range of 0.1-1 SCFM with ±5% full scale accuracy; or FL50002A, OMEGA, USA, flow velocity range of 0.4-4 SCFM with a ±5% full scale accuracy). The sample holder was made of polytetrafluroethylene (PTFE), and the flow channel through the sample holder was 20 mm wide and 5 mm high. All the test instruments were properly mounted on the sample holder. The signals of pressure and temperature were collected by a computer.

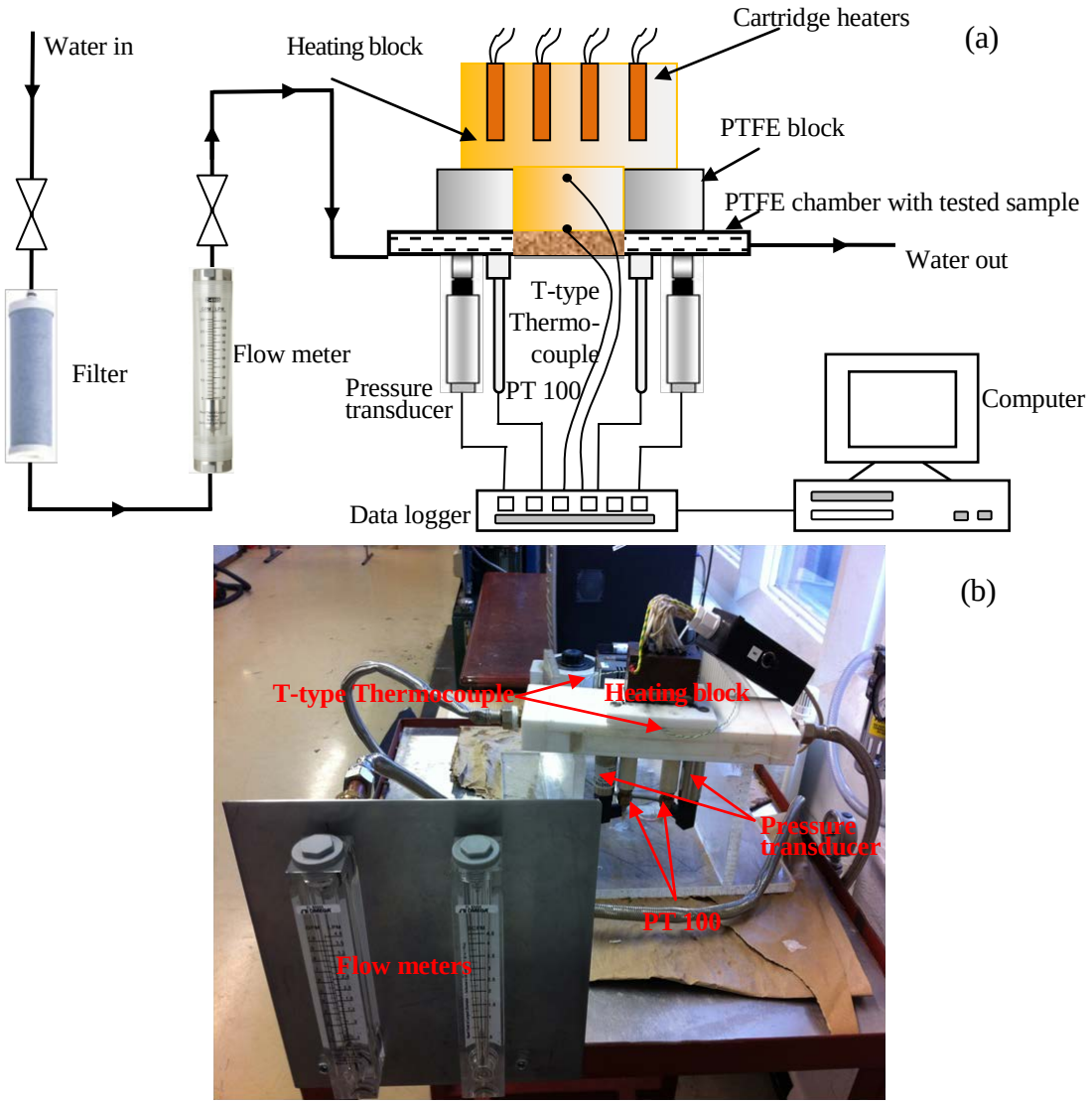

Figure 3.10 *Schematic diagram (a) and photograph (b) of the experimental apparatus for water permeability and heat transfer tests.*

3.3.3 Test procedure

The permeability of samples with different pore sizes and porosities was measured at different air or water flow rates under atmospheric conditions at a temperature of 20±1ºC. All samples had norminal dimensions of 30 mm × 20 mm × 5 mm. The standard deviation of dimensions was less than 0.25% of the average. The test sample was placed within the channel of the sample holder and then the channel was sealed with the PTFE lid using eight hexagonal bolts. The flow rate was varied gradually by the valve. At each flow rate, the inlet and outlet pressures were recorded. With known cross sectional area and length of the sample, viscosity and flow rate of fluid, and input and output pressures, the permeability was calculated from Eq. (3.4) and Eq. (3.5) for water and air, respectively.

3.4 Thermal Conductivity

In this section, the basic principle, experimental apparatus and calculation equations for thermal conductivity measurements will be introduced.

3.4.1 Principle for thermal conductivity measurements

The measurement of the thermal conductivity of moderate to good conductors is normally carried out under steady-state conditions using a longitudinal heat-flow technique or a centre radial heat-flow method. It offers greater flexibility in that the materials having a wide range of conductivity values can be investigated by selecting

the correct specimen size. The basis for this method lies in Fourier's law that the heat flux of a one-dimensional steady state problem can be expressed as (Kaviany 1995):

$$Q = \lambda A \frac{\Delta T}{\Delta x} \tag{3.6}$$

where Q is the heat flow, λ is the thermal conductivity of the material, A is the cross-sectional area of the conductor and $\Delta T/\Delta x$ is the temperature gradient. A method reported by Corsan (1984) can be used to determine the heat flow by measuring temperature difference in a pure copper comparator with known thermal conductivity. Assuming that the porous copper specimen and the comparator are perfectly insulated and ignoring the heat loss at the interface between the comparator and the specimen, the heat flow is a constant throughout the porous specimen and the solid comparator. As the cross sectional area, A, is also the same in both the comparator and the porous specimen, the thermal conductivity of the porous copper, λ_p, is given by:

$$\lambda_p = \lambda_c \frac{(\Delta T / \Delta x)_c}{(\Delta T / \Delta x)_p} \tag{3.7}$$

where λ_c is the thermal conductivity of the solid copper comparator, given by the manufacturer as 391 W/m·K, $(\Delta T/\Delta x)_c$ is the temperature gradient in the solid copper comparator and $(\Delta T/\Delta x)_p$ is the temperature gradient in the porous metal test specimen.

3.4.2 Experimental apparatus

Figure 3.11 shows a schematic diagram of the test apparatus designed and built for heat conductivity test. The porous copper specimen has a square bar geometry with nominal dimensions of 12 mm × 12 mm × 55 mm. The width and height of the specimen were

measured at five positions along the length, and showed a standard deviation less than 0.25% of the average. A solid copper bar imbedded with a 100 W cartridge heater (FIREROD, Watlow, USA) was used as the heat source, and the input power was controlled by a variac. The porous copper sample was clamped onto the bottom of the copper bar. Another solid copper bar with dimensions of 12mm×12mm×150mm was used as the comparator and was clamped onto the other end of the test specimen. The solid copper bars were made from a commercially pure copper (C103, supplied by Merseyside Metal Services Ltd., UK), and had a thermal conductivity of 391 W/mK as given by the manufacturer.

In order to remove the heat conducted through the specimen and comparator and to obtain steady state temperature gradients in them, the bottom end of the comparator was immersed in circulating cold water. A hole was drilled out of the comparator at the bottom and inserted with a piece of porous copper to accelerate heat removal. Thermally conductive grease with a thermal conductivity of 3.6 W/m·K (supplied by CHEMTRONICS, USA) was applied to the heat source/specimen and specimen/comparator interfaces to enhance heat conduction through the interfaces. A load of approximately 10 N was applied to the heater/sample/comparator assembly to further enhance the interfacial contacts. The comparator and the test specimen were housed in grooved PTFE blocks clamped by an aluminium jig to minimise heat losses through the side surfaces.

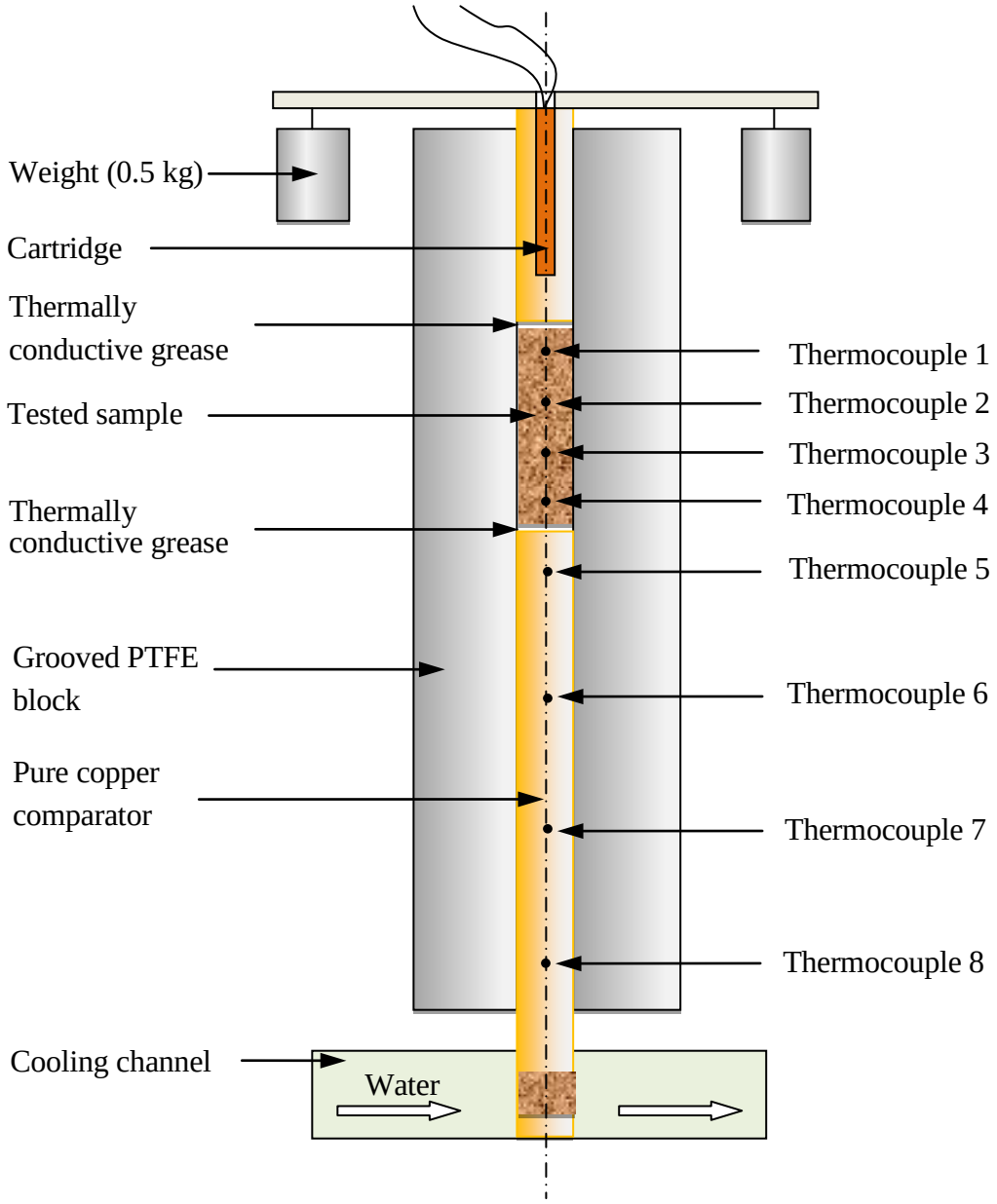

Figure 3.11 *Schematic diagram of the apparatus for thermal conductivity test.*

Holes with a diameter of 1.7 mm and a depth of 6 mm were drilled at specific, measured locations along the length of the comparator and the porous copper test specimen using a pillar drill. There were four holes in the specimen with the interval of 1.5cm, and four holes in the comparator with the interval of 3 cm. T-type thermocouples were inserted into each hole to measure the temperature during heat

conduction. The end of each thermocouple had a heat-shrunk plastic shroud around it to provide a tight fit in the drilled hole and to ensure that the temperature reading was from the precise axial centre of the specimen. All the thermocouples were linked up directly to a USB thermocouple data logger with a resolution of 0.01°C (TC-08, Pico Technology, UK), which can output signals and show the temperature values on the computer using the PLW recorder software.

Different heat flux through the sample/comparator was obtained by changing the voltage of the variac. The test specimen and comparator were insulated circumferentially with PTFE blocks 10 mm thickness to minimise radial heat losses. Calcium-magnesium-silicate wool and polyethylene were added around any naked pure copper bar exposed out of the PTFE blocks.

3.4.3 Test procedure

All of the porous copper specimens used for the permeability tests were also used for heat transfer tests. The test sample was first placed in the PTFE channel and the heater/sample/comparator assembly was secured as described in Section 3.4.2. The heat cartridge was then switched on. The temperatures at the different locations were measured after the steady state was reached (approximately half hour and depending on the relative density of the sample). The temperature gradients in the test specimen and comparator were obtained from the temperature plots along the lengths of the

comparator and the porous copper sample. The thermal conductivity of the porous copper sample was finally determined from the temperature gradients obtained from the test specimen and comparator, following the procedure reported by Thewsey & Zhao (2008). Each specimen was tested at least three times and the average values of heat transfer coefficients were taken.

The apparatus was calibrated with five standard metal bars supplied by Merseyside Metal Services Ltd., UK, made of oxygen-free copper, pure aluminium, AlCu alloy, 7071 alloy and mild steel with thermal conductivities of 391, 238, 143, 138 and 46 W/mK, respectively. Figure 3.12 shows the temperature gradients in the metal bar samples and the pure copper comparator in steady-state conditions with the output heat flux of about 13kW/m^2. The first four data points represent the temperature readings of the four thermocouples in the metal bar sample being tested, and the remaining four data points represent the thermocouple temperature readings in the pure copper comparator. The change in temperature gradient is clearly visible between thermocouples 4 and 5, which span the interface between the comparator and the metal bar. The plots in Figure 3.12 show linear temperature gradients in both the pure copper comparator and the metal bars being tested. Under the condition of 13 kW/m^2 heat flux, the temperature gradients in Oxygen-free copper, pure Al, AlCu alloy, 7071 alloy and mild steel bars and their corresponding comparator are: -0.0339 -0.0332.; -0.0552., -0.0326.; -0.0993., -0.0359.; -0.0934, -0.0326; and -0.3166, -0.0369 K/m; respectively

(shown in Figure 3.12). Using Eq. (3.7), the thermal conductivity for these samples were calculated to be 382.0, 230.9, 141.5, 136.4 and 45.5 W/mK, respectively. The measurement differences, compared with the theoretical values supplied by the manufacturer, were only 2.3%, 3.0%, 1.1%, 1.2% and 2.2%, respectively.

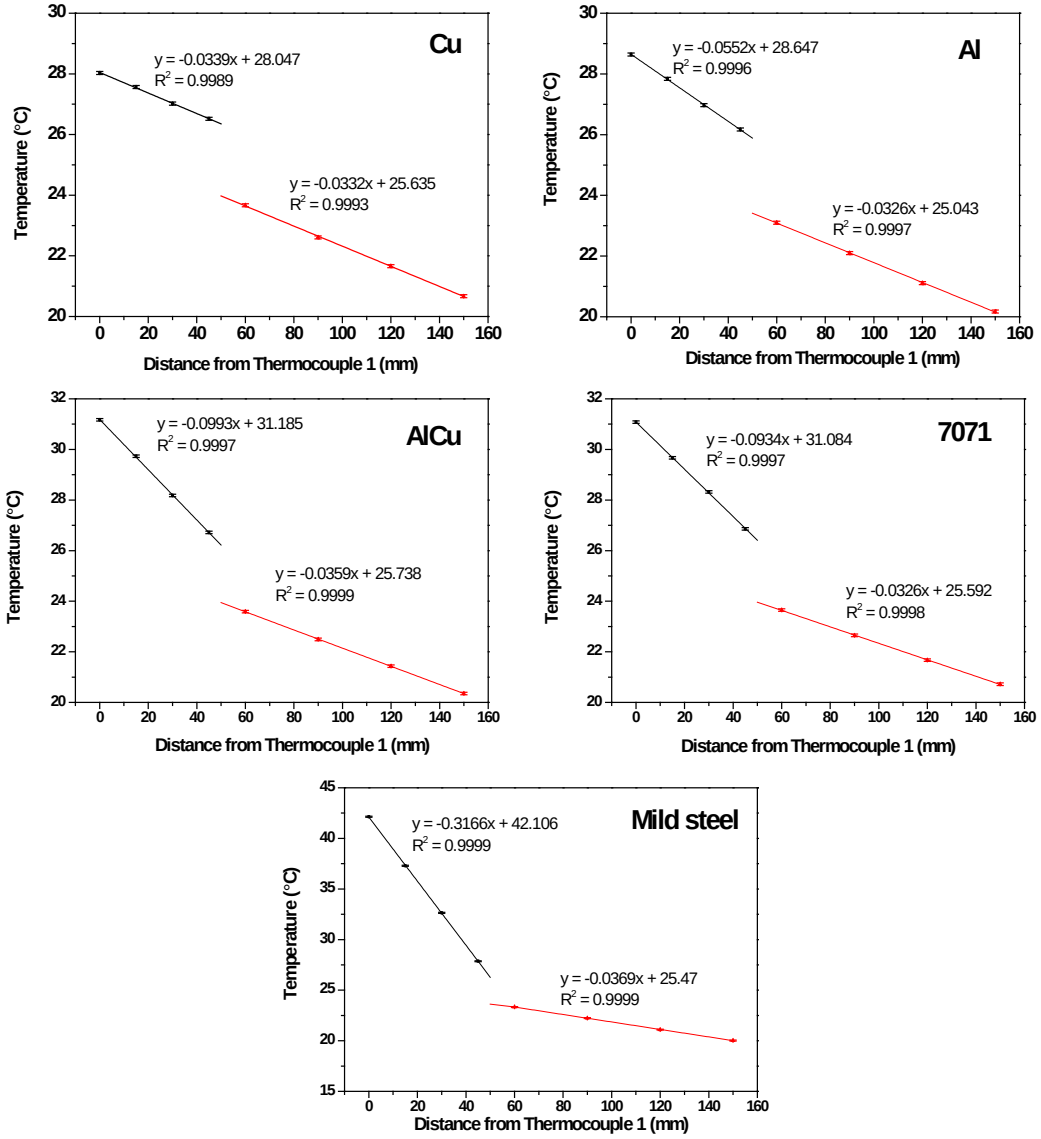

Figure 3.12 *Temperature gradients in the standard calibration samples and the solid copper comparators (Heat flux: ~13 kW/m^2).*

In order to investigate the accuracy of the measurements, various heat fluxes were applied to the test samples. Table 3.1 gives the thermal conductivity calibration results of the apparatus. It was found that the measured values are close to the theoretical values when the heat flux was below or at 13 kW/m^2 but that they deviated from the theoretical values when the heat flux was above 13 kW/m^2. This may be caused by the low thermal conductivity of the conductive grease, which increased radial heat loss. Therefore, the experiments were conducted at heat flux below 13 kW/m^2.

Table 3.1 *Thermal conductivity calibration results of the apparatus (W/mK).*

Reference	Metal	Theoretical Value	Heat Flux ~8 kW/m^2	Heat Flux ~13 kW/m^2	Heat Flux ~18 kW/m^2	Heat Flux ~25 kW/m^2
R1	Oxygen-free Copper	391	380.4	382.0	372.9	360.1
R2	Pure Aluminium	238	232.8	230.9	225.9	217.4
R3	AlCu	143	146.2	141.5	136.4	125.5
R4	7071	138	140.4	136.4	130.3	122.4
R5	Mild steel	46.5	44.5	45.4	45.6	40.6

3.5 Heat Transfer

The aim of the experiment is to investigate the heat transfer performance of the porous copper samples for use as heat exchangers under forced convection cooling. The concept of the experiment is to force the coolant (water) through the sample attached to a heating source and to measure the heat transfer coefficient as an indicator of the heat transfer efficiency of the test sample.

3.5.1 Experimental apparatus

A schematic diagram of the experimental apparatus for heat transfer test has been shown in Figure 3.10. The experimental set-up was basically the same as that used for the permeability tests, with some modifications made to various parts of the apparatus. Specifically, a heating block and a series of cartridge heaters were added as a heat source, and a series of thermocouples were inserted at different locations for heat supply and temperature measurements.

The heating block was made of C103 oxygen-fee copper, with a thermal conductivity of 391 W/mK (value supplied by the manufacturer). The top part of the block (60 mm × 40 mm × 50 mm) was used to hold the cartridge heaters and the bottom part (30 mm × 20 mm × 25 mm) was designed to achieve steady heat conduction so that the input power can be calculated through the temperature gradient. To minimise heat loss, the top part was insulated using calcium-magnesium-silicate wool and polyethylene, while the bottom part was insulated using PTFE. The block was heated externally using eight Watlow FIREROD cartridge heaters, which can deliver a maximum total input power of 0.8 kW. Each cartridge heater was located in 4mm holes drilled at uniformly distributed locations within the copper blocks. The heaters were controlled using a variac so that a variable heating power was generated for different experimental requirements.

The heat delivered through the heat block was conducted into the test sample and eventually transferred into the coolant flowing through it, causing the coolant to heat up. Two T-type thermocouples were inserted into two 1.7 mm holes located in the bottom part of the heat block to measure the temperature difference in the heat block. The distance between these two thermocouples is 24 mm. The temperatures of the coolant flowing in and out of the sample were measured using platinum resistance PT 100 thermometers, which offer a high accuracy of ±0.1 K over a wide temperature range. Two pressure transducers were fixed on the chamber to measure the inlet and outlet pressures of the fluid (as described in Section 3.2.2). The data from the thermocouples and thermometers was acquired using a data logger and processed using the InstrNet software (supplied by Instrument Industry, UK).

3.5.2 Test procedure

The porous copper sample was located into the channel of the sample holder and was then covered by the heating block. The sample holder and the heating block were subsequently clamped together using eight bolts. The eight cartridge heaters were located in the pre-drilled holes within the copper block and were pushed in fully. Fiberglass insulation was placed around the block to minimise the heat loss to the environment into the ambience. Measurements were made at different power inputs to the heating chamber, namely 150 W/m^2, 250 W/m^2 and 500 W/m^2. The heating power was set by controlling the input voltage of the transformer. A series of fluid flow rates

were used in the test for each sample. The flow rate was adjusted to the required level using a valve. It normally took approximately 10-20 minutes to achieve a steady state, i.e., when the heating power supply, fluid flow, inlet temperature and the temperature of the bottom of the heating block no longer change. All the signals were collected by the data logger and recorded by the computer.

For double-layer samples, the layer order is an important factor in the measurements of heat transfer coefficient, due to the heat input mode of the facility used for the heat transfer test (see Figure 3.10). Figure 3.13 shows a schematic diagram of the arrangement of samples with double-layer structures, i.e., two layers with different porosities and/or pore sizes. The layer in direct contact with the heat source is termed the Upper Layer and the other layer is termed Lower Layer. There are two ways to conduct the heat transfer test of a sample, depending on which side is in contact with the heat source. The layer order is represented by (nominal porosity of Upper Layer) / (nominal porosity of Lower Layer). If the layer with high permeability in contact with the heat source, it is termed normal order. If the layer with low permeability in contact with the heat source, we called it as reverse order. For example, sample S51 has two layers with different nominal porosities of 60% and 80%. When the 80% layer was set to in contact with the heat source, this condition is expressed as 80%/60% (Normal order). On contrary, if the 60% layer is in contact with the heat source, the condition is expressed as 60%/80% (Reverse order).

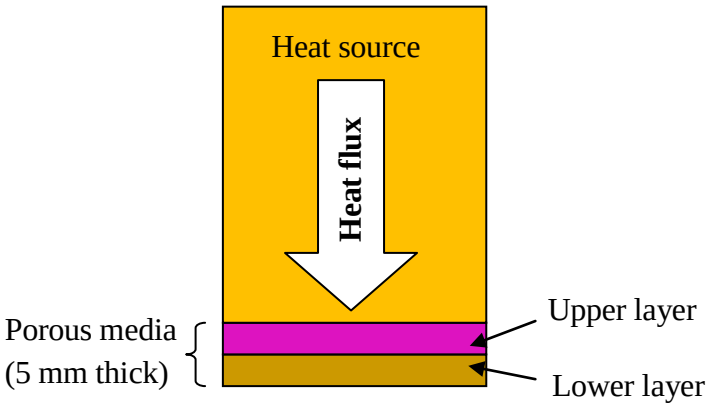

Figure 3.13 *Schematic diagram of heat transfer test for samples with double-layer structures*

3.5.3 Calculation of heat transfer coefficient

The heat transfer between a solid and a fluid can be characterised by an overall heat transfer coefficient of the cooling system. This heat transfer coefficient, *h*, can be determined by Newton's law of cooling in a convection-cooling situation:

$$Q = hA(T_1 - T_2) \tag{3.8}$$

where Q is the heat flow to the coolant, A is the interfacial area between the solid and the coolant, T_1 is the temperature of the solid's surface and T_2 is the temperature of the cooling fluid.

This study is concerned with the performance of the porous copper sample as a heat transfer medium from a heat source to a coolant, so the porous copper sample and the

coolant inside it can be considered as whole. Taking the surface area of the sample in contact with the heat block as A, the temperature of the block at the interface with the sample (T_{pl}) as T_1, and the temperature of the coolant before entering into the sample (T_{in}) as T_2, Eq. (3.8) becomes:

$$Q = hA(T_{pl} - T_{in}) \tag{3.9}$$

Assuming that all heat is transferred from the heating block to the coolant through the porous copper sample without any heat losses, the heat flow to the coolant, Q, is equal to the conductive heat flow in the heating block, which can be calculated through the temperature gradient along the heat conduction direction according to Fourier's law:

$$Q = \lambda A \frac{T_{bl} - T_{pl}}{L} \tag{3.10}$$

where λ is the heat conductivity of the heating block (λ =391 W/mK for the oxygen free copper used in the test), A is the cross sectional area of the heating block and is equal to contact area between the sample and the heating block (5.985×10^{-4} m^2), T_{bl} is the temperature of the block at the top and L is the distance between T_{bl} and T_{pl}.

Combining Eq. (3.9) and Eq. (3.10), the heat transfer coefficient can be expressed as:

$$h = \frac{\lambda(T_{bl} - T_{pl})}{L(T_{pl} - T_{in})} \tag{3.11}$$

3.6 Mechanical Behaviour

The static compression response, bending response and tensile response of porous copper samples were investigated to characterise the mechanical properties of porous copper samples in this thesis. For each set of samples produced under the same condition, three specimens were prepared and tested. The surfaces of the specimens were ground with 800 grit paper to remove any surface defects. The length, width and height of the specimen were measured at five positions, with variations less than 5% of the average.

3.6.1 Static compression tests

The porous copper samples were first cut into cuboid specimens with nominal dimensions of 12 mm × 12 mm × 20 mm. The static compression tests were conducted on a universal testing machine (Instron 4505, UK) with a cross-head speed of 0.5 mm/min. In order to investigate the influence of anisotropy on mechanical behaviour, specimens were cut from the sintered samples from two directions: parallel (//) and normal (⊥). In parallel direction the compression direction is parallel to the compaction direction and in normal direction the compression direction is perpendicular to the compaction direction.

The yield strength of porous copper sample (σ_y) was evaluated from the stress-strain curve, which was the point of intersection between two linear stages of stress-strain curve (shown in Figure 3.14).

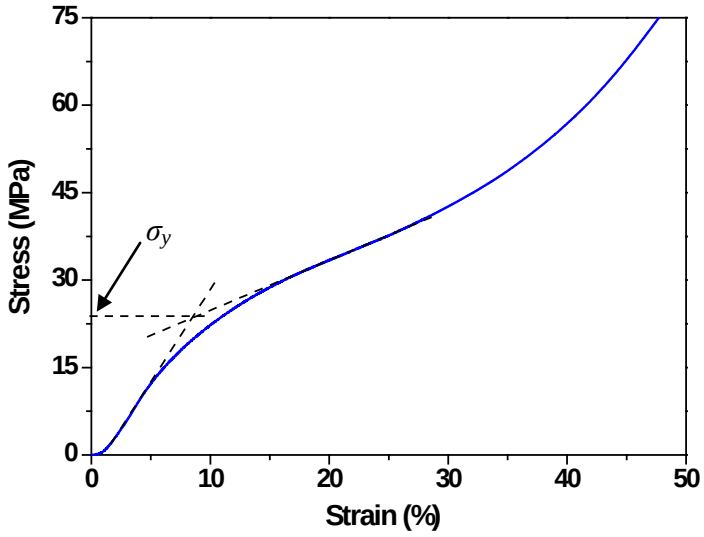

Figure 3.14 *Determination of yield strength of porous copper during compression*

During the compression test, a series of unloading and reloading routines were carried out at about 3%, 4% and 5% strains to determine the elastic modulus values. The load and the displacement of the cross-head were measured by a load cell and recorded by the machine computer. After the test, the recorded load and displacement values were converted into stress and strain values.

The gradients of the unloading curves were taken as the elastic modulus values at the respective strains. This is because during the unloading, the deformation of the

specimen is purely elastic. A set of loading-unloading routes were taken at different strains to examine the amount of plastic deformation occurring during the compression.

A typical loading-uploading compression stress-strain curve is shown in Figure 3.15. The elastic modulus of the porous copper sample (E_c) was obtained in accordance with ASTM Standard E9-89a and ASTM standard E111 and were calculated by the following equation:

$$E_c = \frac{\Delta_{stress}}{\Delta_{strain}} \tag{3.12}$$

where Δ_{stress} and Δ_{strain} are the stress and strain decrement during unloading when the sample is in the linear deformation region.

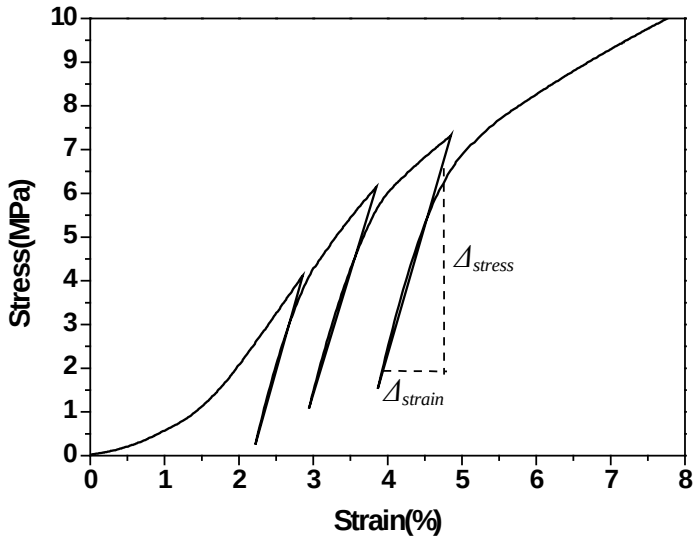

Figure 3.15 *Typical loading-uploading stress-strain curve during compression (for porous copper with porosity of 63.5% and pore size of 425-710 μm)*

3.6.2 Three-point bending tests

The porous copper samples for three-point bending test were first cut into cuboid specimens with a nominal square cross section of 10 mm×10 mm. The nominal length of the specimens was 55 mm, which was greater than the span length between the two supports (35 mm). All samples showed homogenous pore distribution and structure, with no contamination observed on any surfaces when examined under an optical microscope. The opposite sides of the specimen were ensured to be parallel using a square ruler.

The tests were carried out on a universal testing machine (Instron 4505, UK) at a crosshead speed of 1mm/min. The span length between the two supporting points was set at 35 mm. The apparent modulus of linear deformation (E_b) and flexural strength of the porous copper samples (σ_b) were obtained in accordance with ASTM Standard E855-08 and were calculated using the following equations:

$$E_b = \frac{PL^3}{4bh^3\delta} \tag{3.13}$$

$$\sigma_b = \frac{3FL}{2bd^2} \tag{3.14}$$

where P is a load increment when the sample is in the linear deformation region, δ is the deflection increment at middle span corresponding to the load increment P, and F is the maximum load applied to the specimen during the test, L is the span length between the two supports, b is the width of the specimen and d is the depth of the specimen.

3.6.3 Tensile tests

Cuboid specimens with nominal dimensions of 40 mm × 12 mm × 6 mm cut from the porous copper samples were tested. The gauge length of the specimen was about 20 mm. The porous copper specimens were relatively weak and deformed easily with large pressure, so they could not be clamped directly to the test machine. Two steel sheets with a thickness of 1mm were glued (Pattex power epoxy glue, Germany, with the bonding strength higher than 15 MPa) to the specimen and a PTFE bar with the same thickness as the specimen was inserted between the steel sheets so that the specimen can be firmly clamped to the test machine. For each set of specimens produced under the same condition, three specimens were prepared and tested. The tensile tests were conducted on a universal testing machine (Instron 4505, UK) with a cross-head speed of 0.5 mm/min.

Loading of the specimens occurred in two phases. The first phase consisted of loading/unloading for two times within the linear load-displacement region to determine the elastic modulus (the same method as the determination of elastic modulus in compression test, but with the unloading strain at 0.5% and 0.8% here). In the second phase, the specimens were loaded in tension into the plastic regime until failure to investigate the plastic deformation and fracture behavior. The load and the displacement of the cross-head were measured by a load cell and recorded by a computer connected

to the machine. After the test, the recorded load and displacement values were converted into stress and strain values. Figure 3.16 shows a specimen after test.

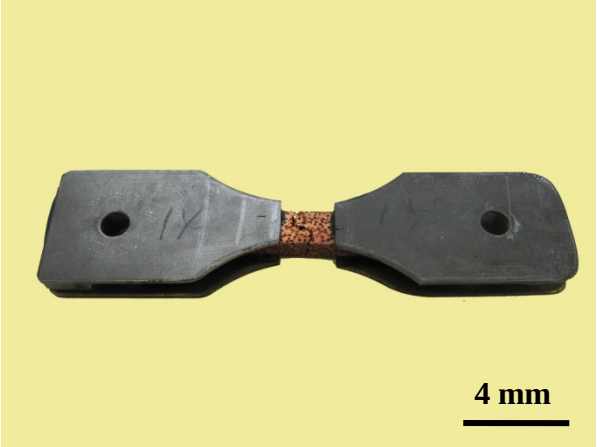

Figure 3.16 *Photograph of a specimen after tensile test.*

3.7 Error and Uncertainty

In this thesis, the error and uncertainty in the measurement are characterised by standard deviation based on the mean values, differences between measured and calculated or theoretical data and experimental uncertainty.

3.7.1 Mean value and standard deviation

For any of the physical parameters measured in this thesis, a finite set of values was obtained by repeating measurement under the same condition. The mean value for *n* measurements was $\overline{X} = \frac{1}{n}\sum_{i=1}^{n} x_i$ and the standard deviation was calculated by:

$$\frac{\Delta X}{\overline{X}} = \frac{\sqrt{\sum_i \left(x_i - \overline{X}\right)^2 / (n-1)}}{\overline{X}} \times 100\% \tag{3.15}$$

The length, width, height, thickness and weight of the porous copper samples were measured at least five times and the standard deviations were less than 0.25%. The permeability, thermal conductivity, and heat transfer coefficient were measured under the same condition at least three times, and the standard deviations were less than 3.5%, 2.8% and 2.4%, respectively.

3.7.2 Differences between measured and calculated or theoretical data

The difference between the measured data (x_i) and the calculated or theoretical data (y_i) was determined by:

$$\zeta = \frac{|x_i - y_i|}{y_i} \times 100\% \tag{3.16}$$

The coefficient of determination (R^2 value) was used to describe the goodness of curve fitting (Colin et al. 1997).

3.7.3 Experimental uncertainty

When several independent variables (x_i) are used in a function Φ, i.e.,

$$\phi = x_1^a x_2^b \cdots\cdots x_N^n \tag{3.17}$$

The uncertainty can be expressed by (Moffat 1988):

$$\frac{\Delta\phi}{\phi}=\sqrt{\left(a\frac{\Delta x_1}{x_1}\right)^2+\left(b\frac{\Delta x_2}{x_2}\right)^2+\cdots\cdots+\left(n\frac{\Delta x_N}{x_N}\right)^2} \tag{3.18}$$

In this thesis, systematic and mechanical errors of facilities and the standard errors of measured length, width, thickness and weight were considered for uncertainties. These uncertainties are summarized in Table 3.2.

Table 3.2 *Uncertainty of physical parameters in this thesis.*

Parameter	Uncertainty
Porosity	< 0.25%
Darcian velocity	< 5.1%
Heat flux in section 3.4	< 2.6%
Thermal conductivity	< 4.1%
Heat flux in section 3.5	< 2.2%
Heat transfer coefficient	< 3.1%
Reynolds number	< 5.2%
Nusselt number	< 3.2%
Yield strength	< 0.4%
Elastic modulus (compression)	< 0.5%
Flexural strength	< 1.1%
Apparent modulus (bending)	< 0.7%
Maximum tensile strength	< 0.4%
Elastic modulus (tensile)	< 0.5%

Chapter 4

Results

This chapter will present the results obtained from the experiments, including microstructure and pore parameters, permeability, thermal conductivity, heat transfer coefficient and mechanical properties of LCS porous copper with single or double layer structure.

4.1 Structure and Pore Parameters of Porous Copper

4.1.1 Structure

The microstructure and topography of the LCS porous copper specimens were examined using SEM. Figure 4.1 shows the representative features of a typical specimen. The macro topography of the porous samples is shown in Figures 4.1(a) and (b). Figure 4.1(a) is the transverse section of the sample (normal to the compacting direction), while Figure 4.1(b) is the longitudinal section of the sample (parallel to the compacting direction). The large pores inside the samples represent the spaces previously occupied by potassium carbonate particles. The compacting process has improved the contacts between the metal particles, which benefited the subsequent sintering process. As can be seen from Figure 3.3, the potassium carbonate granules have spherical shape, which leads to the round morphology of pores in Figure 4.1(a).

Most pores in the longitudinal direction, however, show an elliptical morphology (marked in Figure4.1 (b)). The ratio between the major and minor axes was about 3:2 from the images. This was caused by the compaction pressure applied on the sample. Figure 4.1(c) shows a typical pore in the porous copper sample. The pore walls are composed of the individual sintered copper powder particles, resulting in a high surface area of the matrix. The copper particles assemble tightly around the pore, forming solid walls. Small holes or interstices between the copper particles are also found. This morphology often appears in the samples with low porosity where the potassium carbonate particles have less chance to touch each other. If the adjacent potassium carbonate particles are in contact with each other, a channel or hole would be formed in the wall (Figure 4.1(d)). The walls, formed by clusters of copper particles, provide the strength of the porous metal, while the channels allow fluids flowing through the porous metal. The pores are interconnected by vast numbers of channels. For samples with a higher porosity, connectivity between pores is extremely high.

Figures 4.1(e) and (f) are higher-magnification micrographs of the sintered walls. The spherical shape and smooth surface of the copper powder particles are clearly visible. A very thin oxide film can be seen on the surface of the particles. All the copper particles have bonded well during sintering by forming necks between the particles through atomic diffusion. Some small holes and interstices, in the order of several micrometers, are found between the particles.

The sample shown in Figure 4.1 had a porosity of 67% and pore size of 425-710 μm. In the samples with a higher porosity and smaller pore size, the pores formed by the removal of potassium carbonate particles were connected by more and larger internal channels, which are beneficial to the fluid flow through the porous medium.

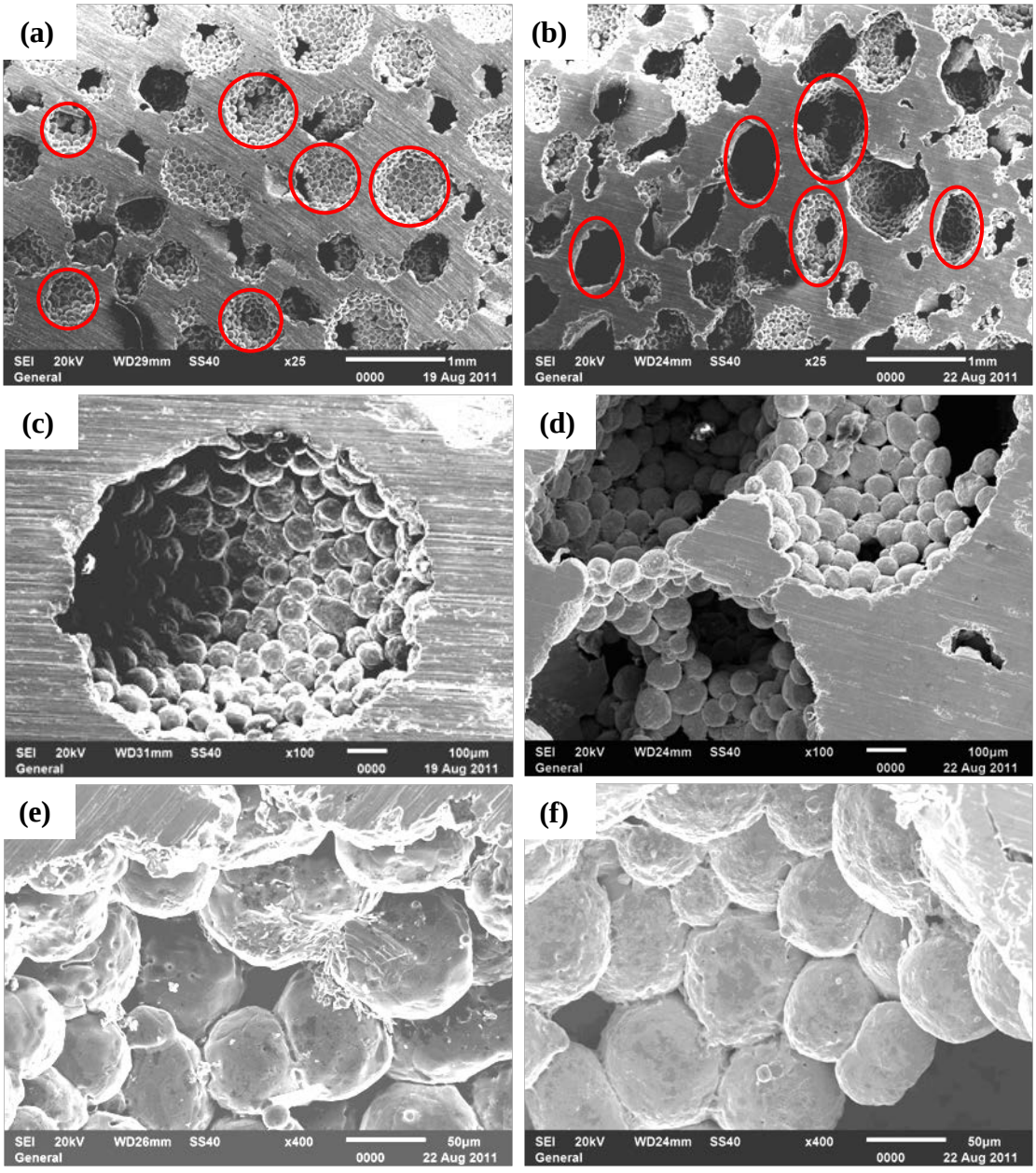

Figure 4.1 *SEM micrographs of an LCS copper sample showing representative features (Porosity: 67%; Copper particle size: 50-100 μm; Pore size: 425-710 μm).*

4.1.2 Porosity and specific surface area

The porosity of twenty-nine porous copper samples (S1 to S29) was measured separately using point counting, direct volume measurement and Archimedes methods. All test samples had nominal dimensions of 40 mm×30 mm×5 mm. Four pore size ranges of 250-425 μm, 425-710 μm, 710-1000 μm and 1000-1500 μm, with porosities ranging between 53.8 and 80.7%, were studied. The porosity of each sample determined by the point-counting method was calculated by Eq. (3.2). The total number of testing points within the selected area for each sample, P_{pore}, was 532 in the experiment. The principles of the direct volume measurement and the Archimedes methods to calculate porosity were described in Section 3.2.2.

Table 4.1 summarizes the data collected from the samples and compares the porosity values obtained using these methods against the nominal porosity values. The porosity values measured by different methods for the samples were plotted against the nominal values in Figure 4.2. In the 250-425 μm pore size range, only samples with a maximum porosity of 77% were tested. At higher porosities, the structural integrity became poor; a high pressure applied to the sample to generate fluid flow can cause structural collapse. As a consequence, samples with higher porosities were not studied.

Table 4.1 *Summary of porosity values measured by different methods for Samples S1 to S29 (P_{tot}=532).*

Sample Reference	Nominal Porosity (%)	Pore Size (μm)	P_{pore}	Porosity-Point Counting (%)	Porosity-Direct Volume Measurement (%)	Porosity-Archimedes Method (%)
S1	50	250-425	273	51.3	53.4	53.8
S2	60	250-425	329	61.8	62.1	61.7
S3	62.5	250-425	323.5	60.7	63.0	63.6
S4	65	250-425	357	67.1	68.8	68.4
S5	70	250-425	378	71.1	71.0	70.6
S6	72.5	250-425	388	72.9	72.4	72.3
S7	75	250-425	396.5	74.4	77.6	77.1
S8	50	425-710	284.5	53.4	55.6	54.8
S9	55	425-710	323	60.7	60.8	59.7
S10	60	425-710	321	60.3	60.8	61.2
S11	62.5	425-710	338.5	63.5	63.7	64.3
S12	65	425-710	343	64.5	67.2	67.0
S13	67.5	425-710	353	66.4	68.8	69.4
S14	70	425-710	386	72.6	72.7	73.3
S15	75	425-710	397.5	74.6	77.0	76.2
S16	80	425-710	410	77.1	80.6	80.3
S17	55	710-1000	300.5	56.4	57.8	58.5
S18	60	710-1000	337	63.3	64.1	63.7
S19	65	710-1000	355	66.7	68.5	68.4
S20	70	710-1000	381	71.6	71.4	71.8
S21	75	710-1000	396	74.4	76.6	76.1
S22	80	710-1000	418.5	78.6	80.9	80.4
S23	55	1000-1500	303.5	57.0	58.2	57.8
S24	60	1000-1500	334	62.8	63.4	63.4
S25	65	1000-1500	348	65.4	65.3	65.0
S26	67.5	1000-1500	364.5	68.4	69.7	69.8
S27	70	1000-1500	387	72.7	73.5	72.7
S28	75	1000-1500	395.5	74.2	74.9	75.7
S29	80	1000-1500	414	77.8	80.6	80.7

Figure 4.2 shows that the measured porosities are generally higher than their nominal porosities. This is because nominal porosity is calculated from the volume ratio of potassium carbonate and copper particles without taking into account the space between copper particles, which makes the actual porosity greater than the volume of potassium carbonate. The porosity values measured by the different methods are very close to each other for the same samples. The porosity measured using the point counting method, however, is generally lower than those measured by the direct volume measurement and Archimedes methods, especially for the samples with high porosities. The porosity values obtained by the Archimedes method, which is the most accurate method, will be used in this thesis.

The specific surface area values (S_v) of samples S1 to S29 were obtained from the micrographs using the point counting method as shown in Figure 3.7 (Section 3.2.2), where the total length of the test lines (L_{test}) was fixed at 130 mm. The data collected from the micrographs and the values of S_v calculated by Eq. (3.3) are summarized in Table 4.2. Column 5 shows the number of intercepts between the grid lines and the pore perimeters. The values of S_v are in the range from 1.79 to 9.14 mm^2/mm^3. Sample S23, with a low porosity of 57.8% and the largest pore size of 1000-1500 μm has the lowest value of S_v, while Sample S7, with a high porosity of 77.1% and the smallest pore size of 250-425μm has the highest value of S_v, followed by Sample S16, with a higher

porosity of 80.3% and a medium pore size of 425-710μm. Figure 4.3 shows the variations of specific surface area with porosity and pore size. It can be seen clearly that S_v increases with porosity, but decreases with pore size.

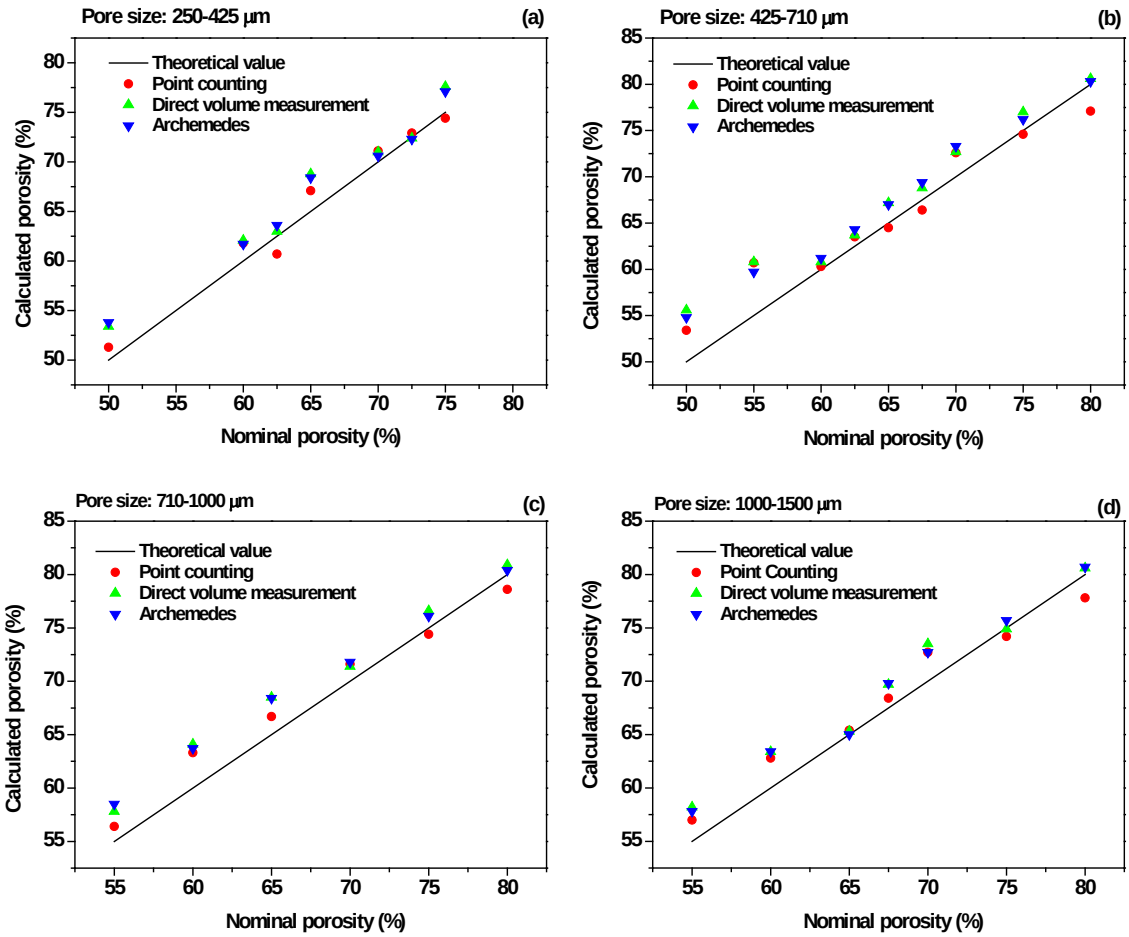

Figure 4.2 *Measured porosity values by different methods versus nominal values for samples with different pore sizes.*

Table 4.2 *Summary of collected data and calculated specific surface areas for samples S1 to S29 (L_{test}=130 mm)*

Sample Reference	Nominal Porosity (%)	Pore Size (μm)	Porosity (%)	P_{inter}	S_V (mm^2/mm^3)
S1	50	250-425	53.8	384	5.92
S2	60	250-425	61.7	449	6.94
S3	62.5	250-425	63.6	459	7.09
S4	65	250-425	68.4	487	7.51
S5	70	250-425	70.6	533	8.23
S6	72.5	250-425	72.3	549	8.47
S7	75	250-425	77.1	592	9.14
S8	50	425-710	54.8	249	3.84
S9	55	425-710	59.7	260	4.01
S10	60	425-710	61.2	295	4.55
S11	62.5	425-710	64.3	300	4.63
S12	65	425-710	67.0	311	4.80
S13	67.5	425-710	69.4	329	5.08
S14	70	425-710	73.3	345	5.32
S15	75	425-710	76.2	366	5.65
S16	80	425-710	80.3	379	5.84
S17	55	710-1000	58.5	181	2.80
S18	60	710-1000	63.7	196	3.02
S19	65	710-1000	68.4	208	3.20
S20	70	710-1000	71.8	213	3.28
S21	75	710-1000	76.1	234	3.61
S22	80	710-1000	80.4	251	3.87
S23	55	1000-1500	57.8	116	1.79
S24	60	1000-1500	63.4	129	1.99
S25	65	1000-1500	65.0	132	2.03
S26	67.5	1000-1500	69.8	141	2.17
S27	70	1000-1500	72.7	150	2.31
S28	75	1000-1500	75.7	153	2.36
S29	80	1000-1500	80.7	161	2.48

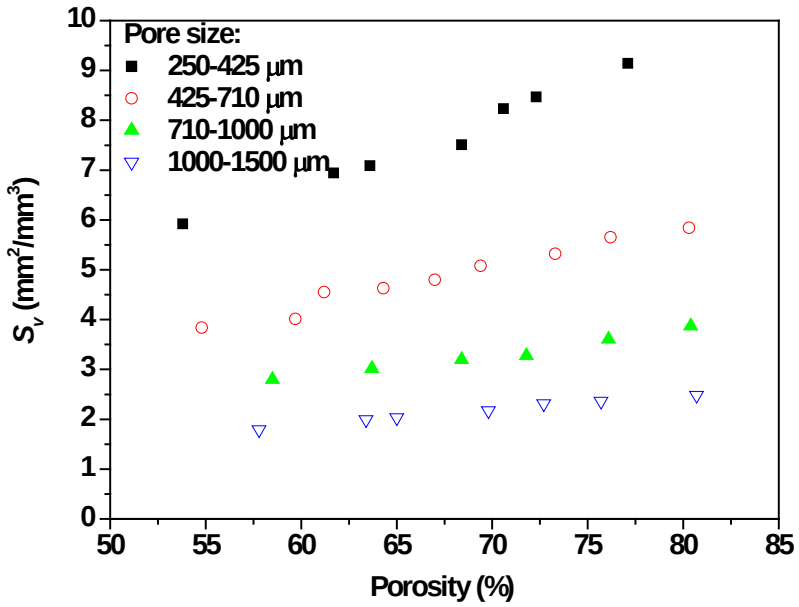

Figure 4.3 *Variations of specific surface area with porosity and pore size*

4.1.3 Tortuosity

The tortuosity of twenty-five porous copper samples (A1 to A25) was obtained by the analytical solution and extrapolation approach from the acoustic absorption curves as described in Section 3.2.3. All test samples had a nominal diameter of 30 mm and a a nominal height of 10 mm. Three copper particle size ranges of 50-100 μm, 100-300 μm and 600-1000 μm, and four pore size ranges of 250-425 μm, 425-710 μm, 710-1000 μm and 1000-1500 μm, with porosities ranging between 53.8 and 80.7%, were studied. The porosity of each sample was measured by the Archimedes method. The pore parameters and the values of tortuosity are summarized in Table 4.3, which shows that all the tortuosity values of the tested porous copper samples are between 1 and 2.5.

Table 4.3 *Tortuosity of samples with different porosity and pore size.*

Group	Sample Reference	Particle Size (μm)	Pore Size (μm)	Porosity (%)	Tortuosity
GA1	**A1**	50-100	250-425	61.9	1.63
	A2	50-100	250-425	67.0	1.52
	A3	50-100	250-425	71.4	1.41
GA2	**A4**	50-100	425-710	61.7	1.85
	A5	50-100	425-710	66.7	1.71
	A6	50-100	425-710	70.7	1.59
	A7	50-100	425-710	75.9	1.49
	A8	50-100	425-710	80.8	1.36
GA3	**A9**	50-100	710-1000	62.6	2.10
	A10	50-100	710-1000	71.4	1.81
	A11	50-100	710-1000	80.6	1.42
GA4	**A12**	50-100	1000-1500	62.5	2.42
	A13	50-100	1000-1500	66.5	2.17
	A14	50-100	1000-1500	72.2	1.91
	A15	50-100	1000-1500	76.1	1.77
	A16	50-100	1000-1500	81.2	1.56
GA5	**A17**	100-300	425-710	62.4	1.52
	A18	100-300	425-710	67.7	1.45
	A19	100-300	425-710	71.5	1.36
GA6	**A20**	100-300	1000-1500	62.5	1.74
	A21	100-300	1000-1500	67.0	1.65
	A22	100-300	1000-1500	72.8	1.53
GA7	**A23**	600-1000	1000-1500	31.1	2.18
	A24	600-1000	1000-1500	41.6	1.83
	A25	600-1000	1000-1500	52.5	1.62

Figure 4.4 shows the variations of tortuosity with porosity for porous copper samples with different copper particle sizes and pore sizes. With increasing porosity, the tortuosity of the porous copper sample decreases. At a given particle size and porosity, the tortuosity of porous copper sample with fine pore size is smaller than that with a large pore size. The sample made by small copper particles has larger tortuosity value comparing with that made by large copper particles.

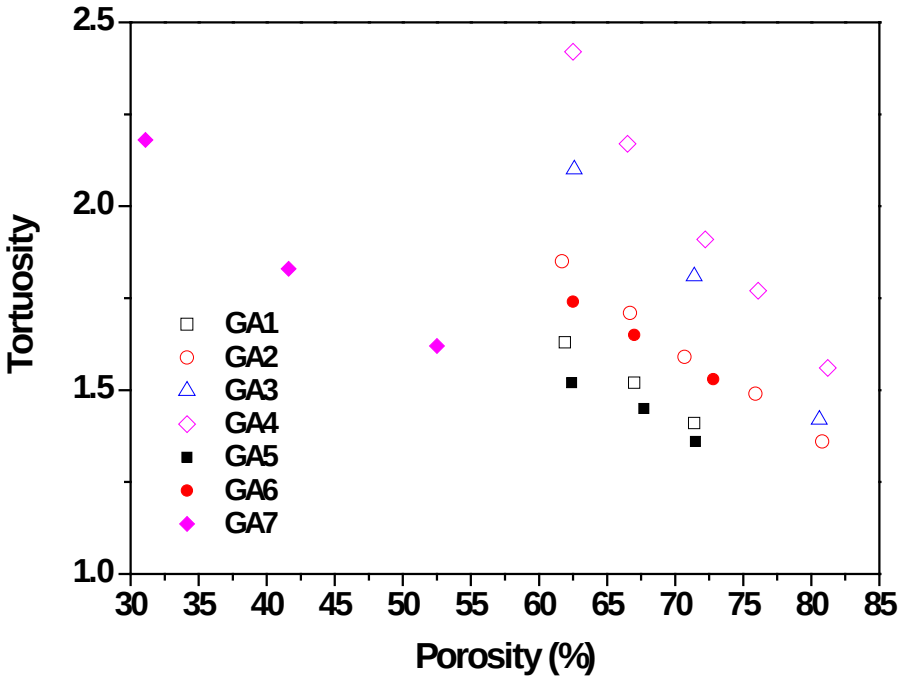

Figure 4.4 *Tortuosity values of the LCS porous copper samples for different groups in Table 4.3:* □ *GA1,* ○ *GA2,* △ *GA3,* ◇ *GA4,* ■ *GA5,* ● *GA6 and* ◆ *GA7.*

4.2 Permeability

The permeability tests were carried out on a purpose-built apparatus described in Section 3.3.2. Both air and water were used as the fluid. Without specific mention, permeability will mean the air permeability (Sections 4.3.1–4.3.5). The water

permeability results will be presented in Section 4.3.6. The standard deviation of measured permeability values calculated by Eq. (3.15) was less than 3.5%.

4.2.1 Effect of porosity and pore size on air permeability of porous copper

Twenty-nine samples (S1-S29) in Table 4.1 were used for permeability testing. The permeability was determined for each specimen in the velocity range of 0-14 m/s by the quadratic function curve fitting according to in Eq. (3.5), and taking the average value. The structural parameters and the permeability values of these samples are summarised in Table 4.4. Each sample was categorised according to its pore size and porosity.

The variations of pressure drop with outlet air velocity for selected specimens with different porosities and different pore sizes are shown in Figure 4.5. The graphs are plotted separately for four pore size ranges: 250-425 μm, 425-710 μm, 710-1000 μm and 1000-1500 μm. The pressure drop increases with the velocity of fluid and all curves fit well with Eq. (3.5), with coefficient of determination, R^2, greater than 99.8%. The values of permeability, K, were obtained by curve-fitting using Eq. (3.5).

Table 4.4 *Permeability values of samples with different porosity and pore size.*

Sample Reference	Pore Size(μm)	Relative Density	Porosity (%)	Permeability ($10^{-10}m^2$)
S1	250-425	0.462	53.8	0.14
S2	250-425	0.383	61.7	0.41
S3	250-425	0.364	63.6	0.58
S4	250-425	0.316	68.4	0.95
S5	250-425	0.294	70.6	1.45
S6	250-425	0.277	72.3	1.85
S7	250-425	0.229	77.1	3.12
S8	425-710	0.452	54.8	0.11
S9	425-710	0.403	59.7	0.23
S10	425-710	0.388	61.2	0.28
S11	425-710	0.357	64.3	0.46
S12	425-710	0.330	67.0	0.63
S13	425-710	0.306	69.4	0.90
S14	425-710	0.267	73.3	1.57
S15	425-710	0.238	76.2	2.22
S16	425-710	0.197	80.3	3.79
S17	710-1000	0.415	58.5	0.14
S18	710-1000	0.363	63.7	0.30
S19	710-1000	0.316	68.4	0.59
S20	710-1000	0.282	71.8	0.89
S21	710-1000	0.239	76.1	1.83
S22	710-1000	0.186	80.4	3.58
S23	1000-1500	0.422	57.8	0.06
S24	1000-1500	0.366	63.4	0.15
S25	1000-1500	0.350	65.0	0.25
S26	1000-1500	0.302	69.8	0.47
S27	1000-1500	0.273	72.7	0.88
S28	1000-1500	0.243	75.7	1.31
S29	1000-1500	0.183	80.7	3.12

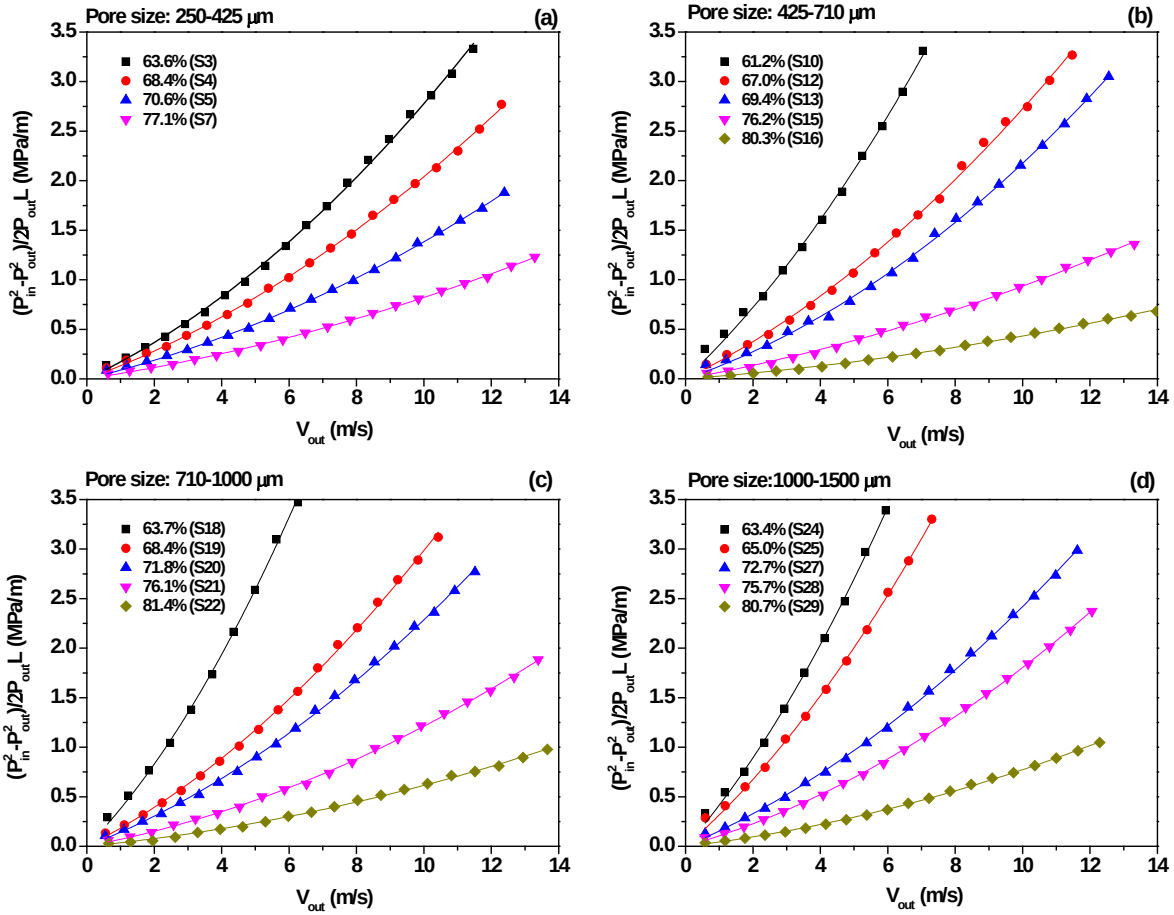

Figure 4.5 *Variations of pressure drop with outlet velocity for specimens with different porosities and a fixed pore size of: (a)250-425µm; (b) 410-710µm;(c) 710-1000µm; and (d) 1000-1500µm.*

Porosity has a significant effect on the pressure drop. The specimen with the highest porosity shows the lowest pressure drop at any given flow rate. The specimen that generated the lowest pressure drop is S16, which has the highest porosity of 80.3% and a medium pore size of 425-710 µm. At the outlet velocity of 5 m/s, the ratio of the pressure drops between the specimens with nominal porosities of 60% and 70% are 2.24, 2.95, 3.10 and 3.23, for pore sizes of 250-425 µm, 425-710 µm, 710-1000 µm and 1000-1500 µm, respectively. Because of the limited pressure range of the transducers

used in the tests, it is impossible to measure the pressure drop for the specimens with low porosities at high velocities.

Comparing the four specimens (S3, S10, S18 and S24) with the same nominal porosity of 60% but different pore sizes shows an interesting phenomenon. The gradient of the curve for S3, with very fine pore size (250-425 μm), is very small, while the other three specimens show a similar large gradient.

Figure 4.6 shows the variation of permeability with porosity at different pore sizes. It can be seen that the permeability is mainly affected by porosity, although pore size also has some influence on it. An exponential relation can be seen between permeability and porosity. Sample S23, with a low porosity of 57.8%, has the lowest permeability (0.06×10^{-10} m^2) while Sample S16, with a high porosity of 80.3%, has the largest permeability (3.79×10^{-10} m^2). At a given pore size (710-1000 μm), the permeability coefficient of the sample S22 with porosity of 80.4% is more than 24 times than that of the sample S17 with a porosity of 58.5% (see Table 4.4).

Figure 4.6 also shows that samples with small pore sizes have larger permeability values, while the permeability of samples with larger pore sizes are relatively low at a given porosity in all tested samples. Comparing the permeability coefficient of the sample S4 and sample S19 with the same porosity of 68.4%, the former sample has a

smaller pore size, but has a larger permeability (see Table 4.4). The porosity of S6 (72.3%) is 4% lower than that of S21 (76.1%); however, they have similar permeability values (1.85×10^{-10} m^2 for S6 and 1.83×10^{-10} m^2 for S21), just because of the smaller pore size of S6 (see Table 4.4).

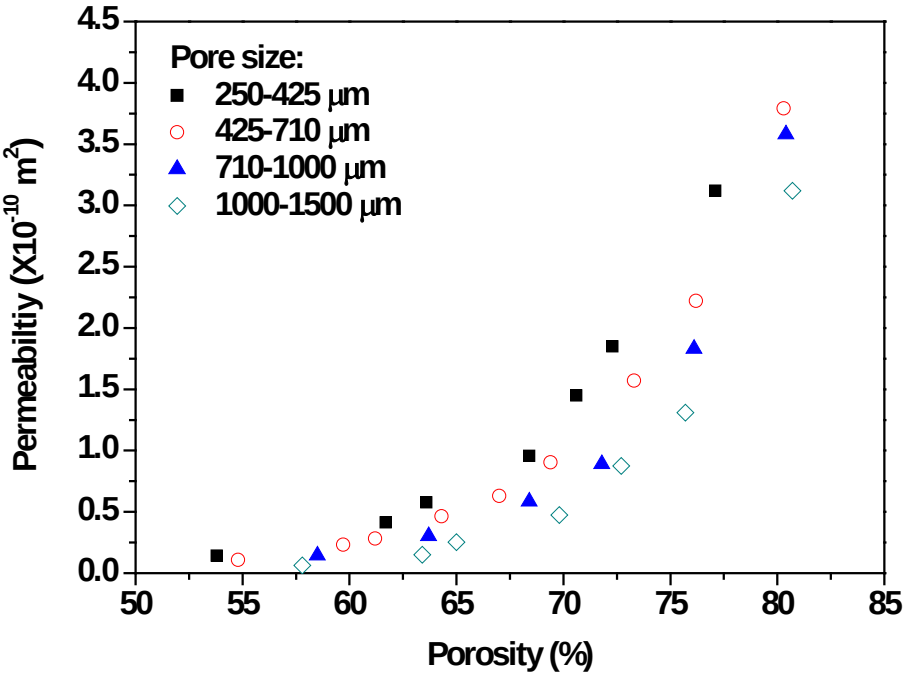

Figure 4.6 *Variation of permeability with porosity for samples with different pore sizes.*

Three samples (S18, S20 and S22) were selected to investigate the effect of sintering time on permeability. Table 4.5 shows the permeability values for the samples sintered with different times. The samples were sintered at 950 °C for 2h with standard route described in Section 3.1.3, re-sintered for another 2h, and then re-sintered for a further 2h. After each sintering period, the permeability was measured. It is observed that sintering time has little effect on the permeability.

Table 4.5 *Permeability of samples sintered for different times.*

Sample Reference	Pore Size(μm)	2h		4h		6h	
		ε (%)	$K(10^{-10}m^2)$	ε (%)	$K(10^{-10}m^2)$	ε (%)	$K(10^{-10}m^2)$
S18	710-1000	63.7	0.30	63.5	0.30	63.5	0.31
S20	710-1000	71.8	0.89	71.7	0.87	71.4	0.87
S22	710-1000	80.4	3.58	81.2	3.49	80.8	3.52

4.2.2 Effect of anisotropy on air permeability of porous copper

Compaction is a very important step in LCS and a compacting pressure of at least 200MPa is needed to obtain porous copper samples of high quality. At this pressure, deformation of the potassium carbonate particles is often unavoidable, resulting in anisotropy.

Seven porous copper samples (S30-S36) with different porosities and pore sizes were produced by the LCS method. Each sample had nominal dimensions of 55mm×30mm×30mm. Three specimens (marked A, B and C) with the same nominal size of 30mm×20mm×5mm were cut from different parts of each sample, as illustrated in Figure 4.7. Because of deformation of the potassium carbonate particles during compaction, the pores on different sections of the sample have different shapes. As shown in Figure 4.1, the pores on the transverse cross section of the sample (normal to the compacting direction, shown as xy plane in Figure 4.7 have circular morphology, while the pores on the longitudinal cross section of the sample (parallel to the compacting direction, shown as yz and xz planes in Figure 4.7 have elliptical

morphology. In the tests, the air flow direction was parallel to the x axis for specimens A and B and parallel to the z axis for specimen C. The specimens had different pore morphologies in the direction of air flow, so their air flow paths were expected to be different.

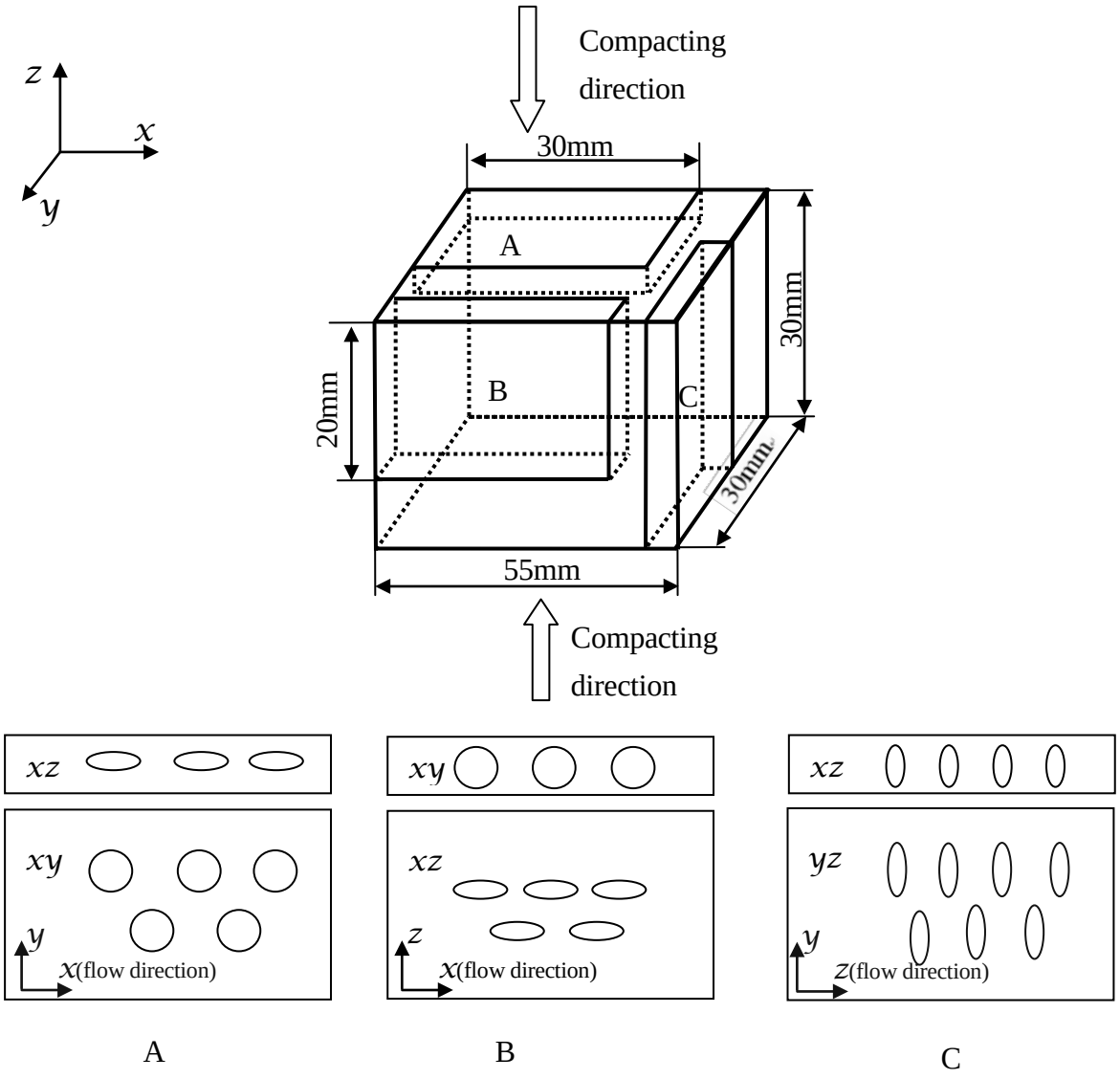

Figure 4.7 *Schematic diagrams showing the pore structures on different cross sections relative to the compaction direction*

Table 4.6 summaries the permeability values at different flow directions for the selected specimens. For specimens cut from the same sample, the permeability of specimen C is slightly lower than those of specimens A and B, which means that the flow resistance for air is higher along the z direction. The variations in permeability are less than 8%. The anisotropy of porous copper fabricated by the LCS method is not significant enough to have a large effect on the permeability.

Table 4.6 *Permeability at different flow directions.*

Sample Reference	Pore Size(μm)	Flow Direction	Relative Density	Porosity (%)	Permeability ($10^{-10}m^2$)
S30A	425-710	x	0.389	61.4	0.29
S30B	425-710	x	0.396	61.1	0.30
S30C	425-710	z	0.390	61.0	0.29
S31A	425-710	x	0.328	67.4	0.61
S31B	425-710	x	0.336	67.2	0.62
S31C	425-710	z	0.331	66.9	0.61
S32A	425-710	x	0.307	69.1	0.91
S32B	425-710	x	0.319	69.0	0.91
S32C	425-710	z	0.312	68.8	0.88
S33A	425-710	x	0.267	73.5	1.58
S33B	425-710	x	0.269	73.1	1.46
S33C	425-710	z	0.270	73.0	1.52
S34A	710-1000	x	0.282	72.4	1.00
S34B	710-1000	x	0.28	72.0	0.95
S34C	710-1000	z	0.278	72.1	0.95
S35A	1000-1500	x	0.350	65.9	0.28
S35B	1000-1500	x	0.345	65.5	0.26
S35C	1000-1500	z	0.343	65.7	0.26
S36A	1000-1500	x	0.302	68.8	0.43
S36B	1000-1500	x	0.312	68.8	0.41
S36C	1000-1500	z	0.313	68.9	0.41

4.2.3 Effect of copper particle size on air permeability of porous copper

All the samples described above were made from the copper powder with the copper particle size of 50-100 μm. Thirty further samples (S37-S49), with copper particle size of either 100-300 μm or 600-1000 μm, were used to investigate the effect of particle size on permeability, the results of which are shown in Table 4.7. For the copper powder with particle size greater than 600 μm, only large potassium carbonate particles (1000-1500 μm) were used in fabricating the samples, because the copper particles need to be smaller than the potassium carbonate particles in LCS (Zhao et al. 2005). It was found difficult to achieve high porosity using big copper particles. It was hard to make samples with the porosity higher than 50% using the copper powder with the particle size of 600-1000 μm.

Table 4.7 *Permeability of samples fabricated with different copper particle sizes*

Sample Reference	Particle Size(μm)	Pore Size(μm)	Relative Density	Porosity (%)	Permeability ($10^{-10}m^2$)
S37	100-300	250-425	0.434	56.6	2.18
S38	100-300	250-425	0.265	73.5	13.52
S39	100-300	425-710	0.458	54.2	1.28
S40	100-300	425-710	0.373	62.7	3.36
S41	100-300	425-710	0.335	66.5	5.12
S42	100-300	425-710	0.294	70.1	8.58
S43	100-300	1000-1500	0.462	53.8	0.60
S44	100-300	1000-1500	0.382	61.8	1.91
S45	100-300	1000-1500	0.336	66.4	4.19
S46	100-300	1000-1500	0.303	69.7	6.68
S47	600-1000	1000-1500	0.683	31.7	0.94
S48	600-1000	1000-1500	0.587	41.3	2.82
S49	600-1000	1000-1500	0.517	48.3	8.74

The effects of the porosity and pore size on permeability for sample S37 to S46, made by 100-300 μm copper particles, are similar to the previous results for samples fabricated using 50-100 μm copper particles. Permeability increases with porosity but decreases with pore size. At any given porosity and pore size, however, their permeabilities are greater than those made by 50-100 μm copper particles. For example, comparing the permeability values of sample S42 (Porosity: 70.1%, Permeability: 8.58×10^{-10} m^2) and sample S13 ((Porosity: 69.4%, Permeability: 0.903×10^{-10} m^2) with the same pore size but different particle size, the former is nearly 10 times than the latter. At the same pore size (425-710 μm) and a similar porosity (54.8% for S8 and 54.2% for S39), the permeability value of S39, made by 100-300 μm copper particles, is more than 10 times of that of S8, made by 50-100 μm copper particles.

Figure 4.8 compares permeability for samples made by copper powders with different particle sizes. Copper particle size was found to play an important role. Increasing copper particle size significantly increased the permeability of the porous copper, at given porosity and pore size. The permeability values of samples made with 100-300 μm copper particles are 4-11 times of those of samples made with 50-100 μm copper particles. With a copper particle size of 100-300 μm, the sample with a porosity of only 34.7% (S47) has a permeability about the same as sample S13, which has a porosity of 69.4% (both have the same pore size).

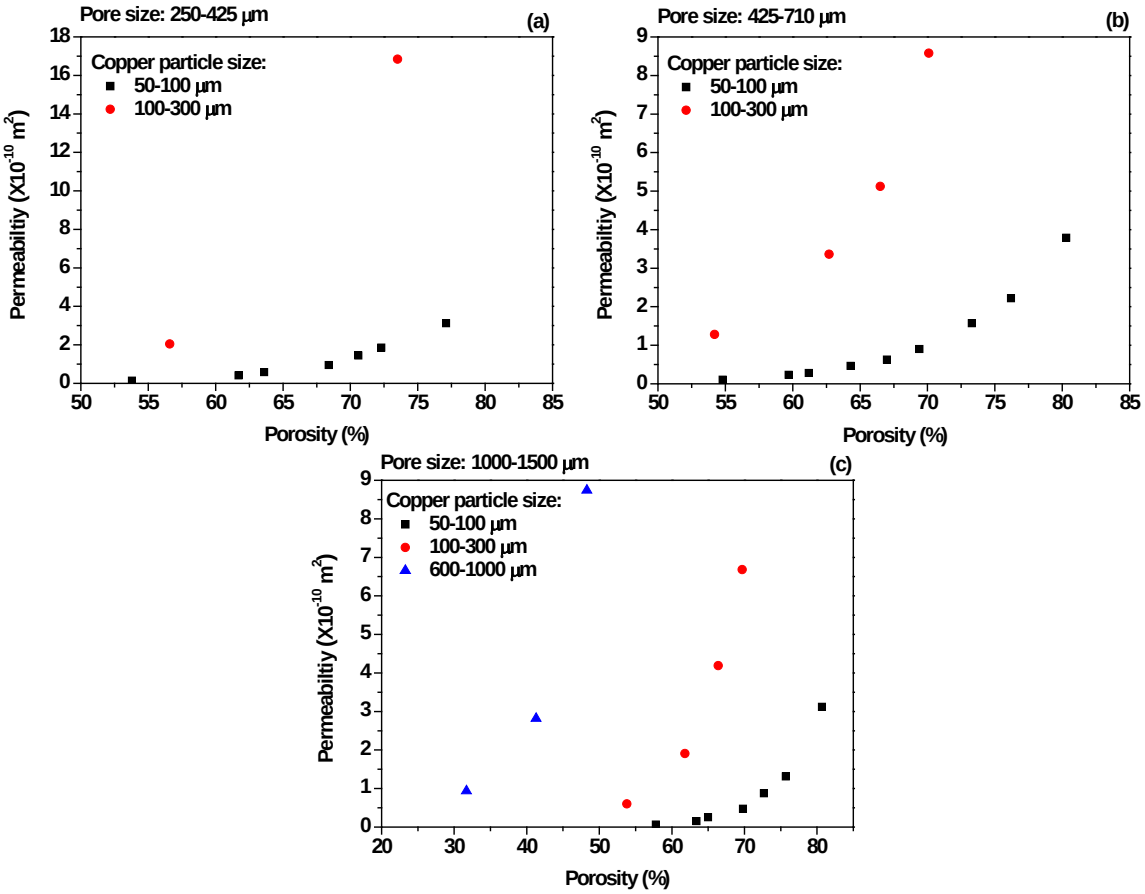

Figure 4.8 *Comparison of permeability for samples made by different copper particle size*

4.2.4 Air permeability of porous copper with double-layer structure

Twelve porous samples with the double-layer structure (S51-S54 and S56-S63) and two samples with single layer (S50 and S55) were manufactured to investigate the effect of a double-layer structure on permeability. The particle size of the copper powder used was 50-100 µm. Each sample had two layers with different porosity or pore size or thickness. Table 4.8 summaries the permeability values of the porous copper samples with different double-layer structures. Column 2 is the pore size or pore size combination. Sample S50 and S55 have a single layer and are included for comparison. Column 3 is the porosity or porosity combination. Column 4 is the

thickness combination. For samples S51-54 and S56-61, the first and second values show the thicknesses of the high-porosity and low-porosity layers, respectively. Sample S62 has a layer of 425-710 μm pore size and a layer of 1000-1500 μm pore size, the nominal porosities being both 60%. Sample S63 has a layer of 425-710 μm pore size and a layer of 1000-1500 μm pore size, the nominal porosities being 60% and 65%, respectively. The total porosity of the whole sample (shown in Column 5) was measured by the Archimedes method. The amount of powder mixture for each layer was controlled as accurately as possible in order to control the thickness of each layer and therefore the total thickness of the sample (5±0.1mm).

Table 4.8 *Permeability coefficients of samples with double-layer structure*

Sample Reference	Pore Size (μm)	Nominal Porosity(%)	Thickness (mm)	Relative Density	Porosity (%)	Permeability ($10^{-10}m^2$)
S50	425-710	60	5	0.375	62.5	0.33
S51	425-710	80/60	1+4	0.345	65.9	0.56
S52	425-710	80/60	2+3	0.303	69.7	1.19
S53	425-710	80/60	3+2	0.264	73.6	1.86
S54	425-710	80/60	1+4	0.225	77.1	2.92
S55	425-710	80	5	0.195	80.5	3.85
S56	425-710	65/60	2.5+2.5	0.354	64.6	0.49
S57	425-710	70/60	2.5+2.5	0.309	67.1	0.68
S58	425-710	70/65	2.5+2.5	0.276	68.9	1.03
S59	1000-1500	65/60	2.5+2.5	0.351	64.9	0.27
S60	1000-1500	70/60	2.5+2.5	0.312	67.4	0.41
S61	1000-1500	70/65	2.5+2.5	0.282	69.2	0.59
S62	425-710/ 1000-1500	60/60	2.5+2.5	0.362	62.8	0.29
S63	425-710/ 1000-1500	65/60	2.5+2.5	0.346	64.4	0.43

Figure 4.9 shows the variables of permeability with porosity for samples with single and double-layer structures. The permeability of samples with single and double-layer structures are close to each other at a given porosity and pore size, but with slight difference for samples with porosity between 67% and 77%.

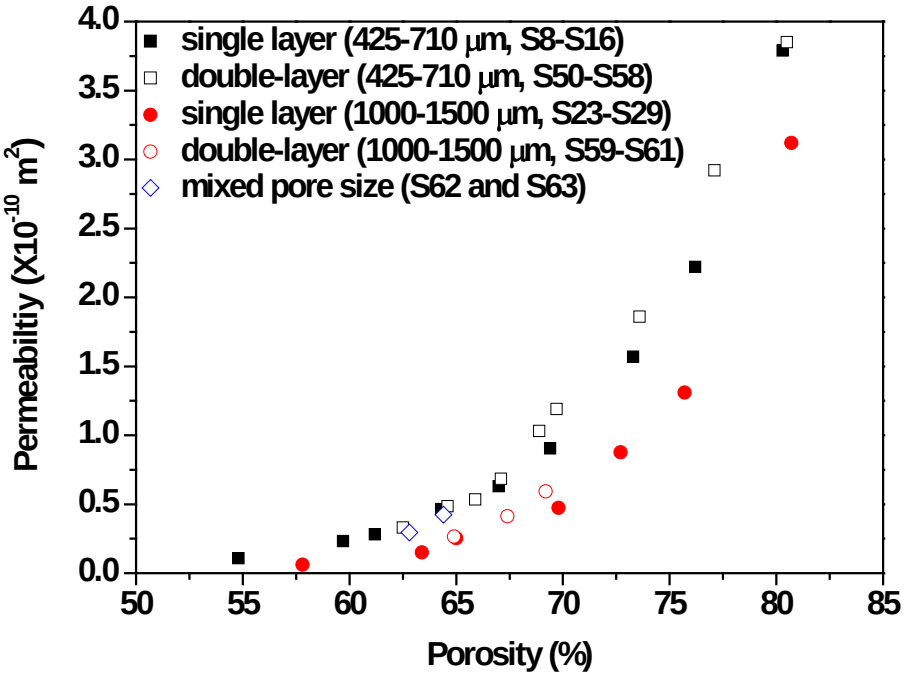

Figure 4.9 *Comparison of permeability values for samples with single- and double-layer structures.*

4.2.5 Air permeability of other porous metals

In order to investigate the effect of different matrix metals on permeability, three metal or alloy powders were selected to produce porous samples by LCS. They were iron, nickel and nickel-copper powders with particle sizes of 75-125 μm, 50-100 μm and 25-75 μm, respectively. The particle size of the potassium carbonate powder used

was 425-710 μm for all these samples. Table 4.9 shows the structural information and the permeability values for the samples.

Table 4.9 *Permeability of porous samples made from different metals*

Sample Reference	Metal	Particle Size (μm)	Pore Size (μm)	Relative Density	Porosity (%)	Permeability ($10^{-10}m^2$)
S64	Fe	75-125	425-710	0.285	71.5	2.04
S65	Fe	75-125	425-710	0.245	75.5	3.27
S66	Ni	50-100	425-710	0.407	59.3	0.21
S67	Ni	50-100	425-710	0.335	66.5	0.52
S68	Ni	50-100	425-710	0.294	70.6	0.97
S69	Ni	50-100	425-710	0.263	73.7	1.51
S70	Ni	50-100	425-710	0.220	78.0	2.71
S71	Ni	50-100	425-710	0.192	80.8	4.72
S72	NiCu	25-75	425-710	0.415	58.5	0.05
S73	NiCu	25-75	425-710	0.329	67.1	0.21
S74	NiCu	25-75	425-710	0.267	73.3	0.53

Figure 4.10 compares the permeability values for different porous metal samples with the same pore size of 425-710 μm. It can be seen that there was no significant difference in permeability between porous iron and porous nickel. The porous nickel-copper samples, however, showed lower permeability values, only $0.526\times 10^{-10}m^2$ for the sample with a porosity of 73.7% (S74), which is less than half of the nickel sample with the same porosity (S69). In addition, the permeability of the porous iron sample was larger than that of the porous copper and porous nickel-copper sample at any given porosity. These may be due to the effect of the particle size of the nickel-copper powder instead of the difference of the material used.

It further confirms that metal particle size plays an important role in affecting permeability.

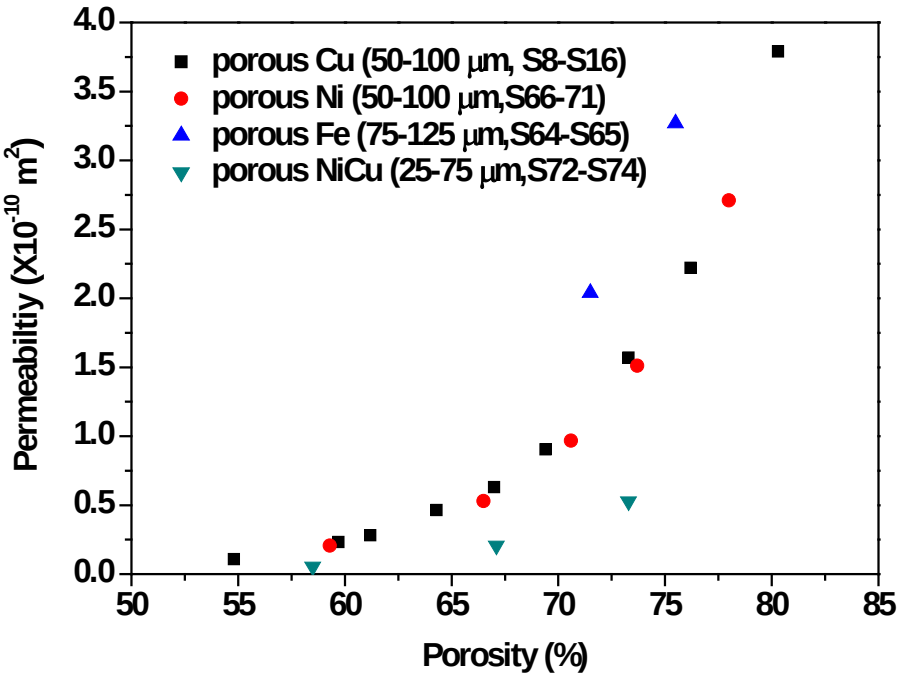

Figure 4.10 *Comparison of permeability of different porous metals (pore size: 425-710 μm).*

4.2.6 Water permeability of porous copper

The water permeability tests were also carried out on the purpose-built apparatus described in Section 3.3.2, and the permeability values were listed in Table 4.10. The permeability values measured with water are slightly greater than those measured with air, with the difference less than 8% (except for sample S23).

Table 4.10 *Water permeability of samples with different pore size and porosity.*

Sample Reference	Pore Size(μm)	Relative Density	Porosity (%)	Air Permeability ($10^{-10}m^2$)	Water Permeability ($10^{-10}m^2$)
S1	250-425	0.462	53.8	0.14	0.14
S2	250-425	0.383	61.7	0.41	0.40
S3	250-425	0.364	63.6	0.58	0.59
S4	250-425	0.316	68.4	0.95	1.01
S5	250-425	0.294	70.6	1.45	1.54
S6	250-425	0.277	72.3	1.85	1.87
S7	250-425	0.229	77.1	3.12	3.27
S8	425-710	0.452	54.8	0.11	0.12
S9	425-710	0.403	59.7	0.17	0.18
S10	425-710	0.388	61.2	0.28	0.31
S11	425-710	0.357	64.3	0.46	0.51
S12	425-710	0.330	67.0	0.63	0.64
S13	425-710	0.306	69.4	0.90	0.95
S14	425-710	0.267	73.3	1.57	1.54
S15	425-710	0.238	76.2	2.22	2.34
S16	425-710	0.197	80.3	3.79	3.87
S17	710-1000	0.415	58.5	0.14	0.14
S18	710-1000	0.363	63.7	0.30	0.33
S19	710-1000	0.316	68.4	0.59	0.60
S20	710-1000	0.282	71.8	0.89	0.89
S21	710-1000	0.239	76.1	1.83	1.92
S22	710-1000	0.196	80.4	3.58	3.70
S23	1000-1500	0.422	57.8	0.06	0.08
S24	1000-1500	0.366	63.4	0.15	0.16
S25	1000-1500	0.350	65.0	0.25	0.27
S26	1000-1500	0.302	69.8	0.47	0.48
S27	1000-1500	0.273	72.7	0.88	0.89
S28	1000-1500	0.243	75.7	1.31	1.26
S29	1000-1500	0.193	80.7	3.12	3.37

4.3 Thermal Conductivity

The thermal conductivity was measured using Corsan's method as described in Section 3.4.2. The effect of porosity, pore size and copper particle size on the thermal conductivity of LCS porous copper was investigated in this section.

4.3.1 Effect of porosity and pore size on thermal conductivity of porous copper

Twenty-five samples (T1-T25) with a nominal porosity from 45% to 80% and pore size of 250-425 μm, 425-710 μm, 710-1000 μm and 1000-1500 μm were made by LCS for thermal conductivity tests. Two specimens were cut from each sample. Each specimen was tested at least three times and the average values of thermal conductivity were taken. The standard deviation of the thermal conductivity calculated by Eq. (3.15) was less than 2.8%. The porosity was measured using the Archimedes method.

The structural properties and the thermal conductivity values of the twenty-five samples are summarised in Table 4.11. Because the thermal conductivity of porous media is related to the volume fraction of the solid matrix, relative density is more convenient than porosity in analyzing thermal conductivity. Therefore, the relative density values, which were equal to $(1-\varepsilon)$, are also listed in Table 4.11. Table 4.11 shows that the thermal conductivity increases with relative density of porous copper. All the test samples have values of conductivity less than 140 W/mK. The highest

value is 138.3 W/mK for Sample T6 with a relative density of 0.6 and pore size of 425-710 μm, followed by 126 W/mK for Sample T19 with a relative density of 0.582 and pore size of 1000-1500 μm. The thermal conductivity decreases very rapidly with decreasing relative density and becomes very low when the relative density is lower than 0.3. Sample T13 with a relative density of 0.165 and pore size of 425-710 μm has a thermal conductivity of only 8.8 W/mK, which is only 2.25% of oxygen-free copper (391 W/mK). Samples T9, T15 and T21 with relative densities between 0.43 and 0.46 and pore sizes of 425- 710μm, 710-1000μm and 1000-1500μm, respectively, have measured thermal conductivity values varying between 77.9 W/mK and 81.6 W/mK. The results show that for a given relative density, the pore size has only a very small effect on the thermal conductivity. Sample T2 with relative density of 0.45 and pore size of 250-425 μm, however, has a thermal conductivity value of only 68.9 W/mK, which is much lower than the other samples with similar relative density but different pore size.

The measured thermal conductivities for samples T1 to T25 are plotted as a function of relative density in Figure 4.11. It can be clearly seen that for a given relative density, the thermal conductivities for the samples with pore size of 425–710 μm, 710–1000 μm and 1000–1500 μm are very similar but those for the samples with pore size of 250 –425 μm are slightly lower.

Table 4.11 *Structural characteristics and thermal conductivity values of porous copper samples with different porosity and pore size*

Sample reference	Pore Size (µm)	Relative Density	Porosity (%)	Thermal Conductivity (W/mK)
T1	250-425	0.524	47.6	95.5
T2	250-425	0.450	55.0	68.9
T3	250-425	0.356	64.4	37.3
T4	250-425	0.318	68.2	29.7
T5	250-425	0.283	71.7	18.2
T6	425-710	0.600	40.0	138.3
T7	425-710	0.521	47.9	108.9
T8	425-710	0.484	51.6	88.2
T9	425-710	0.431	56.9	77.9
T10	425-710	0.375	63.5	56.5
T11	425-710	0.314	68.6	39.6
T12	425-710	0.269	73.1	25.7
T13	425-710	0.165	83.5	8.8
T14	710-1000	0.514	48.6	95.3
T15	710-1000	0.451	54.9	81.6
T16	710-1000	0.401	59.9	68.7
T17	710-1000	0.357	64.3	58.4
T18	710-1000	0.272	72.8	28.3
T19	1000-1500	0.582	41.8	126.0
T20	1000-1500	0.531	46.9	114.1
T21	1000-1500	0.436	56.4	80.0
T22	1000-1500	0.367	63.3	60.5
T23	1000-1500	0.335	67.5	43.1
T24	1000-1500	0.269	73.1	31.1
T25	1000-1500	0.184	81.6	17.9

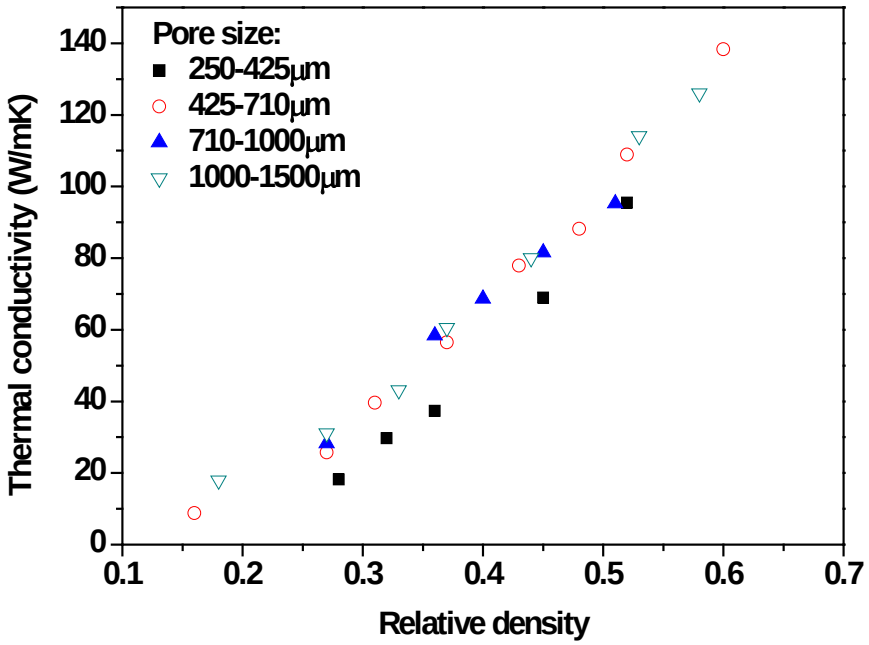

Figure 4.11 *Variation of thermal conductivity with relative density for porous copper samples with different pore sizes.*

4.3.2 Effect of copper particle size on thermal conductivity of porous copper

The structural characteristics and thermal conductivities of seven samples with different copper particle sizes and pore sizes are listed in Table 4.12. With the exception of samples T26 and T34, the thermal conductivity is not significantly affected by the copper particle size, as long as the pore size is larger than the copper particle size. When the copper particle size and the potassium carbonate particle size are comparable (T26 and T34), the fabrication of the samples becomes difficult and the quality of these samples is not very good due to poor bonding between the copper particles. This may explain the low thermal conductivity values of these two samples compared with the other samples with the same relative density.

Table 4.12 *Structural characteristics and thermal conductivities of porous copper samples with different copper particle sizes*

Reference	Particle Size (μm)	Pore Size (μm)	Relative Density	Porosity (%)	Thermal Conductivity (W/mK)
T26	100-300	250-425	0.363	63.7	20.6
T27	100-300	425-710	0.448	55.2	65.4
T28	100-300	425-710	0.383	61.7	40.5
T29	100-300	425-710	0.259	74.1	18.2
T30	100-300	1000-1500	0.35	65.0	35.7
T31	100-300	1000-1500	0.253	74.7	21.7
T32	600-1000	1000-1500	0.618	38.2	87.5
T34	600-1000	1000-1500	0.463	53.7	39.3

4.4 Heat Transfer Coefficient

The heat transfer coefficient was measured using the apparatus as described in Section 3.5.1. The coolant used in the experiment was water, with the flow rate ranging from 0.2 l/min to 1.6 l/min. The effects of porosity, pore size, copper particle size, coolant flow rate, input heat power, anisotropy and double-layer structure on the heat transfer coefficient were studied.

4.4.1 Effect of porosity on heat transfer coefficient of porous copper

Figure 4.12 shows the effect of porosity on the heat transfer coefficient of porous copper samples made using 50-100 μm copper particles (Sample S1-S29) at various coolant flow rates from 0.2 l/min to 1 l/min, presented in four separate graphs for

different pore sizes of 250-425 μm, 425-710 μm, 710-1000 μm and 1000-1500 μm, respectively. The empty chamber with no porous sample is represented as 100% porosity. The heat transfer coefficient of several samples with low porosity could not be measured at large coolant flow rate due to the limited input pressure of the water.

Porosity has a large effect on the heat transfer coefficient. For all samples, generally, the heat transfer coefficient first increases and then decreases with porosity at any given coolant flow rate. The peaks in the heat transfer coefficient for the samples with pore size ranges of 250-425 μm (S2), 425-710 μm (S10), 710-1000 μm (S18) and 1000-1500 μm (S25) are 61.7%, 61.2%, 63.7% and 65%, respectively.

The empty chamber without a porous sample has the lowest heat transfer coefficient. Adding a porous sample to the chamber can increase the heat transfer coefficient by 2 to 10 times. It is evident that the porous sample plays a very important role in improving the heat transfer performance of the system.

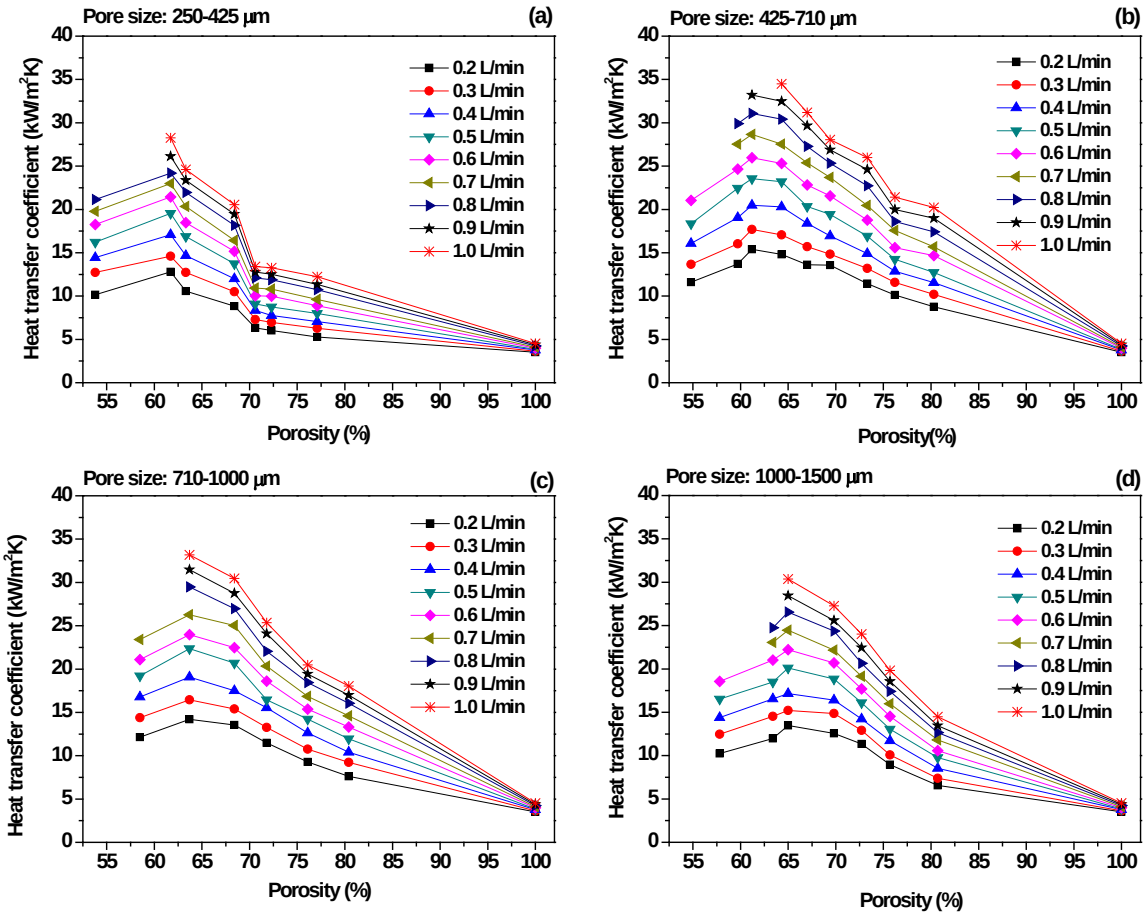

Figure 4.12 *Variation of heat transfer coefficient with porosity at different flow rates and different pore sizes (S1-S29): (a) 250-425 µm (S1-S7); (b) 425-710 µm (S8-S16); (c) 710-1000 µm (S17-22); and (d) 1000-1500 µm (S23-S29). (Copper particle size: 50-100 µm, Input heat power: 250 kW/m^2)*

For samples with medium and large pore sizes, the heat transfer coefficient decreases steadily with porosity at all flow rates after reaching the peak values. It is worth noting that there is a sharp fall in heat transfer coefficient for the samples with the fine pore size (250-425 µm) when the porosity increases from 68.4% to 70.6% (Figure 4.12(a)). The heat transfer performance of samples with porosity higher than 70% is quite poor.

Figure 4.13 shows the effect of porosity on the heat transfer coefficient at various coolant flow rates for samples with large copper particle sizes. Samples S37-S42 (Figure 4.13 (a)) and S43-S46 (Figure 4.13 (b)) have copper particle sizes of 100-300 μm but different pore sizes of 425-710 μm and 1000-1500 μm, respectively, while samples S47-S49 (Figure 4.13 (c)) have the largest particle sizes of 300-600 μm and the largest pore sizes of 1000-1500 μm. At any given coolant flow rate, the heat transfer coefficient generally decreases with porosity and no peaks are found in all the samples tested. The values of the heat transfer coefficient observed in these samples are between 10 kW/m^{2}K and 50 kW/m^{2}K.

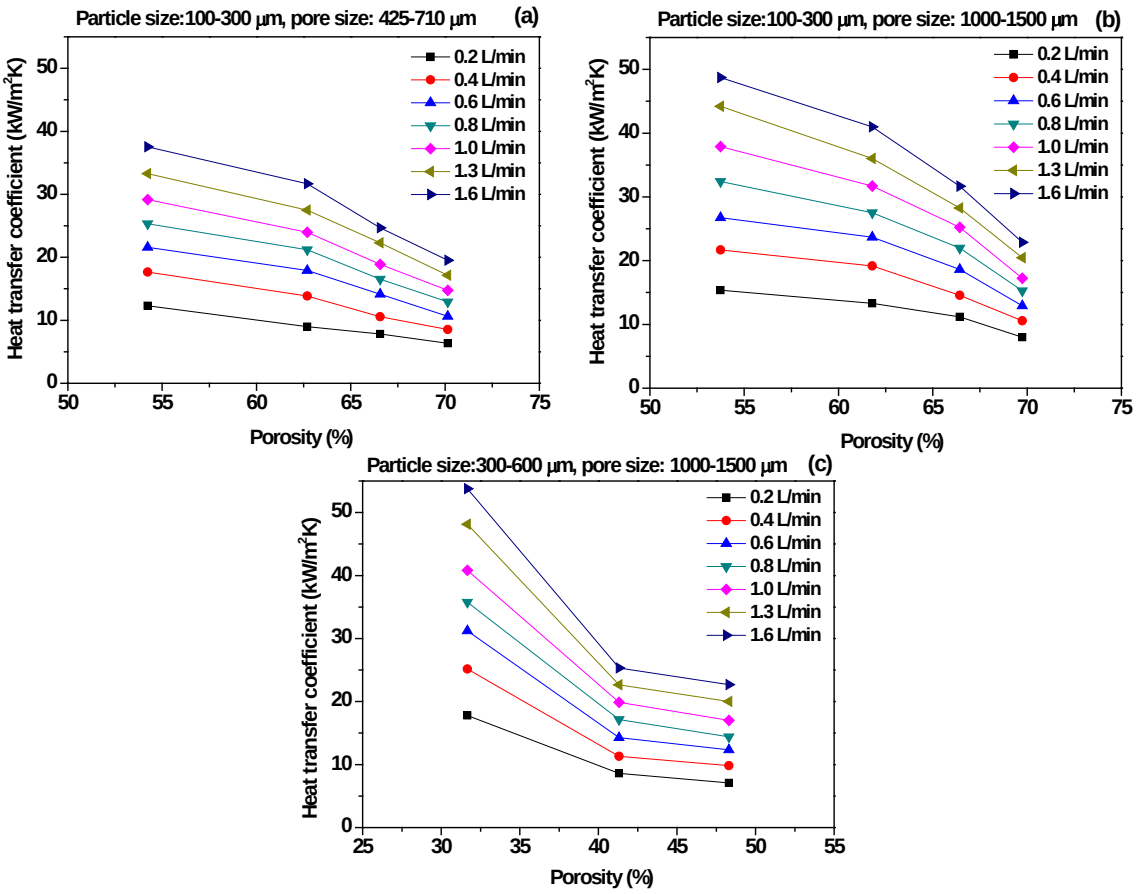

Figure 4.13 *Variation of heat transfer coefficient with porosity at different flow rates for samples with different copper particle sizes and pore sizes(Input heat power: 250 kW/m^2)*

4.4.2 Effect of pore size on heat transfer coefficient of porous copper

Figures 4.14 shows the effect of pore size on heat transfer coefficient for samples S1-S29 with a copper particle size of 50-100 μm at the flow rate of 0.6 L/min. The samples with the medium pore size ranges of 425-710 μm and 710-1000 μm have the best heat transfer performance among the four pore sizes, with their heat transfer coefficients being 1.5-2 times of those of the samples with the fine pore size range (250-425 μm). The heat transfer performance of the samples with the pore size of 1000-1500 μm is moderate and that of the fine pore size samples (250-425 μm) is the poorest.

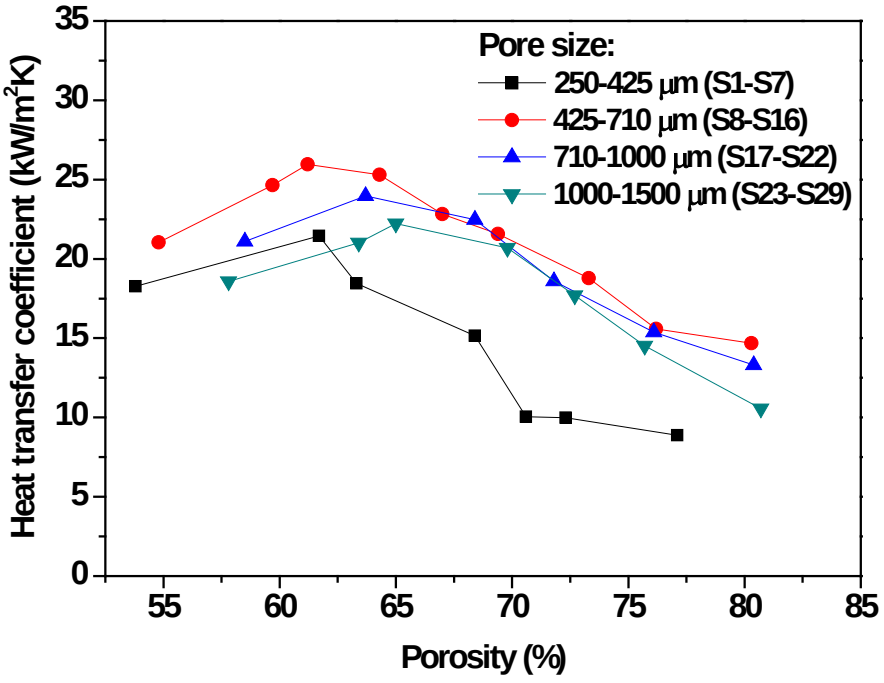

Figure 4.14 *Variation of heat transfer coefficient with porosity for samples S1-S29 with different pore sizes. (Copper particle size: 50-100 μm, Input heat power: 250 kW/m^2, Flow rate: 0.6 L/min)*

Figure 4.15 shows the effect of pore size on heat transfer coefficient for samples S37-S46 with a copper particle size of 100-300 μm at the flow rate of 0.6 L/min. Different from the experimental results of samples S1-S29 which used finer copper particles, the heat transfer performance of the samples with the largest pore size is the best, while that of the samples with the smallest pore size is the poorest. The samples with a large pore size of 1000-1500 μm have a heat transfer coefficient 1.5-1.8 times that of the samples with a small pore size of 250-425 μm.

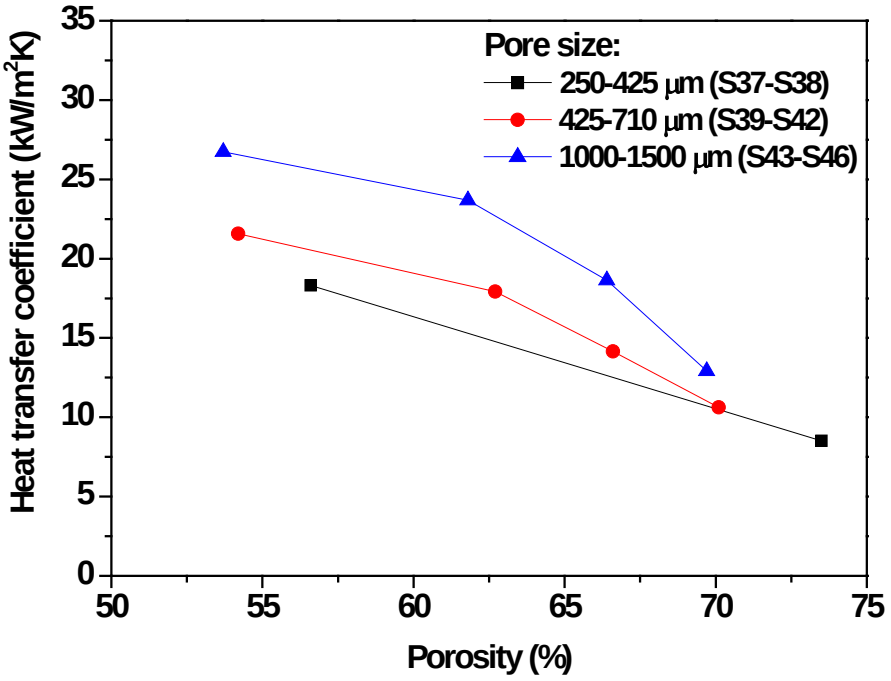

Figure 4.15 *Variation of heat transfer coefficient with porosity for samples S37-S46 with different pore sizes. (Copper particle size: 100-300 μm, Input heat power: 250kW/m^2, Flow rate: 0.6L/min).*

4.4.3 Effect of copper particle size on heat transfer coefficient of porous copper

Figure 4.16 shows the variation of heat transfer coefficient with porosity at a flow rate of 0.6 L/min for samples with a pore size of 425-710 μm and different copper particle sizes: 50-100 μm (samples S8-S16) and 100-300 μm (samples S39-S42). It is found that, when the porosity is higher than 55%, the heat transfer coefficient of the samples with large copper particles is lower than that of the samples with small copper particles at any given coolant flow rate.

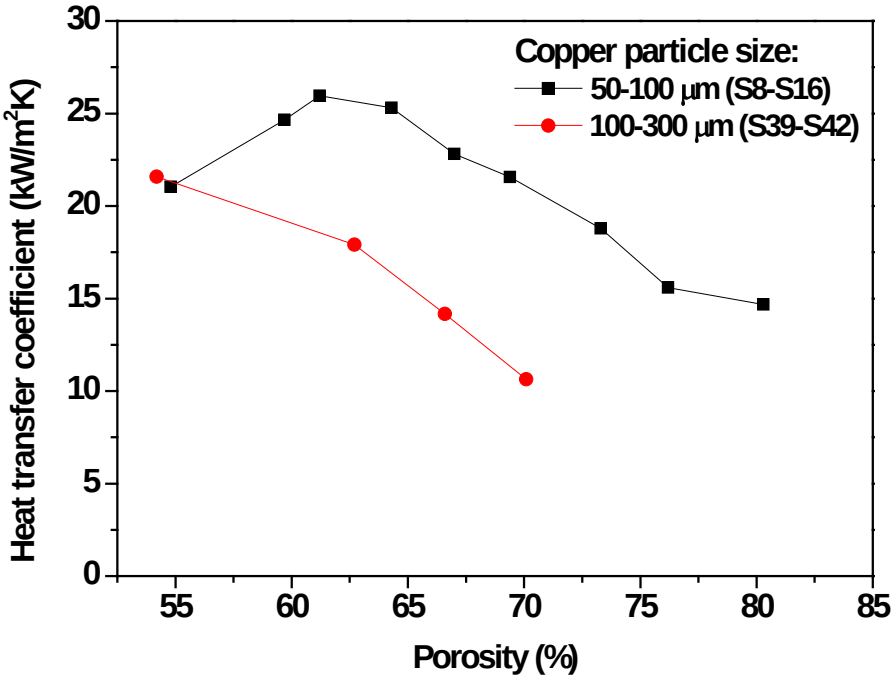

Figure 4.16 *Variation of heat transfer coefficient with porosity for samples with different copper particle sizes. (Pore size: 425-710 μm, Input heat power: 250kW/m^2, Flow rate: 0.6L/min)*

Figure 4.17 shows the variation of heat transfer coefficient with porosity at different coolant flow rates for samples with a pore size of 1000-1500 μm and different copper

particle sizes: 50-100 μm (samples S23-S29), 100-300 μm (samples S43-S46) and 600-1000 μm (samples S47-49). It can be seen that the samples with the largest copper particle size but lowest porosity have the best heat transfer performance.

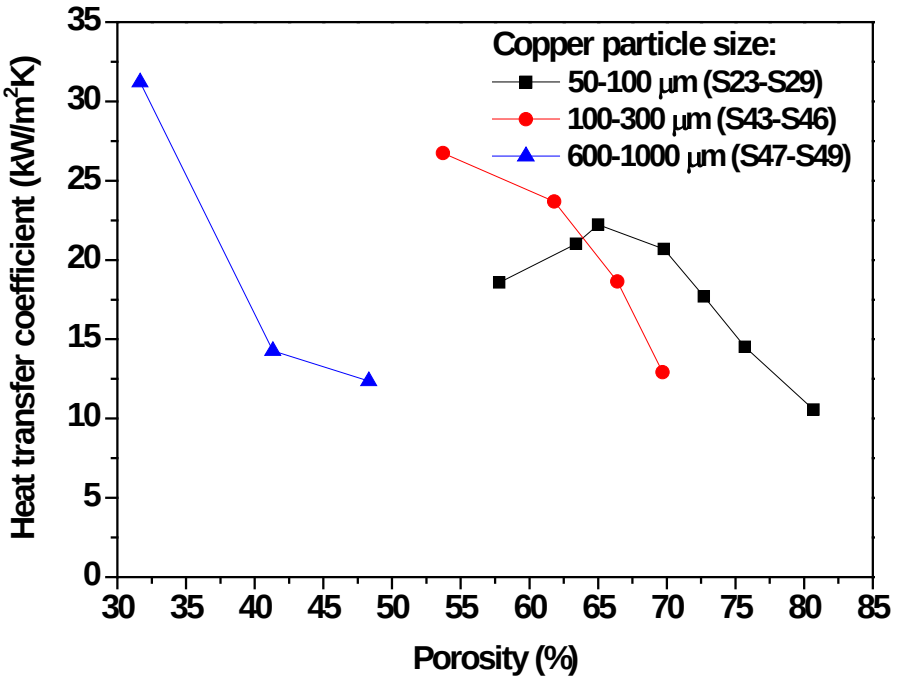

Figure 4.17 *Variation of heat transfer coefficient with porosity for samples with different copper particle sizes. (Pore size: 1000-1500 μm, Input heat power: 250kW/m^2, Flow rate: 0.6L/min)*

4.4.4 Effect of flow rate on heat transfer coefficient of porous copper

Figure 4.18 shows the effect of coolant flow rate on the heat transfer coefficient for samples with different porosities, copper particle sizes and pore sizes. It is clearly seen that coolant flow rate has a large effect on heat transfer across all porosities, copper particle sizes and pore sizes. Heat transfer coefficient was shown to increase

with coolant flow rate and increasing flow rate from 0.2 L/min to 1.6 L/min can increase the heat transfer coefficient about three times.

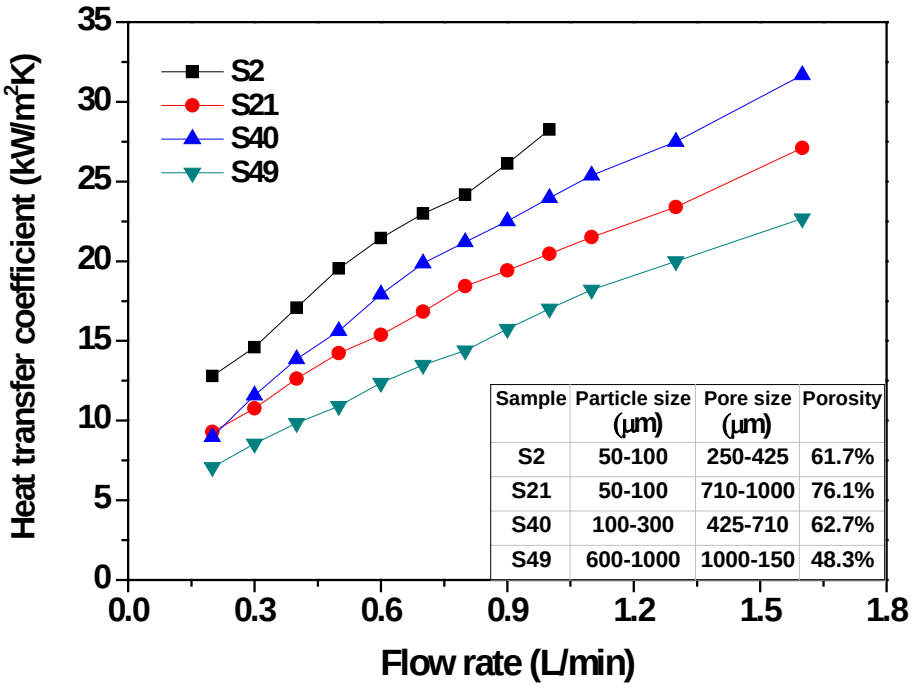

Figure 4.18 *Variation of heat transfer coefficient with coolant flow rate for specimens with different porosities, copper particle sizes and pore sizes*

4.4.5 Effect of input heat flux on heat transfer coefficient of porous copper

Figures 4.19 (a) to (h) show the variation of the heat transfer coefficient with coolant flow rate under different input heat flux for samples S2, S7, S10, S16, S18, S22, S25 and S29 (see Table 4.5 for the pore parameters of samples in detail), respectively. These samples have four different pore sizes and a porosity ranging from 61.2% to 80.7%. It can be clearly seen that the input heat flux has little effect on the heat transfer coefficient for all the specimens tested.

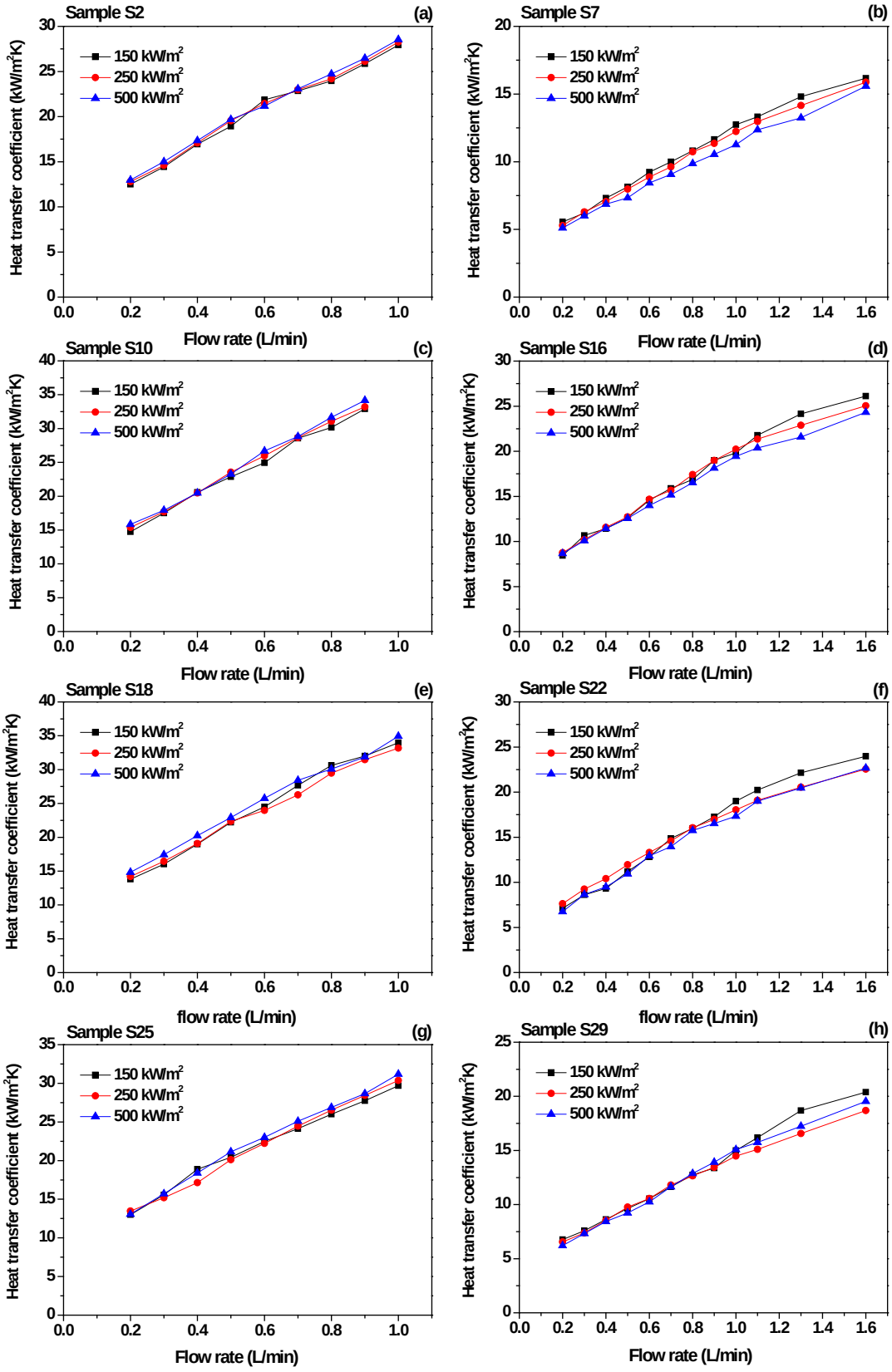

Figure 4.19 *Variation of heat transfer coefficient with coolant flow rates measured with different input heat powers for specimens: (a) S2; (b) S7; (c) S10; (d) S16; (e) S18; (f) S22; (g) S25; and (h) S29.*

4.4.6 Effect of anisotropy on heat transfer coefficient of porous copper

Sixteen specimens (see Table 4.6), each cut at three different directions, A, B and C (see Figure 4.7) from sample S31, S33, S34 and S36, were used to study the effect of anisotropy of porous copper on heat transfer coefficient. These specimens have different pore sizes and different porosities. Figure 4.20 shows the variation of the heat transfer coefficient of these samples. It is shown that the change in heat transfer performance of the porous copper samples is negligible when measured at different directions.

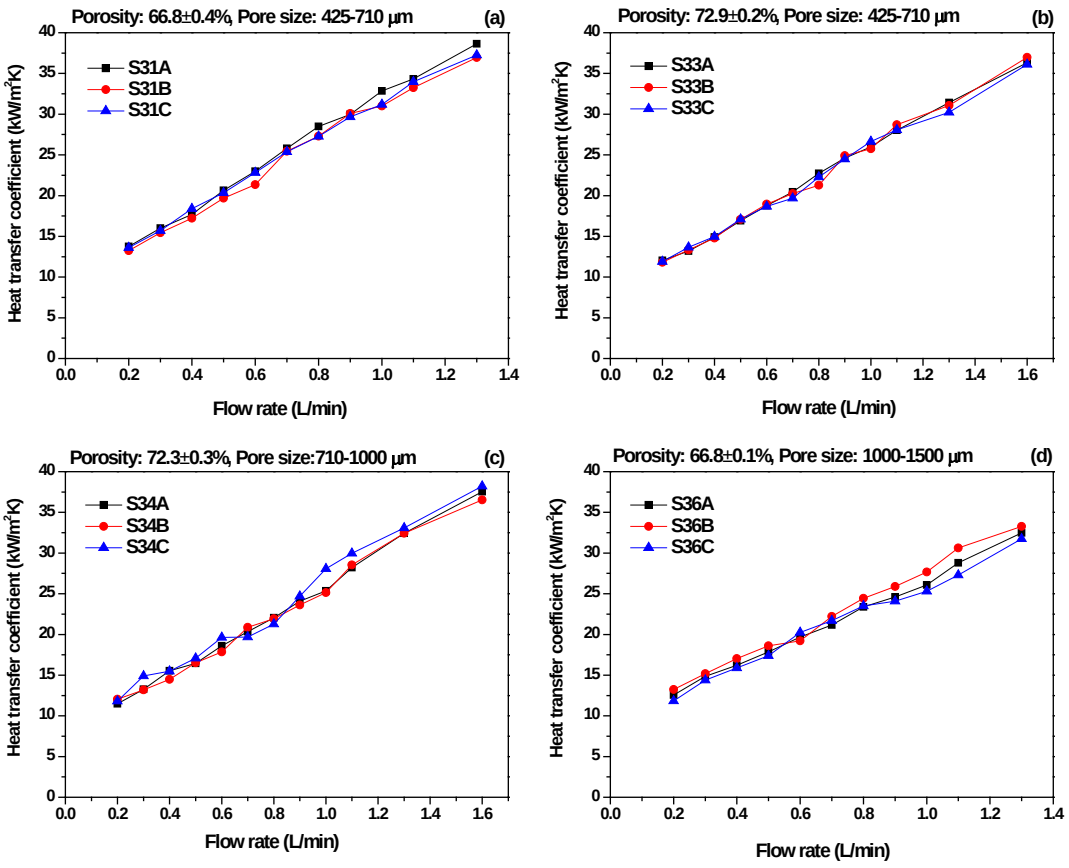

Figure 4.20 *Variation of heat transfer coefficient with coolant flow rate for samples cut from different directions. The pore size and porosity of the samples are (a) 425-710 μm, 66.8±0.4%; (b) 425-710 μm, 72.9±0.2%; (c) 710-1000 μm, 72.3±0.3%; (d) 1000-1500 μm, 68.8±0.1%.*

4.4.7 Heat transfer coefficient of porous copper with double-layer structure

Specimens cut from samples S50-S63 with double-layer structure (Table 4.8) were tested and the heat transfer coefficient for each specimen was measured at different flow rates. As mentioned in Section 3.5.2, there are two ways to conduct the heat transfer tests for double-layer samples, depending on which layer is in contact with the heat source. For the same specimen, it was found that the heat transfer performance would be better if the layer with higher permeability is in contact with the heat source (normal order). If not mentioned specifically, the experiments described in this section (except Section 4.4.7.4) were conducted under the normal order arrangement condition (H/L order).

4.4.7.1 Normal order double-layer porous copper samples with different thickness ratios

The heat transfer coefficients of sample S50-S55 with double-layer structure (80%/60%) in Table 4.7 were measured at different flow rates. The variation of heat transfer coefficient with combined porosity at different coolant flow rates is shown in Figure 4.21. The heat transfer coefficient decreases with the combined porosity. The maximum heat transfer coefficient is 37.33 kW/m^2K) and occurs for sample S51 with combined porosity of 65.9% at the flow rate of 1 L/min.

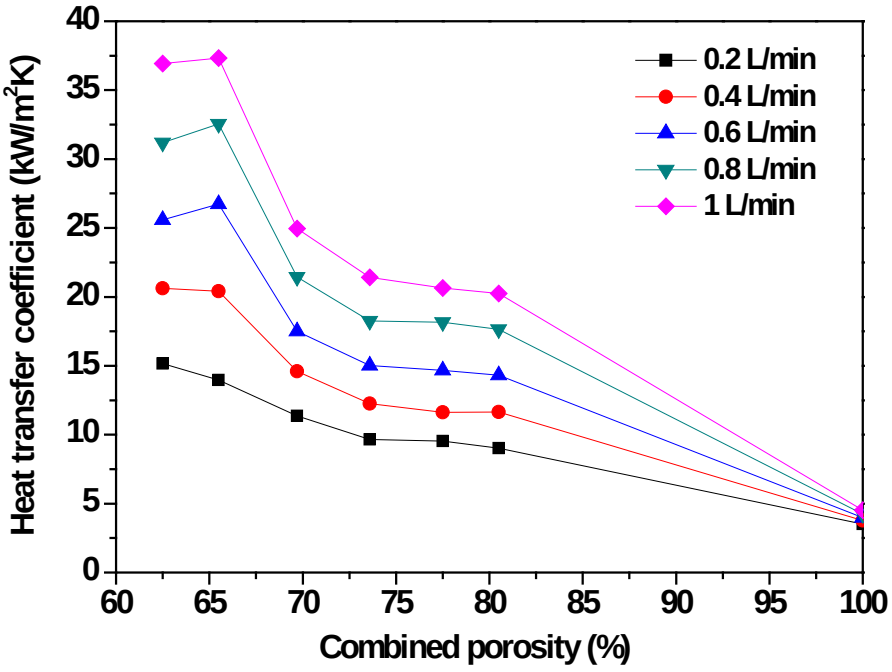

Figure 4.21 *Variation of heat transfer coefficient with total sample porosity at different flow rates for double-layer samples S50-S55 (Porosity combination: 80%/60%, Thickness ratio: 0:5 to 5:0, Pore size: 425-710 μm, Input heat power: 250kW/m^2).*

4.4.7.2 Normal order double-layer porous copper samples with different porosity combinations

Figure 4.22 shows the variation of heat transfer coefficient with coolant flow rate for samples S56-S58 (pore size: 425-710 μm) with double-layer structure (Table 4.8). It is obvious that the heat transfer coefficient of sample S56 with the 65%/60% layer structure is higher than the other two samples.

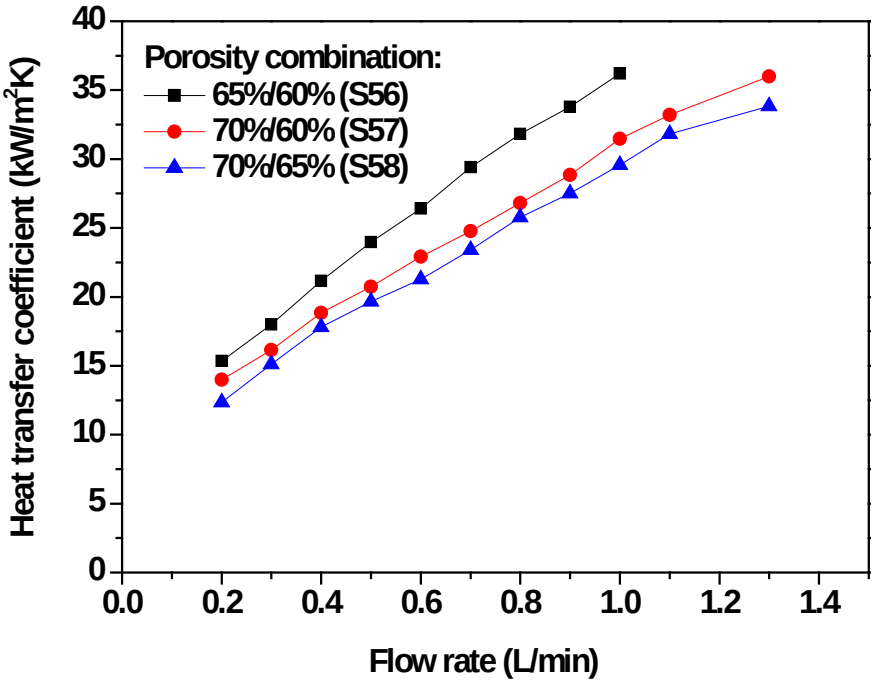

Figure 4.22 *Variation of heat transfer coefficient with coolant flow rate for double-layer samples S56-S58 (Copper particle size: 50-100 μm, Pore size: 425-710 μm, Heat flux: 250kW/m^2)*

Figure 4.23 shows the variation of heat transfer coefficient with coolant flow rate for samples S59-S61 (pore size: 1000-1500 μm) with double-layer structure (Table 4.8). Sample S59 with a combined porosity of 64.9% and S60 with a combined porosity of 68.8% have similar heat transfer coefficient values. Sample S61 with a combined porosity of 70%/65% has a lower heat transfer coefficient.

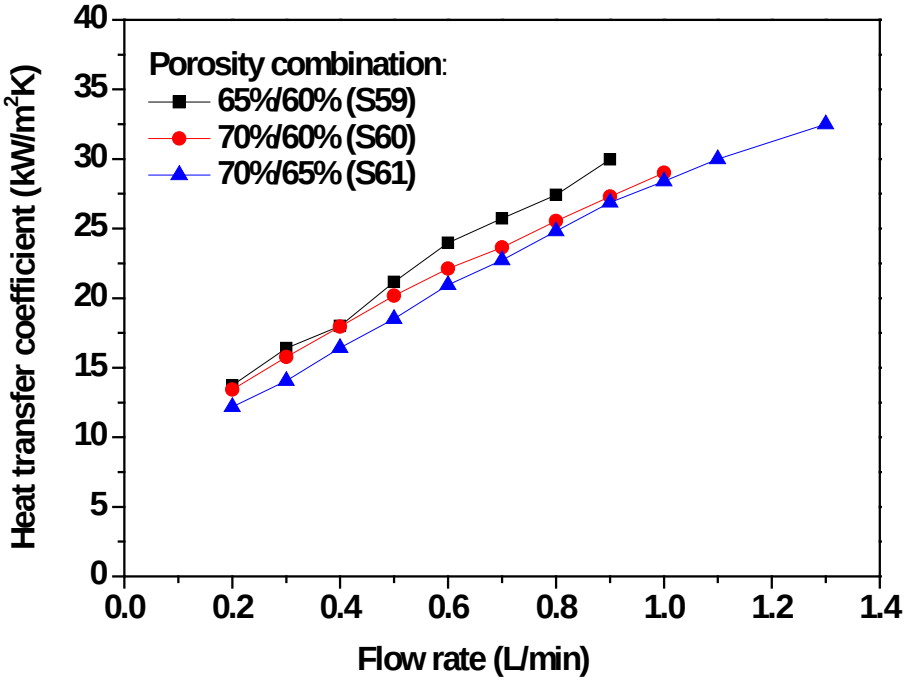

Figure 4.23 *Variation of heat transfer coefficient with coolant flow rate for double-layer samples S59-S61 (Copper particle size: 50-100 μm, Pore size: 1000-1500 μm, Heat flux: 250kW/m^2)*

A comparison of the heat transfer coefficients for three samples with a similar combined porosity (69.3±0.4%) and the same pore size (pore size: 425-710 μm) but different layer combinations, at different coolant flow rates, is shown in Figure 4.24. Sample S13 has a single layer, sample S52 has a 80%/60% double-layer structure with a thickness ratio of 2:3, and sample S58 has a 70%/65% double-layer structure with a thickness ratio of 1:1. Sample S58 has the similar heat transfer performance with sample S13, while the heat transfer performance of sample S52 is relatively poor.

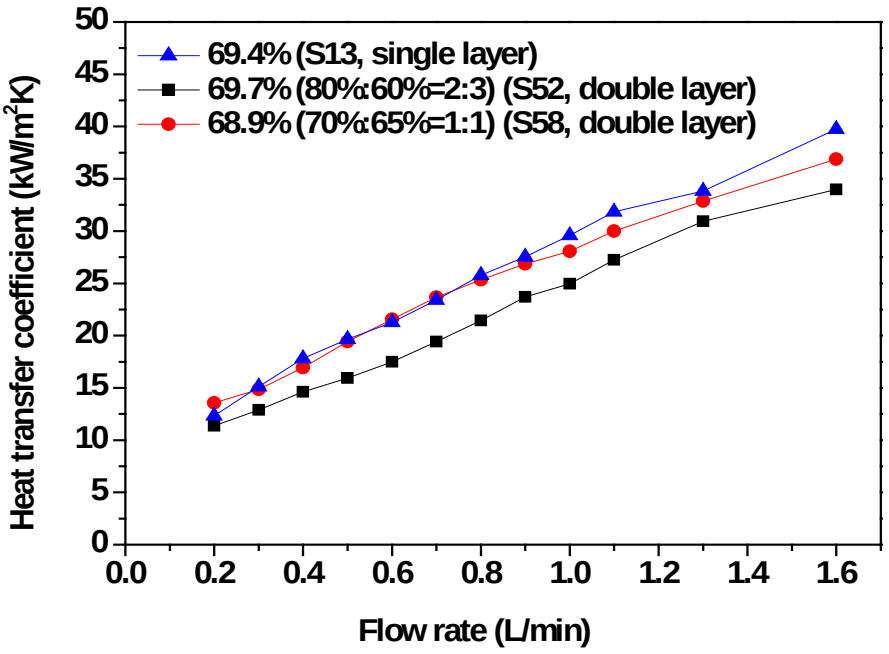

Figure 4.24 *Comparison of heat transfer coefficients for samples with different porosity combinations but a similar combined porosity of 69.3±0.45% at different coolant flow rates (Copper particle size: 50-100 μm, Pore size: 425-710 μm, Input heat flux: 250kW/m^2).*

4.4.7.3 Normal order double-layer porous copper samples with different pore size combinations

Specimens cut from two samples (S62 and S63) with special double-layer structures of different pore sizes and/or porosities were tested. The heat transfer coefficient at different flow rates was measured, and the results were compared with those of the samples with the constituent single layers, as shown in Figures 4.25 and 4.26. Sample S62 was compared with samples S10 and S24 (Figure 4.25) and sample S63 with samples S10 and S25 (Figure 4.26). It is shown that the samples with the double-layer structures have better heat transfer performance than the samples with the single layers alone.

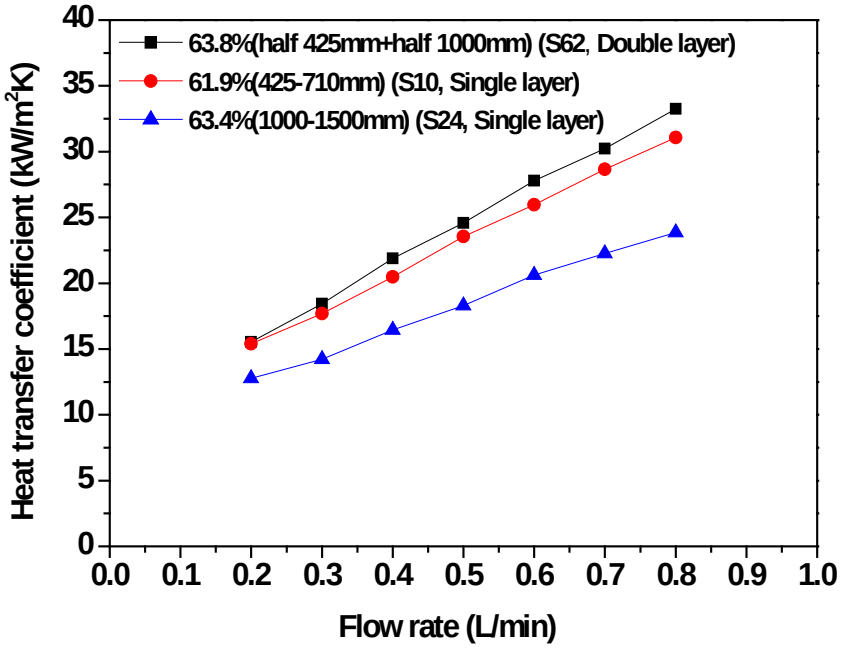

Figure 4.25 *Comparison of heat transfer coefficient between the sample with double layers (S62) and the samples with the constituent single layers (Copper particle size: 50-100 μm, Input heat flux: 250kW/m^2).*

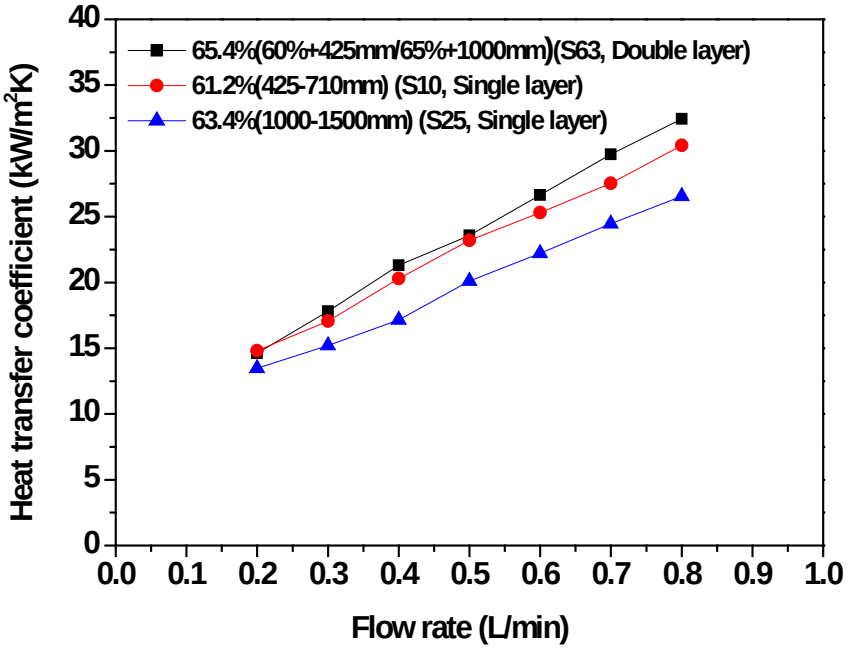

Figure 4.26 *Comparison of heat transfer coefficient between the sample with double layers (S63) and the samples with the single layers (Copper particle size: 50-100 μm, Input heat flux: 250kW/m^2).*

4.4.7.4 Effect of layer order

As mentioned above, there are two ways to conduct heat transfer coefficient measurements for porous samples with double-layer structures. Again, the arrangement with the high porosity layer in contact with the heat source is called normal order (e.g. 80%/60%), and that with the low porosity layer in contact with the heat source is reverse order (e.g. 60%/80%).

Figure 4.27 shows the effect of layer order on heat transfer coefficient for samples S50-S55 at different flow rates. For samples with reverse order (60%/80%), the heat transfer coefficient decreased rapidly with porosity. When the porosity is lower than 65%, the values of heat transfer coefficient are even lower than that of sample S55 with a single layer of a porosity of 80.5%. For the same sample, the heat transfer performance was better when the high porosity side was in contact with the heat source. At all flow rates, the heat transfer coefficients for samples with normal order (80%/60%) are about 1.5 times of those with reverse order (60%/80%).

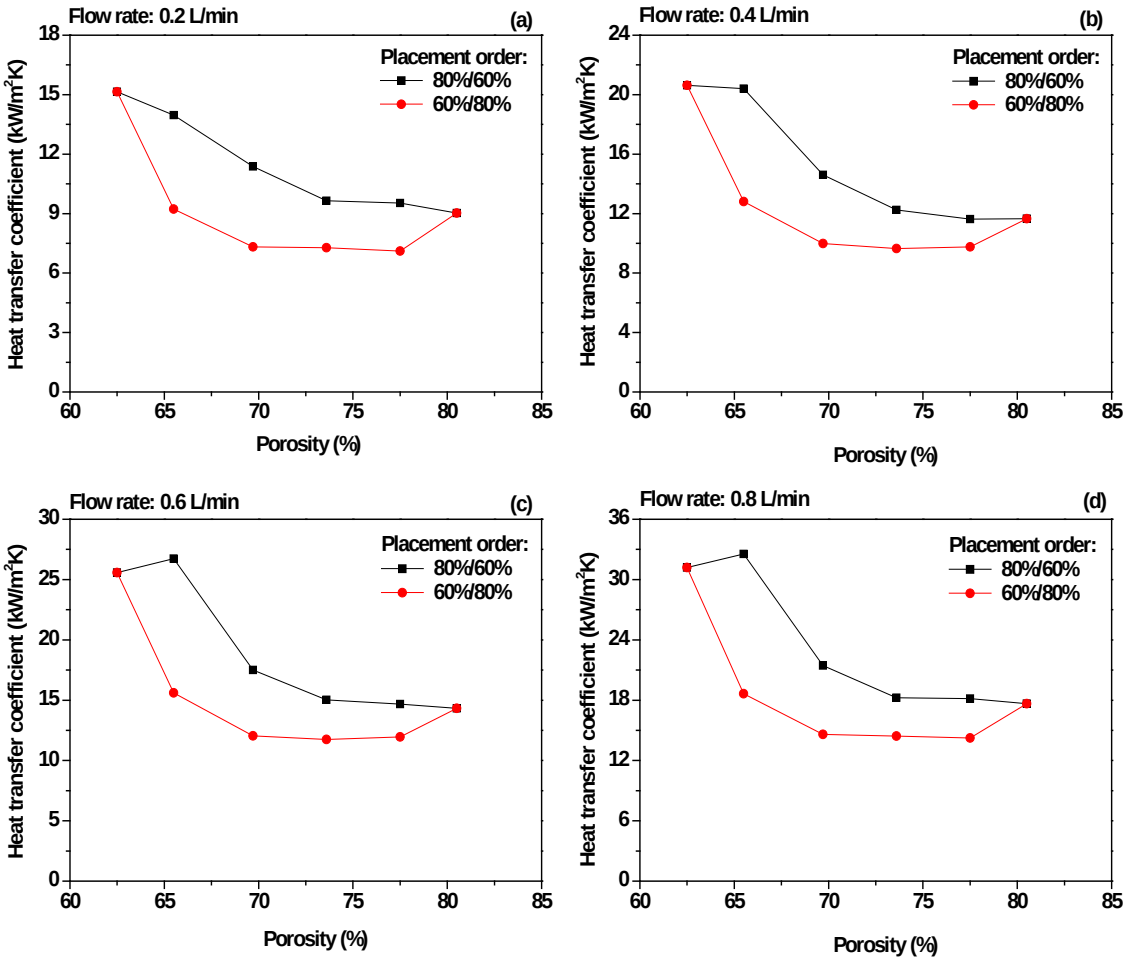

Figure 4.27 *Comparison of heat transfer coefficient of double layer samples (S50-S55) with different layer orders measured at four coolant flow rates (Porosity combination 60%&80%, Copper particle size: 50-100 μm, Pore size: 425-710 μm, Input heat flux: 250kW/m^2).*

Figures 4.28 shows the variations of heat transfer coefficient with coolant flow rate for samples S56-S63, measured with different layer orders. The normal order had better heat transfer performance than the reverse order for all the tested samples at any given coolant flow rate.

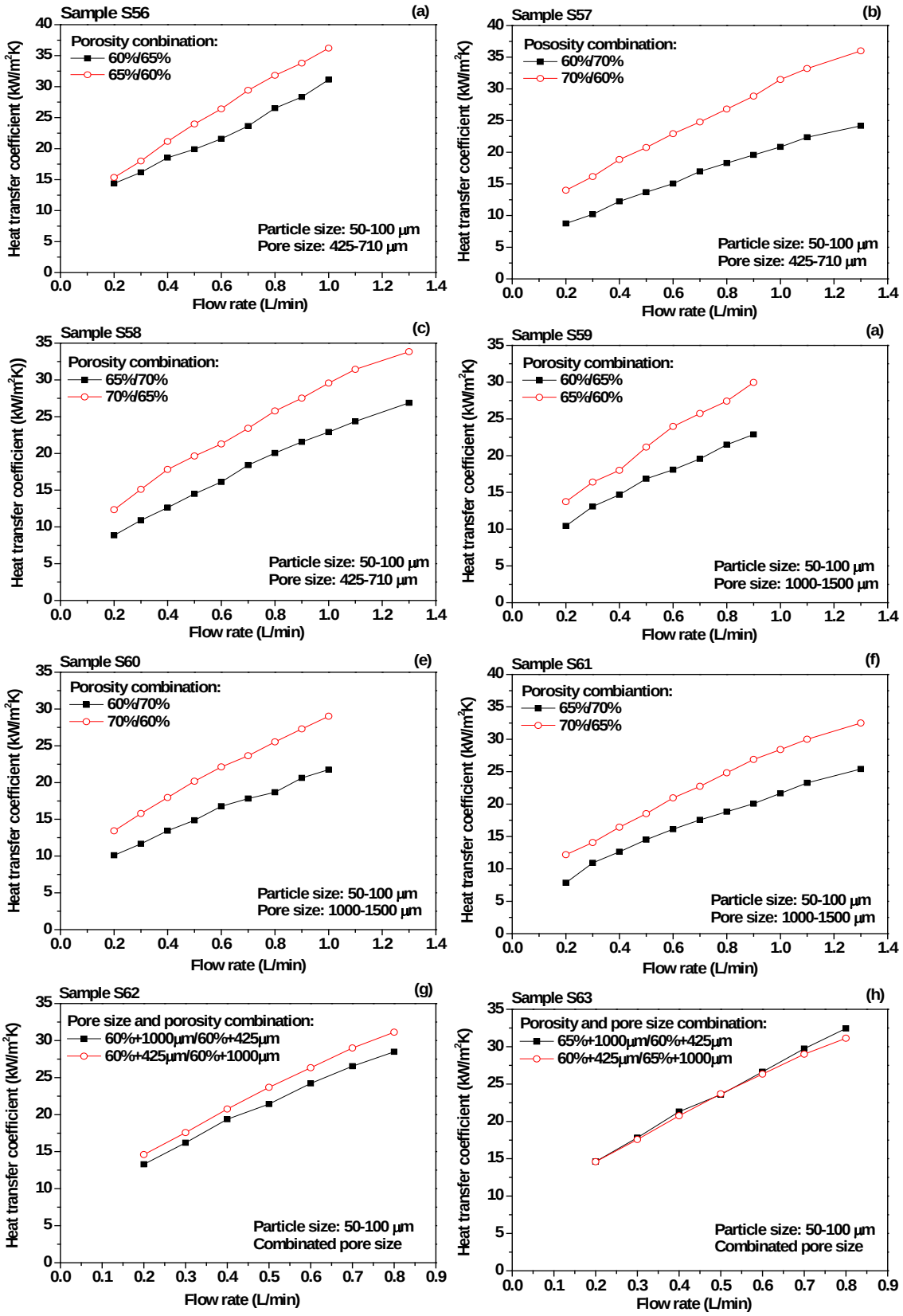

Figure 4.28 *Comparison of heat transfer coefficient of double-layer samples measured with different layer orders for Sample: (a) S56; (b) S57; (c) S58; (d) S59; (e) S60; (f) S61; (g) S62; and (h) S63. (Input heat flux: 250 kW/m^2).*

4.4.8 Effect of thickness on heat transfer coefficient of porous copper

In this section, LCS porous copper samples with different thicknesses were studied to investigate the effect of thickness on heat transfer performance. Seventeen specimens with different porosity, pore size and copper particle size were selected from samples S1-S49 and their pore parameters were summarized in Table 4.13. These samples were divided into four group: 1) G1 with copper particle size of 50-100 μm and pore size of 250-425 μm; 2) G2 with copper particle size of 50-100 μm and pore size of 425-710 μm; 3) G3 with copper particle size of 50-100 μm and pore size of 1000-1500μm; 4) G4 with copper particle size of 100-300 μm and different porosity and pore size. The original specimen with a nominal thickness of 5mm was first tested. A 1 mm thick layer was carefully removed by a handsaw each time before a further test. The precision of thickness for the samples was controlled carefully to within ±0.1 mm. It was hard to cut samples S25, S27, S28 S29 and S43 into 1 mm thickness because of their large pore sizes (1000-1500 μm). Sample S41 was weak, and 1mm thick sheet was crushed during the cutting process. In the specimen of sample S10 with a thickness of 1 mm, no water flow could be detected by the flowmeter even under the maximum pressure supply of the experimental apparatus.

The samples used in the previous section for comparisons of heat transfer coefficient have a similar cross section, so volume flow rate was used to describe the flow conditions. For the same volume flow rate, however, varying sample thickness will

change the cross section area of the porous medium and thus change the Darcian velocity of fluid flowing through the porous medium. In this section, Darcian velocity, instead of volume flow rate, will be used when comparing heat transfer coefficients for samples with different thicknesses.

Table 4.13 *Pore parameters of selected samples for thickness effect study*

Group	Sample Reference	Particle Size (μm)	Pore Size (μm)	Porosity at Different Thickness (%)				
				5 mm	4 mm	3 mm	2 mm	1 mm
G1	S2	50-100	250-425	61.7	61.3	61.4	61.8	62.1
	S4	50-100	250-425	68.4	68.3	68.7	68.9	68.8
	S7	50-100	250-425	77.1	76.9	76.5	77.0	77.4
G2	S10	50-100	425-710	61.2	61.4	60.9	61.5	--
	S12	50-100	425-710	67.0	67.2	66.7	66.9	67.2
	S14	50-100	425-710	73.3	73.5	73.6	73.3	73.1
	S15	50-100	425-710	76.2	75.8	75.8	75.6	76.0
	S16	50-100	425-710	80.3	80.6	80.4	80.7	81.1
G3	S24	50-100	1000-1500	63.4	63.6	63.3	63.8	--
	S25	50-100	1000-1500	65.0	65.4	65.2	65.6	--
	S27	50-100	1000-1500	72.7	72.6	73.1	73.0	--
	S28	50-100	1000-1500	75.7	76.0	76.0	76.2	--
	S29	50-100	1000-1500	80.7	81.3	81.1	81.5	--
G4	S37	100-300	250-425	56.6	56.3	56.7	57.0	56.4
	S39	100-300	425-710	54.2	54.5	54.8	55.3	55.7
	S41	100-300	425-710	66.5	67.2	67.0	67.4	--
	S43	100-300	1000-1500	53.8	54.2	54.5	54.7	--

Figure 4.29 shows the typical variation of heat transfer coefficient with Darcian velocity for Sample S2 with different thicknesses. The variation of heat transfer coefficient of other samples in Table 4.13 with different thicknesses are shown in Appendix B. All samples showed similar characteristics of the thickness effect.

Specimens with thicknesses of 3mm or more had similar heat transfer coefficients (except samples S10, S24 and S43). The heat transfer coefficients were decreased by 25% to 35% when the thickness was reduced to 2mm， accompanied by a decrease in the slope of the h-v_d curve. The heat transfer coefficients of the1mm-thick specimens were very low at any Darcian velocity.

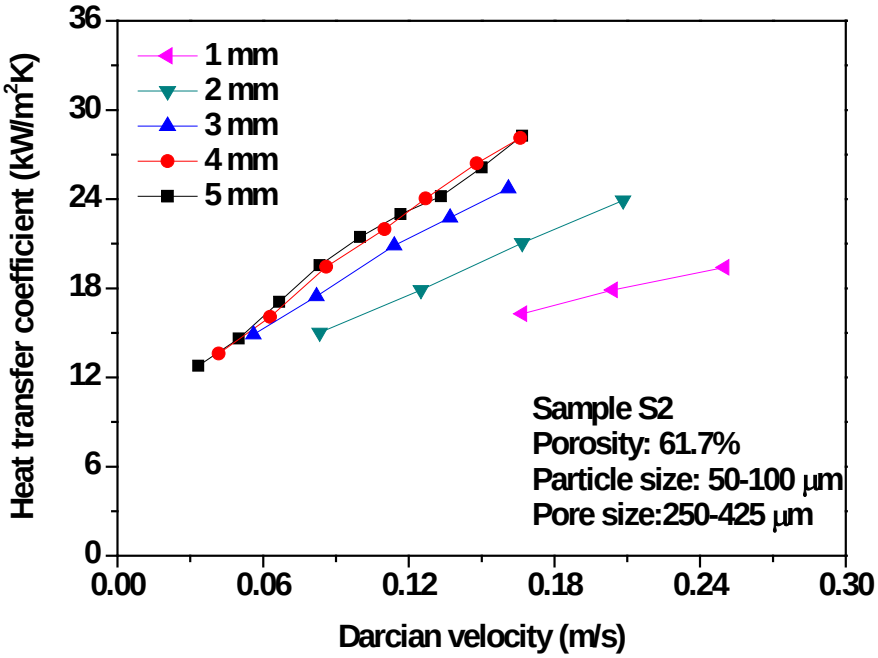

Figure 4.29 *Variation of heat transfer coefficient with Darcian velocity for porous copper samples (Input heat power: 250 kW/m^2).*

Figure 4.30 shows the thickness effect on heat transfer coefficient of seventeen porous copper samples. The heat transfer coefficient remains constant with thickness greater than 3mm, and then rapidly decreases with decreasing thickness. The heat transfer coefficient of the samples with very low porosity (S2, S10, S24 and S25) increases gently with increasing thickness. Slight decrease of heat transfer coefficient is

observed in some samples with high porosity with thickness increasing from 3 mm to 5 mm, such as samples S7, S14, S15, S16, S27, S28 and S29, even if not very clear.

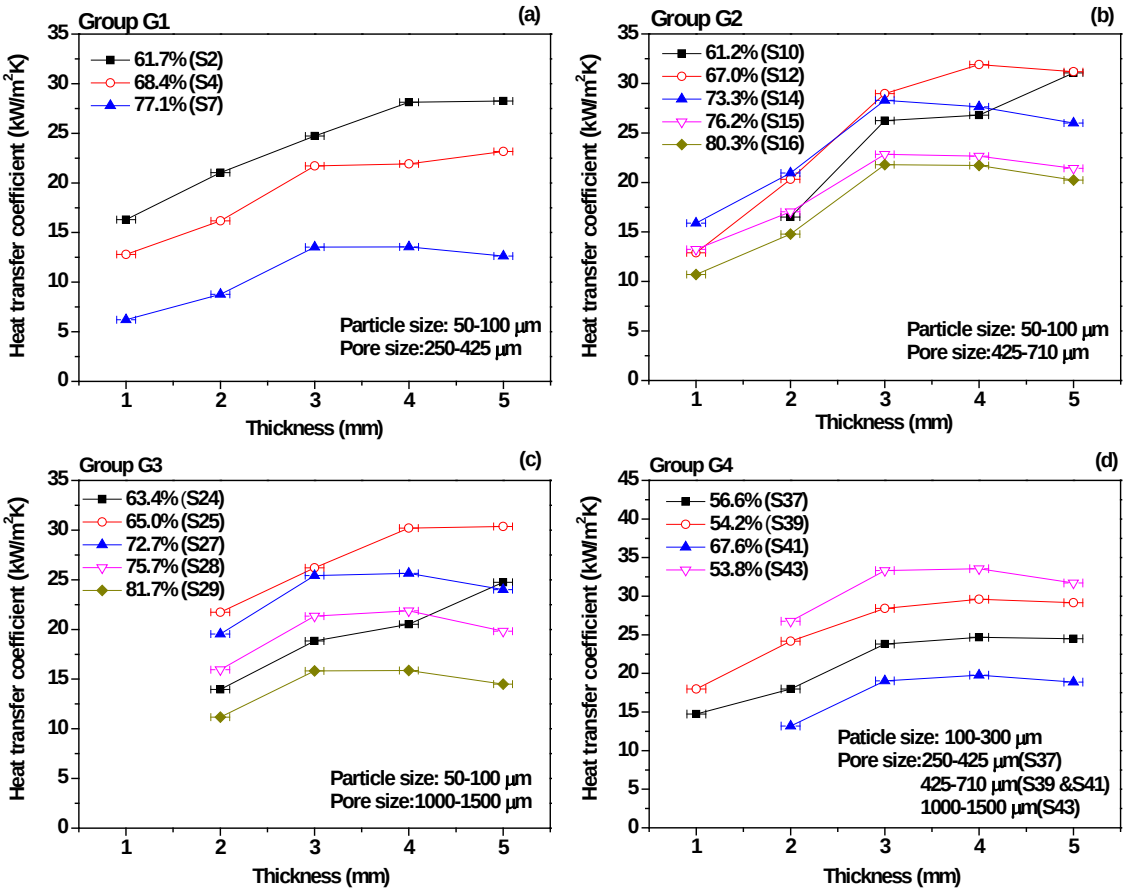

Figure 4.30 *Variation of heat transfer coefficient for porous copper samples with different thicknesses at Darcian velocity of 0.165 ±0.005m/s. (except sample S10 and S24, where v_d=0.13 ±0.007 m/s) (Input heat power: 250 kW/m^2), (a) Group G1; (b) Group G2; (c) Group G3; (d) Group G4.*

4.4.9 Heat transfer coefficient of other porous metals

Figure 4.31 shows the variation of heat transfer coefficient with porosity at different flow rates for porous nickel. The results are similar to the results for porous copper. The heat transfer coefficient gradually decreases with porosity. Sample S66 with a porosity of 59.3% and sample S67 with a porosity of 66.5%, however, show the same

heat transfer performance. For example, both have a heat transfer coefficient value of about 25 kW/m^{2}K) at the flow rate of 1L/min.

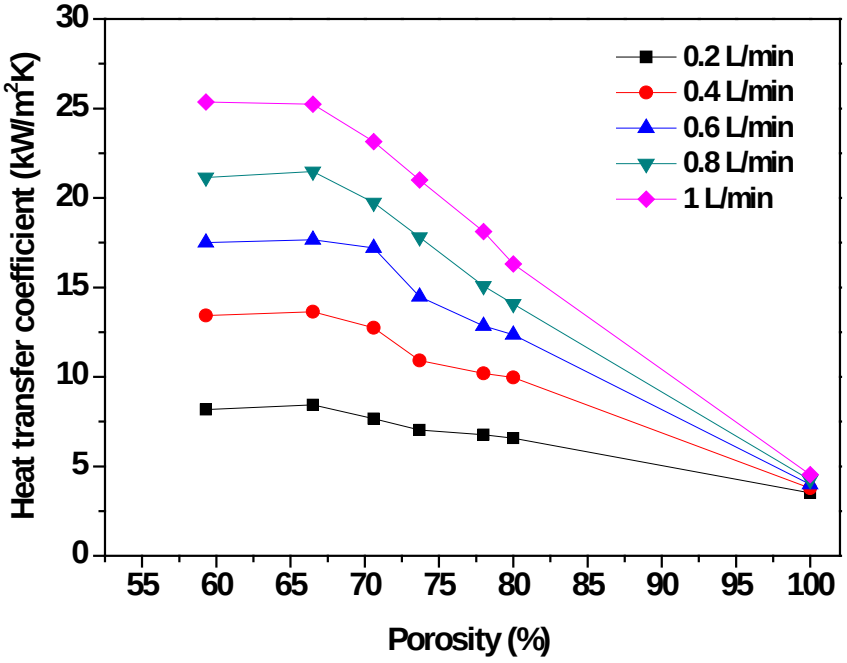

Figure 4.31 *Variation of heat transfer coefficient with porosity at different flow rates for porous Ni (Sample S66-71, Pore size 425-710μm, Input heat power: 250kW/m^2).*

Figure 4.32 shows the variation of heat transfer coefficient with coolant flow rate for different porous metals, namely copper, iron, nickel and a nickel-copper alloy, with a similar porosity. It can be clearly seen that the porous copper has the best heat transfer performance among these four porous metals, while the other three porous metals have similar heat transfer performance.

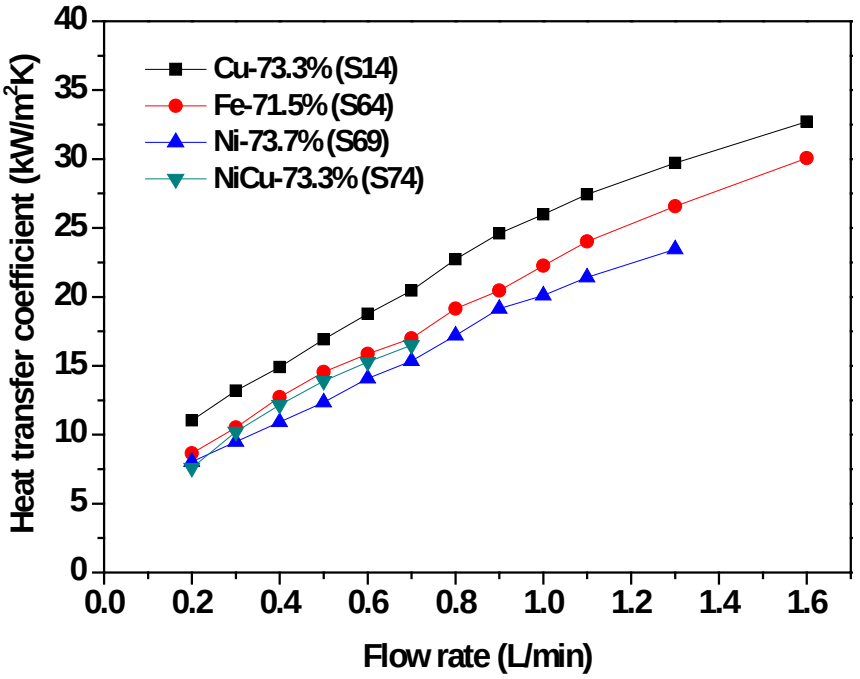

Figure 4.32 *Variation of heat transfer coefficient with coolant flow rate for different porous metals (Pore size 425-710 μm, Input heat power: 250 kW/m^2).*

4.5 Mechanical Properties

The static compression test, three point bending test and tensile test were carried out on a large number of porous copper samples and the mechanical properties were summarized in this section.

4.5.1 Compressive behaviour of porous copper

Eleven samples (P1-P11) with different porosity and pore size were made by LCS method. The compression tests were conducted on Instron 4505. The elastic modulus and yield strength were calculated with the methods described in Section 3.6.1. The relative density or porosity of each sample was measured using the Archimedes method.

Eleven porous copper samples with porosity ranging from 42% to 81% and two different pore sizes of 425-710 μm and 1000-1500 μm were fabricated. The detailed structural information and their compression properties are summarized in Table 4.14.

Table 4.14 *Structural characteristics and properties of samples with different porosities for compression test.*

Reference	Pore Size (μm)	Relative Density	Porosity (%)	Direction Relation	Elastic Modulus (GPa)	Yield Strength (MPa)
P1	425-710	0.574	42.6	//	1.52	39.12
P2	425-710	0.488	51.2	//	1.09	25.41
				⊥	1.25	33.36
P3	425-710	0.439	56.1	//	0.88	22.83
P4	425-710	0.365	63.5	//	0.66	12.63
				⊥	0.82	18.78
P5	425-710	0.324	67.6	//	0.51	7.82
P6	425-710	0.279	72.1	//	0.35	5.01
				⊥	0.49	7.52
P7	425-710	0.253	74.7	//	0.28	2.55
P8	425-710	0.191	80.9	//	0.16	1.54
				⊥	0.28	1.77
P9	250-425	0.357	64.3	//	0.54	3.62
				⊥	0.67	5.71
P10	710-1000	0.367	63.3	//	0.62	13.37
				⊥	0.75	19.35
P11	1000-1500	0.366	63.4	//	0.62	13.72
				⊥	0.80	20.16

4.5.1.1 Effect of porosity

Specimens cut from samples P1-P8 with pore size of 425-710 μm and porosity ranging from 42% to 81% were tested in the '//' direction. Specimens cut from samples P2, P4, P6 and P8 were also tested in the '⊥' direction.

Figure 4.33 shows the representative quasi-static compressive stress-strain curves of specimens compressed at the'//' direction. The compressive stress-strain curves of the samples exhibit the classic regimes for cellular solids, which are firstly linear, then plateau, and finally densification regimes. All the curves are very smooth, with no fluctuation of stress during the whole deformation process. Specimens with low porosity (such as specimen P1 with a porosity of 42.6%) have much higher stress than those with high porosity (such as specimen P8 with a porosity of 80.9%) at any given strain.

All the curves have an initial region with a linear stress-strain relationship when the strain is below 3%. The stress then increases slowly with strain after yielding of the specimen, which is characterised by the change in the gradient of the curve. Obvious plateau regions are found in the samples with high porosities, especially in samples P7 and P8 (Figure 4.33b). Although no apparent plateau regions appear in the low porosity samples, stress increases more slowly with strain (Figure 4.33a), indicating pore deformation.

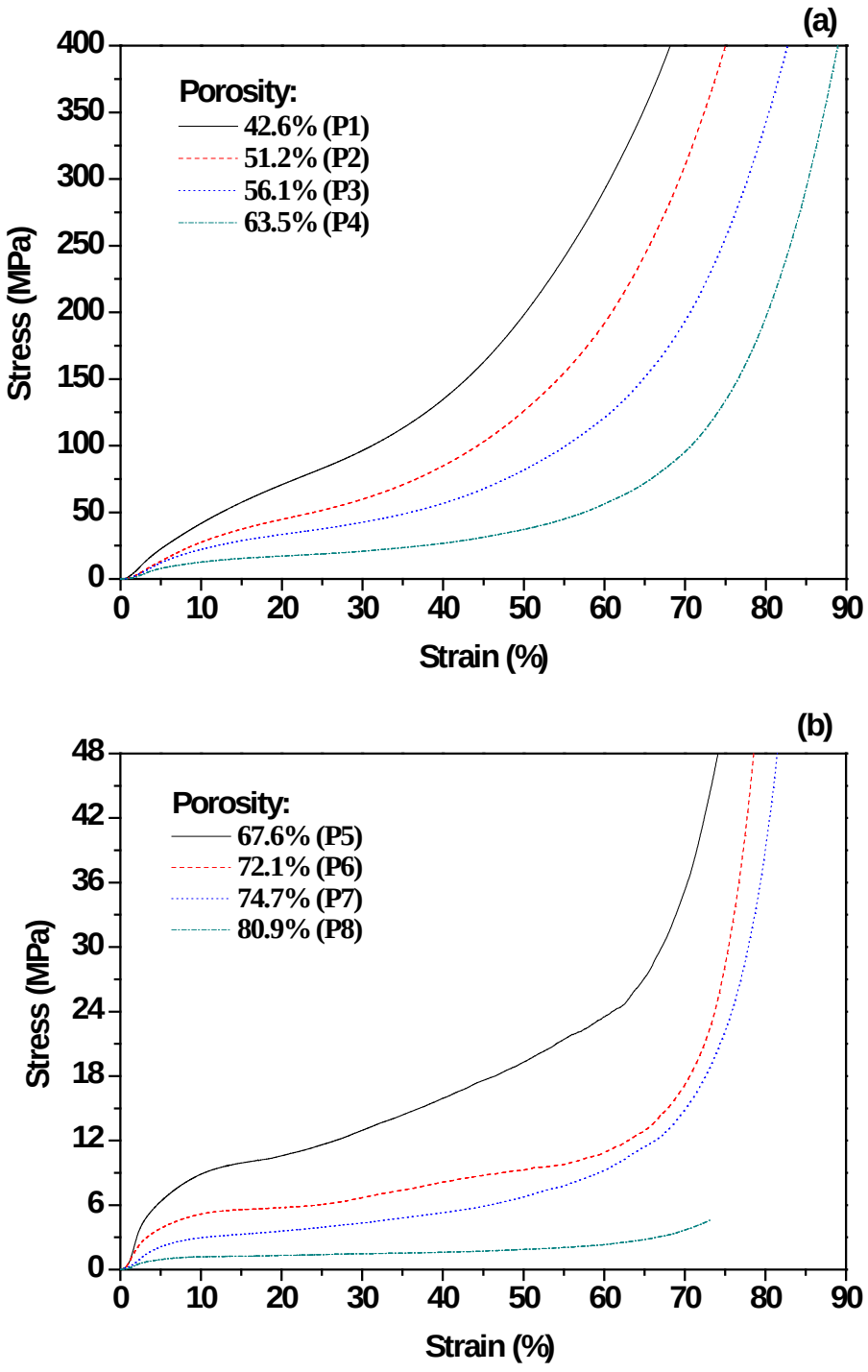

Figure 4.33 *Compressive curves of samples compressed at the // direction. The samples have a pore size of 425-710 μm and porosity of (a) 42%-64% and (b) 67%-81%.*

Densification occurs when pore deformation is nearly completed. The stress then increases rapidly. The specimens are densified during the compression process without fracture. For specimens with low porosities, like samples P1 and P2, the densification occurs at a relatively low strain. This is because low porosity samples have limited capability of pore deformation. The high porosity samples (P6, P7 and P8) have large densification strains over 60%, indicating that LCS porous copper can have good energy absorption properties.

Specimens for tests at the '//' direction were cut from four samples (P2 with a porosity of 51.2%, P4 with a porosity of 63.5%, P6 with a porosity of 72.1% and P8 with a porosity of 80.9%). Figure 4.34 shows the compressive stress-strain curves of specimens at the '//' direction, with the porosity ranging from 51% to 81%. The results of the compression test of these four specimens are consistent with the previous results for specimens tested at the '⊥' direction. The yield stress of specimens with low porosities (samples P2 and P4) is greater than that with high porosities (samples P6 and P8), while high porosity specimens (sample P6 and P8) are characterised by a stress plateau and a large densification strain.

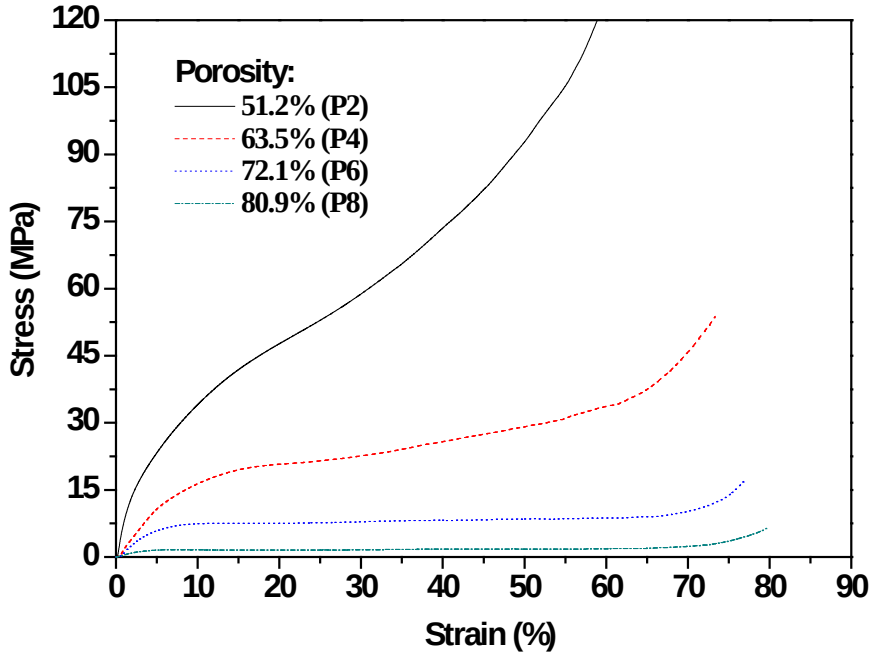

Figure 4.34 *Compressive curves of samples with different porosities compressed at the ⊥ direction (pore size 425-710 μm).*

Figure 4.35 shows the variations of the elastic modulus and yield strength with porosity at different compression directions. It shows that the elastic modulus decreased with increasing porosity. The elastic modulus of the specimen with a porosity of 42.6% is more than 9 times that of the specimen with a porosity of 80.9%. The yield stress decreases with increasing porosity, i.e., specimens with a high porosity can only support a small stress (specimens P7 and P8 in Figure 4.33). The yield strength decreased with increasing porosity. The maximum yield stress is 39.12 MPa for sample P1 with a porosity of 42.6% or a relative density of 0.574.

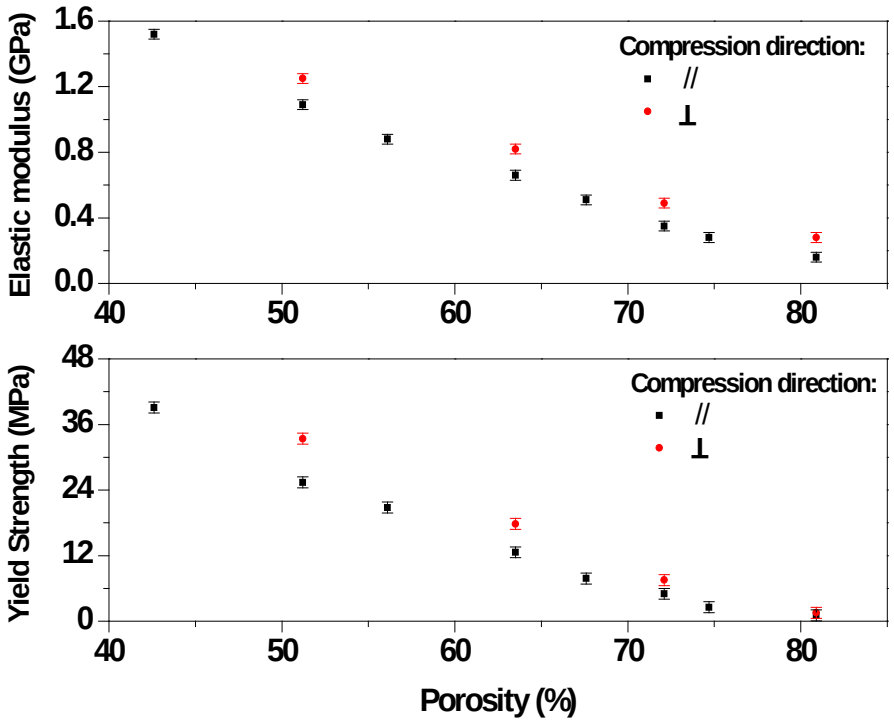

Figure 4.35 *Effect of porosity on elastic modulus and yield strength of LCS porous copper samples compressed at different directions (Sample P1-P8, Pore size: 425-710 μm).*

4.5.1.2 Effect of pore size

Additional samples P9 to P11 were fabricated to investigate the effect of pore size on compressive behaviour of LCS porous copper. The structural properties of these specimens are shown in Table 4.14. The specimens have a porosity of around 63% and three different pore size ranges of 250-425 μm (sample P9), 710-425 μm (sample P10), 1000-1500 μm (sample P11). Specimens were cut from different directions from these samples. The compression results of these specimens were compared with samples P4 with a pore size of 425-710 μm.

Figure 4.36 shows the compressive stress-strain curves of typical specimens with four different pore size ranges and two different compression directions. The stress decreases with pore size at a given strain, i.e., specimens with a large pore size can only support a small stress. This difference, however, is small when the pore size is larger than 425 μm (specimens P4, P10 and P11 in Figure 4.36).

The specimens with the fine pore size of 250-425 μm (sample P9) have very different behavior from the others. The stress-strain curves have a plateau region, where the stress fluctuates slightly with the strain. The specimen cut from P9, with the pore size of 250-425 μm and compressed at the '//' direction, has the worst compression performance. The stress drops significantly in the strain range from 40% to 65%, followed by the densification process. This is caused by the non-uniform deformation or fracture of the matrix and pores during the compression process (Gong et al 2010, 2011).

Figure 4.37 shows the variations of the elastic modulus and yield strength with pore size at different compression directions. Both the elastic modulus and yield strength increases with pore size at any compression directions. The values of both properties, however, change slightly when the pore size is larger than 425 μm.

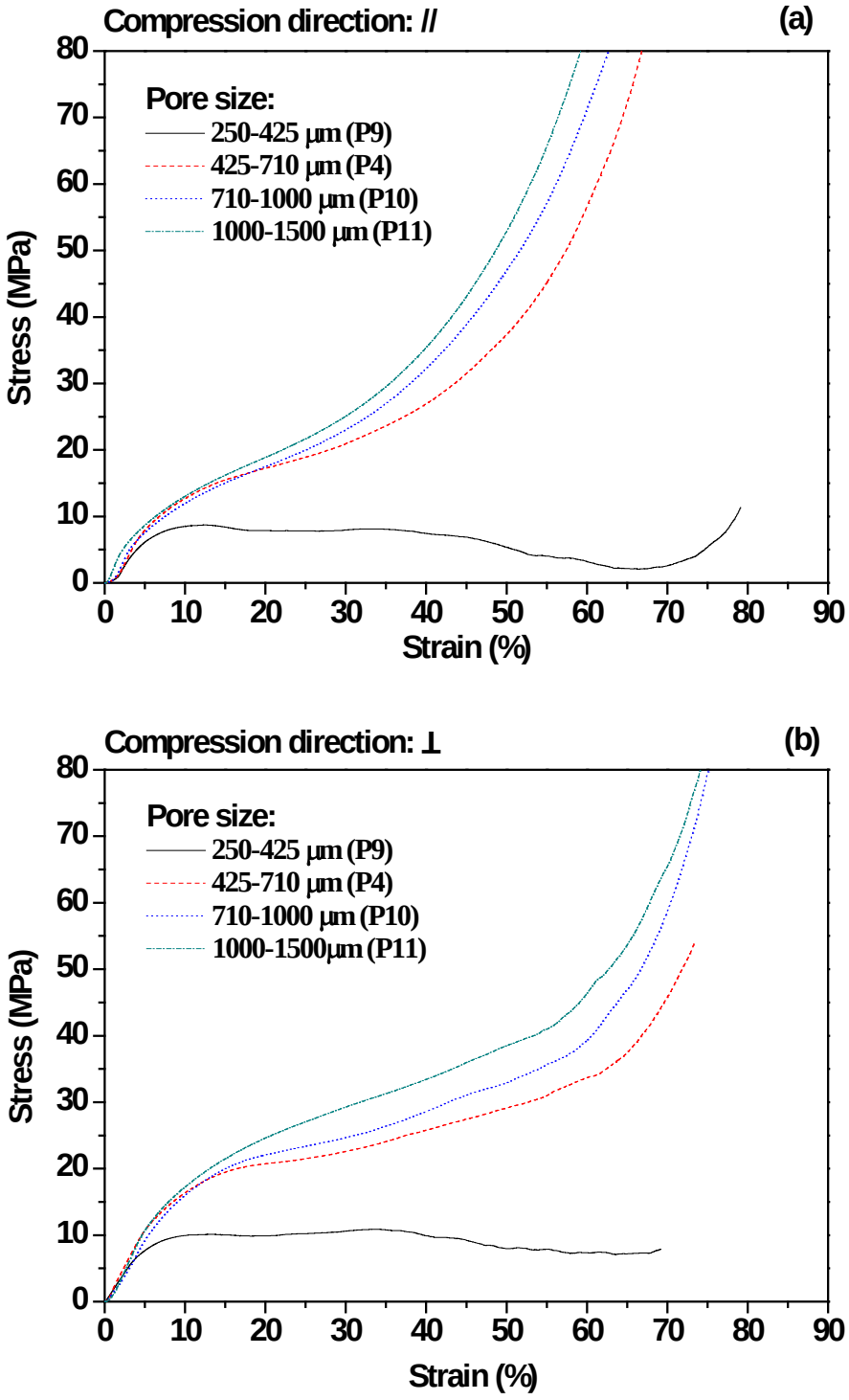

Figure 4.36 *Compressive curves of samples with different pore sizes and a porosity of around 63.8%, compressed at different directions: (a) // and (b) ⊥.*

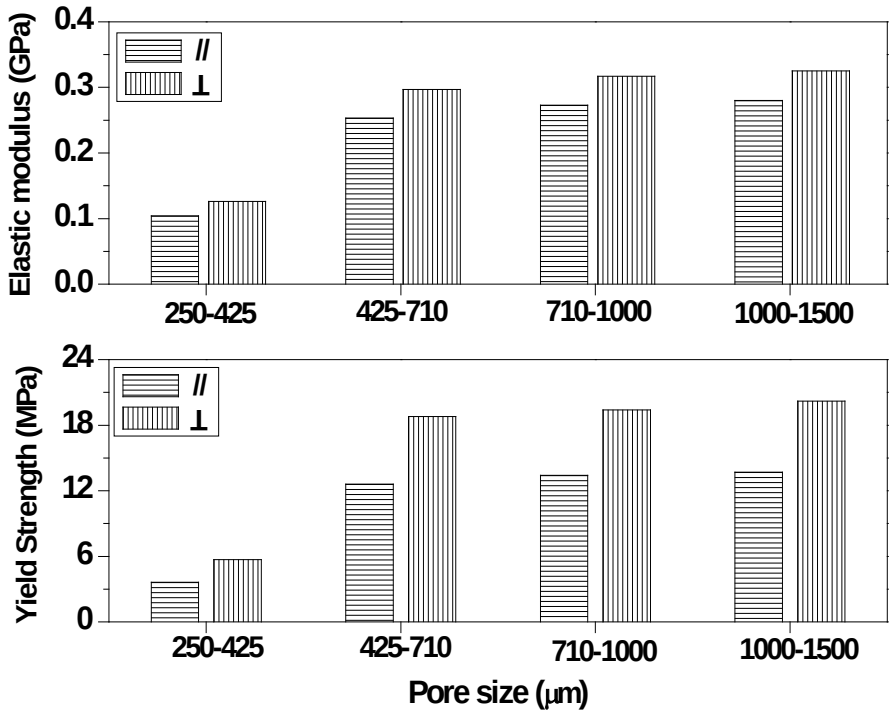

Figure 4.37 *Effect of pore size on elastic modulus and yield strength of LCS porous copper samples compressed at different directions (Porosity: 63.8±0.5%).*

4.5.1.3 Effect of anisotropy

Figure 4.38 shows compressive stress-strain curves of typical specimens with different porosities compressed at different directions. The stress of the specimens compressed at the '⊥' direction increases more rapidly with strain than that compressed at the'//'direction at the earlier stage of compression. It means that the specimens are hard to deform at the '⊥' direction at the earlier stage. It is also found that the densification strain of the specimens compressed at the '⊥' direction is much larger than that at the'//'direction, indicating that the specimens are much easier to be densified at the'//'direction.

There is a cross-over of stress-strain curves of the two compression directions for each specimen. Comparing the four Figures 4.38(a), (b), (c) and (d) shows that the inflection moves to a higher strain with increasing porosity.

All specimens show smooth compressive stress-strain curves. Even when the yield stress is low (approximately 16MPa for sample P2), there is no sudden fracture during the compression process. The results are consistent with the morphological observations in Section 4.1.1, indicating that the LCS porous copper has good metallurgical bonding between powder particles and has good ductility.

Comparing the elastic modulus and yield strength of samples compressed at different directions shows that both properties in the normal direction is higher than that in the parallel direction (see Figures 4.35 and 4.37). The yield strength in the normal direction is about 1.5 times of that at the parallel direction (see Table 4.14).

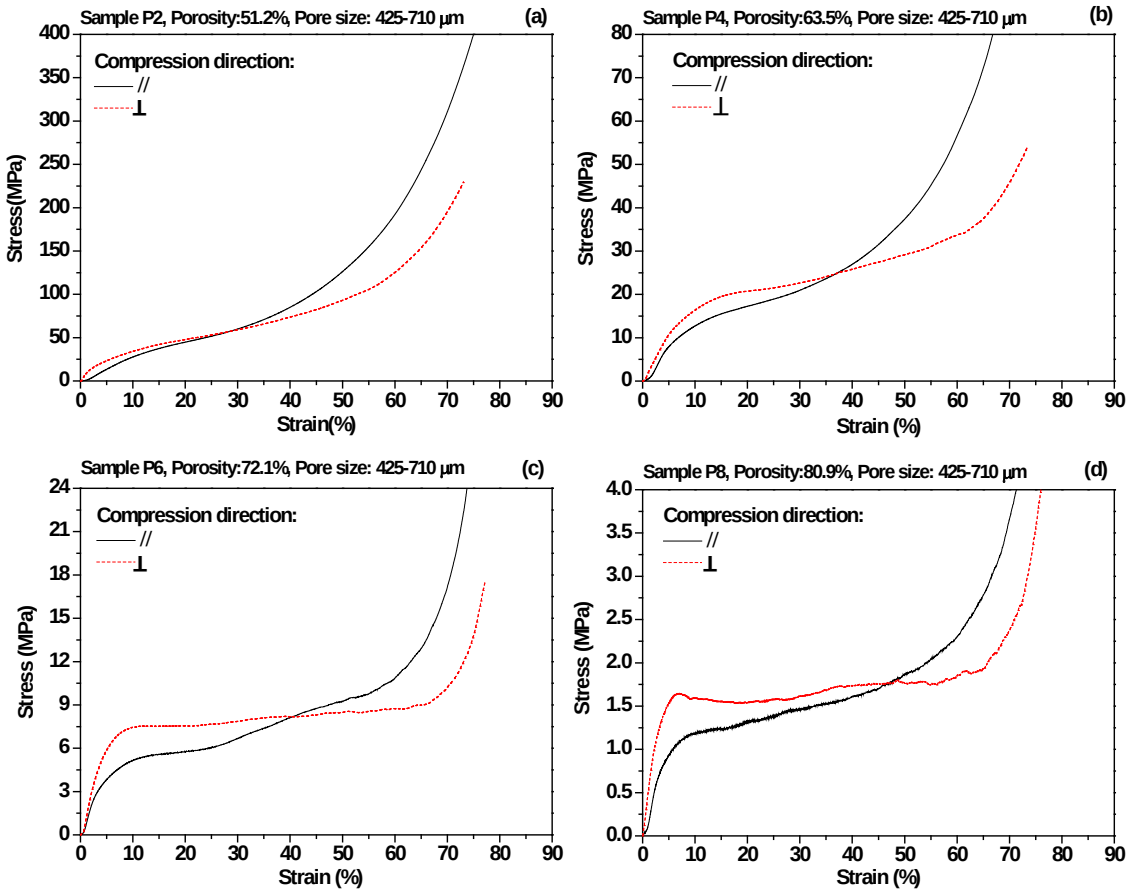

Figure 4.38 *Compressive curves of samples compressed at different directions.*

4.5.2 Bending behaviour of porous copper

Sixteen samples (B1-B16) with different porosity and pore size were fabricated for bending test. Table 4.15 shows the detailed information of the sixteen tested samples and their properties. Each sample can be tested in two directions: the bending direction being either parallel or perpendicular to the compaction direction, designated as parallel (//) and normal (⊥), respectively. All the bending test specimens were tested in the parallel direction, except that the some extra specimens cut from samples B3, B5, B11 and B13 were also tested in the normal direction, which were used to investigate the

effect of anisotropy in Section 4.5.2.3. The apparent modulus and flexural strength of the porous copper samples were calculated from Eq. (3.13) and Eq. (3.14) and averaged over the values of the specimens.

Table 4.15 *Pore parameters and properties of samples in three-point bending test.*

Reference	Pore Size (μm)	Relative Density	Porosity (%)	Apparent Modulus (GPa)	Flexural Strength (MPa)
B1	250-425	0.387	66.1	0.63	15.91
B2	250-425	0.228	77.2	0.20	3.45
B3	425-710	0.378	62.2	0.95	27.70
B4	425-710	0.345	65.5	0.75	20.42
B5	425-710	0.320	68.0	0.65	16.32
B6	425-710	0.273	72.7	0.50	12.08
B7	425-710	0.233	76.7	0.36	7.74
B8	425-710	0.183	81.7	0.22	3.82
B9	710-1000	0.350	65.0	0.79	21.33
B10	710-1000	0.235	76.5	0.37	7.89
B11	1000-1500	0.387	61.3	1.02	28.81
B12	1000-1500	0.352	64.8	0.83	22.77
B13	1000-1500	0.316	68.4	0.66	16.05
B14	1000-1500	0.288	71.2	0.55	13.81
B15	1000-1500	0.230	77.0	0.37	7.75
B16	1000-1500	0.191	80.9	0.25	4.69

4.5.2.1 Effect of porosity and pore size

Figure 4.39 shows the three point bending load-displacement curves of the typical specimens with different porosities. The load increases linearly at the earlier stage of bending. At the maximum value, the specimen starts to fracture. The load decreases with further deformation. The maximum load that the specimen can support before

breaking decreases with increasing porosity. Figure 4.39 also shows that the amount of displacement at the maximum load increases slightly with porosity. The change is small, with values from about 1.5 mm for the specimen with the largest porosity of 81.7% to 1.8 mm for the specimen with the lowest porosity of 61.3%.

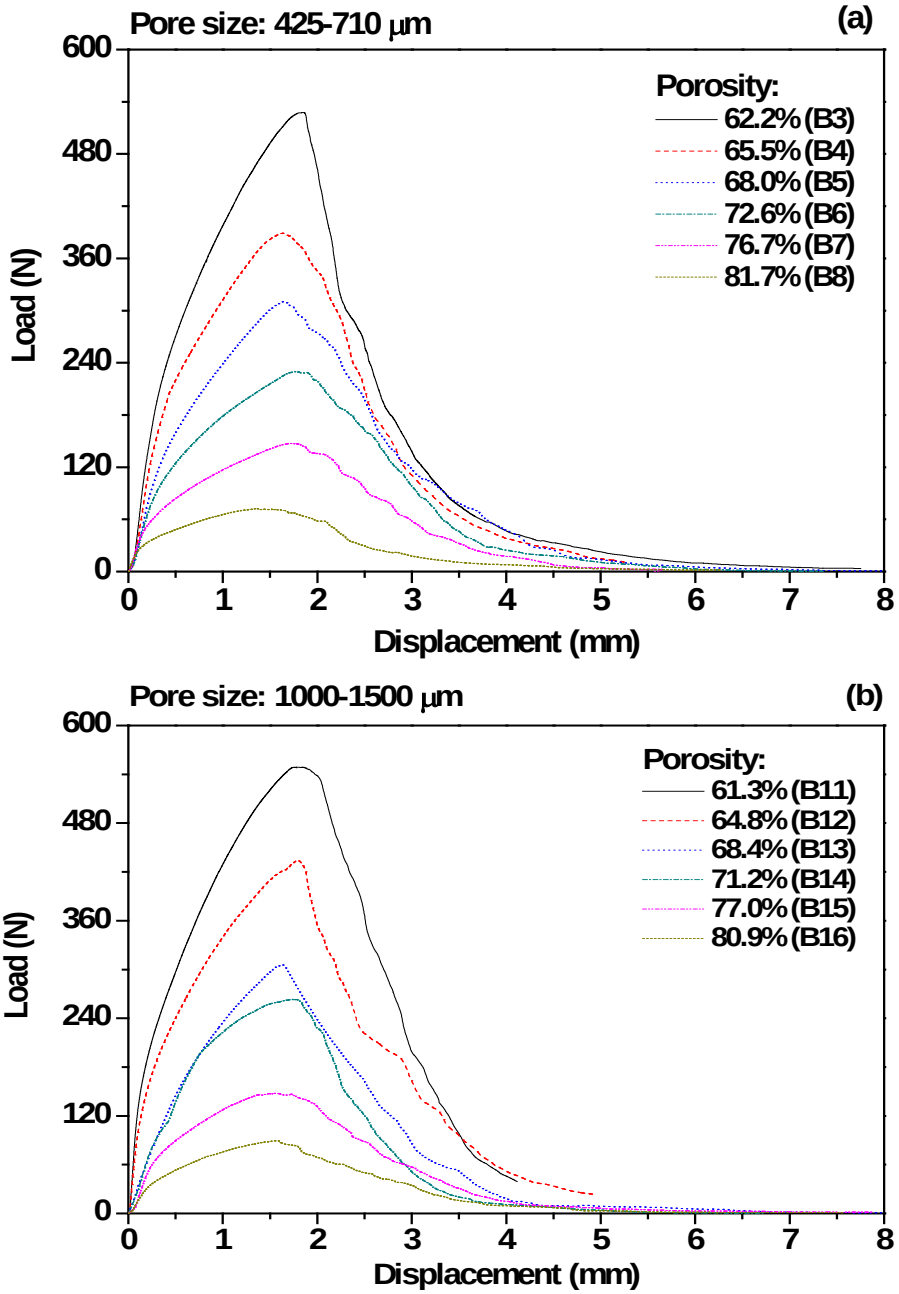

Figure 4.39 *Three point bending load-displacement curves of samples with different porosities and pore sizes: (a) 425-710μm; (b) 1000-1500μm.*

The load-displacement curves of specimens cut from two groups of samples B1, B4, B9 and B12 with porosity around 65.5%, and B2, B7, B10 and B15 with porosity around 77%, were compared to investigate the effect of pore size on the three-point bending behaviour. Figure 4.40 shows the three point bending load-displacement curves of specimens with different pore sizes. Comparing the four specimens with the porosity around 65.5% (B1, B4, B9 and B12 in Figure 4.40a) shows that the maximum load increases with pore size. The maximum loads of specimens B4, B9 and B12 are very similar, while the maximum load of specimen B1 with a porosity of 66.1% and a pore size of 250-425 μm is much lower. The effect of pore size on three point bending behaviour for specimens with a porosity about 77% (Figure 4.40b) is similar. There is very little difference among the specimens with pore size larger than 425μm (B7, B8 and B15).

There is little difference in the displacement of specimens at maximum load when the pore size is greater than 425 μm. Specimens B1 and B2, both of which have a pore size of 250-425 μm, have smaller displacements. These results show that the pore size does not affect the mechanical property very much, as long as the pore size is large enough.

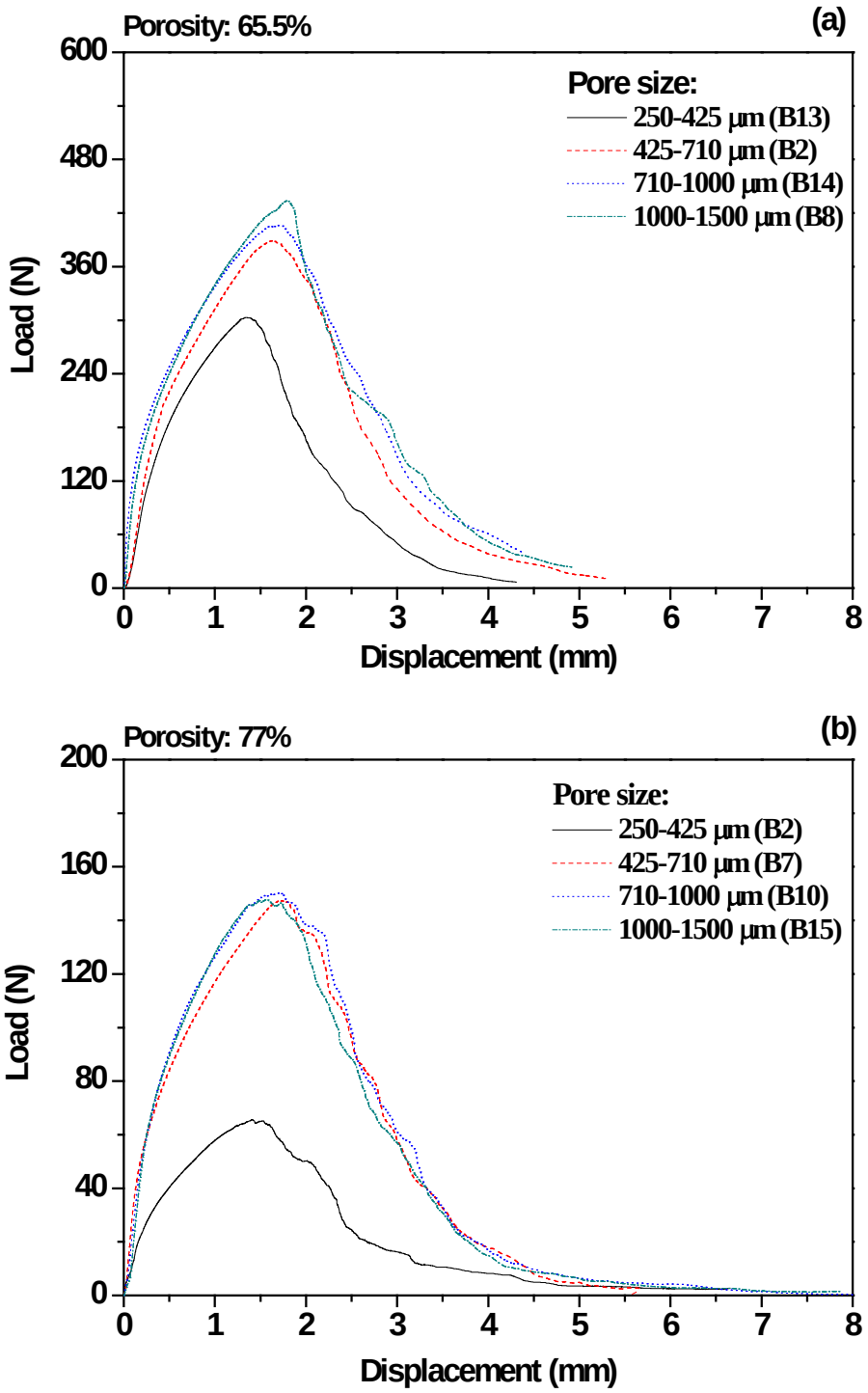

Figure 4.40 *Three point bending load-displacement curves of specimens with different pore sizes and different porosities: (a) 65.5 ±0.8%; (b) 77 ±0.5%.*

Figure 4.41 plots the values of the apparent modulus and flexural strength of porous copper samples with different porosity and pore size. It shows that the apparent modulus and flexural strength decrease with porosity. For porous copper samples with the pore size of 425-710 μm, the flexural strength changes from 3.82 MPa for sample B3 with a porosity of 62.2% to 27.7 MPa for B8 with a porosity of 81.7%. For the porous copper samples with the pore size of 1000-1500 μm, the flexural strength is about 28.81 MPa for sample B11 with a porosity of 61.3%, which is about 6 times of that for sample B16 with a porosity of 80.9% (see Table 4.15).

The apparent modulus and flexural strength are not sensitive to pore size if it is greater than 425μm, but decreased considerably when the pore size was reduced to 250-425 μm (Figure 4.41). For porous copper samples with a similar porosity of 65.5% (sample B1, B4, B9 and B12), sample B12 with pore size of 1000-1500 μm has the largest flexural strength of 22.77 MPa and apparent modulus of 0.83 GPa. The samples with the finest pore size (250-425 μm) have very small flexural strength and apparent modulus, which are only about 2/3 of the samples with the largest pore size (1000-1500 μm) at the porosity of about 65.5% and about 1/2 at the porosity of about 77% (see Table 4.15).

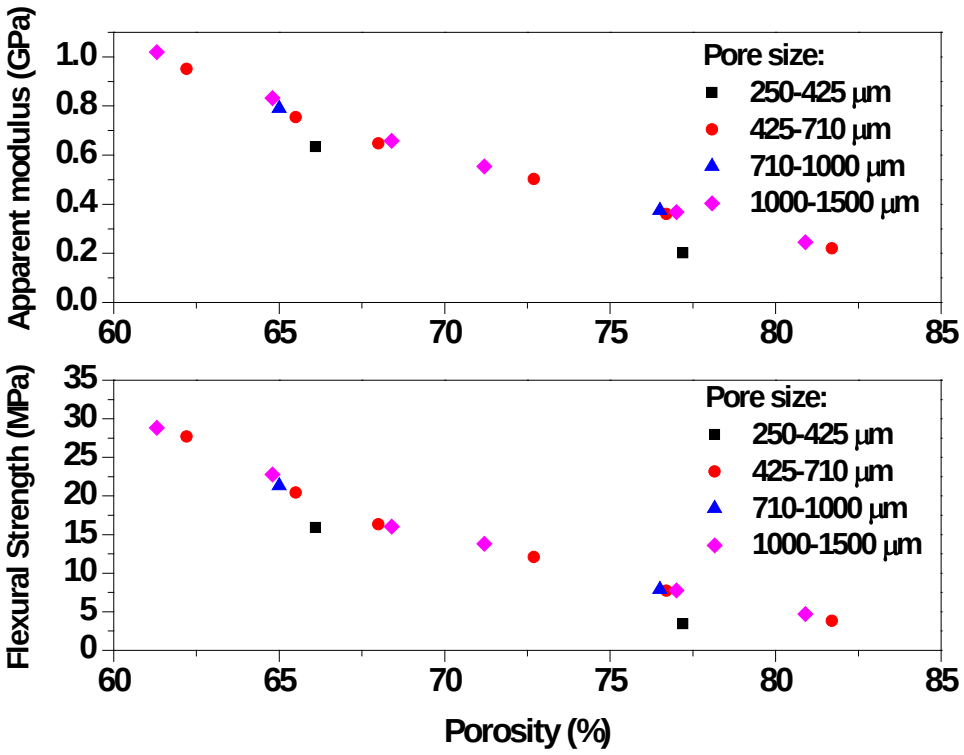

Figure 4.41 *Variations of apparent modulus and flexural strength with porosity for porous copper samples with different pore sizes*

4.5.2.2 Effect of anisotropy

Specimens cut from samples B3, B5, B11 and B13 were tested in three-point bending in different direction: parallel (//) and normal (⊥). Figure 4.42 shows the three point bending load-displacement curves of typical specimens tested in different direction. It is apparent that the maximum load and the displacement at the maximum load in the normal direction is greater than that in the parallel direction.

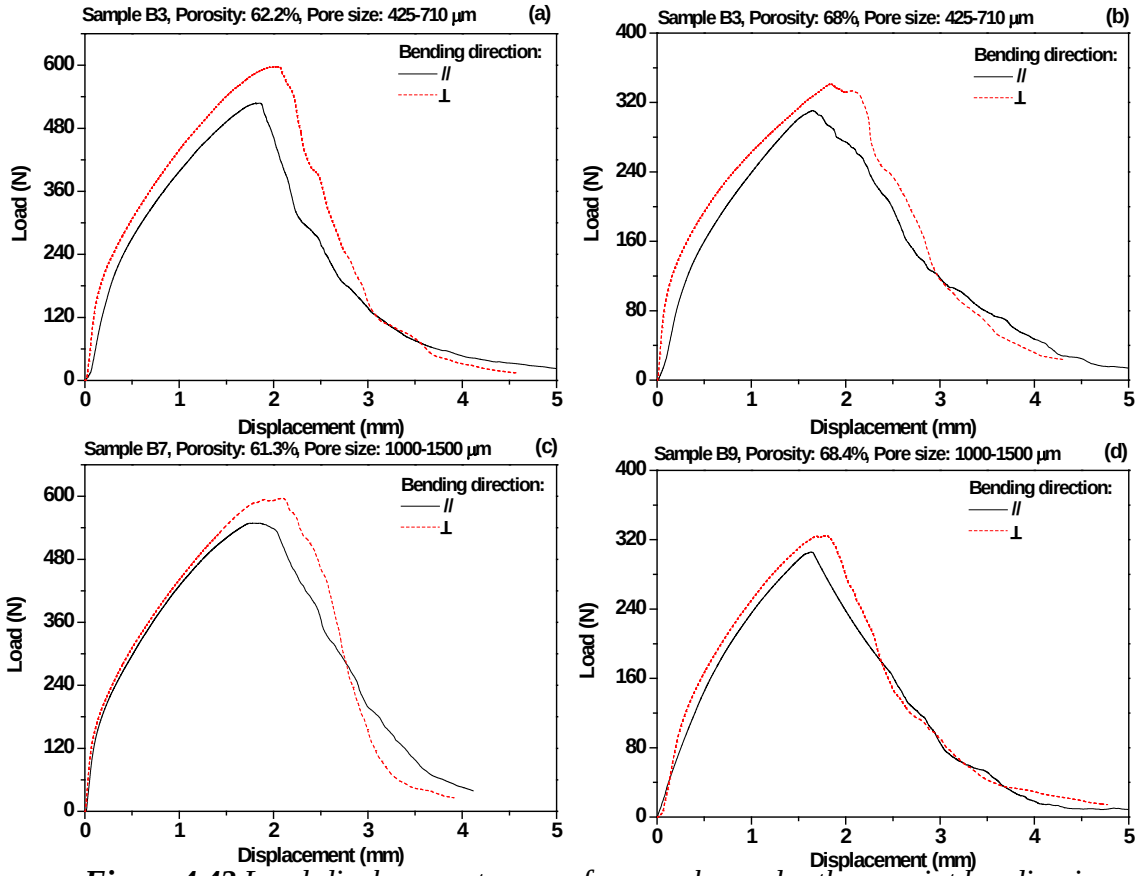

Figure 4.42 *Load-displacement curves for samples under three-point bending in different bending directions.*

Table 4.16 compares the apparent modulus and flexural strength of these four samples. Both the apparent modulus and flexural strength in the parallel direction are about 10% less than in the normal direction.

Table 4.16 *Comparison of bending properties of samples tested in different direction.*

Reference	Pore Size (μm)	Relative Density	Porosity (%)	Bending Direction	Apparent Modulus (GPa)	Flexural Strength (MPa)
B3	425-710	0.378	62.2	//	0.95	27.70
				⊥	1.14	30.20
B5	425-710	0.320	68.0	//	0.65	16.32
				⊥	0.77	18.11
B11	1000-1500	0.387	61.3	//	1.02	28.81
				⊥	1.04	30.65
B13	1000-1500	0.316	68.4	//	0.66	16.05
				⊥	0.69	17.58

4.5.3 Tensile behaviour of porous copper

Eight samples (T1 - T8) with different combinations of porosity and pore size were fabricated. The structural properties and tensile strength of the samples are summarized in Table 4.17. Samples T1 to T5 have a pore size of 425-710 μm and a porosity ranging from 61% to 82%. Samples T6, T7 and T8 have a porosity around 62% but different pore sizes of 250-425 μm, 710-1000 μm and 1000-1500μm, respectively. Specimens were cut from each sample for tensile tests as described in Section 3.6.3. All the specimens were tested with the tensile direction normal to the compacting direction when the samples were fabricated.

Table 4.17 *Tensile strength of samples with different structural characteristics*

Reference	Pore Size (μm)	Relative Density	Porosity (%)	Elastic Modulus (GPa)	Tensile Strength (MPa)
T1	425-710	0.381	61.9	0.80	9.32
T2	425-710	0.336	66.4	0.66	6.23
T3	425-710	0.283	71.7	0.43	4.72
T4	425-710	0.235	76.5	0.32	2.70
T5	425-710	0.181	81.9	0.19	1.59
T6	250-425	0.381	61.9	0.66	6.79
T7	710-1000	0.378	62.2	0.78	10.66
T8	1000-1500	0.383	61.7	0.84	11.03

Figure 4.43 shows the stress-strain curves of specimens with different porosities (samples T1 to T5). These specimens, except specimen T1, show a uniform plastic deformation regime where the strain increases extensively under a relatively narrow range of stress. The slope of the plateau decreases with porosity and becomes negative

for specimens T3 and T4. The maximum strain of specimen T1 is about 11.7%, showing that the porous copper has a relative high ductility. The maximum strain decreases with porosity, especially when the porosity is higher than 76%. It is clearly seen that the tensile strength decreases with porosity. The value of the tensile strength of specimen T1 with a porosity of 61.9% is about 9.32 MPa, which is nearly 6 times of that of specimen T5 with a porosity of 81.9% (see Table 4.17).

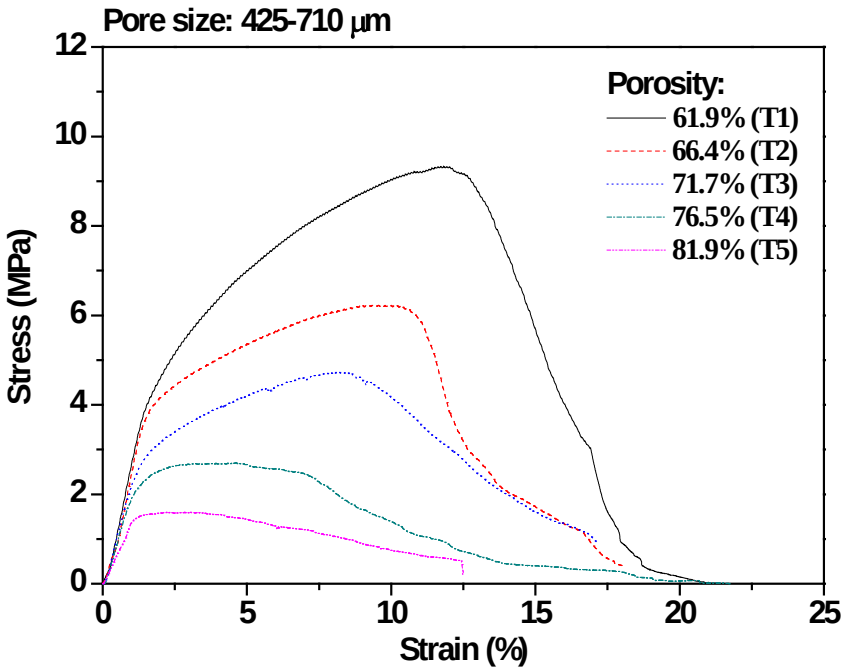

Figure 4.43 *Stress-strain curves of specimens with different porosities (Pore size 425-710 μm).*

Figure 4.44 shows the stress-strain curves of specimens with different pore sizes (samples T6, T1, T7 and T8). It is found that a specimen with a large pore size has a higher tensile strength than that with a small pore size. Specimen T6 with the fine pore size (250-425 μm) shows poor tensile property compared with the other three

specimens. It has a tensile strength of 6.69 MPa, which is similar to the value of specimen T2 with a porosity of 66.4% (see Table 4.17). It can also be seen from Figure 4.44 that the maximum strains of specimens T1, T7 and T8 are similar, but that of specimen T6 with the fine pore size is about half this value.

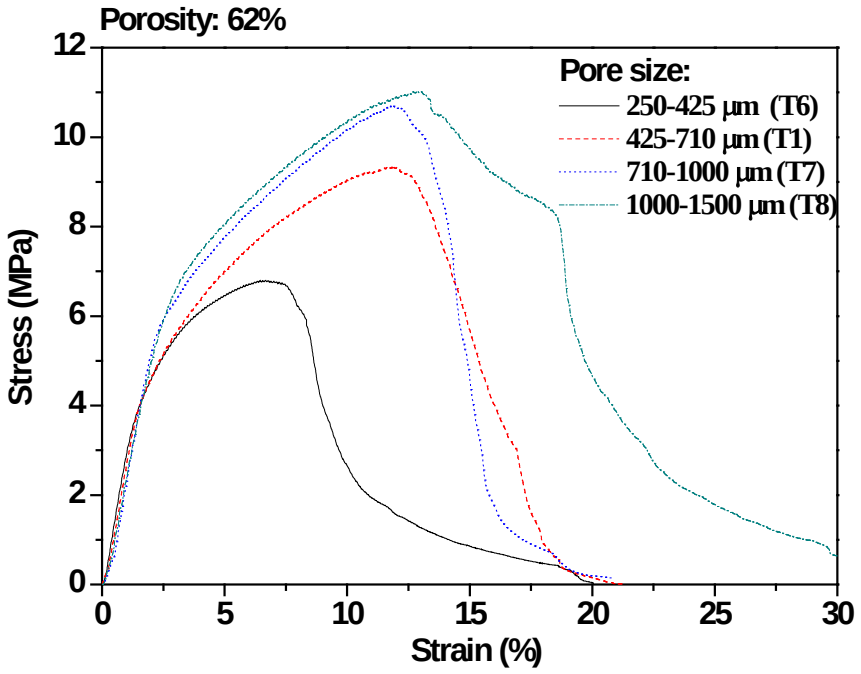

Figure 4.44 *Stress-strain curves of specimens with different pore sizes (Porosity: 62 ± 0.3%)*

Chapter 5

Discussion

In this section, the effect of pore parameters of LCS porous copper on permeability, thermal conductivity, heat transfer coefficient and mechanical properties will be discussed and several models will be used to characterise these properties.

5.1 Methods to Control the Pore Parameters of Porous Metals

The Lost Carbonate Sintering (LCS) process is an efficient manufacturing method to produce porous metals with controlled pore parameters (Zhao et al 2005, Thewsey & Zhao 2008, Mahmoud 2012, Paravanian & Panjepour 2013). In the experiments described, copper powders with three different particle sizes, 50-100 μm, 100-300 μm and 600-1000 μm, and potassium carbonate powders with four different particle sizes, 250-425 μm, 425-710 μm, 710-1000 μm and 1000-1500 μm, were used to produce porous copper samples with different porosities and pore sizes. The SEM micrographs of the copper powder and potassium carbonate granules are shown in Figures 3.2 and 3.3. Both the copper powder particles and potassium carbonate granules are spherical in shape, with slight deviations on the sphericity. It is important to mix the powders uniformly in order to obtain porous copper samples with uniform porosity and pore distribution. Ethanol is a good binder and it was found that 1-2% ethanol (by weight) is

enough in the experiment to stick the fine copper particles on large potassium carbonate particles. The mixing time should be controlled as ethanol is easy to evaporate during the powder mixing process.

The objective of compacting is to obtain a green part with a certain density to make sure the particles mechanically bind together. In the experiment, compacting was performed at a pressure of 200 MPa, which is sufficient to make the green compact dense according to Zhao et al. (2005). Density distribution has to be taken into account as it affects the properties of porous metal samples. Inhomogeneous distribution of density is the main characteristic for uniaxial compacting process. Improvement of compaction is important to obtain compacts with a uniform density distribution. There are mainly two ways of pressing in engineering applications: single-action pressing and duplex-action pressing. The distribution of compact density along the compacting direction for the two ways of pressing is shown in Figure 5.1. In single-action pressing, the average cross-sectional density of the compact decreases linearly along the compacting direction. In the present study, duplex-action pressing was adopted to obtain porous copper samples with uniform porosity distribution, as shown in Figure 3.4. During the compacting process described in Section 3.1.2, the carbonate granules are visibly deformed under the compacting pressure of 200 MPa, which can be seen in Figure 4.1b. The deformation is unavoidable as the potassium carbonate particles are much softer than the copper particles. As pore shape is controlled by the potassium carbonate, the

porous copper samples show anisotropy with elliptical pores. The anisotropy has little influence on permeability and heat transfer coefficient, however, it affects the mechanical properties of porous copper.

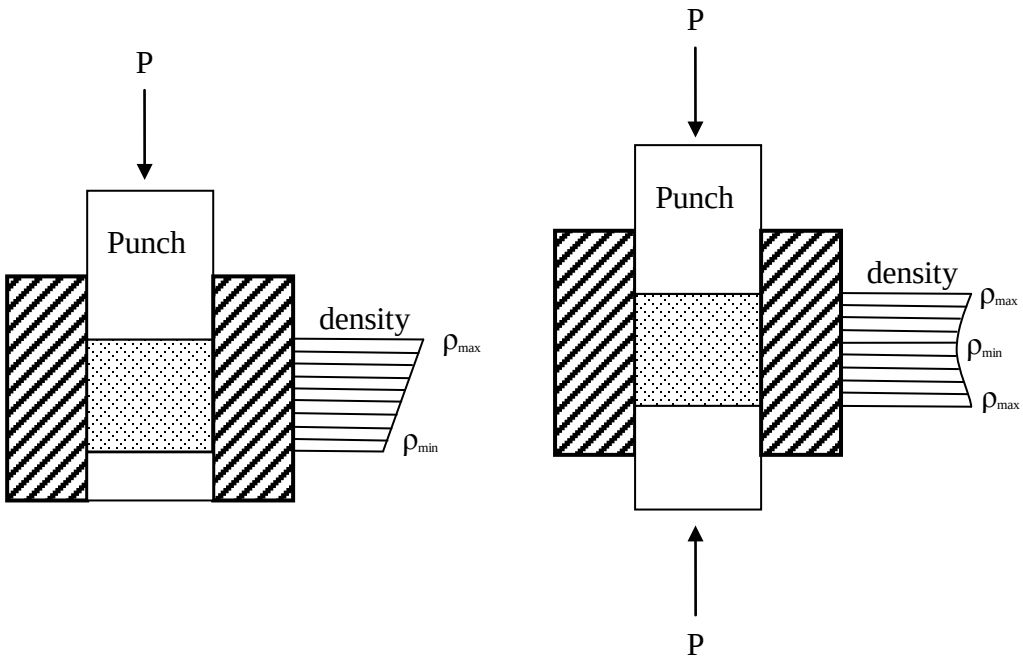

Single-action pressing Duplex-action pressing

Figure 5.1 *Density distribution along the compaction direction in the compacts pressed in different ways*

Sintering is a core process of powder metallurgy. It proceeds in three stages (Lenel 1980): 1) necks form along the contact surfaces of adjacent particles, but powder particles remain discrete; 2) particles diffuse into each other, grain boundaries develop on the neck and the voids between the particles develop into pores; and 3) necks grow and isolated pores tend to shrink and become spheroidal. Densification progresses rapidly during the second stage. Two main parameters play an important role during the

sintering process: sintering temperature and sintering time. Figure 5.2 illustrates the progress of densification of compacted copper powder as a function of time and temperature (Cable & Gupta 1967). Sintering temperature affects the densification significantly; and the higher the sintering temperature is, the larger the relative density is.

As seen from Figure 5.2, the relative density of copper powder compact shows a logarithmic relationship with sintering time. The density of the compact increases rapidly at the earlier stage of sintering and then slowly with time. It is not practical in industry, however, to extend sintering time excessively. Sintering atmosphere is also important in the sintering process. Vacuum sintering was used in the LCS method, as it will: (1) reduce the oxidizing species in the atmosphere, such as H_2O and O_2; and (2) shorten the sintering time at the same temperature due to the vacuum in the pores. Wang et al. (2010) investigated the effect of sintering temperature on the microscopic morphologies of porous copper samples and produced some unusual results. They found that at relatively low sintering temperature (below 920°C), the copper particles could not be bonded effectively, but when the sintering temperature was above 960°C, some Cu precipitated from the surface of the compacts in the form of globules, and the cell wall and pores distributed inhomogeneously.

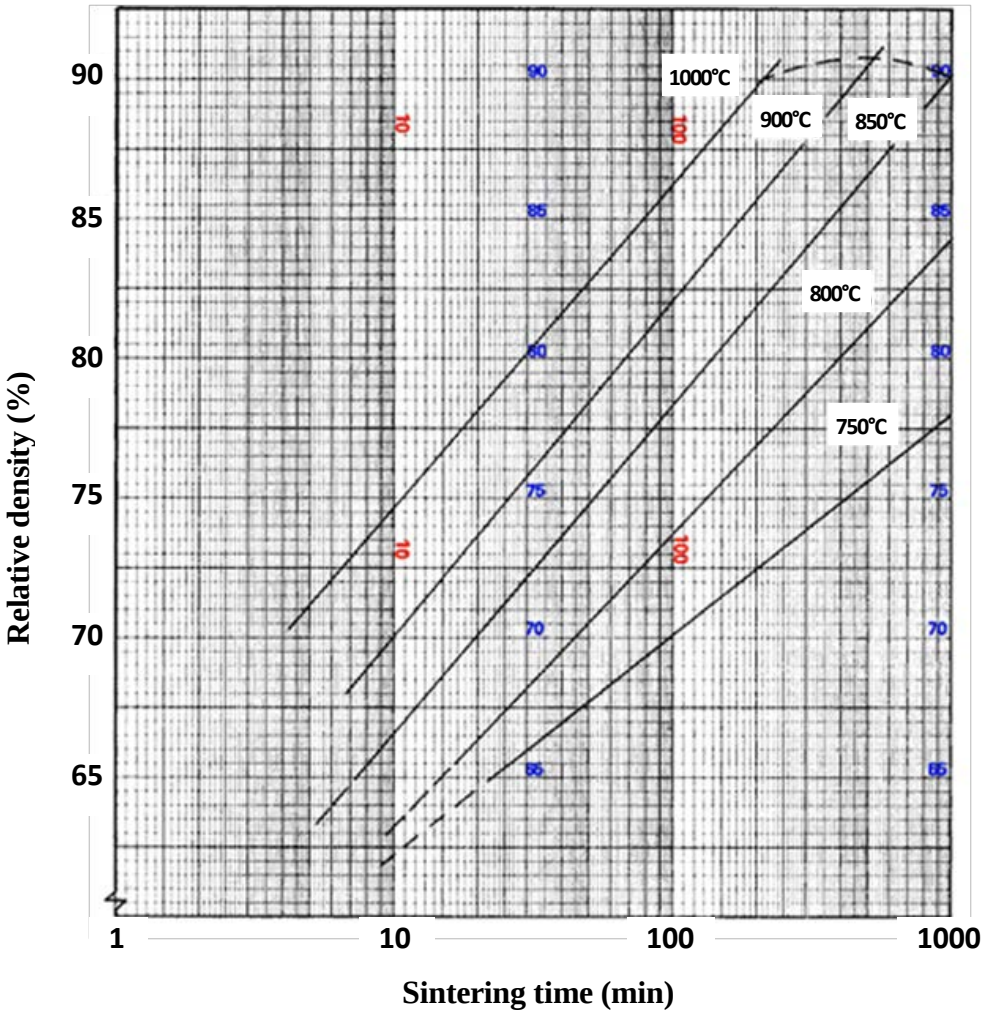

Figure 5.2 *Effect of sintering temperature and time on densification of copper powder compacts (Cable & Gupta 1967)*

In the present study, the compacts were first sintered at a temperature below the melting point of potassium carbonate, 850°C for 2 h, so that the potassium carbonate particles stayed in the samples to support the porous copper frame and prevent it from collapsing or excessive shrinking. The final sintering temperature was 950°C and the sintering time was 2 h to ensure the complete decomposition of potassium carbonate and the achievement of enough strength for the porous copper samples.

5.2 Pore Parameters of Porous Copper

The characteristics of the LCS porous copper, including porosity, pore size, pore shape, specific surface area and tortuosity will be discussed in this section.

5.2.1 Porosity

Porosity is one of the most important parameters of any porous metals. Table 4.1 and Figure 4.2 gave the measured porosity values by different methods, including the Archimedes, point counting and direct volume measurement methods, against the nominal values. Nearly all the measured porosities of a sample are higher than the nominal porosity, due to some interstices between the copper and potassium carbonate powders.

The network of metal particles would normally experience shrinkage during the high-temperature sintering process, which could lead to deformation of pores and decrease in pore size. No evidence for these phenomena, however, was found from the observations of the microstructure of the porous copper samples (shown in Figure 4.1). The values of porosity calculated from the direct volume measurement and Archimedes methods are very similar, but the ones calculated from the point counting method are slightly lower. It should be noted that the point counting method could only obtain an estimated value from one surface, and the uniformity of pore size and pore distribution

would significantly affect the accuracy of the calculated porosity. This may explain that the error of the point counting method is a little larger than the other two methods.

5.2.2 Pore size and characteristic length

Pore size is controlled by the potassium carbonate powder selected. In this study, the potassium carbonate powder was sieved into four different particle size ranges: fine size range of 250-425 μm, two medium size ranges of 425-710 μm and 710-1000 μm, and large size range of 1000-1500 μm. It was found from Figure 4.1 that the pore size range was nearly the same as that of the potassium carbonate used for the porous copper sample. There are two types of inter-connecting pore linking one big pore to another in the LCS porous copper samples. One is the channel at the conjunction edge of the big pores (shown in Figures 4.1b and d). This is formed when two potassium carbonate particles are in contact with each other during the fabrication process. The channel between the pores form after the removal of the carbonate particles. The other one is the interstices between the copper particles (shown in Figures 4.1e and f). Most of the interstices are very small, only several micrometers in size. Both the conjunction channels and the interstices play very important roles in fluid flow in the porous copper samples. It should be kept in mind that the pore size used in this thesis represents the size of the pores created by the potassium carbonate particles. The interstices between copper particles are also a kind of pore (micropores). In LCS porous copper samples,

the volume fraction of these interstices is very small, according to the comparison of nominal and actual porosity in Section 4.1.2.

As described in Section 2.3.2, pore size is just one apparent parameter describing the LCS porous copper sample. When handling flow through porous media, the characteristic length should be used. The hydraulic diameter, D_h, which is used in this thesis, is a commonly used term as the characteristic length (Carman 1956, Bear 1979, Dullien 1991, Kaviany 1995, Incropera & DeWitt 2007, Kreith et al. 2011), and is defined as:

$$D_h = \frac{4 \times cross\ sectional\ area}{wetted\ \ perimeter} = \frac{4 \times void\ volume}{surface\ area} \tag{5.1}$$

5.2.3 Pore shape

Similar to pore size, pore shape is also controlled by the potassium carbonate particles. As mentioned above, the spherical potassium carbonate granules are deformed under the high compacting pressure and form elliptical pores. The ratio between the major and minor axes was about 3:2 as seen from the SEM images. This representative pore shape would lead to anisotropy of LCS porous copper samples.

5.2.4 Specific surface area

The specific surface area measured by the quantitative stereology method (Section 3.2.2) is specific surface area per unit volume of porous media (S_v), and it has the following relationship with specific surface area per unit volume of solid (S_0):

$$S_v = (1-\varepsilon)S_0 \tag{5.2}$$

For the porous medium with a uniform pore diameter , the specific surface area per unit volume of solid can be expressed by Eq. (2.6). Substituting Eq. (2.6) to Eq. (5.2), the specific surface area based on the whole volume of the porous medium is therefore:

$$S_v = (1-\varepsilon)S_0 = \frac{4\varepsilon}{d_{pore}} \tag{5.3}$$

The experimental results showed that the specific surface area , S_v, increases with porosity and decreases with pore size, which is good agreement with Eq. (5.3).

Figure 5.3 compares the theoretical value and the measured values of the specific surface area. The theoretical specific surface area per unit volume of the porous metal was calculated by Eq. (5.3), taking ε and d_{pore} as the actual porosity (measured by the Archimedes method) and the average pore size (average diameter of the potassium carbonate particles, i.e., arithmetical mean value between the largest size and the smallest size), respectively. The actual values are close to the theoretical values. The differences may come from the following factors:

1) Micro-porosity. The theoretical calculations considered only the large pores, but ignored the contribution of the interstices between particles to the porosity.

2) The pore connection effect. The theoretical values of the specific surface area used a cylinder to represent the surface of an idealized pore. In practice, there are many windows or micropores that connect the big pores (as shown in Figure 4.1d), instead of a continuous cylinder channel.

3) Error of quantitative stereology. Under the metallographic observation conditions, the micro-pores were difficult to observe, so a large number of points that should be counted are ignored, leading to a low surface value by the quantitative stereology method.

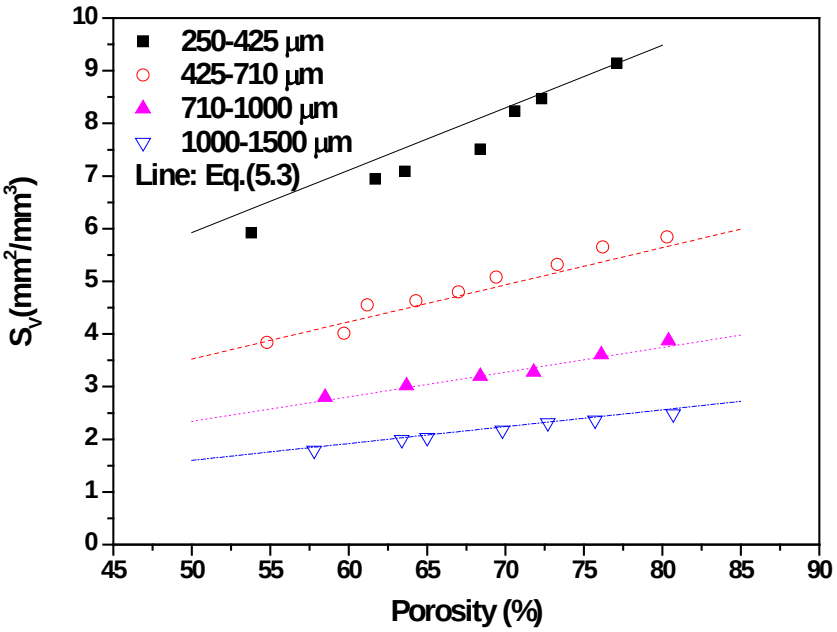

Figure 5.3 *Comparison of the theoretical and measured values of specific surface area. The theoretical values (Calculated by Eq.(5.3)) are represented by lines: Solid: 250-425 μm; dash: 425-710 μm; dot: 710-1000 μm; and dash-dot: 1000-1500 μm.*

The values of specific surface area calculated by Eq. (3.3) and Eq. (5.3) are very close, as they both only consider the surface area around the large pores. The actual specific

surface area would much higher than the calculated values due to the existence of micro-pores inside the LCS porous copper samples.

5.2.5 Tortuosity

Several empirical correlations between tortuosity and porosity have been developed, some of which were summarized in Section 2.3.2.4. For porous media with packed granular particles, the power law relationship, i.e., $\tau = \varepsilon^{-n}$ (Eq. (2.9)), was used most frequently (Archie 1942, Bear 1972, Dullien 1979, Mota et al. 2001, and Dias et al. 2006). This power law relationship is also in good agreement with the experimental results shown in Section 4.1.3. The fitting parameters are given in Table 5.1.

Table 5.1 *Fitting parameter for tortuosity using Eq. (2.9)*

Group	Particle Size(μm)	Pore Size(μm)	*n*	R^2
GA1	50-100	250-425	1.027	0.999
GA2	50-100	425-710	1.319	0.987
GA3	50-100	710-1000	1.629	0.990
GA4	50-100	1000-1500	1.985	0.988
GA5	100-300	425-710	0.852	0.995
GA6	100-300	1000-1500	1.228	0.994
GA7	600-1000	1000-1500	0.645	0.992

Archie (1942) measured the tortuosity of water-saturated sands by electrical measurement method and found that n=0.5, and the same value was also found by Zhang & Bishop (1994). Delgado (2006) investigated the packed beds of sand and

found n=0.4, and this value was also obtained by Mota et al. (2001) in testing the packed beads. Dias et al. (2006) proposed that the exponent index for granular beds describing the dependence of tortuosity on porosity ranges from 0.4 (loose packing) to 0.5 (dense packing).

It is obvious that n in Table 5.1 is much larger than that for packed beds in the literature reported above. Actually, the distribution of pores and voids in LCS porous copper is different from the packed bed. The large pores created by the potassium carbonate particles can lead to much tortuosity for LCS porous copper samples compared with packed particle beds.

LCS porous copper has a uniform structure, with nearly spherical pores of a certain pore size homogeneously distributed in the metallic matrix composed of sintered copper particles. The ratio between the average diameter of copper particles (particle size, $\overline{d}_{part}$) and the average diameter of potassium carbonates particles (pore size, $\overline{d}_{pore}$), which has an effect on tortuosity, is introduced:

$$s = \frac{\overline{d}_{part}}{\overline{d}_{pore}} \tag{5.4}$$

Figure 5.4 shows the relationship between n and s, and an approximate expression can be obtained:

$$n = \frac{0.5}{\sqrt{s}} \quad (0.06 \le s \le 0.64,\ R^2 = 0.988) \tag{5.5}$$

An empirical equation to describe the tortuosity as a function of porosity and particle/pore size ratio can be obtained for LCS porous metal as:

$$\tau = \varepsilon^{-\frac{0.5}{\sqrt{s}}} \quad (0.06 \le s \le 0.64) \tag{5.6}$$

The experimental data and the empirical equation predictions with different values of *s* are plotted in Figure 5.5.

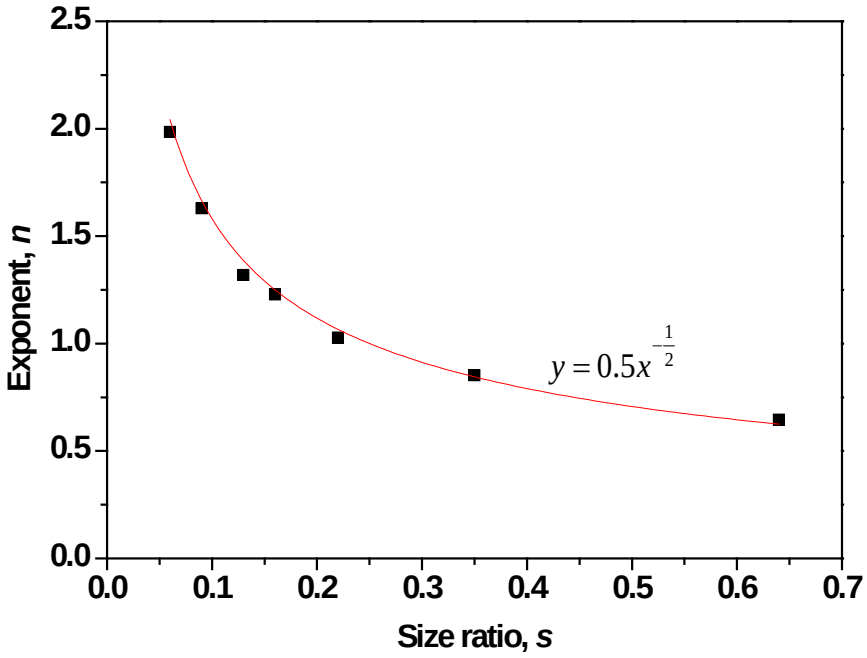

Figure 5.4 *Relationship between copper particle/pore size ratio and exponent of Eq. (2.9).*

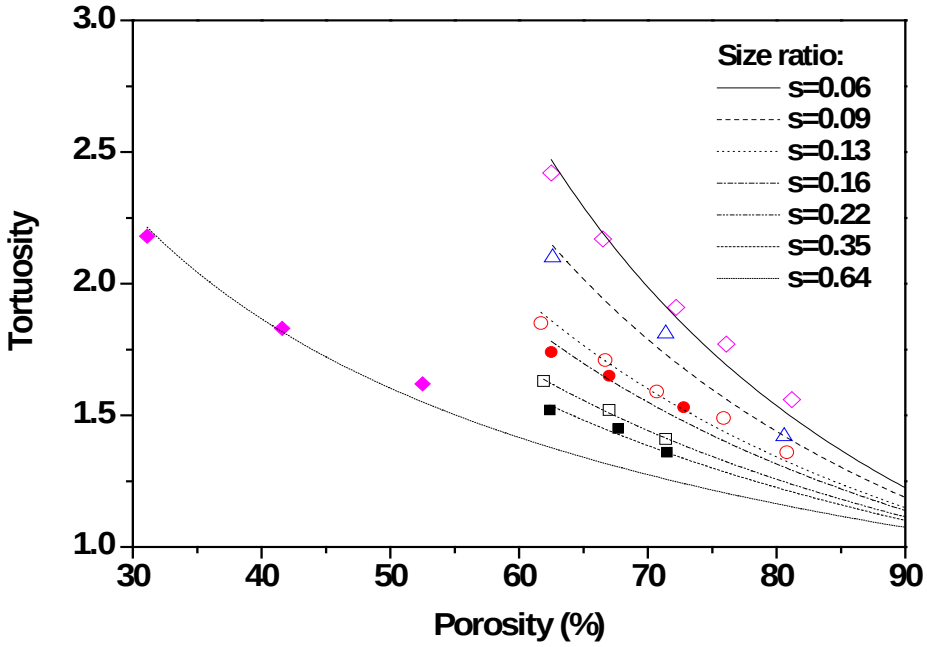

Figure 5.5 *Tortuosity of LCS porous copper with different particle/pore size ratio s (Symbols: experimental data; and lines: prediction of empirical Eq. (5.6)).*

5.3 Permeability

5.3.1 Pressure drop of porous copper

The pressure drop of the porous copper samples was measured by the test apparatus using an open flow arrangement. The experimental results presented in Section 4.2.1 clearly show that lower pressure drops are generated for the tested samples with higher porosities or smaller pore sizes. This effect was consistent over all samples. As shown in Figure 4.1, the pores within the porous copper samples are connected by small cavities and interstices. An increase in porosity means smaller solid fraction within the porous copper and more channels for the fluid to flow through, significantly reducing the flow resistance of fluid. Similarly, smaller pores within a sample result in increased

pore density (or number of pores per unit volume), which means that more pores are interlinked, i.e., a higher connectivity. This gives the fluid more channels per unit volume to flow through, giving rise to lower flow resistance and thus a lower pressure drop at any given flow rate.

A large amount of research has shown that Darcy's law is valid at low Darcian velocity and the quadratic Forcheimer relationship is needed at high Darcian velocity (Hakamada et al. 2006, Khayargoli et al. 2004, Montillet 2004, Despois & Mortensen 2005). Figure 5.6 shows the pressure drop curves of RECEMET metal foams (RECEMAT International, Netherlands) from a study carried out by Khayargoli et al. (2004). A quadratic relationship is evident in this case. The pressure drop curves for the LCS porous copper in the present study also follows the quadratic relationship.

For the RECEMET metal foams (RECEMAT International, Netherlands), pressure drops decreases with the pore diameter, as also shown by others (Antohe et al. 1996, Khayargoli et al. 2004, Hakamada et al. 2006). The LCS metals showed a different pore size effect. The reason for this difference may be attributed to micropores, which do not exist in other metal foams. The pores created by the potassium carbonate particles often have different morphologies from the cells of the other porous metals, so the effect of pore size for LCS porous copper is not directly comparable with the other metals.

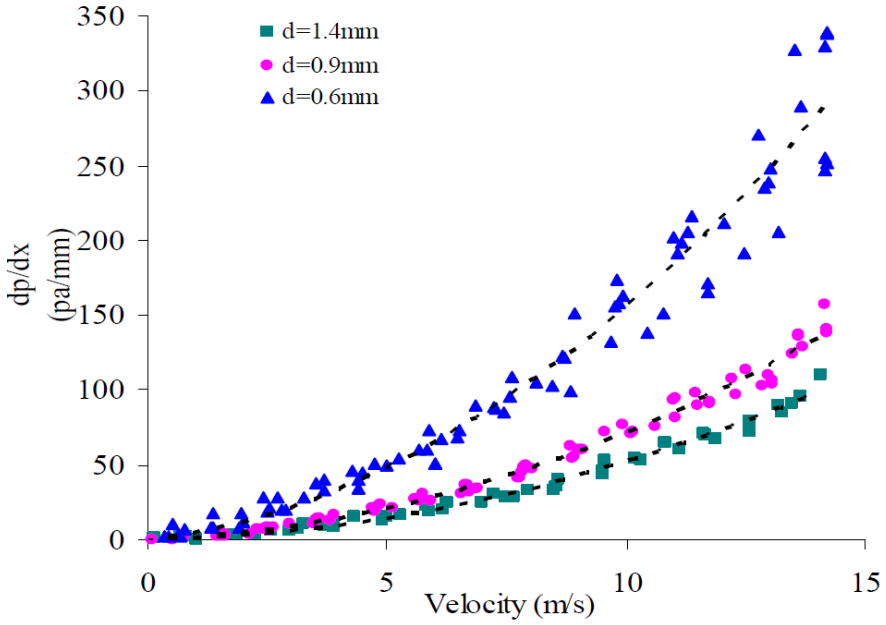

Figure 5.6 *Effect of pore diameter on the pressure drop for RECEMAT metal foams (RECEMAT International, Netherlands) (Khayargoli et al. 2004).*

5.3.2 Effects of porous structure on permeability

The permeability of LCS porous metals with different pore parameters, including porosity, pore size, copper particle size, anisotropy and double-layer structure, have been summarized in Section 4.2. The samples can be divided into eight groups according to pore size and copper particle size (Table 5.2).

Table 5.2 *Fitting parameters of power law permeability*

Group	Particle Size(μm)	Pore Size(μm)	*s*	*a* (×10^{-9})	*n*	R^2	Data Points
GS1	50-100	250-425	0.22	2.89	8.66	0.995	7
GS2	50-100	425-710	0.13	2.92	9.48	0.992	9
GS3	50-100	710-1000	0.09	2.61	9.90	0.990	6
GS4	50-100	1000-1500	0.06	3.46	11.71	0.994	7
GS5	100-300	250-425	0.59	11.58	6.98	1	2
GS6	100-300	425-710	0.35	10.42	7.23	0.993	4
GS7	100-300	1000-1500	0.16	18.61	9.31	0.996	4
GS8	600-1000	1000-1500	0.64	33.55	5.18	0.976	3

Figure 5.7 shows the relationship between permeability and porosity for these 8 groups. The permeability increases exponentially with porosity for LCS porous copper samples with different porosity, pore size and copper particle size:

$$K = a\varepsilon^n \quad \text{or} \quad \log K = n\log\varepsilon + \log a \tag{5.7}$$

where *a* and *n* are fitting constants. The fitting parameters of the power law relationship between permeability and porosity are listed in Table 5.2.

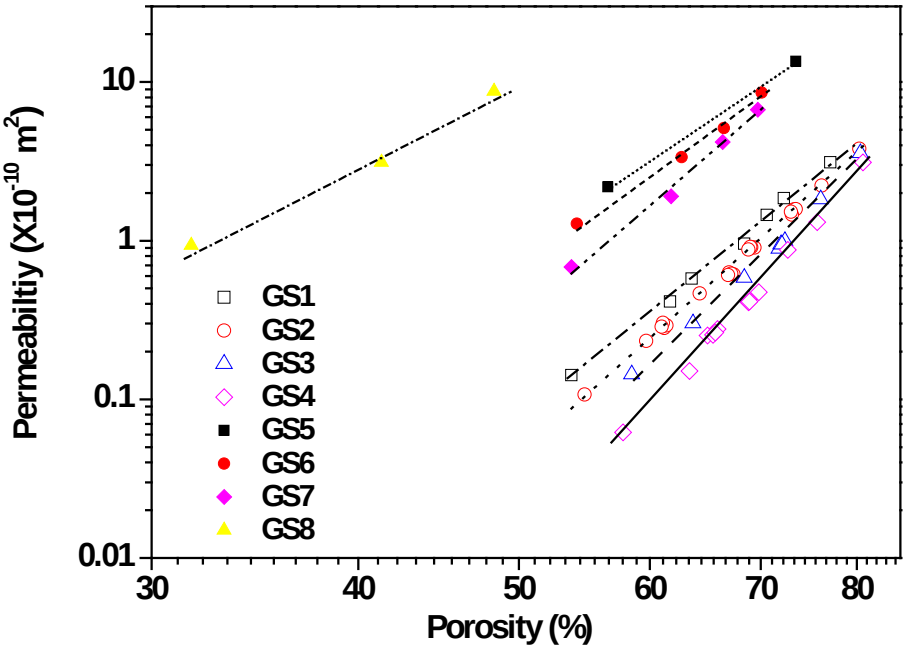

Figure 5.7 *Relationship between permeability and porosity for LCS porous copper samples in different groups in Table 5.2:* □ *GA1,* ○ *GA2,* △ *GA3,* ◇ *GA4,* ■ *GA5,* ● *GA6,* ◆ *GA7 and* ▲ *GS8.*

An interesting finding is that the exponent *n* is inversely proportional to particle/pore size ratio *s*. At a given particle size, the exponent *n* increases with the pore size, which means that the permeability of the porous copper sample with a large pore size is more

sensitive to porosity than that with a small pore size. At a given pore size, the exponent *n* decreases with copper particle size, which means that the permeability of the porous copper sample made with large copper particles is less sensitive to porosity than that made with fine copper particles.

The permeability of LCS porous copper samples with different pore parameters can be explained qualitatively by the connectivity of the pores. Low porosity means that the pores produced by the potassium carbonate particles are interlinked by few large windows and more small interstices between the copper particles, leading to a less permeable porous sample. As the porosity increases, the chances of one pore being connected to another will increase exponentially (Thewsey 2008), resulting in an exponential increase in permeability.

With small pore size, the path for fluid flow in porous samples would be less tortuous. The pore size effect on permeability is more obvious at low porosity than at high porosity (shown in Figure 5.7). As discussed previously, there are two kinds of channels to connect pores created by the potassium carbonate particles in LCS porous metals: micropores between copper particles and pore windows created between potassium carbonate particles in contact. At low porosity, there are fewer pore windows. Changing the size of potassium carbonate particles (pore size) can have a more significant influence on the permeability.

As shown in Figure 5.7, the copper particle size has a huge influence on the permeability of LCS porous copper samples. Samples produced with larger copper particles are more permeable. This is especially true for samples made with 600-1000μm copper particles. This is attributed to its effect on tortuosity. As tortuosity decreases with increasing size ratio, samples made with large particles will be less tortuous, and therefore have high permeability.

The effect of anisotropy on permeability is insignificant. Thewsey (2008) compared the LCS porous copper samples with spherical and irregular shaped pores at a similar porosity and found that pore shape had no significant effect on the permeability. In the present study, only spherical potassium carbonate particles were used and they were deformed slightly during the compacting process (ellipse shaped with the axial ratio of approximately 3:2). This slight change in pore shape does not have a significant effect on the path of fluid flow, resulting in a constant permeability at any given porosity and pore size.

The gas and water permeability are close to each other in the present study. Sometimes the gas permeability can be somewhat different from the water permeability in the same sample, as the permeability is affected by a molecular phenomenon known as gas slippage (Klinkenberg 1941, Carman 1956). The slippage of gas at the interface with the solid, however, will only affect the permeability value when the gas mean free path

is comparable to the pore size at a range of 0.01-0.1 μm (Klinkenberg 1941). Bloomfield and Williams (1995) investigated the air permeability and water permeability experimentally and obtained a logarithmic relationship between them. They observed that there was little difference between air and water permeability when the material's permeability was larger than 2.4×10^{-12} m^2. In the present study, the pore sizes are larger than 250 μm, and all the porous sample have permeability values larger than 4×10^{-12} m^2. In these conditions, the permeability of porous copper would not change much regardless of the fluid (air or water) used.

5.3.3 Theoretical prediction of permeability

There is no universal relationship between effective porosity and permeability. The few existing empirical, semi-empirical, and special geometric-model-based correlations listed in Section 2.3.3 have to be used within the restrictions for which they have been developed. These models may not suitable for the prediction of permeability of LCS porous copper.

Assuming a fully developed flow in a porous medium with a porosity of ε and a number of straight tubes of diameter *d*, the pressure gradient (∇p) can be found from the integration of the one-dimensional Navier-Stokes equation, which results in the Hagen-Poiseuille equation (Carman 1956, Dullien 1979, Kaviany 1995),

$$\nabla p = -\frac{32\mu}{d^2} v_p = -\frac{32\mu}{\varepsilon d^2} v_d \tag{5.8}$$

where v_p is the average pore velocity and v_d is Darcian velocity.

For porous media with pores of random shapes and sizes, the pressure gradient should be modified by introducing the shape factor (k_0), tortuosity (τ) and characteristic length (D_c) according to (Kozeny 1927, Carman 1956):

$$\nabla p = -\frac{16\mu k_0 \tau^2}{\varepsilon D_c^{\ 2}} v_d \tag{5.9}$$

Comparing Eq. (5.9) with Darcian equation (Eq. (2.2)), the permeability, K, can be expressed as:

$$K = \frac{\varepsilon D_c^{\ 2}}{16 k_0 \tau^2} \tag{5.10}$$

Eq. (5.10) is a form of the Carman-Kozeny equation. For random porous media, the pore parameters become very complex. Various attempts have been made to derive the characteristic diameter, D_c, as discussed in Section 2.3.2.2. The most widely used and accepted is the hydraulic diameter expressed in Eq. (5.1).

For porous media composed of spherical particles, it was widely accepted that the hydraulic diameter (D_h) is linked to the porosity and diameter of spheres (d_{part}) by:

$$D_h = \frac{2\varepsilon}{3(1-\varepsilon)} d_{part} \tag{5.11}$$

Eq. (5.11) was proved to be suitable to represent the characteristic length of a wide range of porous media (Ergun & Oming, 1949, Childs & Collis-George 1950, Ergun 1952, Carman 1956, Epstein 1989, Kaviany 1995, Khayargoli et al. 2004, Glover & Walker 2010).

For LCS porous metal, a modified Carman-Kozeny equation for permeability can be obtained by inserting Eq. (5.6) and Eq. (5.11) to Eq. (5.10):

$$K = \frac{\varepsilon^{3+\frac{1}{\sqrt{s}}} d_{part}^2}{36 k_0 (1-\varepsilon)^2} \tag{5.12}$$

where *s* is the size ratio between metal particle size and pore size.

Figure 5.8 compares the measured permeability of LCS porous metals and the calculated results from Eq. (5.12), with $k_0=2.5$, a common and universal value for porous media composed by granular spheres. The experimental data are in reasonably good agreement with the theoretical values. The slight mismatch may be attributed to the limitations of Eq. (5.12) when applied to LCS porous metals. Firstly, k_0 is assumed constant for the range of pore shapes. The effect of pore parameters on the shape factor, however, is still unknown. Secondly, the size ratio *s* is set as the ratio of the average particle size and pore size, regardless of the size distribution. In fact, particle size and pore size vary in wide ranges in LCS porous copper. Finally, the characteristic length is

assumed to be equivalent to the hydraulic diameter based on the simple model of packed bed in Eq. (5.11). The microstructure of LCS porous metal is different from a packed bed because of the introduction of large space holder particles. If the copper particles are heavily metallurgically bonded, the hydraulic diameter in Eq. (5.11) is not a correct characteristic length for permeability calculations, and hence Eq. (5.12) should be modified.

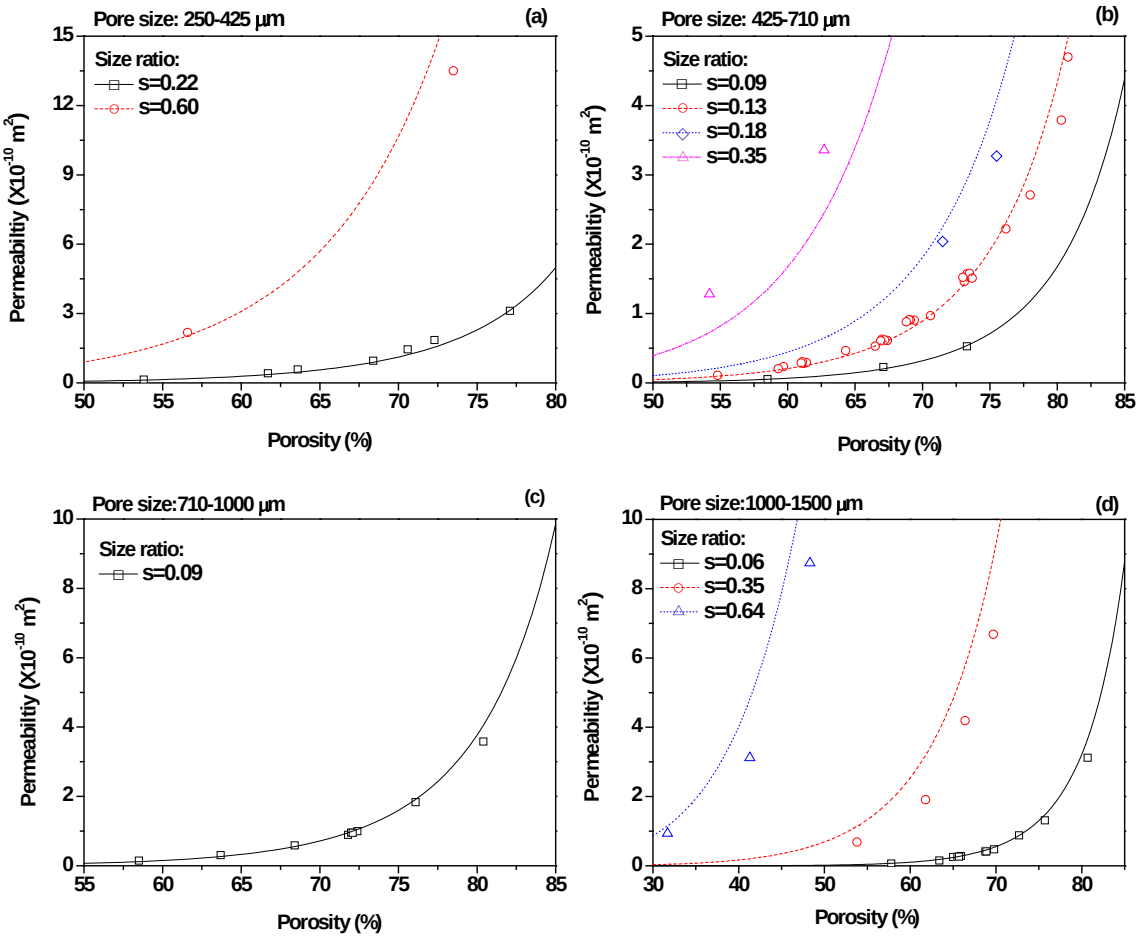

Figure 5.8 *Comparison of the experimental data and theoretic permeability (Symbols: experimental data; and lines: prediction of Eq. (5.12)).*

5.3.4 Theoretical prediction of permeability for samples with double-layer structures

According to Darcy's law, the pressure drop across a homogeneous porous medium for steady fluid flow can be described by Eq. (2.1). In porous medium with double layer structures, the fluid velocities in the high porosity layer (with porosity of ε_h) and low porosity layer (with porosity of ε_l) are different. According to Eq. (2.2), Darcian velocity is proportional to permeability. Assuming the permeabilities in the high and low layers are K_h and K_l and their thickness fractions are f_h and f_l (f_h+f_l=1), the Darcian velocities in the high (v_h) and low layers (v_l) are related by:

$$\frac{v_h}{v_l} = \frac{K_h}{K_l} \tag{5.13}$$

The overall Darcian velocity follows the rule of mixture, i.e.,

$$v = f_h v_h + f_l v_l \tag{5.14}$$

Combining Eqs. (5.12), (5.13) and (5.14), results in:

$$\frac{\varepsilon_{eff}^{3+1/\sqrt{s}}}{(1-\varepsilon_{eff})^2} = f_h \frac{\varepsilon_h^{3+1/\sqrt{s}}}{(1-\varepsilon_h)^2} + f_l \frac{\varepsilon_l^{3+1/\sqrt{s}}}{(1-\varepsilon_l)^2} \tag{5.15}$$

where ε_{eff} is the equivalent porosity of the double-layer porous metal.

The permeability of double-layer samples can be calculated by inserting Eq. (5.15) into Eq. (5.12):

$$K = \frac{d_{part}^2}{36k_0}\left[f_h \frac{\varepsilon_h^{3+1/\sqrt{s}}}{(1-\varepsilon_h)^2} + f_l \frac{\varepsilon_l^{3+1/\sqrt{s}}}{(1-\varepsilon_l)^2} \right] \tag{5.16}$$

Figure 5.9 shows the theoretical of relationship between ε_{eff}, ε_h and ε_l for LCS double-layer porous metals with a pore size of 425-710 μm under the condition of f_h=f_l=0.5. It can be seen that the equivalent porosity is close to the average porosity of the sample ($\frac{\varepsilon_h + \varepsilon_l}{2}$) when the high layer and lower layer have a similar porosity. For double-layer samples with a large porosity difference, the equivalent porosity is larger than the average porosity of the sample, indicating that the permeability would be higher than the single layer sample with a porosity of $\frac{\varepsilon_h + \varepsilon_l}{2}$.

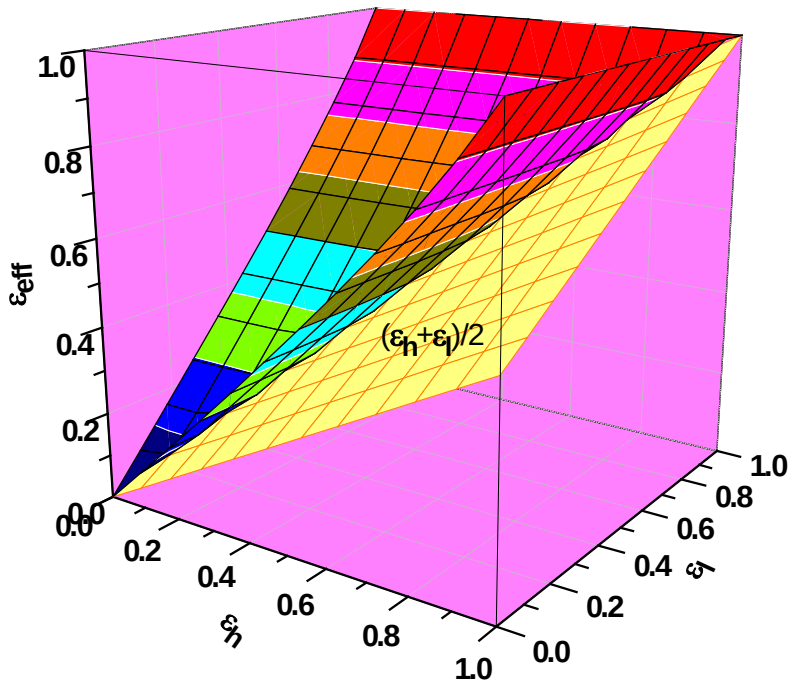

Figure 5.9 *Theoretical relationship between ε_{eff}, ε_h and ε_l for LCS double-layer porous metal (Pore size: 425-710 μm, f_h=f_l=0.5).*

Table 5.3 shows the calculated values of permeability of samples S50-S63 with a double-layer structure. The theoretical values are a litter higher comparing with the measured permeability, but the deviations calculated by Eq. (3.16) are lower than 10%.

Table 5.3 *Permeability of samples with double-layer structure*

Sample Reference	Pore Size (μm)	Nominal Porosity (%)	f_h	Porosity (%)	Measured Permeability ($10^{-10}m^2$)	Calculated Permeability ($10^{-10}m^2$)	Deviation (%)
S50	425-710	60	0	62.5	0.33	0.33	0
S51	425-710	80/60	0.2	65.9	0.56	0.54	1.3
S52	425-710	80/60	0.4	69.7	1.20	1.31	9.1
S53	425-710	80/60	0.6	73.6	1.86	2.02	7.9
S54	425-710	80/60	0.8	77.1	2.92	3.23	9.3
S55	425-710	80	1	80.5	3.85	3.85	0
S56	425-710	65/60	0.5	64.6	0.49	0.49	1.8
S57	425-710	70/60	0.5	67.1	0.68	0.73	6.5
S58	425-710	70/65	0.5	68.9	1.03	1.14	9.7
S59	1000-1500	65/60	0.5	64.9	0.27	0.27	2.2
S60	1000-1500	70/60	0.5	67.4	0.41	0.45	8.2
S61	1000-1500	70/65	0.5	69.2	0.59	0.64	6.9
S62	425-710/ 1000-1500	60/60	0.5	62.8	0.29	0.31	5.2
S63	425-710/ 1000-1500	65/60	0.5	64.4	0.43	0.45	4.9

5.4 Thermal Conductivity

The experimental apparatus shown in Section 3.4.2 was used to test the thermal conductivity of porous copper samples. The apparatus was calibrated with the standard solid metal samples and the experimental results in Table 3.1 showed that the apparatus had enough accuracy when the heat flux was less than 13kW/m^2. The increased errors above 13kW/m^2 were due to the limitations of the experimental apparatus used in the experiment. Firstly, the cross sectional area of the samples is relatively small, so it cannot bear large heat flux through it. Secondly, the thermal conductivity of the conductive grease used between the tested sample and the pure copper comparator is low, further limiting the heat conducted from the tested sample to the pure copper comparator.

As described in Section 2.4.1, there have been a few models to predict the thermal conductivity of porous media. Some are simple algebraic models, e.g., Calmidi and Mahajan Model (Calmidi & Mahajan 1999), Tetrakaidecahedron model (Boomsma & Poulikakos 2001) and symmetric and interconnected skeleton structure (SISS) model (Wang et al. 2008b). These models are based on a specific structure of porous media and cannot be applied widely. Many fundamental structural models, including the parallel, series, Maxwell-Eucken (ME) (Maxwell, 1954), effective media theory (EMT) (Laudauer, 1952) and co-continuous (CC) model (Wang et al. 2008a), have been established to predict the thermal conductivity of porous media. None of these, however,

can accurately predict the effective thermal conductivity across the full range of volume fraction. There are also some empirical models which modify these fundamental structural models in order to fit the experimental data.

A percolation theory based (PB) empirical correlation has shown that the relationship between the thermal conductivity and the relative density of the porous metal can be expressed by the power low (Phani et al. 1988, Ashby et al. 2000):

$$\lambda = \lambda_s (1-\varepsilon)^n = \lambda_s (\frac{\rho}{\rho_s})^n \tag{5.17}$$

where λ is the thermal conductivity of the porous metal, λ_s is the thermal conductivity of the bulk material (for pure copper, λ_s =391 W/mK), ρ is the density of the porous metal, ρ_s is the density of the bulk metal (for pure copper, ρ_s=8.9 g/cm^3) and n is the exponent for thermal conductivity.

As shown in Figure 4.11, for a given relative density, the thermal conductivities of the samples with pore sizes of 425-710μm, 710-1000μm and 1000-1500μm were very close. The predictions by the different models mentioned in Section 2.4 (including Parallel, Series, ME, EMT, SISS and percolation models with n=2) for a range of relative density are compared with the experimental data for samples T6-T25 with different porosity and pore size larger than 425 μm in Figure 5.10. It is obvious that the PB power law with an exponent n = 2 describes the experimental data well.

Some observations can be made from Section 4.3. For samples produced by fine copper particles (50-100 μm), the conductivity of porous copper with small pore size (250-425μm) is lower than that with large pore sizes. For samples made by different particle sizes, the conductivity of samples produced by large copper particles is much smaller than that of samples produced by fine copper particles.

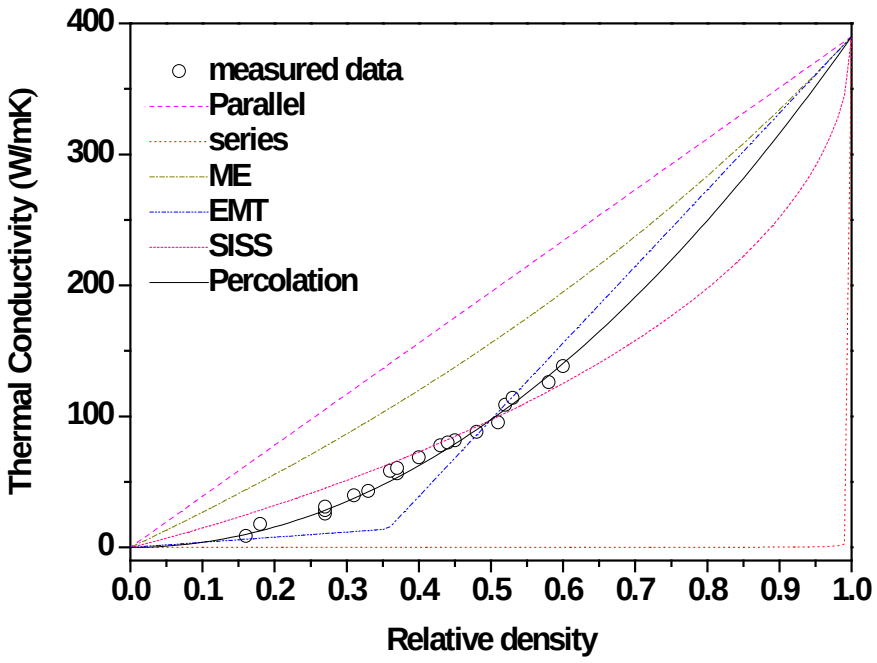

Figure 5.10 *Comparison between experimental data and predictions by different models (measured data for sample T6-T25).*

According to the experimental results of thermal conductivities shown in Table 4.11, the relative thermal conductivities for porous copper are plotted as a function of relative

density in Figure 5.11. Nearly all the measured data fall within the range bounded by the lines calculated using Eq. (5.17) with exponent (*n*) of 1.9 and 3.

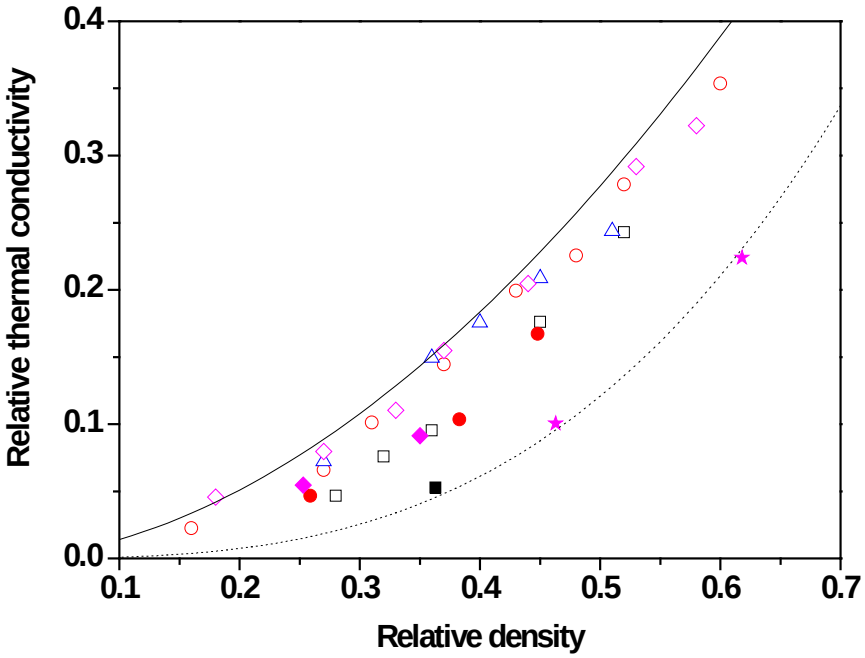

Figure 5.11 *Relative thermal conductivity of the LCS porous copper samples as a function of relative density, with different copper particle size /pore size combinations: (□50-100μm/250-425μm, ○50-100μm/425-710μm, △50-100μm/ 710-1000μm, ◇50-100μm/1000-1500μm, ■100-300μm/250-425μm, ●100-300μm/ 425-710μm, ◆ 100-300μm/1000-1500μm, ★ 600-1000μm/1000-1500μm; solid line: Eq. (5.17) with exponent of 1.9, dot line: Eq. (5.17) with exponent of 3).*

The thermal conductivity of LCS porous copper is not only influenced by relative density but also by copper particle size and pore size, especially when the copper particle size is close to the pore size. The effects of copper particle size and pore size on thermal conductivity stem from the specific structure of the LCS porous copper. According to the percolation theory, all copper particles should ideally cluster together to form one dense network, so that the heat could flow smoothly through the network.

This is not the case for LCS porous copper with randomly packed particles. Dead ends exist in the porous samples, i.e., some particle clusters or cell walls are discontinuous. These dead ends contribute to the mass of the network but do not carry heat flux. When the sizes of the copper particles and potassium carbonate particles are close to each other, the cell wall may be more discontinuous because copper particles cannot fit into the interstices of the potassium carbonate particle network, leading to the decrease of the probability for copper particles contacting each other. Small pores and large copper particles result in the increase of dead ends in LCS porous samples, and thus decrease their thermal conductivity and consequently increase the exponent in Eq. (5.17). In other words, the copper particle size/pore size ratio, *s*, also affects the thermal conductivity.

The fitting exponent and standard deviation values derived from the experimental data, as well as the particle/pore size ratio, for each group of samples are listed in Table 5.4. All the coefficients of determination (R^2) are larger than 0.98, which indicates that the PB power law is suitable to predict the thermal conductivity of LCS porous copper.

The relation between exponent (*n*) and size ratio (*s*) is shown in Figure 5.12. It can be seen that the exponent increases with the size ratio, and a nearly linear relationship between *s* and *n* is obtained from the data: $n=1.82s+1.81$. Combined with Eq. (5.17), an

approximate expression can be obtained for thermal conductivity of LCS porous copper:

$$\lambda = \lambda_s (1-\varepsilon)^{1.82s+1.81} \tag{5.18}$$

Table 5.4 *Fitting parameters of thermal conductivity*

Group	Particle Size(μm)	Pore Size(μm)	*s*	*n*	R^2
GT1	50-100	250-425	0.22	2.26	0.994
GT2	50-100	425-710	0.13	2.01	0.996
GT3	50-100	710-1000	0.09	1.97	0.987
GT4	50-100	1000-1500	0.06	1.94	0.991
GT5	100-300	250-425	0.60	2.91	1
GT6	100-300	710-1000	0.35	2.37	0.999
GT7	100-300	1000-1500	0.16	2.20	1
GT8	600-1000	1000-1500	0.64	3.04	1

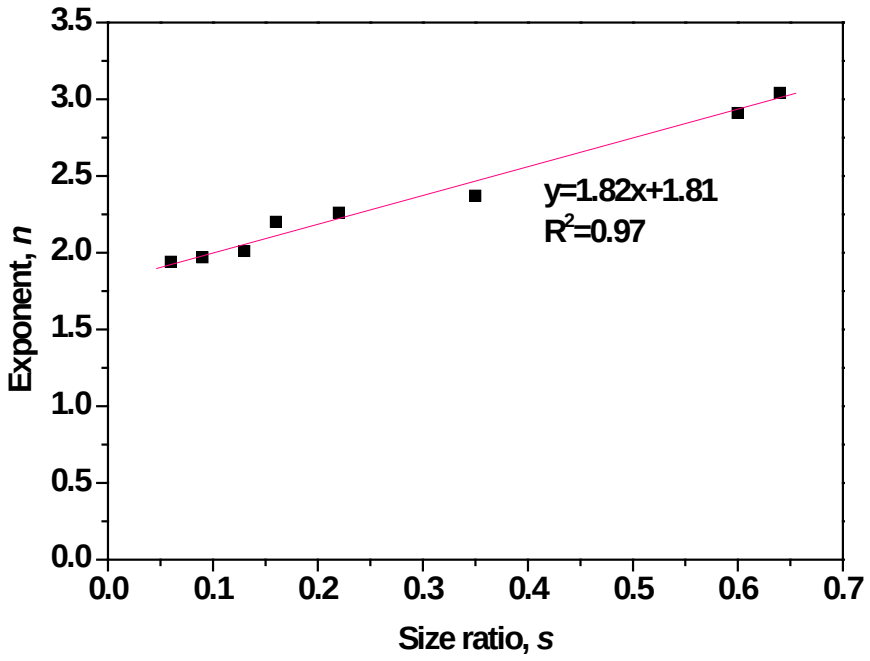

Figure 5.12 *Relationship between exponent and particle/pore size ratio of Eq. (5.18)*

5.5 Heat Transfer Coefficient

5.5.1 Measurement of heat transfer coefficient

The heat transfer coefficient of the porous copper samples was measured using the experimental apparatus and test procedure described in Section 3.5. The thermal equilibrium of the system was calculated by the method described as follows.

The heat flux in the copper block was calculated by Eq. (3.10), with the expression of:

$$Q_{in} = \lambda_{Cu} A \frac{T_{bl} - T_{pl}}{L} \tag{5.19}$$

where λ_{cu} is the heat conductivity of the copper block (λ_{Cu} =391 W/m·K for the oxygen free copper used in the test); A is the cross-sectional area of the heat block (A=5.985×10^{-4} m^2); T_{bl} and T_{pl} are the upper and lower block temperatures, respectively, and L is the distance between T_{bl} and T_{pl} (L=24.5 mm).

The heat removed by the coolant per unit time was calculated by the following equation:

$$Q_{out} = c_p \rho_f u (T_{out} - T_{in}) \tag{5.20}$$

where c_p is the specific heat of water (c_p=0.6 kJ/kgK), ρ_f is the density of water (ρ_f=1.0×10^3 Kg/m^3), and u is the volume flow rate of water.

Figure 5.13 shows a comparison between these two heat flux values for specimen cut from sample S11. Theoretically, ignoring the heat loss of the whole system, Q_{in} should be equal to Q_{out}. In practice, there is a difference between them because of heat losses and measurement errors, especially in T_{in} and T_{out}.

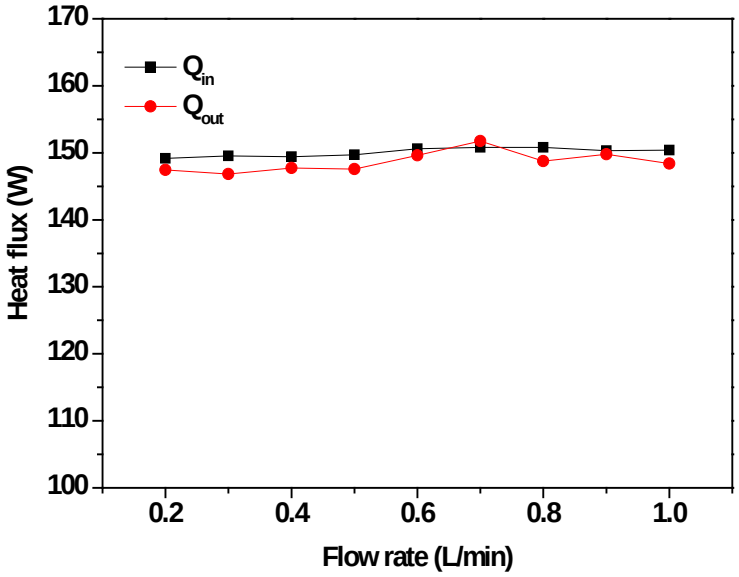

Figure 5.13 *Comparison of Q_{in} and Q_{out} at different flow rates for specimen S11*

In all measurements, Q_{out} was very close to but a little smaller than Q_{in}. One reason is the heat loss which was dissipated from the heat block, porous copper or coolant to the insulating PTFE block. This was not significant as the flowing water could remove the heat efficiently in the present study. Another reason is the inaccuracy of temperature measurements. According to Eq. (5.20), accurate readings of inlet and outlet coolant temperatures are crucial to the experimental determination of Q_{out}. The channel of the

testing apparatus is 5 mm high. During the heat transfer process, the heat flux in the region of the porous copper close to the heating plate is high, leading to high coolant temperature in this region. The region far away from the heating plate plays a less important role in removing heat, resulting in low coolant temperature in this region. In other words, the outlet temperature distribution across the flow channel is not uniform. The PT100 thermometer probe was located at the middle of the channel and the temperature was considered as representative to the average outlet temperatures of the coolant, which may bring about some errors. In all cases, however, the temperature difference (T_{bu}-T_{bl}) was found to be steady at any given input heat power (i.e. a given voltage of transformer), and was a constant for all porous samples at the same experimental condition. In addition, T_{in} was easy to control when the ambient temperature did not change. Eq. (5.19), which was used to calculate the heat flux, is therefore reliable for the calculations of the heat transfer coefficients of different porous samples.

5.5.2 Effect of pore parameter on heat transfer coefficient

Heat transfer from the heat source (heating block or heating plate in this case) to the coolant consists of three stages: heat transfer from the heating block to the porous copper, thermal conduction in the copper matrix of the porous copper sample and convection between the copper matrix and the coolant. The first stage can be well controlled if the surface of the sample is smooth and has a good contact with the heat

plate. Thermal conduction in the copper matrix is determined by the thermal conductivity of the porous sample. The pore parameters affecting the last stage are mainly permeability of the porous sample and the interfacial surface area between the porous sample and the coolant.

5.5.2.1 Effect of porosity

Figures 4.12 and 4.13 showed how the heat transfer coefficient changed with the porosity, at a fixed pore size. In each group of samples made with small copper particles, the heat transfer coefficient first increased until reaching the highest value at a certain porosity and then gradually decreased (as shown in Figure 4.12). This trend was consistent over all coolant flow rates. For a limited number of samples made with large copper particles, the heat transfer coefficient just decreased with porosity. The heat transfer performance of the empty chamber (100% porosity) was very poor even under high flow rates, due to the small contact area between the heating plate and the coolant.

The surface area, permeability and thermal conduction of porous copper samples are three key parameters which affect the heat transfer performance. The results in Chapter 4 showed that the surface area and permeability increase with porosity, while the thermal conductivity decreases with porosity. The effect of porosity on heat transfer coefficient can be analyzed by the combined effect of the internal surface area and the permeability of the porous sample.

The overall heat transfer performance depends not only on the thermal conduction in the copper matrix but also on the heat removal to the fluid. The optimum porosity can be achieved by balancing these two processes.

At very low porosity, even if the thermal conductivity of porous copper samples is superior, the internal surface area and the fluid permeability of the sample are low, both of which lead to poor heat removal of fluid. Low porosity is conducive to better thermal conduction from the heat source to the porous copper, but bad for convectional heat transfer from the porous copper to the coolant. In this situation, thermal convection by the coolant is the limiting factor, so that the permeability is critical at low porosity.

High porosity has the opposite effect. The samples with high porosity are more permeable, with permeability increasing exponentially with porosity. The specific surface area also increases with porosity. The samples with high porosity, however, have lower thermal conductivity than those with low porosity. The limiting factor for samples with high porosity is thermal conduction in the copper matrix.

It should be pointed out that even though the samples with low porosity are less permeable and have lower surface area than those with high porosity, the heat transfer performance is still at a relatively high level. Therefore, it can be speculated that the

influence of thermal conductivity plays a very important role in heat transfer process of LCS porous copper. The optimum porosity of LCS porous copper (Figure 4.12) or porous nickel (Figure 4.31) made by small particles was found to be between 60% and 66%.

5.5.2.2 Effect of pore size

Figures 4.14 and 4.15 showed the effect of pore size on heat transfer coefficients of porous copper samples at a given flow rate. For porous copper made with small copper particles, the samples with the medium pore size ranges of 425-710 μm and 710-1000 μm had heat transfer coefficients 1.5 times of those with the small pore size range. The heat transfer performance of the samples with large pore sizes was moderate. For porous copper made with large copper particles, the heat transfer performance of samples with larger pore size was better.

The effect of pore size on the heat transfer coefficient is due to its effects on the thermal conductivity, surface area and fluid permeability. For the same porosity, samples with smaller pores have higher specific surface areas and permeability, but their thermal conductivities are poor. Therefore, the thermal conductivity plays a much more important role in heat transfer for the LCS porous samples with the fine pore size of 250-425 μm.

For sample with the largest pores, its thermal conductivity is similar to those with medium pores, but it is less permeable, leading to a slightly worse heat transfer performance. For the test samples with copper particle sizes of 100-300 μm and 600-1000 μm, the heat transfer coefficient was also found to increase with the pore size (as shown in Figure 4.15).

5.5.2.3 Effect of copper particle size

The copper particle size has a significant influence on heat transfer coefficient. Figures 4.16 and 4.17 compared the heat transfer coefficients of porous copper made by copper powders with different particle sizes. At a given pore size, increasing the copper particle size decreased the heat transfer coefficient, when the porosity was higher than 65%. This may be attributed to the decrease of thermal conductivity of porous copper sample with increasing particle size (see Section 4.3). At low porosity, however, the samples made with large copper particles had higher heat transfer coefficients, as shown in Figures 4.16 and 4.17. According to the permeability test, samples made with large copper particles are more permeable. Furthermore, the thermal conductivity of porous copper increases with decreasing porosity. Both would enhance the heat transfer ability. Although the samples made with fine copper particles at low porosity have better thermal conductivity than those made with large copper particles, their permeability is extremely low, which may be the key reason for the decrease of heat transfer coefficient.

5.5.2.4 Effect of flow rate

The experimental results in Sections 4.4.4, 4.4.5, 4.4.6 and 4.4.8 showed that the heat transfer coefficient increases linearly with flow rate. For a sample with a given porosity and pore size, convection is enhanced as the flow rate increases, because heat is removed by the coolant more rapidly. Besides, increasing the flow rate may cause turbulence within the porous medium. This extra turbulence will cause the coolant to mix and access more of the small interstices within the structure, giving rise to more heat exchange between the solid copper surfaces and the coolant.

Based on the experimental data in Section 4.4, the heat transfer coefficient (h) as a function of Darcian velocity (v_d) can be expressed by:

$$h = a v_d^n \tag{5.21}$$

where a and n are constants. The values of a, n and the coefficients of determination, R^2, corresponding to the samples are given in Tables 5.5 and 5.6. The exponent, n, has a value between 0.45 and 0.65, while the constant, a, has a value between 3000 and 11000.

Table 5.5 *Fitting parameters of Eq. (5.21) of samples for heat transfer coefficient (single layer samples)*

Sample Reference	*a (×100)*	*n*	R^2	Sample Reference	*a (×100)*	*n*	R^2
S1	61.3	0.529	0.998	S28	50.5	0.529	0.992
S2	67.1	0.498	0.993	S29	36.6	0.525	0.992
S3	65.2	0.542	0.997	**S37**	66.8	0.547	0.995
S4	54.9	0.550	0.996	**S38**	29.8	0.512	0.992
S5	32.9	0.501	0.992	**S39**	75.6	0.537	0.999
S6	33.8	0.525	0.991	**S40**	70.2	0.600	0.999
S7	32.1	0.547	0.993	**S41**	52.2	0.567	0.995
S8	70.6	0.539	0.987	**S42**	43.7	0.588	0.984
S9	85.6	0.578	0.99	**S43**	103.0	0.568	0.996
S10	88.5	0.527	0.992	**S44**	82.5	0.538	0.999
S11	89.6	0.542	0.993	**S45**	62.1	0.515	0.993
S12	80.6	0.538	0.993	**S46**	43.8	0.513	0.992
S13	69.0	0.500	0.987	**S47**	107.0	0.532	0.998
S14	64.9	0.522	0.983	**S48**	50.9	0.536	0.992
S15	52.6	0.506	0.986	**S49**	46.6	0.565	0.995
S16	50.3	0.53	0.983	**S50**	87.9	0.512	0.991
S17	71.1	0.526	0.994	**S64**	65.9	0.607	0.996
S18	88.7	0.554	0.988	**S65**	53.4	0.562	0.992
S19	80.2	0.542	0.99	**S66**	87.1	0.644	0.999
S20	66.9	0.538	0.987	**S67**	84.4	0.639	0.999
S21	52.1	0.519	0.996	**S68**	80.0	0.643	0.996
S22	47.1	0.543	0.996	**S69**	57.9	0.601	0.988
S23	63.0	0.538	0.995	**S70**	51.8	0.600	0.997
S24	70.5	0.527	0.98	**S71**	44.1	0.556	0.997
S25	76.1	0.528	0.984	**S72**	54.1	0.564	0.981
S26	64.2	0.488	0.993	**S73**	56.2	0.588	0.996
S27	57.6	0.499	0.983	**S74**	63.5	0.617	0.995

Table 5.6 *Fitting parameters of Eq. (5.21) of samples for heat transfer coefficient (double-layer samples)*

Sample Reference	Order	*a (×100)*	*n*	R^2
S51	Normal	108.0	0.608	0.996
	Reverse	50.2	0.500	0.997
S52	Normal	67.0	0.545	0.982
	Reverse	37.9	0.487	0.993
S53	Normal	43.3	0.469	0.981
	Reverse	36.6	0.481	0.985
S54	Normal	42.9	0.482	0.982
	Reverse	37.8	0.494	0.996
S56	Normal	94.7	0.546	0.995
	Reverse	68.2	0.475	0.98
S57	Normal	77.9	0.520	0.991
	Reverse	57.0	0.565	0.995
S58	Normal	77.5	0.545	0.996
	Reverse	67.8	0.609	0.996
S59	Normal	79.1	0.524	0.988
	Reverse	59.9	0.513	0.997
S60	Normal	67.5	0.482	0.996
	Reverse	50.6	0.483	0.993
S61	Normal	75.2	0.551	0.993
	Reverse	64.7	0.607	0.996
S62	Normal	94.9	0.556	0.997
	Reverse	86.9	0.555	0.998
S63	Normal	101.0	0.574	0.995
	Reverse	94.9	0.556	0.997

5.5.2.5 Effect of heat flux

Figure 4.19 showed the effect of input heat flux on the heat transfer coefficient. Three different input heat flux values (150 kW/m^2, 250 kW/m^2 and 500 kW/m^2) were applied by adjusting the voltage of the transformer. The input heat flux has little effect on heat transfer coefficient. An increase in input heat power (Q) resulted in increased block temperature (T_{bl}). With both Q and T_{bl} being directly related by Eq. (3.11), the convective heat transfer coefficient is expected to remain the same at any given input heat power.

The porous copper-water system can remove heat efficiently under the input heat flux conditions in the test. In the present study, the maximum heat flux, which is fixed at 500 kW/m^2 due to the limitation of the apparatus, can be removed efficiently by the porous copper-water system. Zhang et al. (2009) reported that the LCS porous copper with a diameter of 10 mm and a thickness of 4 mm can remove the heat at a rate of 1.3MW/m^2. It shows that the LCS porous copper can be an ideal candidate material for heat exchanger application.

5.5.2.6 Effect of anisotropy

The results in Section 4.4.6 showed that the anisotropy in LCS porous copper resulted from the fabrication process did not affect the heat transfer performance. Firstly, the porous copper samples with anisotropy have similar permeability values according to

the experimental results in Section 4.2.2. Secondly, the anisotropy is not significant, so the thermal conductivity should not change very much. Thirdly, the specific surface area would not be affected by anisotropy. All these factors lead to similar heat transfer coefficient measured at different directions.

5.5.3 Effect of double-layer structure

Figures 4.21 to 4.23 showed the variations of heat transfer coefficient with porosity for double-layer porous copper samples with different placement orders. As seen from Figure 4.21, the variation of heat transfer coefficient of double-layer LCS porous copper was similar to that of single-layer LCS porous copper. A peak value was found at the combined porosity of 62.5% or 65.5% (when the thickness of the 80% porosity layer was 1 mm or 2 mm). The heat transfer coefficient was much lower and very little when the combined porosity was 73.6% or higher, where the thickness of 80% layer was 3 mm or more. Sample S51 with 80%/60% placement showed the best heat transfer performance among all the tested samples. The other samples with double-layer structure had worse heat transfer performance than that of their single-layer counterparts with a similar overall porosity.

When the heat plate is in direct contact with the high porosity layer, such as the samples with 80%/60% placement, increasing the thickness of the high porosity layer is not an

efficient way to improve the thermal conduction from the heat source to the porous copper. The experiment results showed that a rapid decrease of heat transfer coefficient occurred when the thickness of 80%-layer exceeded 2 mm in the test.

The effect of double-layer on the heat transfer performance can be understood by analyzing the thermal conductivity, the internal surface area and the permeability of the porous sample. Porous copper with a high porosity (such as porosity of 80%) has a low thermal conductivity, which will reduce the conductive heat transfer from the heat plate (Thewsey & Zhao 2008, Zhang et al. 2009), however, high porosity provides a high internal surface area and a high fluid permeability, which enhance the heat removal from the porous copper to the fluid flow. The samples with 1mm 80%-layer achieved the balance of these two factors according to the experiment.

It should be noted that the heat transfer coefficient of the double-layer LCS porous copper with 60% layer in contact with the heat plate (60%/80% placement) has a very low heat transfer coefficient, even lower than that of the single-layer porous copper with a nominal porosity of 80% (see in Figure 4.27).

Heat coming from the heat block flows through the water-saturated porous copper and is removed by the water. Therefore, the layer close to the heat plate plays a dominant role in the heat transfer of the double-layer LCS porous copper. According to Ho &

Webb (2006), the fluid often preferentially chooses the strata with higher permeabilities. As a result, a large amount of the displaced fluid can be left behind in the strata with low permeability. This may be the main reason that the 80%/60% placement is much efficient to remove heat than the 60%/80% placement.

For the fluid flow through the double-layer porous copper samples at a given overall flow rate, the flow rate in the high porosity layer is much greater than that in the low porosity layer. As the flow rate has significant effect on heat transfer coefficient (Zhang et al. 2009), increasing flow rate would enhance the heat transfer performance significantly. Although the 80% porosity layer has a dominant effect on heat transfer for both 80%/60% and 60%/80% placements, there are still some differences. In the former situation, most water flows through the region close to the heat plate, which will enhance the heat transfer performance. In the latter situation, little water flows through the region close to the heat plate; the 60% porosity layer here may enhance heat conduction but does not favour convection. Although the flow rate in the 80% layer is high, its contribution to heat transfer is low, because it is farther away from the heat plate and the local temperature of the copper matrix is low. Nevertheless, it is worth to be mentioned that when the high porosity layer is thin (sample S51 with 1 mm in the test), the overall heat transfer coefficient was optimal compared with the single-layer porous samples with a similar porosity, because it allows high flow rate near the heat plate while maintaining a moderate overall thermal conductivity.

5.5.4 Effect of thickness on heat transfer coefficient

The effect of sample thickness on heat transfer coefficient of LCS porous copper was studied by testing seventeen samples. The samples, with different porosity, pore size and copper particle size, were the same as those used in permeability and heat transfer coefficient tests. The original thickness of each sample was 5 mm, and 1 mm was cut from the sample each time for next test.

The experimental results (Figures 4.29 and 4.30) showed that at a constant Darcian velocity, the heat transfer coefficient increased with thickness and then remained constant with the thickness increasing from 3 mm to 5 mm. At a given Darcian velocity, a thick porous metal sample means more capability as the cross section area increases. Further increasing thickness may not improve the heat transfer, as the solid of the porous metal far away from the heat surface does not contribute to the heat removal but decreases the Darcian velocity at a given flow rate. Therefore, when the thickness exceeds a critical value, the heat transfer coefficient may decrease with thickness of sample. In the present study, it was found that this critical value of thickness was between 3 mm to 5 mm for LCS porous copper with a contacting surface of 600 mm^2.

Shih et al. (2008) investigated the effect of sample size on heat transfer characteristics of aluminium foam. Cylinder samples (with a diameter of *D* and a thickness of *t*) were used in the test. A dimensionless height, *t /D* was introduced to characterise the effect of height on heat transfer performance. It was found that the aluminium foam with dimensionless height between 0.23 and 0.31 had the best heat transfer performance. In the present study, all the tested samples had dimensions of 30 mm$\times$20 mm$\times$5 mm. The surface area in contact with the heat plate is about 600 mm^2. It is difficult to compare the size effect between the data in the present study and data from Shih et al (2006) because of the different shapes of contact surfaces.

A dimensionless area can be defined as the ratio of heat dissipating surface and heating surface, which is similar to *t/D* in Shih's experiment. In the present study, the dimensionless areas for samples with different thicknesses of 5 mm, 4 mm, 3 mm, 2 mm and 1 mm are 0.33, 0.28, 0.20, 0.13 and 0.07, respectively. The LCS porous copper with dimensionless area between 0.20 and 0.33 had the best heat transfer performance. The results are consistent with those reported by Shih et al. (2006).

5.5.5 Heat transfer coefficient of different porous metals

The variation of heat transfer coefficient with porosity at different flow rates for porous nickel was shown in Figure 4.31. The trend is similar to that found in porous copper, i.e., heat transfer coefficient decreased with the porosity and there was a maximum value at

porosity between 60% and 65%. The reasons behind the trend have been discussed in the previous sections.

The heat transfer coefficient of LCS porous copper, porous nickel, porous nickel-copper and porous iron with similar porosity and pore size were compared in Figure 4.32. Porous copper has the best heat transfer performance among these four porous metals, while the other three porous metals have similar heat transfer performance. It is easy to understand the results as copper has much better conductivity than the others. The thermal conductivity of pure iron (80 W/mK) is a slightly lower than that of pure nickel (90.5 W/mK), however, a relatively low porosity of porous iron caused it to have a similar heat transfer coefficient with porous nickel (see Figure 4.32). The porous nickel-copper alloy has a much lower thermal conductivity (44 W/mK), but it had the same heat transfer performance as the porous nickel and porous iron samples. This may be attributed to the much finer particle size of nickel-copper alloy, which results in much larger effective surface area.

5.5.6 Correlation of dimensionless parameters

In solving the heat transfer problem in porous media, three important dimensionless parameters, Prandtl number (*Pr*), Reynolds number (*Re*) and Nusselt number (*Nu*), are used:

$$Pr = \frac{c_p \mu}{\lambda_f} \tag{5.22}$$

$$\mathrm{Re} = \frac{\rho v_d D_h}{\mu} \tag{5.23}$$

$$Nu = \frac{h D_h}{\lambda_f} \tag{5.24}$$

where c_p, μ, ρ and λ_f are the specific heat, viscosity, density and thermal conductivity of the fluid, and D_h is the hydraulic diameter. *Pr* is approximately equal to 7 for water at 20°C.

Nusselt number is generally a function of the Reynolds number and the Prandtl number, i.e., *Nu=f(Re, Pr)*, in the form of (Incropera et al 2013):

$$Nu = a\,\mathrm{Re}^n\,\mathrm{Pr}^{1/3} \tag{5.25}$$

where *a* and *n* are constants which are often independent of the nature of fluid.

For LCS porous samples, the following expression can be obtained by combining Eqs. (5.21), (5.23) and (5.24):

$$Nu = \frac{\mu^n D_h^n}{\lambda_f \rho_f^n}\mathrm{Re}^n \tag{5.26}$$

This expression is similar to Eq. (5.25). The value of the exponent *n* varies with the nature of the surface geometry and the pore parameters of porous metal.

Figure 5.14 shows the correlation between Nusselt number and Reynolds number for experimental data for the LCS porous copper samples. The results indicate a power law dependence of the Nusselt number on the Reynolds number with the following correlation:

$$Nu = 0.963\,\mathrm{Re}^{0.537} \quad (R^2 = 0.881) \tag{5.27}$$

This empirical expression may be used to characterise the heat transfer performance of LCS porous copper.

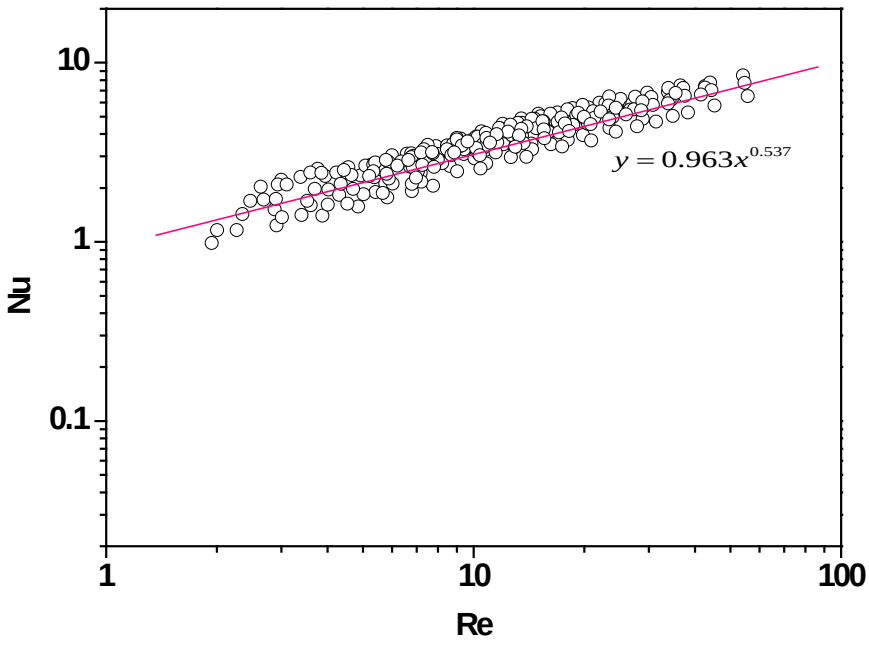

Figure 5.14 *Correlation between Nusselt number and Reynolds number*

5.6 Theoretical Analysis of Heat Transfer of LCS Porous Copper

5.6.1 Heat transfer effectiveness along the thickness for homogeneous structure

Consider a energy generating plane wall and a medium with a constant cross section and constant thermal conductivity, λ, in Figure 5.15, and a uniform heat flux (q). According to one-dimensional Fourier's law, the heat equation in this situation is:

$$q = \lambda \frac{dT}{dx} \tag{5.28}$$

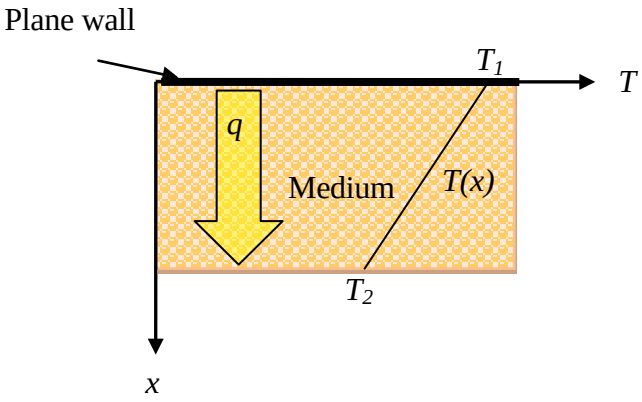

Figure 5.15 System with conduction

The heat flux, q, is the heat transfer rate in the x direction per unit area perpendicular to the direction of heat transfer. The above equation shows that the temperature and heat distribution depend on the thermal conductivity of the strut at a given heat flux. For an open channel without porous medium, λ is the thermal conductivity of water. Adding porous metal with a higher thermal conductivity than water in the channel would significantly decrease the temperature gradient (dT/dx). The added porous metal can also be seen as an extended surface. The heat transfer in the experiment involves conduction in a fluid-saturated porous metal and convection from the internal surfaces

of the porous metal. Consider a system composed of a plane wall generating a constant heat flux (q) and a medium (porous metal), a cross section which there is a fluid flow (water with input temperature of T_{in}), as shown in Figure 5.16. In steady state, temperature gradients in the x-direction sustains heat conduction in the strut. With $T_1 > T_2 > T_{in}$, however, there is concurrent heat transfer by convection to the fluid, causing q_x, and hence the magnitude of the temperature gradient, dT/dx, to decrease with increasing x.

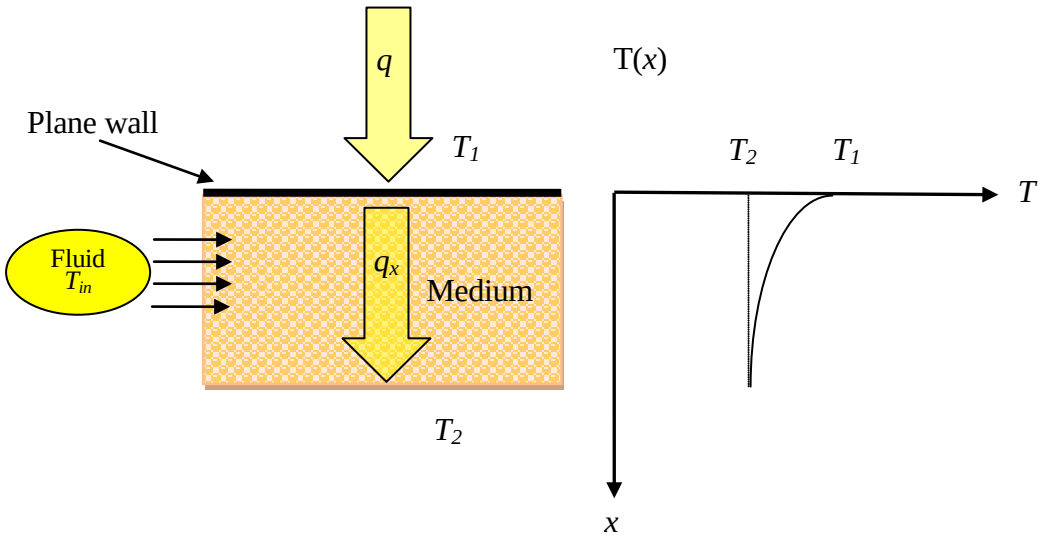

Figure 5.16 System with convection

Considering the convection to remove heat from the plate at a given temperature of T_1, there are two ways to increase the heat transfer rate. One is to increase the convection coefficient by increasing the fluid velocity, and the other is to increase the surface area across which the convection occurs. The thermal conductivity of the porous medium

has a strong effect on the temperature distribution along the porous medium and therefore influences the degree to which the heat transfer rate is enhanced. Ideally, the porous medium should have a large thermal conductivity to minimise temperature variation from the upper surface to the bottom surface. In the extreme case of infinite thermal conductivity, the entire porous medium would be at the temperature of the plate, T_1, thereby providing the maximum possible heat transfer enhancement.

As a first order approximation, the porous copper attached to a hot plate with forced fluid flow can be regarded as a one-dimensional conduction-convection problem. Assuming that the increase in the temperature of the cooling fluid within the porous media is negligible, the porous media can be simulated as an infinite fin of uniform cross-sectional area. Adapting the approach detailed in ref. Incropera et al (2013), the governing equation for temperature distribution in the porous media can be expressed as:

$$\frac{d^2T}{dx^2} - m^2(T - T_f) = 0 \tag{5.29}$$

where T is the temperature of the porous medium at distance x from the heating plate-medium interface, T_f is the temperature of the cooling fluid, and m is a constant depending on the local convective heat transfer coefficient, the effective thermal conductivity of the porous medium and the specific surface area of the porous medium.

The solution of the above equation is:

$$\frac{T - T_f}{\Delta T} = e^{-mx} \tag{5.30}$$

$$J = mA\lambda\Delta T \tag{5.31}$$

where ΔT is the temperature difference between the hot plate at the plate-medium interface and the cooling fluid (*i.e.* $T_{pl} - T_f$), A is the cross-sectional area of the porous medium, and λ is the effective thermal conductivity of the porous medium, and J is the total heat transfer rate of the porous medium, which is equal to the heat input rate from the hot plate to the porous medium.

From Fourier's law, the conductive heat flow rate in the porous medium at x can be obtained by,

$$J_{cond} = -\lambda A\frac{dT}{dx} = Je^{-mx} \tag{5.32}$$

The above equation shows that the conductive heat flow rate decreases exponentially with distance x, with the steepness of the decline being affected by the parameter m. Therefore, the accumulative convective heat transfer rate up to x within the porous media with a thickness t is therefore:

$$J_{conv} = J - J_{cond} = J(1 - e^{-mx}) \tag{5.33}$$

For this model to be valid as an approximation for a porous medium with a finite thickness t, the conductive heat transfer flow rate at $x = t$ should be sufficiently small.

As a first order approximation, we can assume that the conductive heat flow rate is reduced to 2% of the total heat flow rate at t, i.e. 98% of the heat has been removed by the convective heat transfer into the coolant. This assumption leads to $m \approx 4/t$. The accumulative convective heat transfer rate up to x within the porous medium with a thickness t is therefore:

$$J_{conv} = J - J_{cond} = J(1 - e^{-\frac{4x}{t}}) \tag{5.34}$$

5.6.2 Segment model for heat transfer coefficient of double layer LCS porous copper

Again, to simplify the description of the place order of double layer porous copper samples, the layer with high porosity or high permeability is termed as the high layer, with the symbol of H, and the other layer with low porosity or low permeability is termed as the low layer, with symbol of L. H/L means that the H layer is in contact with the heat plate, while L/H means that the L layer is in contact with the heat plate.

5.6.2.1 Flow partition

As we discussed in Section 5.3.4, the Darcian velocity in double layer porous copper can be expressed by Eqs. (5.13) and (5.14). A scale factor, j, can be introduced to solve Eqs. (5.13) and (5.14):

$$j_h = \frac{v_h}{v} = \frac{K_h}{f_h K_h + f_l K_l} \tag{5.35a}$$

$$j_l = \frac{v_l}{v} = \frac{K_l}{f_h K_h + f_l K_l} \tag{5.35b}$$

where j_h and j_l are the scale factors for high and low layers, K_h and K_l are their permeability (defined in Eq. (5.13)), and f_h and f_l are their thickness fractions (defined in Eq. (5.14)), respectively.

Finally, the flow flux distributed in each layer can be defined by partition factor (p):

$$p_h = \frac{q_h}{q} = \frac{f_h v_h}{v} = f_h j_h \tag{5.36a}$$

$$p_l = \frac{q_l}{q} = \frac{f_l v_l}{v} = f_l j_l \tag{5.36b}$$

where p_h and p_l are partition factor of high layer and low layer, q_h *and* q_l are fluid flux through the high layer and low layer, respectively, and q is the total fluid flux.

Table 5.7 shows the thickness fractions, scale factors and partition factors of the high layer of LCS porous copper samples. It can be seen that even if the thickness of the 80% porosity layer (sample S51) is only 1 mm, over 70% of water chooses this layer to flow through. Increasing the thickness of 80% porosity layer, less water will flow through the low layer with low porosity, which is the main reason that the heat transfer coefficient decreases sharply for samples S51-S54. Only 2% water could flow through the low porosity layer for sample S54.

Table 5.7 *Scale factor and partition factors for samples with double layer structure*

Sample Reference	Pore Size(μm)	Porosity Combination	Thickness Ratio	f_h	j_h	j_l	p_h
S51	425-710	60%:80%	4:1	0.2	3.61	0.34	0.72
S52	425-710	60%:80%	3:2	0.4	2.19	0.21	0.88
S53	425-710	60%:80%	2:3	0.6	1.57	0.15	0.94
S54	425-710	60%:80%	1:4	0.8	1.22	0.11	0.98
S56	425-710	60%:65%	1:1	0.5	1.30	0.70	0.65
S57	425-710	60%:70%	1:1	0.5	1.71	0.29	0.86
S58	425-710	65%:70%	1:1	0.5	1.52	0.48	0.76
S59	1000-1500	60%:65%	1:1	0.5	1.36	0.65	0.68
S60	1000-1500	60%:70%	1:1	0.5	1.66	0.34	0.83
S61	1000-1500	65%:70%	1:1	0.5	1.40	0.60	0.70
S62	425&1000	60%:60%	1:1	0.5	1.25	0.75	0.63
S63	425&1000	60%:65%	1:1	0.5	1.06	0.94	0.53

5.6.2.2 Segment model

For simplicity, a porous copper sample with a double layer structure in the experiment can be divided into 10 layers, each of which has a thickness of 0.5 mm and a heat transfer coefficient of h_i (i represents the layer number and i=1,2,3,4,5,6,7,8,9,10). The convective contribution of a particular layer of the sample, from $x=x_1$ to $x=x_2$, to the overall heat transfer can be expressed by a weighting factor from Eq. (5.34):

$$w = \frac{J_{conv}^{x=x_2} - J_{conv}^{x=x_1}}{J} = e^{-\frac{4x_1}{t}} - e^{-\frac{4x_2}{t}} \tag{5.37}$$

The overall heat transfer coefficient, h, is the weighted average of the heat tranfer coefficients of the ten layers:

$$h = \sum_{i=1}^{10} w_i h_i \tag{5.38}$$

where h_i is the heat transfer coefficient for the i^{th} layer, and w_i is the weighting factor. Assuming that the thermal boundary layer is 5 mm and the efficiency of heat transfer decreases to zero at 5 mm, the weighting factors are determined by Eq. (5.37) as: 0.33, 0.22, 0.15, 0.10, 0.07, 0.04, 0.028, 0.02, 0.014 and 0.01, corresponding to layer 1 to 10. The weighting factor decreases with the distance away from the heating plate, representing that the layers far away from the heating plate have less contribution to remove heat. It can be seen that the first two layers play a dominant role in heat transfer performance of porous media, while the last four layers are only about 10% of the total weighting factor.

The heat transfer coefficients correlated with Darcian velocity by Eq. (5.21) were used for the values for the individual layers for porous copper samples with double layers. Typically, the heat transfer coefficients of sample S10, S12, S14, S24, S25 and S27 were used for calculation. The prediction curve of overall heat transfer coefficients using weighting factors are shown in Figure 5.17. It can be seen that the simple segment model can predict the most of the experimental results well, especially for porous copper samples with L/H placement.

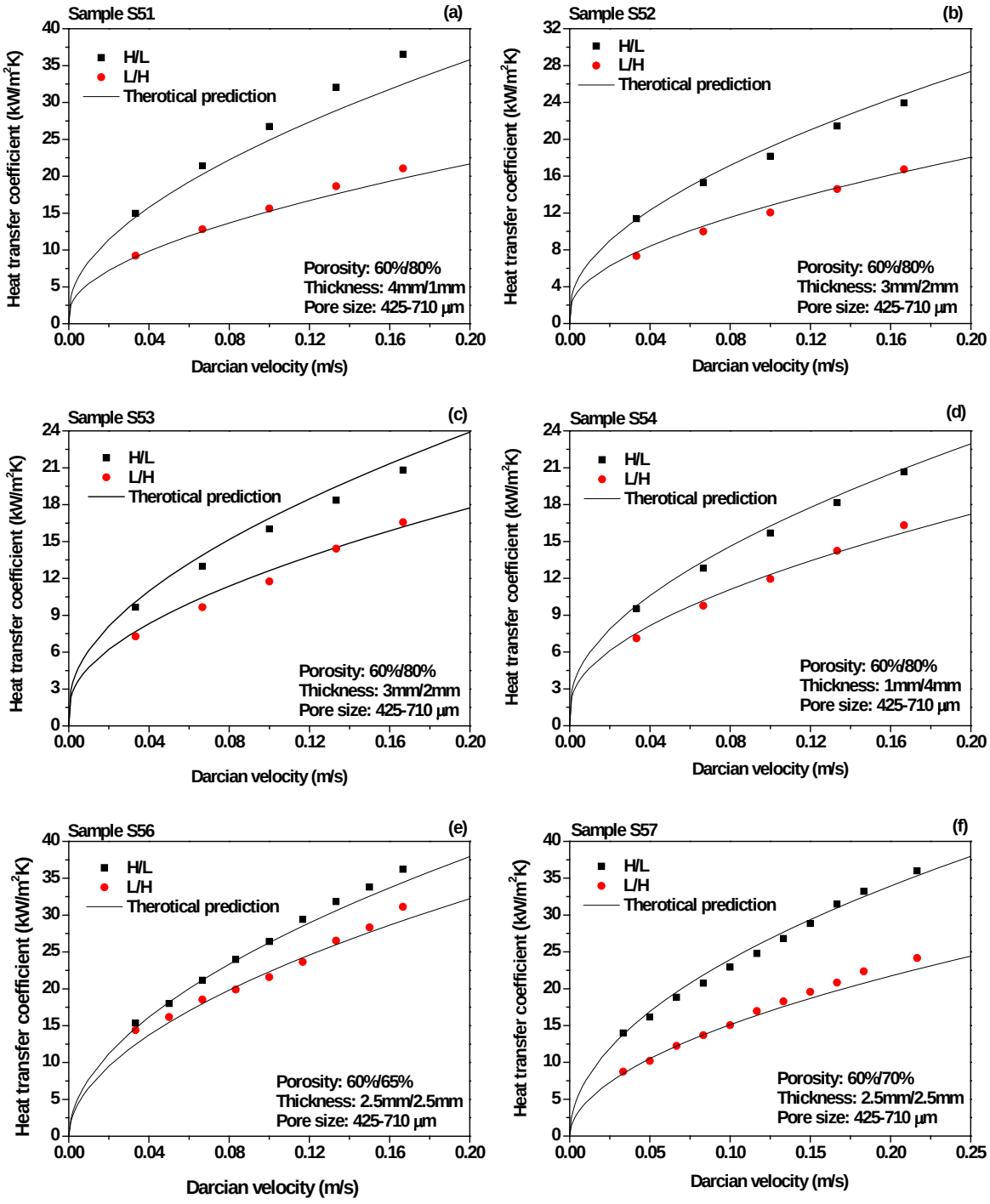

Figure 5.17 *Comparison between the measured values of heat transfer coefficients and the predictions by the segment model for porous copper samples with double layers. (a) S51, (b) S52, (c) S53, (d) S54, (e) S56, (f) S57, (g) S58, (h) S59, (i) S60, (j) S61, (k) S62, (l) S63. (C**ontinued)***

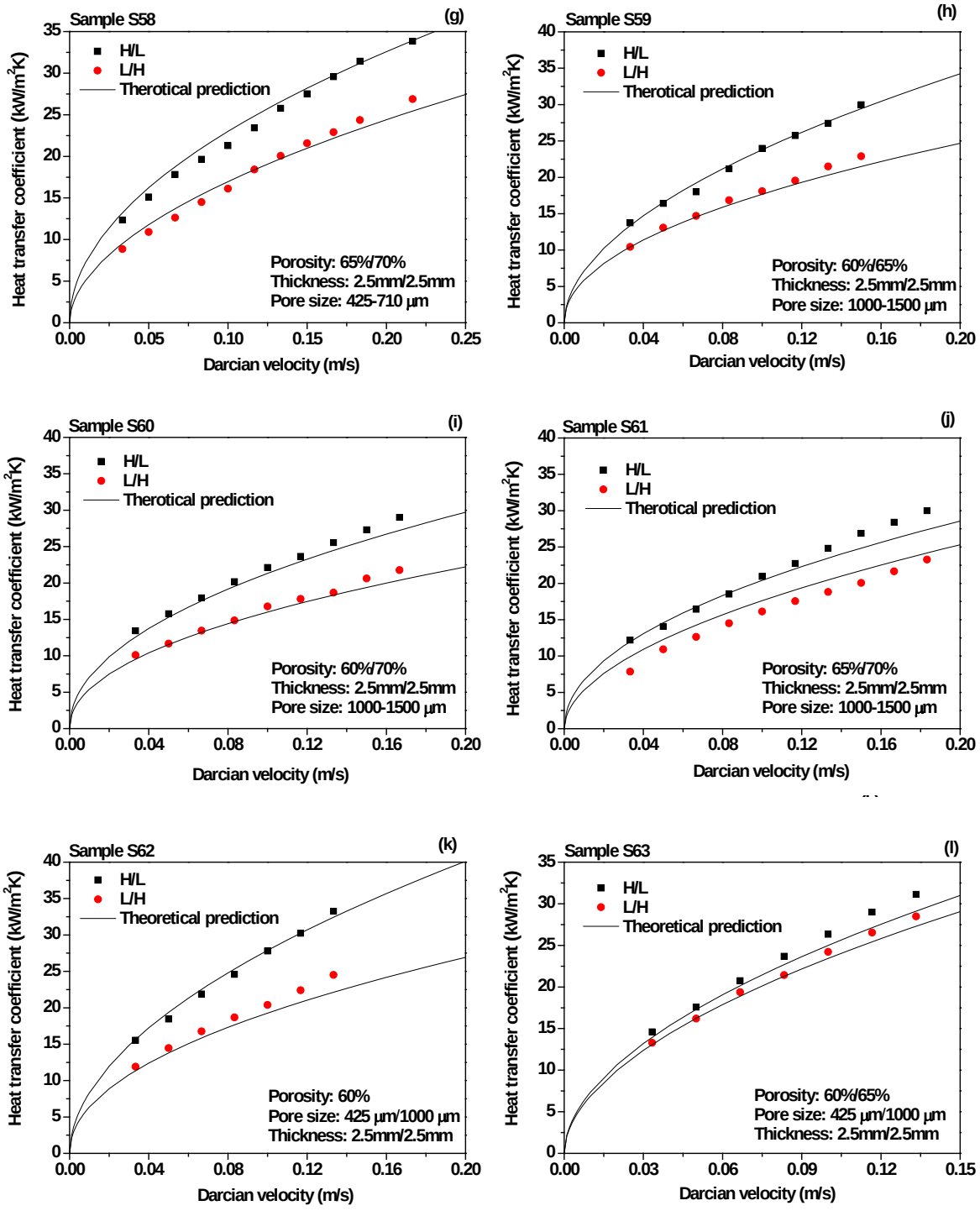

Figure 5.17 *Comparison between the measured values of heat transfer coefficients and the predictions by the segment model for porous copper samples with double layers. (a) S51, (b) S52, (c) S53, (d) S54, (e) S56, (f) S57, (g) S58, (h) S59, (i) S60, (j) S61, (k) S62, (l) S63.*

5.7 Mechanical Properties

As shown in Section 4.5, the mechanical behaviour of LCS porous copper, including bending, tensile and compression response, was affected by the porosity, pore size and anisotropy.

5.7.1 Compression response

The compressive curves of the LCS porous copper samples have similar shapes to those of Al foams reported by Zhao & Sun (2001) (Figure 5.18). Normally, the compression process of porous materials can be divided into three stages: linear-elasticity, plateau and densification. The experimental results in Section 4.5.1 showed that there was no obvious plateau for the porous samples with low porosity. For LCS porous samples with porosity higher than 65%, however, all the three stages were clearly observed. This may be attributed to the different degrees of effect of porosity on the deformation. For porous copper samples with low porosity, the quantity of pores was small so they had limited effect on the compression curve. The curve is more determined by the solid matrix. For porous copper samples with high porosity, a large number of pores existed in porous samples, so the deformation of pores plays a more important role, leading to a visible plateau.

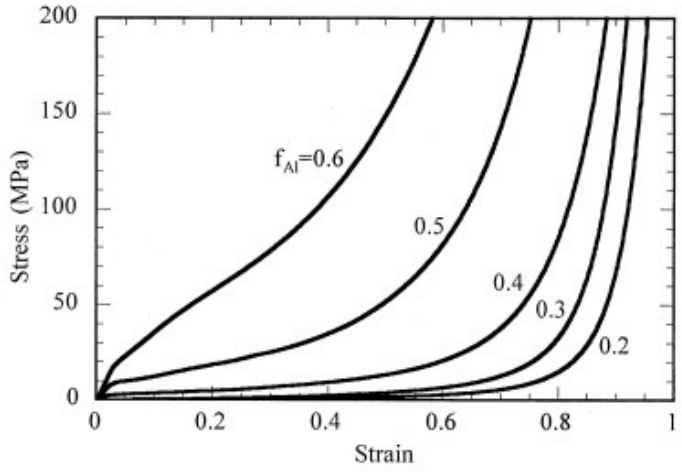

Figure 5.18 *Compressive stress-strain curves of Al foams with different Al mass fractions (Zhao & Sun 2001)*

The effect of pore size on compression behavior was given in Section 4.5.1.2. Increasing the pore size may increase the compression properties. For samples with pore size larger than 425 μm, however, the pore size effect on the compression properties is very small. The change in the compression properties of the porous copper samples was not considered owing to the change in pore size itself but the change in the amount of sintering defects characteristic of the LCS process (Tao et al. 2007). The mechanical properties of the porous metal depend on the integrity of its cell walls, which in turn depends on the particle size ratio between the metal and potassium carbonate powders. In LCS, the potassium carbonate particles should be larger than the metal particles. The metal particles firstly need to fill the interstices between the potassium carbonate particles. For smaller potassium particles, the interstices between them are small and it is difficult for the metal particles to fill in completely. In the

narrow parts of the network of interstices, the metal particles may be disconnected with each other and the cell walls of the resultant porous metal are weak. Increasing the size of potassium carbonate particles can lead to stronger cell walls of the resultant porous metal. When the size of potassium carbonate particles is big enough compared with the metal particles, this effect may be less important and the strength of porous metal depends strongly on the porosity but not pore size. The results are in accordance with those reported by Zhang & Wang (2005), who produced porous copper using copper powders with different particle sizes (5 μm and 45 μm) and space holder particles of 600 μm, and found that there was no difference in their mechanical properties at a given porosity.

It was found from Section 4.5.1.3 that anisotropy in LCS porous copper samples affected the compression behaviour. Two types of compression curves were found by compressing the porous copper samples from different directions (Figure 4.38). Comparing the compression curves of samples compressed at different directions showed that the yield stress in the normal direction was higher than that in the parallel direction, and the densification in the normal direction started at a greater strain than that in parallel direction. This may be attributed to two different deformation forms during compression.

As seen from Figure 4.1, most of the pores in the LCS porous copper are elliptical. Figure 5.19 illustrates the ellipse pore arrangement related to the compression direction and the deformation of pores during compression process.

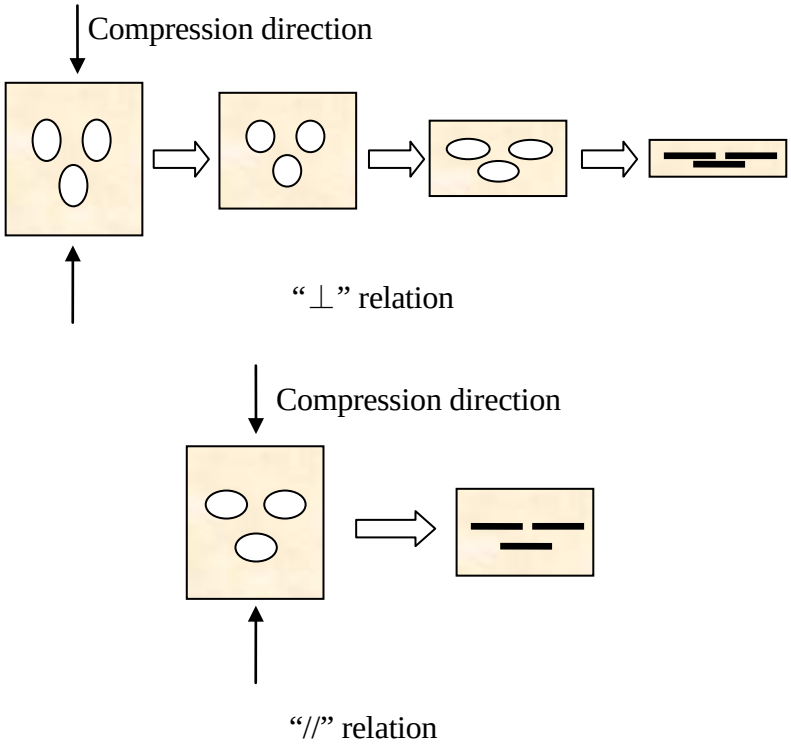

Figure 5.19 *Illustration of the ellipse shape of pores and their deformation during compression*

Assuming that the spherical potassium carbonate particles distribute uniformly in the mixture during mixing with copper particles, the cell walls between the potassium carbonate particles are the same everywhere. During compacting, the potassium carbonate particles start to deform and the cell walls on the cross section of compression become thinner. The traces of these thin cell walls can be found in Figure 4.1b. During the compression test, the effective cross section area (solid area on the

cross Section in porous copper) of the samples with "//" relation will be less than those with "⊥" relation. This difference may result in higher stress for samples compressed at the "⊥" direction at the earlier stage of the compression process.

When applying a pressure from different directions, the deformation of the pores would be different. For samples with "//" relation, the pores are firstly compressed to round shape and then flattened to ellipse shape. For samples with "⊥" relation, this first step does not exist. This difference causes the densification of samples compressed at the "//" direction starting earlier than those compressed at the "⊥" direction.

Gong et al. (2010) studied the compression deformation behaviour of a cellular CuAlMn alloy at two directions. The results are shown in Figure 5.20. A typical plastic collapse regime with a long, flat or wave-like horizontal plateau in the stress-strain curve was found, which indicated that plastic yielding of cell wall occurred. The abruption did not occur in LCS porous copper samples, with the compression curves being smooth in the whole compression process. This may be because: 1) copper was much more ductile than the CuAlMn alloy, which is a little brittle at room temperature; 2) the sphericity of the pores in the LCS porous copper samples is higher than that in the CuAlMn porous metal samples.

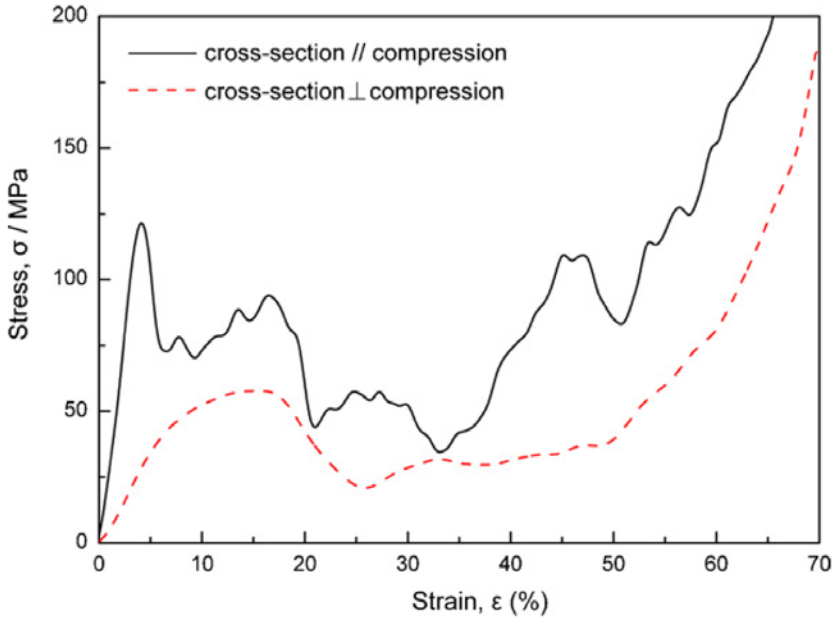

Figure 5.20 *Compressive stress-strain curves of cellular CuAlMn alloy with compression directions parallel and perpendicular to the cross-section. (Gong et al. 2010)*

5.7.2 Bending response

The variations of apparent modulus and flexural strength with porosity for porous copper samples with different pore sizes are shown in Figure 4.41. The apparent modulus was calculated by Eq. (3.14) based on the linear region of the load-displacement curve. It should be pointed out that this region of the curve was neither exactly linear nor elastic. As mentioned above, pores were easy to deform and some plastic deformation already took place in this region. The apparent modulus, flexural strength and bending energy absorption all decreased exponentially with *(1-ε)*. These were consistent with the behaviour of the conventional metal foam, where the relationship between the relative elastic modulus and relative density followed the power law (Gibson & Ashby 1988).

Elastic deformation of LCS porous copper specimen was not very discernable, especially for the samples with large porosity, as a large number of pores inside the porous medium can deform at the earlier stage of bending. The point at which the sample was broken is distinct. It was found that the amount of deformation of the porous copper sample before fracture was not very large. For most of the tested samples with the thickness of 10 mm, the fracture displacement during bending was no more than 2 mm. This may be attributed to the weaker cell walls of porous copper and sintering necks than the matrix.

The experimental data in Figures 4.39 and 4.41 showed the effect of porosity on the bending behaviour of LCS porous copper samples. The flexural strength decreased with the porosity, because the amount of metal in the component was reduced. A small load could result in deformation of the porous copper sample with a large porosity. In addition, the cell walls in the porous copper samples with large porosity were thinner and thus much easier to be fractured.

Figures 4.40 and 4.41 showed the effect of pore size on the bending properties of LCS porous copper samples. The porous samples with small pore sizes were found to be much weaker than those with large pore sizes. In LCS, the metal particles should be significantly smaller than the potassium carbonate particles in order to fill in the

interstices between the potassium carbonate particles. For larger potassium carbonate particles, the interstices between them were larger and therefore easier to be filled. The sintering of these particles would lead to stronger cell walls of the resultant porous metal. For fine potassium carbonate particles, however, the interstices between them were smaller and it was more difficult for them to be filled completely. In the narrow parts of the network of interstices, the metal particles may be disconnected from each other. As a consequence, the cell walls of the resultant porous metal had more defects and became weaker, leading to low flexural strength. It was found that the flexural strength of porous copper with pore size greater than 425 μm had little difference. A pore size of 425-710 μm is large enough for the copper particles with size of 50-100 μm to fill the interstices completely. As a general rule, when the size ratio (*s*) defined in Section 5.3 is smaller than 0.13, the pore size effect on bending behaviour is small.

5.7.3 Tensile response

Figures 4.43 to 4.44 show the tensile stress-strain behavior of porous copper specimens. The curves are similar to these of the other metallic foams, e.g., the tensile stress-strain curves of Alulight foams in Figure 5.21. The slope of the stress-strain curve before general yielding is less than the elastic modulus, implying considerable micro-plasticity even at very small strains. Beyond yielding, the porous copper hardens up to the ultimate tensile strength, subsequently followed by failure of specimen.

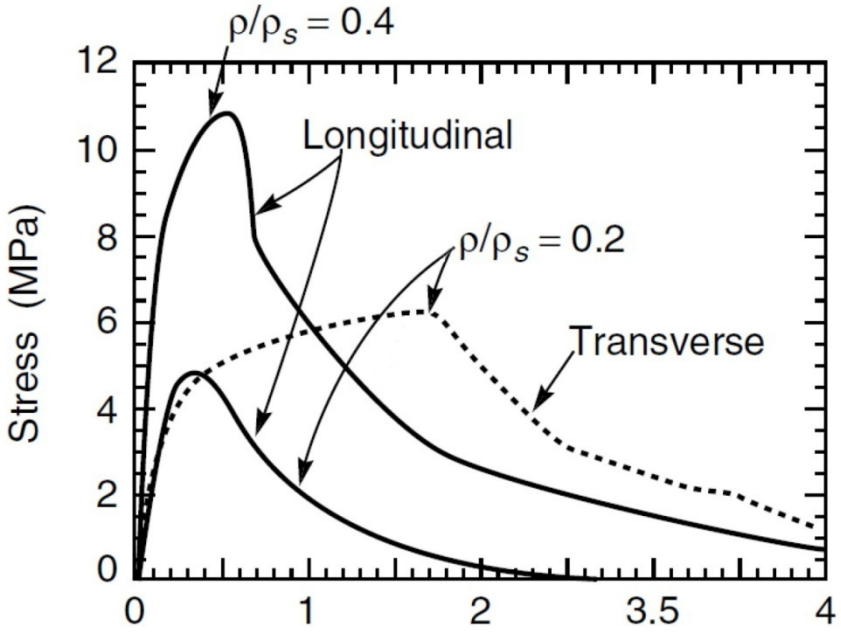

Figure 5.21 *Tensile stress-strain curves of Alulight foams (Ashby 2000)*

Figure 5.22 shows the effects of relative density on the elastic modulus or ultimate tensile strength of LCS porous samples. The ultimate tensile strength and elastic modulus increased exponentially with the relative density. The reasons for these results are the same as for the bending results.

Kovácik (1998) investigated the tensile behaviour of porous metals made by the GASAR process and found that the percolation power-law dependence of the tensile properties on porosity was observed. A power law relationship between ultimate tensile strength and relative density, in accordance with the percolation theory, was also found in the present study.

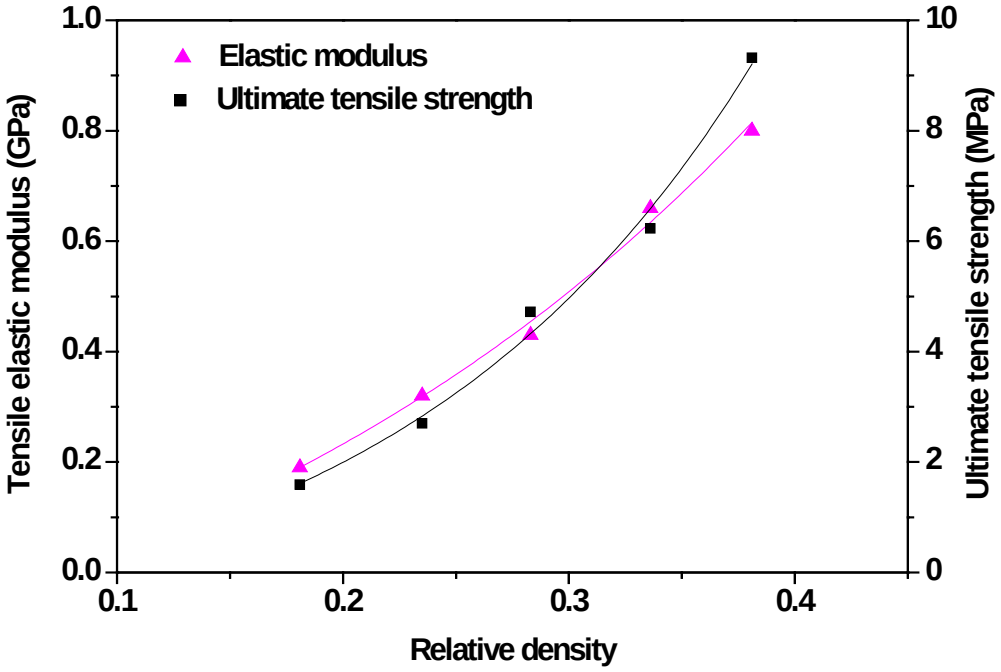

Figure 5.22 *Effects of relative density on tensile response of LCS porous copper samples (Testing direction:'//').*

5.7.4 Correlation between mechanical properties

The most common tests used to determine a material's mechanical properties are the compression and tension tests, both of which are simple to carry out. The sample being tested usually gets longer during tension, and shorten during compression. Bulk materials during compressing can withstand much larger stresses than those under tension, as it is more difficult for atoms to be forced together on an atomic level (Roylance 2008). The difference between compression strength and tensile strength, however, is often smaller (Joshus 2013). In porous media, the tensile strength is often smaller than the compressive strength and bending flexural strength. Chen et al (2013)

reported that the ultimate tensile strength of cement mortar with porosity of 25% was only 3/5 of its bending flexural strength, and 1/10 of its compressive strength.

Porous copper is a ductile metals, where ultimate compression strength cannot be measured as ductile metals can bear large plastic deformation. The compressive yield strength was measured for comparison. The LCS porous copper with a porosity range between 60-85% has a yield strength (compression) between 1.5-20 MPa, a flexural strength (bending) between 3-30 MPa, and a ultimate tensile strength between 1-10 MPa. This shows that the LCS porous copper also has a lower tensile strength compared to the bending flexural strength and compressive yield strength.

Odler and Robler (1985) suggested that the ratio of compressive strength and split tensile strength is porosity dependent for porous media. They found a linear relation between compressive/tensile strength ratio and porosity when the porosity was lower than 50%. The compression yield strength (σ_c), bending flexural strength (σ_b) and ultimate tensile strength (σ_t) of LCS porous copper tested at the // direction, according to experimental data in Tables 4.14, 4.15 and 4.17, can be expressed by power law relationship with porosity (ε):

$$\sigma_c = 606.2(1-\varepsilon)^{3.85} \quad (R^2 = 0.991,\ 0.6 \le \varepsilon \le 0.85) \tag{5.39a}$$

$$\sigma_b = 352.6(1-\varepsilon)^{2.65} \quad (R^2 = 0.995,\ 0.6 \le \varepsilon \le 0.85) \tag{5.39b}$$

$$\sigma_t = 97.4(1-\varepsilon)^{2.45} \quad (R^2 = 0.993,\ 0.6 \le \varepsilon \le 0.85) \tag{5.39c}$$

From Eq. (5.39), new expressions for the ratio between compression yield strength, bending flexural strength and ultimate tensile strength can be written as a function of porosity as:

$$\frac{\sigma_c}{\sigma_b}=1.72(1-\varepsilon)^{1.2} \quad (0.6\leq\varepsilon\leq0.85) \tag{5.40c}$$

$$\frac{\sigma_c}{\sigma_t}=6.22(1-\varepsilon)^{1.4} \quad (0.6\leq\varepsilon\leq0.85) \tag{5.40c}$$

Both ratio decreases with increasing porosity, indicating that the mechanical properties become more uniform at high porosity. The mechanical properties of porous metals determine the range of usefulness of porous material in service. The compression yield strength and bending flexural strength of LCS porous copper are 1.5-3 times of its ultimate tensile strength, giving a conclusion that the LCS porous copper is much suitable for a compression or bending strut.

5.7.5 Elastic modulus prediction

5.7.5.1 Elastic modulus of solid materials

During the last decades, progress in predicting the elastic properties of porous materials over an entire porosity range has been closely related to the power-law empirical relationship of Kovácik & Simancík (1999):

$$E = E_s(1-\frac{\varepsilon}{\varepsilon_{crit}})^n \tag{5.41}$$

where E_s and E are the elastic modulus of the solid material and the porous material with porosity ε, respectively, ε_{crit} is the porosity at which the effective elastic modulus of the porous material becomes zero, and n is a parameter dependent on the grain morphology and pore geometry of the porous material. There has been a large amount of literature where the experimental data were fitted to Eq. (5.41) and giving ε_{crit}=1.

It was found that Eq. (5.41) could not predict the elastic modulus of LCS porous copper. Given E_{Cu}=115 GPa for bulk copper, the best fitting parameter, n, is as large as 9.275 with a large deviation of 54.2%. In addition, Eq. (5.41) does not consider the anisotropy of LCS porous copper generated by pore shape change during the compressive test. Similar results were also found in porous copper produced by another space holder method, where there existed a large difference between the calculated and the measured moduli (Wen et al. 2002, Zhang & Wang 2005). The main difference may come from the discrepancy of microstructure of the samples produced by power metallurgy method and conventional casting method, owing to the large difference of elastic modulus of the solid materials.

In order to obtain a realistic modulus for the solid matrix, a standard copper sample was produced by powder metallurgy without potassium carbonate to obtain the density and elastic modulus of the near-solid bulk copper. The production procedures were the same with those to make porous copper samples. Although expecting to produce a “solid”

sample with as low a porosity as possible, the sintered solid sample was still had a density of 8.56 g/cm^2 (porosity: 96.2%). It was obvious that complete densification is hard to achieve using the powder metallurgy method. There was still 3.8% micro-porosity inside the copper matrix under the fabrication condition in the experiment. This result is in accordance with the fact that the actual porosity of the LCS porous copper samples is often a little higher than its nominal porosity.

The elastic modulus (compression), apparent modulus (bending), and elastic modulus (tensile) and of the standard sample were measured as 4.35GPa, 5.96 GPa , and 5.07 GPa, respectively. The three moduli were much smaller than that of bulk copper (115 GPa). In LCS porous copper, the mechanical properties depends significantly on the bonding strength between copper particles, which is weaker than that of the grain boundaries in cast copper. Therefore, the elastic and plastic deformation behaviour of materials produced by powder metallurgy is different from those made by conventional casting method (Ren 1998).

5.7.5.2 Numerical model

The Mori-Tanaka (MT) model is one of the best known analytical approaches to determine the effective material constants of composite materials (Mori & Tanaka 1973). So far, it has been widely used to predict the physical and mechanical properties of materials, by using Eshelby's equivalent inclusion theory to calculate the Eshelby

tensors and applying the homogenization technique to determine the properties of the composite materials. This model, however, is only suitable for composites with low volume fractions of inclusions, and the microstructure is assumed to be homogeneous, ignoring the effects of size and number of inclusions. EI-Hadek & Kaytbay (2008) compared the experimental results of elastic modulus of LCS porous copper with Mori-Tanaka predictions and it showed that the MT model overestimated the values of elastic modulus of LCS porous copper.

Several improved models were developed to address these limitations. Recently, Gong et al. (2011) proposed a stepped equivalent substitution approach to extend MT model and developed a semi-infinite domain mechanics model to determine the Eshelby's tensors of the surface regions. Their model can predict the properties of the porous metal with anisotropy made by space holder method well. The model is described as follows:

By considering a composite material containing pores as an Eshelby's inhomogeneous inclusion, the stiffness matrix of which is zero, according to the Mori-Tanaka model, the constitutive equation can be solved and the equivalent stiff matrix, L^e, can be obtained as follows:

$$\boldsymbol{L^e = L^m (I + CN)^{-1}} \tag{5.42}$$

where L^e is the equivalent stiff matrix for porous metal, L^m is the stiff matrix of the

solid, I is a fourth rank identity tensor, C is the volume fraction of the pores, and N is a variable related to the Esheby tensor, S, with $A = \left\{ L^m - L^m \left[CI + (1-C)S \right] \right\}^{-1} L^m$.

The effect of pore number was considered in the extended MT model. Pores are divided into n groups according to the shape, volume, orientation and position. The solid matrix with the first group of pores is converted into an equivalent medium by the MT model, which has the stiffness matrix of L^1. The equivalent medium is then taken as a new matrix and combined with the second group of pores to form a new porous medium with the stiffness matrix L^2. By repeating this process until all groups of pores are taken into account for calculation, the final stiffness matrix, L^n could be taken as the effective stiffness matrix of the porous medium. The pore shape effect was considered by using the Eshelby's tensor for spheroid inclusion (shown in Appendix C).

The volume fraction of pores of the ith group of pores can be obtained by:

$$C_i = \frac{C/n}{1 - C + (i \times C/n)} \tag{5.43}$$

where n is the group number and C is the volume fraction of all pores in the initial matrix.

Numerical calculations for the stiffness matrix of a porous material containing pores using the SES approach were carried out using the MATLAB software. The stiffness matrix of the first equivalent medium was obtained using the stiffness matrix of the

initial matrix, $L^m=\lambda^m\delta_{ij}\delta_{kl}+\mu^m\delta_{ik}\delta_{jl}+\mu^m\delta_{il}\delta_{jk}$ and substituting Eqs. (5.43) and (C1) (in Appendix C) into Eq. (5.42). λ^m and μ^m are Lamé constants of the initial matrix, and δ_{ij} is the Kronecker delta. The equivalent flexibility matrix is therefore:

$$M^e=(L^e)^{-1} \tag{5.44}$$

For transversely isotropic materials M^e can be written as:

$$\begin{bmatrix} M_{11}^e & M_{12}^e & M_{13}^e & 0 & 0 & 0 \\ M_{12}^e & M_{11}^e & M_{13}^e & 0 & 0 & 0 \\ M_{13}^e & M_{13}^e & M_{33}^e & 0 & 0 & 0 \\ 0 & 0 & 0 & M_{44}^e & 0 & 0 \\ 0 & 0 & 0 & 0 & M_{44}^e & 0 \\ 0 & 0 & 0 & 0 & 0 & 2(M_{11}^e-M_{12}^e) \end{bmatrix}$$

The effective modulus of the porous material on parallel orientation and normal orientation can be obtained by:

$$E_{\perp}=(M_{11}^e)^{-1} \tag{5.45a}$$

$$E_{//}=(M_{33}^e)^{-1} \tag{5.45b}$$

During the calculation process, the Eshelby's tensors for spheroid inclusion in Appendix C was calculated with a_1/a_3=3/2 for LCS porous copper with ellipse pores. The equivalent matrix elastic modulus was fixed as the apparent modulus of the standard porous copper (see in Section 5.5.4.1) in the compression test. Gong (2011) reported that the micropores effect on the elastic modulus of porous metals produced by the space holder method can be ignored in the extended MT model when the fraction of micropores is lower than 5%. The micropores fraction in LCS porous copper is lower than 3%; therefore, its effect was not taken into account during the calculation. As the

standard sample with a relative density of 0.962 was used as the matrix in the calculations, the pore volume fraction C (in Eq. (5.43)) for each sample should be taken as the equivalent pore volume fraction: $C=C_{eff}=(\varepsilon-0.038)/0.962$, where ε is the actual porosity of the porous copper.

The relationship between the relative elastic modulus and relative density of porous copper sample is shown in Figure 5.23. The relative density and relative elastic modulus were calculated with respect to the measured density and elastic modulus of the standard sample. The calculated values from the Ex-MT model are in good agreement with the experimental values of elastic modulus, no matter which direction the porous copper samples were tested. This model, however, could not predict the elastic modulus of the samples with fine pore sizes. As mentioned in the previous section, the samples with the fine pore size had low thermal conductivity and poor mechanical properties, which were all caused by the poor bonding between the copper particles and the dead ends with little contribution to the physical and mechanical properties of the porous samples. The Ex-MT model did not consider these effects. Therefore, in the case of pore sizes being close to the copper particle sizes, the Ex-MT model is not applicable.

In some cases, the Ex-MT model can be approximated by exponent expressions for simplicity. The approximate expressions for the normalized elastic modulus of LCS

porous copper are:

$$E'_{\perp} = 0.91\rho_{eff}^{1.61} \quad (\text{for } \perp \text{ relation}) \tag{5.46a}$$

$$E'_{//} = 1.01\rho_{eff}^{1.94} \quad (\text{for } // \text{ relation}) \tag{5.46b}$$

where $E'_{\perp}$ and $E'_{//}$ is the relative elastic modulus, and ρ_{eff} is the relative density of LCS porous copper samples. The approximate expressions are similar to the Gibson-Ashby formula $E_{foam} \approx E_{solid}(\rho_{foam}/\rho_{solid})^2$, indicating that the elastic modulus of LCS porous copper still follows the power law.

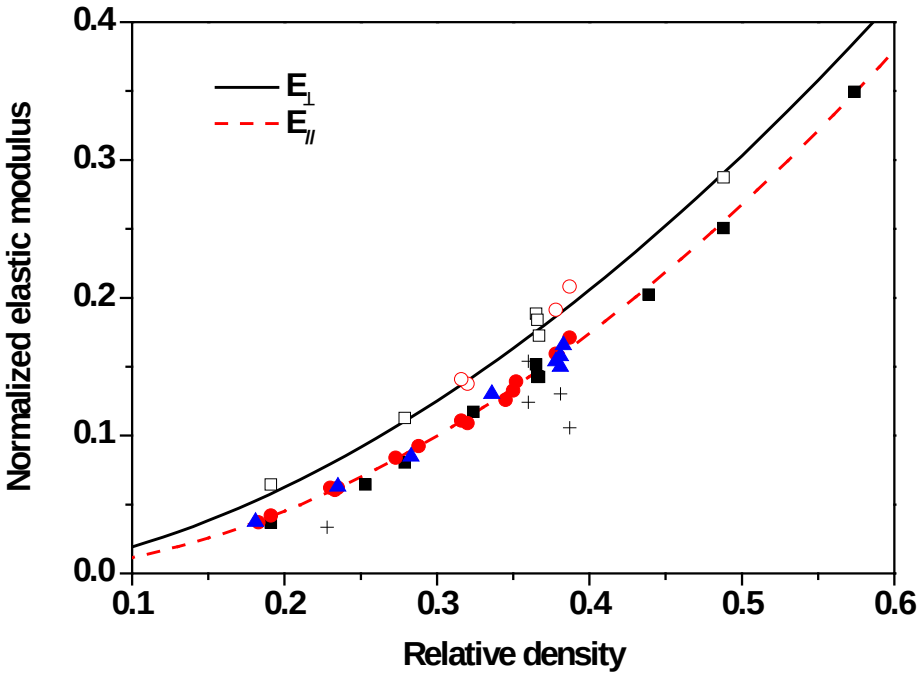

Figure 5.23 *Comparison of the measured elastic modulus values and the calculated ones by Ex-MT model. (■ elastic modulus(compression) at the '//' direction; □ elastic modulus (compression) at the '⊥' direction; ● apparent modulus (bending) at the '//' direction; ○ apparent modulus at the '⊥' direction; ▲ elastic modulus (tensile) for samples at the '//' direction; + elastic modulus for samples with fine pore size of 250-425 μm).*

Chapter 6

Conclusions and Future Work

6.1 Conclusions

Porous copper samples with different pore structures have been manufactured using LCS method. Copper powders with different particle size ranges, 50-100 μm, 100-300 μm and 600-1000 μm, were used as the raw material. Potassium carbonate powders with different particle size ranges, 250-425 μm, 425-710 μm, 710-1000 μm and 100-1500 μm were used as the space holders. The as-manufactured samples have porosities between 30% and 85%, and pore sizes between 250 and 1500 μm in diameter. The fluid transport, heat transfer and mechanical properties were investigated. It shows that LCS porous copper displays a wide range of good functional properties, making it a promising and attractive material for practical applications.

6.1.1 LCS porous metals and pore structures

The morphology and microstructure of porous copper were observed by means of optical microscopy and SEM. The pore morphology of the LCS porous copper closely matches that of the potassium carbonate particles. There are slight deviations from sphericity due to the large pressure applied during compacting. The cell walls are formed by clusters of copper particles, which are metallurgically bonded to each other.

The specific surface areas of the LCS porous copper samples were measured by the quantitative stereology method. The experimental results agree with the theoretical calculation based on the average pore size. The tortuosity values of the LCS porous copper samples were obtained from the acoustic test. It can be expressed by an empirical equation related to the porosity and the size ratio between the copper particles and the pores.

6.1.2 Fluid permeability

A purpose-built apparatus was used to measure the permeability of a range of samples. The pressure drop of LCS porous copper fits well with the Forchheimer-extended Darcy equation. The relationships between the permeability with porosity and pore size were evaluated. The permeability increases with porosity and copper particle size, but decreases with pore size. By introducing the tortuosity, a modified Carman-Konezy relationship as a function of porosity and particle/pore size ratio is established. The relationship can predict the permeability of LCS porous metals with single and double layer structures.

6.1.3 Thermal conductivity

Thermal conductivity tests were carried out on a number of porous metal samples with different pore structures. Correlations between the thermal conductivity and pore structures, such as relative density, pore size and copper particle size, have been

investigated. The thermal conductivity increases with relative density, following the power law. The exponent of the power law depends strongly on the size ratio between the copper particle and the pore. An empirical equation is established to describe this relation.

6.1.4 Heat transfer coefficient

Heat transfer performance was characterised by heat transfer coefficient in this study. The values of heat transfer coefficient vary amongst the test samples, with large pore sizes and low porosities showing excellent heat exchange capabilities. The heat transfer coefficient generally decreases with porosity, but increases with pore size. Samples with very low permeability have low heat transfer coefficients. Copper particle size strongly affects the heat transfer coefficient of LCS porous copper. The samples made with fine copper particles possess high heat transfer coefficient, at a given porosity and pore size. Heat transfer coefficients of porous copper samples with double-layer are sensitive to the placement-order. A segment model is developed for this phenomenon and the theoretical results show a good agreement with the experimental data.

6.1.5 Mechanical response

Three different mechanical tests, compression, bending and tensile test, were conducted to investigate the mechanical behavior of LCS porous copper. Increasing the relative

density and pore size can improve the mechanical properties of LCS porous copper. The apparent modulus of LCS porous copper can be predicted by the Ex-MT model.

6.2 Future Work

The LCS method is an effective way to produce porous metals with different pore structures. This thesis used spherical copper particles and potassium carbonate particles. The particle shape of the raw materials may be changed to see whether it will make a difference. The narrow particle or pore size distribution can be adopted to compare with the results already obtained to investigate the effect of particle/pore size ratio on properties in detail. Furthermore, the effects of the compacting pressure and sintering temperature or sintering time can be investigated in more detail.

The permeability test can be carried out with different gases or liquids to investigate the viscosity effect. Samples with three layers or more can be done to improve the theoretical model developed in the thesis. The entrance effect on the pressure drop in LCS porous metal can be investigated by stacking the LCS porous copper samples along the direction of the fluid flow. The thickness effect on permeability can also be studied. For the turbulent flow in porous media, the drag coefficient is the other parameter to characterise the permeable materials, and clarification of this parameter is worth investigating.

The temperature distribution in the porous copper during the heat transfer process need to be studied. Further work on the theoretical modeling of the heat transfer performance of single LCS porous copper can be carried out, especially on the investigation of the balance between permeability and thermal conductivity and the thickness effect on the heat transfer coefficient. Comparison between the heat transfer performance of LCS porous metal and other commercial heat sink can be done under the same experimental conditions. Besides, to study the balance of pressure drop and heat transport would help to place the performance of LCS porous copper in better context.

All the theoretical calculations in this thesis ignored the effects of sample size and the distribution of copper particle size and pore size. Further investigation should address these aspects. The mechanisms of the effects of the size ratio between the copper particle and the pores on the fluid transport, heat transfer and mechanical properties should also be studied in more detail.

References

Aksoz, S., Ocak, Y., Marasli, N., Cadirli, E., Kaya, H., & Boyuk, U. 2010. Dependency of the thermal and electrical conductivity on the temperature and composition of Cu in the Al based Al-Cu alloys. Experimental Thermal and Fluid Science, 34(8): 1507-1516.

Allard, J. F., & Atalla, N. 2009. Propagation of sound in porous media: modelling sound absorbing materials. Hoboken, New Jersey, USA: John Wiley &Sons Ltd.

Andersson, L., Jones, A. C., Knackstedt, M. A., & Bergstrom, L. 2011. Permeability, pore connectivity and critical pore throat control of expandable polymeric sphere templated macroporous alumina. Acta Materialia, 59(3): 1239-1248.

Antohe, B. V., & Lage, J. L. 1997. A general two-equation macroscopic turbulence model for incompressible flow in porous media. International Journal of Heat and Mass Transfer, 40(13): 3013-3024.

Antohe, B. V., Lage, J. L., Price, D. C., & Weber, R. M. 1996. Numerical characterization of micro heat exchangers using experimentally tested porous aluminum layers. International Journal of Heat and Fluid Flow, 17(6): 594-603.

Archie, G. E. 1942. The electrical resistivity log as an aid in determining some reservoir characteristics. Trans. AIME, 146: 54-61.

Ashby, M. F., Evans, T., Fleck, N. A., Hutchinson, J. W., Wadley, H. N. G., Gibson, L. J. 2000. Metal Foams:A Design Guild(1st edit). Oxford, UK: Butter- worth-Heinemann.

Aydoğmuş, T., & Bor, Ş. 2009. Processing of porous TiNi alloys using magnesium as space holder. Journal of Alloys and Compounds, 478(1-2): 705-710.

Bahadur, R., & Bar-Cohen, A. 2005. Thermal design and optimization of natural convection polymer pin fin heat sinks. IEEE Transaction on Components and Packaging Technologies, 28(2): 238-246.

Banhart, J. 2000. Manufacturing Routes for Metallic Foams. JOM, 52(12): 22-27.

Banhart, J., & Baumeister, J. 1998. Production methods for metal foams, MRS proceedings, 521: 121.

Bastawros, A. F., & Evans, A. G. 1997. Characterization of open-cell aluminum alloy foams as heat sinks for high power electronic devices. Proceeding Symposium on the Application of Heat Transfer in Microelectronics Packaging, IMECE, Dallas, TX, USA.

Bear, J. 1972. Dynamics of Fluids in Porous Media. New York, USA: Elsevier.

Bear, J. 1979. Hydraulics of groundwater. Haifa, Israel: Mc Graw-Hill International Book Co.

Beavers, G. S., & Sparrow, E. M. 1969. Non-Darcy flow through fibrous porous media. Transactions of the ASME. Series E, Journal of Applied Mechanics, 36(4): 711-714.

Bhattacharya, A., Calmidi, V. V., & Mahajan, R. L. 2002. Thermophysical properties of high porosity metal foams. International Journal of Heat and Mass Transfer, 45(5): 1017-1031.

Bloomfield, J. P. and Williams, A. T. 1995. An empirical liquid permeability-gas permeability correlation for use in aquifer properties studies. Quarterly Journal of Engineering Geology & Hydrogeology, 28:S143-S150

Boomsma, K., & Poulikakos, D. 2001. On the effective thermal conductivity of a three-dimensionally structured fluid-saturated metal foam. International Journal of Heat and Mass Transfer, 44(4): 827-836.

Boomsma, K., Poulikakos, D., & Zwick, F. 2003. Metal foams as compact high performance heat exchangers. Mechanics of Materials, 35(12): 1161-1176.

Cable, R. I., & Gupta, T. K. 1967. Intermediate Stage Sintering, Sintering and Related Phenomena. New York: Gordon and Breach.

Callister, W. D. 2000. Materials Science and Engineering: An Introduction (Fifth edit.) New York, USA: John Wiley & Sons.

Calmidi, V. V., & Mahajan, R. L. 1999. The effective thermal conductivity of high porosity fibrous metal foams. Journal of Heat Transfer-Transactions of the Asme, 121(2): 466-471.

Calmidi, V. V., & Mahajan, R. L. 2000. Forced convection in high porosity metal foams. Forced convection in high porosity metal foams, 122(3): 421-429.

Carman, P. C. 1956. Flow of gases through porous media. London, UK: Butterworth.

Chiba, H., Ogushi, T., & Nakajima, H. 2010. Heat transfer capacity of Lotus-type porous copper heat sink for air cooling. Journal of Thermal Science and Technology, 5(2): 222-237.

Childs, E. C., & Collis-George, N. 1950. The permeability of porous materials. Proceedings of the Royal Society A, 20: 392-405.

Chen, X., Wu, S., Zhou, J. 2013. Influence of porosity on compressive and tensile strength of cement mortar. Construction and Building Materials, 40:869-874.

Chu, C., Li Bo, Wang Shidong, Zhang Shuge, Yang Xiaoxi, & Yin, Z. 1997. Preparation of TiNi shape memory alloy porosint by SHS. Trans. Nonferrous Met. Soc. China 7(4): 84-87.

Colin Cameron, A., & Windmeijer, F. A. G. 1997. An R-squared measure of goodness of fit for some common nonlinear regression models. Journal of Econometrics, 77(2): 329-342.

Collins, R. E. 1961. Flow of Fluids through Porous Materials. Princeton, New Jersey, USA: Von Nostrand-Reinhold.

Comiti, J., & Renaud, M. 1989. A new model for determining mean structure parameters of fixed beds from pressure drop measurements: application to beds packed with paralleleplopedal particles. Chemical Engineering Science, 44(7): 1539-1545.

Corsan, J. M. 1984. A compact thermal conductivity apparatus for good conductors. Journal of Physics E: Scientific Instruments, 17(9): 800-807.

Dai, Z., Nawaz, K., Park, Y., Chen, Q., & Jacobi, A. M. 2013. A comparison of metal-foam heat exchangers to compact multilouver designs for air-side heat transfer applications. Heat Transfer Engineering, 33(1): 21-30.

Darcy, H. 1856. Les fontaines publiques de la ville de Dijon. Paris, France: Dalmont

Davies, G. J., & Zhen, S. 1983. Metallic foams: their production, properties and applications. Journal of Materials Science, 18(7): 1899-1911.

Degischer, H. P., & Kriszt, B. 2002. Handbook of Cellular Metals. Weinheim, Germany: Wiley-VCH.

Delgado, J. M. P. Q. 2006. A simple experimental technique to measure tortuosity in packed beds. The Canadian Journal of Chemical Engineering, 84: 651-655.

Despois, J.F., & Mortensen, A. 2005. Permeability of open-pore microcellular materials. Acta Materialia, 53(5): 1381-1388.

Dias, R., Teixeira, J. A., Mota, M., & Yelshin, A. 2006. Tortuosity variation in a low density binary particulate bed. Separation and Purification Technology, 51(2): 180-184.

Du Plessis, J. P., & Roos, L. I. 1994. Predicting the hydrodynamic permeability of sandstone with a pore-scale model. Journal of Geophysical Research, 99(B10): 19771-19776.

Dukhan, N. 2006. Correlations for the pressure drop for flow through metal foam. Experiments in Fluids, 41(4): 665-672.

Dullien, F. A. L. 1979. Porous Media: Fluid Transport and Pore Structure. New York, USA: Academic Press.

Dullien, F. A. L. 1991. Characterization of porous media-pore level. Transport in Porous Media, 6: 581-606.

Dupuit, J. 1863. Estudes Thèoriques et Pratiques sur le mouvement des Eaux dans les canaux dècouverts et à travers les terrains permèables (2nd ed.). Paris:Dunod.

Dyga, R., & Placzek, M. 2010. Efficiency of heat transfer in heat exchangers with wire mesh packing. International Journal of Heat and Mass Transfer, 53: 5494-5508.

EI-Hadek, M. A., & Kaytbay, S. 2008. Mechanical and physical characterization of copper foam. Int J Mech Mater Des, 4: 63-69.

Elliott, J. C. 1956. Method of producing metal foam. US patent:2751259.

Epstein, N. 1989. On tortuosity and the tortuosity factor in flow and diffusion through porous media. Chemical Engineering Science, 44(3): 777-779.

Ergun, S. 1952. Fluid flow through packed columns. Chemical Engineering Progress 48: 89-94.

Ergun, S., & Orning, A. A. 1949. Fluid flow through randomly packed columns and fluidized beds. Industrial and Engineering Chemistry, 41(6): 1179-1184.

Forchheimer, P. 1901. Wasserbewegung durch Boden. Zeitschrift des Vereines Deutscher Ingenieuer, 45: 1782-1788.

Fourie, J. G., & Du Plessis, J. P. 2002. Pressure drop modelling in cellular metallic foams. Chemical Engineering Science, 57: 2781-2789.

Fuganti, A., Lorenzi, L., Hanssen, A. G., & Langseth, M. 2000. Aluminium foam for automotive applications. Advanced Engineering Materials, 2(4): 200-204.

Ghassemi, A., & Pak, A. 2011. Pore scale study of permeability and tortuosity for flow through particulate media using Lattice Boltzmann method. International Journal for Numerical and Analytical Methods in Geomechanics, 35(8): 886-901.

Gibson, L. J. 2000. Mechanical behavior of metallic foams. Annu. Rev. Mater. Sci. 2000. 30:191–227.

Gibson, L. L., & Ashby, M. F. 1988. Cellular solids. Structure & properties. Oxford, UK: Pergamon Press.

Glover, P., & Walker, E. 2010. Permeability models of porous media: Characteristic length scales, scaling constants and time-dependent electrokinetic coupling. Geophysics, 75(6): E235-E246.

Gong, S. 2011. Fabrication of porous CuAlMn shape memory alloy and its fundamental issue. PhD thesis, Central South University, Changsha, China.

Gong, S., Xiao, Z. A., Li, Z. 2010. Porous CuAlMn Shape-Memory Alloys with Controlling Porosity and Pores Structural Parameter Produced by Sintering-Evaporation Process. Advanced Materials Research, 123-125: 1011.

Gong, S., Li, Z., & Zhao, Y. Y. 2011. An extended Mori-Tanaka model for the elastic moduli of porous materials of finite size. Acta Materialia, 59: 6820-6830.

Haack, D. P., Butcher, K. R., Kim, T., & Lu, T. J. 2001. Novel lightweight metal foam heat exchangers, Proceedings of 2001 ASME International Mechanical Engineering Congress and Exposition, New York, USA.

Hakamada, M., Wajima, T., Ikegami, Y., Chen, Y., Kusuda, H., & Mabuchi, M. 2006. Fluid conductivity of porous aluminum fabricated by powder-metallurgical spacer method. Japanese Journal of Applied Physics, 45(22): 575-577.

Ho, C. K., & Webb, S. W. 2006. Gas Transport in Porous Media. Albuquerque, USA: Springer.

Incropera, F. P., & DeWitt, D. P. 2007. Fundamentals of heat and mass transfer (6th ed.). New Yoke, USA: Wiley.

Incropera, F. P., Dewitt, D. P., Bergman, T. L., & S., A. A. 2013. Principles of Heat and Mass Transfer. New Jersey: John Wiley & Sons.

Innocentini, M. D. M., Antunes, W. L., Baumgartner, J. B., Seville, J. P. K., & Coury, J. R. 1999a. Permeability of ceramic membranes to gas flow. Materials Science Forum, 299-300:19-28.

Innocentini, M. D. M., Salvini, V. R., Pandolfelli, V. C., & Coury, J. R. 1999b. Assessment of Forchheimer's equation to predict the permeability of ceramic foam. Journal of the American Ceramic Society, 82(7): 1945-1948.

Iversen, N., & Jørgensen, B. B. 1993. Diffusion coefficients of sulfate and methane in marine sediments: Influence of porosity. Geochimica et Cosmochimica Acta, 57(3): 571-578.

Jang, W., & Kyriakides, S. 2009. On the crushing of aluminum open-cell foams: Part I Experiments. International Journal of Solids and Structures, 46:617 – 634

Jiang, P. X., Li, M., Lu, T. J., Yu, L., & Ren, Z. P. 2004. Experimental research on convection heat transfer in sintered porous plate channels. International Journal of Heat and Mass Transfer, 47(10-11): 2085-2096.

Jin, I., Kenny, L. D., & Sang, H. 1992. Stabilized metal foam body. US Patent:5112697.

Joseph, D. D., Nield, D. A., & Papanicolaou, G. 1982. Nonlinear equation governing flow in a saturated porous medium. Water Resources Research, 18: 1049-1052.

Joshus, P. 2013. Mechanical Properties of Materials. New York, USA: Springer.

Katz, A. J., & Thompson, A. H. 1986. Quantitative prediction of permeability in porous rock. Physical Review B (Condensed Matter), 34(11): 8179-8181.

Kaviany, M. 1995. Principles of Heat Transfer in Porous Media. New York, USA: Springer-Verlag.

Khayargoli, P., Loya, V., Lefebvre, L. P., & Medraj, M. 2004. The impact of microstructure on the permeability of metal foams. Proceedings of the CSME, London.

Kim, S. J., & Jang, S. P. 2002. Effects of the Darcy number, the Prandtl number, and the Reynolds number on local thermal non-equilibrium. International Journal of Heat and Mass Transfer, 45: 3885-3896.

Kim, S. Y., Kang, B. H., & Kim, J. 2001. Forced convection from aluminum foam materials in an asymmetrically heated channel. International Journal of Heat and Mass Transfer, 44: 1451-1454.

Kim, S. Y., Peak, J. W., & Kang, B. H. 2000. Flow and heat transfer correlations for porous fin in a plate-fin heat exchanger. Journal of Heat Transfer, 122(3), 572-578

Klemens, P. G. 1969. Theory of the thermal conductivity of solids, in Thermal Conductivity. Tye, R. P., ed., vol. 2, London: Academic Press.

Klinkenberg, L. J. 1941. The permeability of porous media to liquids and gases, Drilling and Production Practice, 1941, Document ID:41-200.

Koo, J. -M., & Jung, S. -B. 2006. Mechanical properties of copper hollow sphere manufactured by sintering process. Materials science forum, 510-511: 730-733.

Koplik, J., Lin, C., & Vermett, M. 1984. Conductivity and permeability from microgeometry. Journal of Applied Physics, 56(11): 3127-3131.

Koponen, A., Kataja, M., & Timonen, J. 1996. Tortuous flow in porous media. Physical Review E, 54(1): 406-410.

Kovácik, J., & Simancík, F. 1999. Modelling of the aluminium foam properties according to percolation theory. MetFoam '99 Proceedings, Metall Innovation Technologie MIT.

Kovács, G. 1981. Seepage Hydraulics (Developments in Water Science). New York, USA: Elsevier North-holland, Inc.

Kovácik, J. 1998. The tensile behavior of porous metals made by gasar process. Acta Materialia, 46(15): 5413-5422.

Kovácik, J. 1999. Correlation between Young's modulus and porosity in porous materials. Journal of Materials Science Letters, 18: 1007-1010.

Kozeny, J. 1927. Über kapillare Leitung des Wassers im Boden. Sitzungsber Akad. Wiss., Wien, 136(2a): 271-306.

Kreith, F., Manglik, R. M., & Bohn, M. S. 2011. Principles of heat transfer (seventh edition). Stamford, USA: Global Engineering.

Laudauer, R. 1952. The electrical resistance of binary metallic mixtures. J Appl Phys, 23: 779.

Lee, S. C., & Cunnington, G. R. 2000. Conduction and radiation heat transfer in high-porosity fiber thermal insulation. Journal of Thermophysics and Heat Transfer, 14(2): 121-136.

Lee, Y. H., Choi, J.E., & Kang, K.J. 2006. A new periodic cellular metal with kagome trusses and its performance. Paper at the ASME Conference Proceedings (2006 ASME International Mechanical Engineering Congress and Exposition), Chicago, USA.

Lenel, F. V. 1980. Powder Metallurgy: Principles and Applications. Princeton NJ, USA: Metal Powder Industries Federation

Li, B. Y., Rong, L. J., Li, Y. Y., & Gjunter, V. E. 2000. Synthesis of porous Ni–Ti shape-memory alloys by self-propagating high-temperature synthesis: reaction mechanism and anisotropy in pore structure. Acta Materialia, 48(15): 3895-3904.

Li, D. S., Zhang, Y. P., Ma, X., & Zhang, X. P. 2009. Space-holder engineered porous NiTi shape memory alloys with improved pore characteristics and mechanical properties. Journal of Alloys and Compounds, 474:1-5

Lienhard IV, J. H., & Lienhard V, J. H. 2005. A Heat Transfer Textbook (Third Edition). Cambridge, Massachusetts, USA: Phlogiston Press.

Liu, J. F., Wu, W. T., Chiu, W. C., & Hsieh, W. H. 2006. Measurement and correlation of friction characteristic of flow through foam matrixes. Experimental Thermal and Fluid Science, 30(4): 329-336.

Long, Y. 2009. Physical Properties of Materials. Changsha, China: Central south univeristy Press.

Lu, T. J., & Chen, C. 1999. Thermal transport and fire retardance properties of cellular aluminium alloys. Acta Materialia, 47(5): 1469-1485.

Mahjoob, S., & Vafai, K. 2008. A synthesis of fluid and thermal transport models for metal foam heat exchangers. International Journal of Heat and Mass Transfer, 51(15-16): 3701-3711.

Mancin, S., Zilio, C., Rossetto, L., & Cavallini, A. 2010. Experimental and analytical study of heat transfer and fluid flow through aluminum foams. Porous Media and its Applications in Science, Engineering, and Industry: 3rd International Conference , Montecatini, Italy.

Masuoka, T., & Takatsu, Y. 1996. Turbulence model for flow through porous media. International Journal of Heat Mass Transfer, 39(13): 2803-2809.

Maxwell, J. C. 1954. A Treatise on Electricity and Magnetism. New York: Dover.

McLaughlin, E. 1969. Theory of the thermal conductivity of fluids, in Thermal Conductivity. Tye, R. P., ed., vol. 1, London: Academic Press.

Medraj, M., Baril, E., Loya, V., & Lefebvre, L. P. 2007. The effect of microstructure on the permeability of metallic foams. Journal of Materials Science, 42(12): 4372-4383.

Ming, T. Z., Zheng, Y., Liu, J., Liu, C., Liu, W., & Huang, S. Y. 2010. Heat transfer enhancement by filling metal porous medium in central area of tubes. Journal of the Energy Institute, 83(1): 17-25.

Moffat, R. J. 1988. Describing the uncertainties in experimental results. Experimental Thermal and Fluid Science, 1(1): 3-17.

Mokadam, R. G. 1961. Thermodynamic analysis of the Darcy law. Journal of Applied Mechanics, 28(2): 208-212.

Montillet, A. 2004. Flow through a finite packed bed of spheres. Journal of fluids engineering, 126: 139.

Mori, T., & Tanaka, K. 1973. Average stress in matrix and average elastic energy of materials with misfitting inclusions. Acta Materialia, 27: 315-583.

Mota, M., Teixeira, J. A., Bowen, W. R., & Yelshin, A. 2001. Binary spherical particle mixed beds : porosity and permeability relationship measurement. Transactions of the Filtration Society, 1: 101-106.

Mahmoud, M. M. 2012, Manufacturing, testing, and modeling of copper foams, Global Journal of Pure and Applied Science and Technology, 212:5-13.

Niebyski, L. M., Jarema, C. P., & Lee, T. E. 1974. Preparation of metal foams with viscosity increasing gases.US Patent:3816952

Nield, D. A., & Bejan, A. 1999. Convection in Porous Media (2nd ed.), New York, USA: Springer-Verlag.

Odabaee, M., Hooman, K., & Gurgenci, H. 2011. Metal foam heat exchangers for heat transfer augmentation from a cylinder in cross-flow. Transpport in Porous Media, 86: 911-923.

Older, I., Robler, M. 1985. Investigations on the relationship between porosity,structure and strength of hydrated Portland cement pastes II-Effect of pore structure and degree of hydration. Cem Concr Res, 15:401-410.

Ogushi, T., Chiba, H., Nakajima, H., & Ikeda, T. 2004. Measurement and analysis of effective thermal conductivities of lotus-type porous copper. Journal of Applied Physics, 95(10): 5843-5847.

Parvanian, A. M., Panjepour, M. 2013, Mechanical behavior improvement of open-pore copper foams synthesized through space holder technique, Materials and Design, 49:834-841.

Phani, K. K., Niyogi, S. K., & De, A. K. 1988. Porosity dependence of fracture mechanical properties of reaction sintered Si_3N_4. Journal of Materials Science Letters, 7(11): 1253-1256.

Qiao, J. C., Xi, Z. P., Tang, H. P., Wang, J. Y., & Zhu, J. L. 2008. Compressive property and energy absorption of porous sintered fiber metals. Materials Transactions, 49(12): 2919-2921.

Qu, W., Mala, G. M., & Li, D. 2000. Heat transfer for water flow in trapezoidal silicon microchannels. International Journal of Heat and Mass Transfer, 43: 3925-3936.

Ren, X. 1998. The theory and applications of powder plastic deformation. Beijing, China: Metallurgical Industry Press.

Richardson, J. T., Peng, Y., & Remue, D. 2000. Properties of ceramic foam catalyst supports: pressure drop. Applied Catalysis a-General, 204(1): 19-32.

Ridgway, C. J., Schoelkopf, J., & Gane, P. A. C. 2003. A new method for measuring the liquid permeability of coated and uncoated papers and boards. Nordic Pulp and Paper Research Journal, 18(4): 377-381.

Roylance, D. 2008. Mechanical Properties of Materials. Cambridge, USA: MIT

Scheidegger, A. E. 1974. The Physics of Flow through Porous Media (third edition). Toronto, Canada: University of Toronto Press.

Schuetz, M. A., & Glicksman, L. R. 1984. A basic study of heat transfer through foam insulation. Journal of Cellular Plastics, 20: 114.

Schwartz, D. S., & Shih, D. S. 1998. Porous and cellular materials for structural applications. Paper presented at the Materials Research Society Proceedings, Warrendale PA, USA

Schwartz, J., & Probstein, R. F. 1969. Experimental study of slurry separators for use in desalination. Desalination, 6: 239-266.

Sevostianov, I., Kovacik, J., & Simancik, F. 2006. Elastic and electric properties of closed-cell aluminum foams cross-property connection. Materials Science and Engineering A 420: 87-99.

Shen, S., Xu, J. L., Zhou, J. J., & Chen, Y. 2006. Flow and heat transfer in microchannels with rough wall surface. Energy Conversion and Management, 47: 1311-1325.

Shapovalov, V. I. 1993. Method for manufacturing porous articles. US Patent:5181549

Shapovalov, V. I., Withers, J. C. 2011, Main Types of Gasar Structure and Production Methods, Presented in John & Virginia Towers Lecture Series, Spring 2011, Michigan Technological University, USA, on line at http://www.metalfoam.net/Papers-conference/2007-Montreal-Paper.pdf

Shih, W. H., Chiu, W. C., & Hsieh, W. H. 2006. Height effect on heat-transfer characteristics of aluminum foam heat sinks. Transactions of the ASME, 128: 530-537.

Singh, R., & Kasana, H. S. 2004. Computational aspects of effective thermal conductivity of highly porous metal foams. Applied Thermal Engineering, 24(13): 1841-1849.

Skochdopole, R. E. 1965. Cellular Materials. In Mark, H. F. & Gaylord N. G. (Eds.), Encyclopedia of Polymer Science and Technology, Vol. 3: 80-130. New York, USA: John Wiley & Sons.

Sosnick, B. 1948. Process for making foamlike mass of metal. US Patent:2434775.

Sullins, A. D., & Daryabeigi, K. 2001. Effective thermal conductivity of high porosity open cell nickel foam. Paper presented at the 35th AIAA Thermophysics Conference, Anaheim, CA. USA

Tamayol, A., & Hooman, K. 2011. Thermal assessment of forced convection through metal foam heat exchangers. Journal of Heat Transfer-Transactions of the ASME, 133: 111801(1)-111801(7).

Tao, X. F., Zhang, L. P., & Zhao, Y. Y. 2007. Mechanical response of porous copper manufactured by Lost Carbonate Sintering process. Materials Science Forum, 539-543: 1863.

Thewsey, D. J. 2008. Multifunctionality of porous copper manufactured by Lost Carbonate Sintering. PhD thesis, University of Liverpool, Liverpool, UK

Thewsey, D. J., & Zhao, Y. Y. 2008. Thermal conductivity of porous copper manufactured by the lost carbonate sintering process. Physica Status Solidi A, 205(5): 1126-1131.

Underwood, E. E. 1970. Quantitative Stereology. Marietta, Georgia: Addison-Wesley Publishing Company.

Vallabh, R., Banks-Lee, P., & Seyam, A.F. 2010. New approach for determining tortuosity in fibrous porous media. Journal of Engineered Fibers and Fabrics, 5(3): 7-15.

Venkataraman, P., & Rao, P. R. M. 2000. Validation of Forchheimer's law for flow through porous media with converging boundaries. Journal of Hydraulic Engineering, 126(1): 63-71.

Vidal, D., Ridgway, C., Pianet, G., Schoelkopf, J., Roy, R., & Bertrand, F. 2009. Effect of particle size distribution and packing compression on fluid permeability as predicted by lattice-Boltzmann simulations. Computers & Chemical Engineering, 33(1): 256-266.

Wang, J. F., Carson, J. K., North, M. F., & Cleland, D. J. 2008a. A new structural model of effective thermal conductivity for heterogeneous materials with co-continuous phases:. Int J Heat Mass Transfer 51: 2389.

Wang, J. F., Carson, J. K., Willix, M. F., North, M. F., & Cleland, D. J. 2008b. A symmetric and interconnected skeleton structural (SISS) model for predicting thermal and electrical conductivity and Young's modulus of porous foams. Acta Materialia, 56: 5138-5146.

Wang, Q. Z., Cui, C. X., Liu, S. J., & Zhao, L. C. 2010. Open-celled porous Cu prepared by replication of NaCl space-holders. Materials Science and Engineering: A, 527(4-5): 1275-1278.

Ward, J. 1964. Turbulent flow in porous media. Journal of Hydraulics Division American Society of Civil Engineers, 90:1-12.

Weissberg, H. L. 1963. Effective diffusion coefficient in porous media. Journal of Applied Physics, 34(9): 2636-2639.

Wen, C. E., Yamada, Y., Shimojima, K., Chino, Y., Asahina, T., & Mabuchi, M. 2002. Processing and mechanical properties of autogenous titanium implant materials. Journal of Materials Science: Materials in Medicine, 13(4): 397-401.

White, M. A. 2011. Physical Properties of Materials. Boca Raton, FL, USA: CRC Press, Taylor & Francis Group.

Wong, P., Koplik, J., & Tomanic, J. P. 1984. Conductivity and permeability of rocks. Physical Review B (Condensed Matter), 30(11): 6606-6614.

Yu, C. J., Eifert, H. H., Banhart, J., & Baumeister, J. 1998. Metal foaming by a powder metallurgy method: production, properties and applications. Materials Research Innovations, 2(3): 181-188.

Zhang, E., & Wang, B. 2005. On the compressive behaviour of sintered porous coppers with low to medium porosities—Part I: Experimental study. International Journal of Mechanical Sciences, 47(4–5): 744-756.

Zhang, H. Y., injala, D., Joshi, Y. K., Wong, T. N., Toh, K. C., & Iyer, M. K. 2005a. Fluid flow and heat transfer in liquid cooled foam heat sinks for electronic packages. IEEE Transactions on Components and Packaging Technologies, 28(2): 272-280.

Zhang, H. Y., Pinjala, D., Wong, T. N., & Joshi, Y. K. 2005b. Development of liquid cooling techniques for flip chip ball grid array packages with high heat flux dissipations. IEEE Transactions on Components and Packaging Technologies, 28(1): 127-135.

Zhang, L., Mullen, D., Lynn, K., & Zhao, Y. 2009. Heat transfer performance of porous copper fabricated by the Lost Carbonate Sintering process. Materials Research Society Symposium Proceedings, 1188: 213-218

Zhang, T. C., & Bishop, P. L. 1994. Evaluation of tortuosity factors and effective diffusivities in biofilms. Water Research, 28(11): 2279-2287.

Zhao, C. Y., Kim, T., Lu, T. J., & Hodson, H. P. 2004. Thermal transport in high porosity cellular metal foams. Journal of Thermophysics and Heat Transfer, 18(3): 309-317.

Zhao, X., Sun, H., Lan, L., Huang, J., Zhang, H., & Wang, Y. 2009. Pore structures of high-porosity NiTi alloys made from elemental powders with NaCl temporary space-holders. Materials Letters, 63(28): 2402-2404

Zhao, Y. Y., Fung, T., Zhang, L. P., & Zhang, F. L. 2005. Lost carbonate sintering process for manufacturing metal foams. Scripta Materialia, 52(4): 295-298.

Zhao, Y. Y., & Sun, D. X. 2001. A Novel Sintering-Dissolution Process for Manufacturing Al Foams. Scripta Materialia, 44: 105-110.

Zhu, J., Zhang, B., & Zhang, W.-Y. 2012. Determination of the acoustical parameters of porous metals based on Johnson-Champoux-Allard model. 16th International Conference on Mechatronics Technology, Tianjin, China.

Zou, C., Zhang, E., Li, M., & Zeng, S. 2008. Preparation, microstructure and mechanical properties of porous titanium sintered by Ti fibres. Journal of Materials Science: Materials in Medicine, 19(1): 401.

Appendies

Appendix A Determination of tortuosity of porous copper samples based on Johnson- Champoux-Allard Model

Assuming that the porous medium is isotropic and the skeleton of material is stiff (i.e.: ignoring the vibration of its solid frame and only taking acoustic waves propagating in the fluid inside the pores into account), its sound absorption properties can be described by means of the equivalent fluid models and calculated by an equivalent dynamic density and a dynamic bulk modulus. While propagating through the porous materials, the sound waves are attenuated due to the viscous and thermal dissipation mechanisms existing in porous materials. The dynamic density accounts for the viscous losses, and the dynamic bulk compression modulus for the thermal losses. The model (Johnson-Champoux-Allard model) can be expressed by the following equation:

$$\rho_{eff} = \tau^2 \rho_0 \left[1 + \frac{\sigma \varepsilon}{j \rho_0 \omega \tau^2} G_J(\omega) \right] \tag{A1}$$

$$G_J(\omega) = \sqrt{1 + \frac{4 j \tau^4 \mu \rho_0 \omega}{\sigma^2 \Lambda^2 \varepsilon^2}} \tag{A2}$$

$$K_{eff} = \frac{\gamma P}{\gamma - (\gamma - 1)\left[1 + \frac{8\mu}{j \Lambda'^2 B^2 \rho_0 \omega} \sqrt{1 + \frac{j \Lambda'^2 B^2 \rho_0 \omega}{16 \mu}} \right]^{-1}} \tag{A3}$$

$$\Lambda = \frac{1}{c} \sqrt{\frac{8 \tau^2 \mu}{\sigma_0 \varepsilon}} \tag{A4}$$

$$\Lambda' = \frac{1}{c'} \sqrt{\frac{8 \tau^2 \mu}{\sigma_0 \varepsilon}} \tag{A5}$$

$$k_{eff} = \omega\sqrt{\frac{\rho_{eff}}{K_{eff}}} \tag{A6}$$

$$Z_f = \left(\frac{Z_c}{\varepsilon}\right)\left(\frac{-jZ_b\cot(k_{eff}l) + Z_c}{Z_b - jZ_c\cot(k_{eff}l)}\right) \tag{A7}$$

$$Z_c = \sqrt{K_{eff}\rho_{eff}} \tag{A8}$$

$$R = \frac{Z_f - Z_0}{Z_f + Z_0} \tag{A9}$$

$$A_0 = 1 - |R|^2 \tag{A10}$$

where ε is the porosity, σ the static flow resistivity, τ^2 the tortuosity factor, Λ is the viscous characteristic length, Λ' is the characteristic thermal length, c is the viscous shape factor, c' is the thermal shape factor, ρ_{eff} is the effective density of air in pore in porous materials, ρ_0 is the static density of air, K_{eff} is the effective bulk modulus, k_{eff} is the complex wave number, l is the thickness of samples, Z_b is the acoustic impedance at the rear face of samples, Z_f is the surface normal acoustic impedance of materials, Z_0 is the characteristic impedance of free air, ω the angular frequency, γ is the specific heat ratio of air, P is the static pressure, μ the dynamic viscosity of air, $j = \sqrt{-1}$, Prandtel number $B^2 = 0.71$, and R and A_0 are the sound reflection and absorption coefficient of materials at normal incidence, respectively.

The process of the determination of the acoustic parameters of porous metals is given as follows:

i. Determine the varying ranges of the acoustic parameters in acoustic model.

ii. Start global search in feasible domain of optimization variables using hybrid genetic algorithm together with simulated annealing penalty function to obtain a set of acoustic parameters.

iii. Make the substitution of the acoustic parameters obtained in step (ii) into Eq. (A1)-(A10) and further calculate the theoretical acoustic impedance and sound absorption coefficients of porous materials as a theoretical observing data.

iv. Compare the measured data with those observing data.

v. Repeat the steps (i)- (iv) and choose the acoustic parameters, from which the best fits with measured data are achieved, as the final inverse results.

There are seven acoustic parameters that involved in Johnson-Champoux-Allard model (from Eq. (A1) to (A10)): ε, σ, τ^2, Λ, Λ', c and c'. Commonly, to enhance the computational accuracy of determining the acoustic parameters, the less unknown independent acoustic parameters of materials are encouraged to be included in models. The porosity and the static flow resistivity of materials have been got in advance by means of Archimedes method and permeability test, respectively. Λ and Λ' can be obtained with given parameters of σ, τ^2, c and c'. The array vector of $\vec{a} = [c\ \tau^2\ c']^T$ is chosen as variants for computation. It has been pointed that $1 < \tau^2 < 10$ and $0.3 < c, c' < 3.3$ for many porous materials (Allard & Atalla 2009). Therefore, the same varying quantitative ranges are used in the work also. Because the normalized surface acoustic

impedance of sintered porous metals can be measured conveniently, in inverse computations we choose real and imaginary part of above impedance among the frequency ranges of 500 - 6400Hz as the computational objective so that the least errors between the theoretically calculated $(Z_f^{(c)})$and measured acoustic impedance $(Z_f^{(m)})$ mentioned above may be easily achieved simultaneously. The final objective function $f_{obj}(\omega,\vec{a})$ is defined as :

$$f_{obj}(\omega,\vec{a}) = \sum_{i=1}^{N} \left| Z_f^{(m)}(\omega_i,\vec{a}) - Z_f^{(c)}(\omega_i,\vec{a}) \right|^2 \qquad \text{(A11)}$$

where $\vec{a} = [c\ \tau^2\ c']$.

In the genetic computations, the maximum number of individuals is equal to 100; the individuals are coded using binary system. The coding lengths of individuals are all set to be nine bits such that the computational results can be expressed by two bits behind decimal point. As for the genetic operators, we select random ergodic sampling manner, the generation gap is 0.9, the probability of crossover (one-point crossover) P_c is 0.9, and the probability of mutation P_m is 0.04.The termination of evolutional algorithm are controlled by the maximum numbers of generations which are made to be 500 and 50, respectively.

Appendix B Heat transfer coefficient of samples in Table 4.13 with different thicknesses

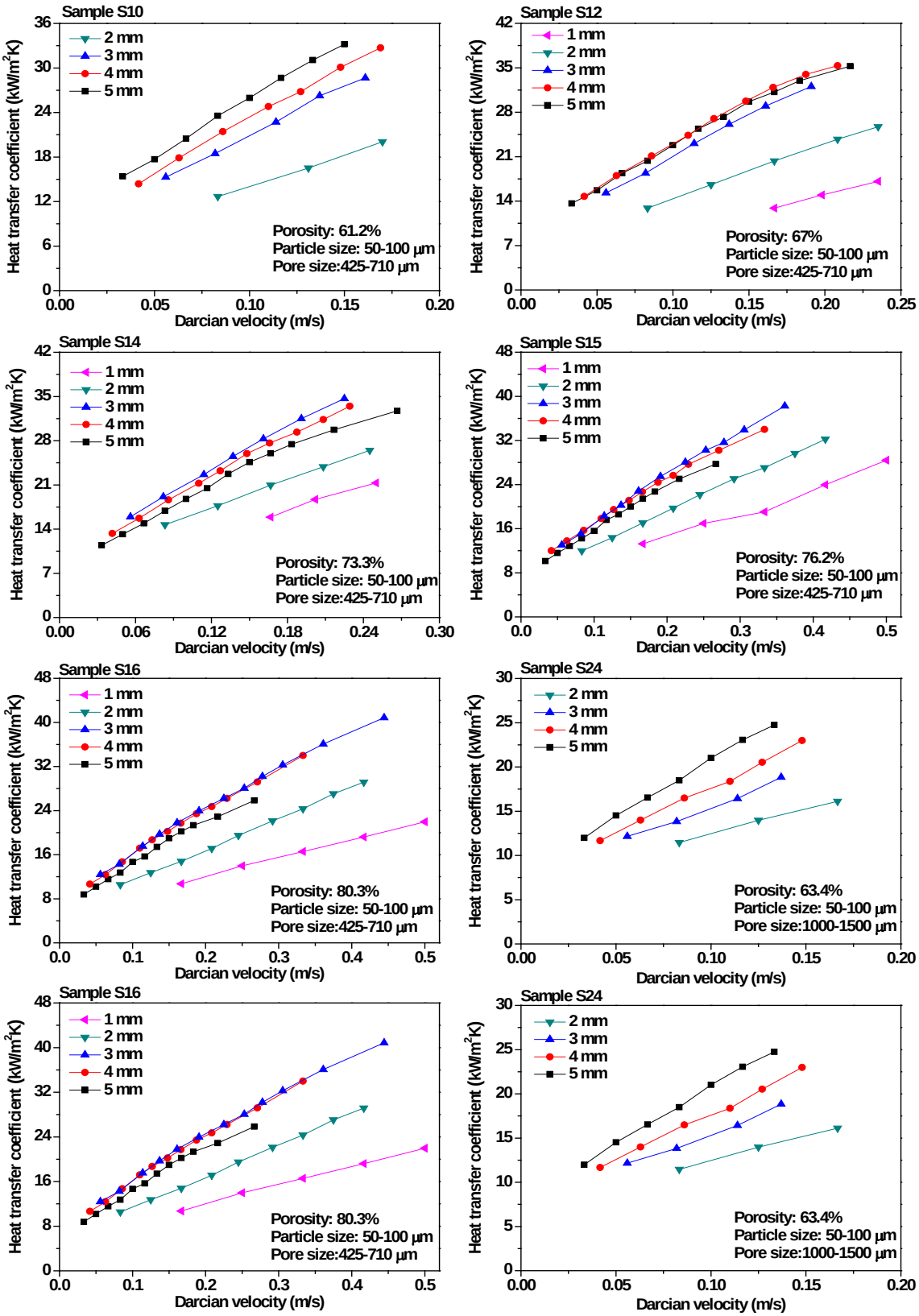

Figure 4.29 *Variation of heat transfer coefficient with Darcian velocity for porous copper samples with different thicknesses (Input heat power: 250 kW/m^2).*

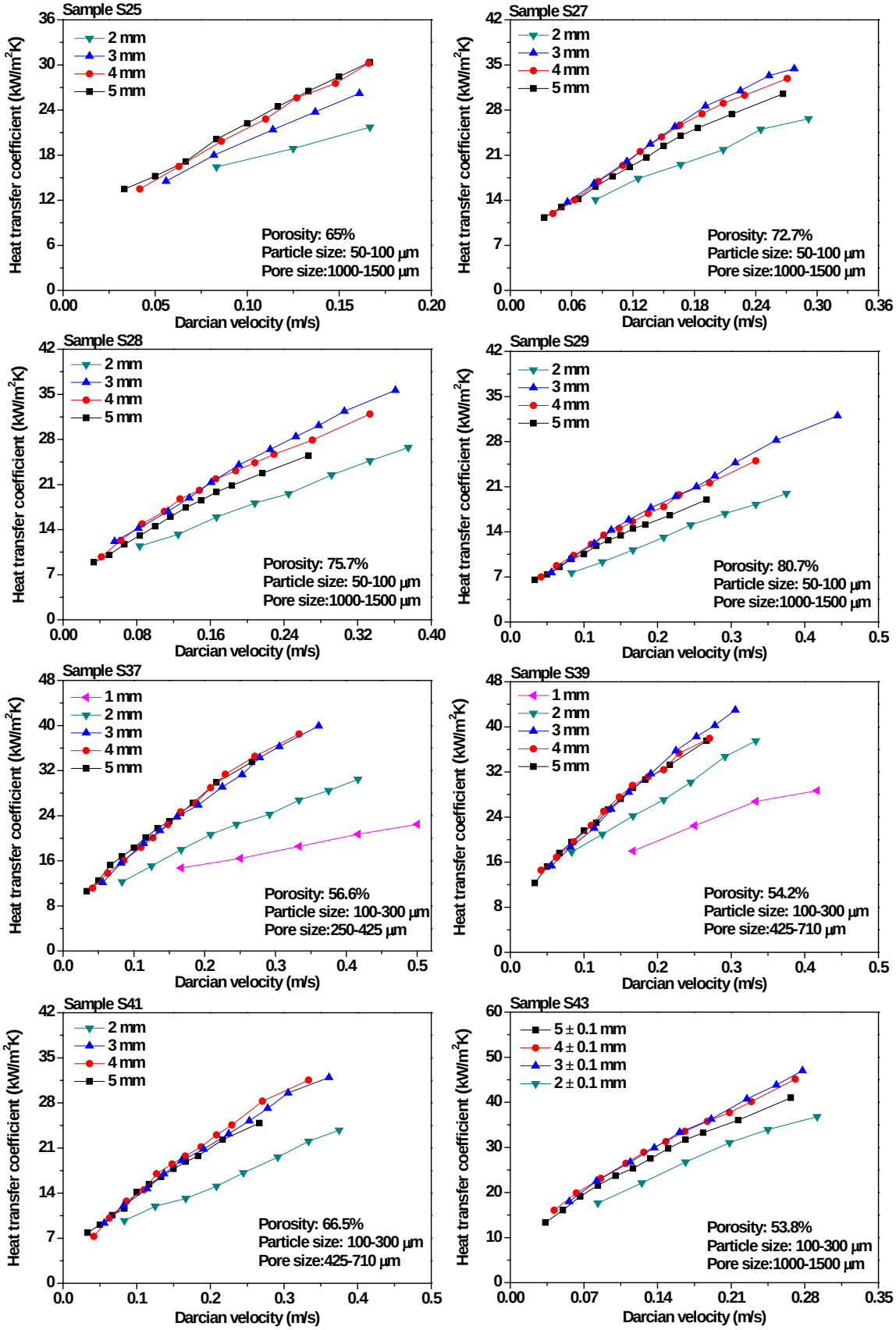

Figure 4.29 *Variation of heat transfer coefficient with Darcian velocity for porous copper samples with different thicknesses (Input heat power: 250 kW/m^2).*

Appendix C Eshelby's tensor for spheroid inclusions in a transversely isotropic matrix

For a transversely isotropic matrix, the elastic moduli are denoted by:

$L_{11}^m = d$, $\frac{1}{2}(L_{11}^m - L_{12}^m) = e$, $L_{44}^m = f$, $L_{13}^m + L_{44}^m = g$, $L_{33}^m = h$;

where L_{ij}^m is the Voigt constants.

For ellipse pores with an axis ratio of $\kappa = a_1/a_3$ (where a_1 is the major axis, and a_3 is the minor axis), the Eshelby's tensor S is calculated by:

$$S_{ijmn} = \frac{1}{8\pi} L_{pqmn}^m (\bar{G}_{ipjq} + \bar{G}_{jpiq}) \tag{C1}$$

$\bar{G}_{ijkl}$ is the non-zero components and given below:

$$\bar{G}_{1111} = \bar{G}_{2222} = \frac{1}{2}\pi \int_0^1 \Delta(1-x^2)\left\{\left[f(1-x^2) + h\kappa^2 x^2\right] \times \left[(3e+d)(1-x^2) + 4f\kappa^2 x^2\right] - g^2\kappa^2 x^2 (1-x^2)\right\} dx$$

$$\bar{G}_{3333} = 4\pi \int_0^1 \Delta\kappa^2 x^2 \left[d(1-x^2) + f\kappa^2 x^2\right]\left[e(1-x^2) + f\kappa^2 x^2\right] dx$$

$$\bar{G}_{1122} = \bar{G}_{2211} = \frac{1}{2}\pi \int_0^1 \Delta(1-x^2)\left\{\left[f(1-x^2) + h\kappa^2 x^2\right] \times \left[(e+3d)(1-x^2) + 4f\kappa^2 x^2\right] - 3g^2\kappa^2 x^2 (1-x^2)\right\} dx$$

$$\bar{G}_{1133} = \bar{G}_{2233} = 2\pi \int_0^1 \Delta\kappa^2 (1-x^2)\left\{\left[(d+e)(1-x^2) + 2f\kappa^2 x^2\right] \times \left[f(1-x^2) + h\kappa^2 x^2\right] - g^2\kappa^2 x^2 (1-x^2)\right\} dx$$

$$\bar{G}_{3311} = \bar{G}_{3322} = 2\pi \int_0^1 \Delta(1-x^2)\left\{\left[d(1-x^2) + f\kappa^2 x^2\right] \times \left[e(1-x^2) + h\kappa^2 x^2\right] - g^2\kappa^2 x^2 (1-x^2)\right\} dx$$

$$\bar{G}_{1212} = \frac{1}{2}\pi \int_0^1 \Delta(1-x^2)\left\{g\kappa^2 x^2 - (d-e)\left[f(1-x^2) + h\kappa^2 x^2\right]\right\} dx$$

$$\bar{G}_{1313} = \bar{G}_{2323} = (-2\pi)\int_0^1 \Delta g\kappa^2 x^2 (1-x^2)\left[e(1-x^2) + f\kappa^2 x^2\right] dx$$

where $\Delta^{-1} = \left[e(1-x^2) + f\kappa^2 x^2\right]\left\{\left[d(1-x^2) + f\kappa^2 x^2\right] \times \left[f(1-x^2) + h\kappa^2 x^2\right] - g^2\kappa^2 x^2 (1-x^2)\right\}$